Modeling of time-dose-LET effects in the cellular response to radiation

Modellierung von Zeit-Dosis-LET Effekten in der zellulären Reaktion auf Bestrahlung
Zur Erlangung des Grades eines Doktors der Naturwissenschaften (Dr. rer. nat.)
genehmigte Dissertation von M.Sc. Lisa Antje Herr aus Frankfurt am Main
Tag der Einreichung: 26.06.15, Tag der Prüfung: 20.07.15
Darmstadt 2015 — D 17

1. Gutachten: Prof. Dr. Marco Durante
2. Gutachten: Prof. Dr. Barbara Drossel

TECHNISCHE UNIVERSITÄT DARMSTADT

Fachbereich Physik
Institut für Festkörperphysik

Modeling of time-dose-LET effects in the cellular response to radiation
Modellierung von Zeit-Dosis-LET Effekten in der zellulären Reaktion auf Bestrahlung

Genehmigte Dissertation von M.Sc. Lisa Antje Herr aus Frankfurt am Main

1. Gutachten: Prof. Dr. Marco Durante
2. Gutachten: Prof. Dr. Barbara Drossel

Tag der Einreichung: 26.06.15
Tag der Prüfung: 20.07.15

Darmstadt 2015 — D 17

Abstract

This work is dedicated to the elucidation of time-dose- and if applicable linear energy transfer (LET) effects in the cellular response to ion or photon radiation. In particular, the common concept of the Local Effect Model (LEM) and the Giant Loop Binary Lesion (GLOBLE) model, which explains cell survival probabilities on the hand of clustering of double-strand breaks (DSB) in micrometer-sized sub-structural units of the DNA, was investigated with regard to temporal aspects. In previous studies with the LEM and GLOBLE model, it has been demonstrated that the definition of two lesion classes, characterized by single or multiple DSB in a DNA giant loop, with two repair fidelities is adequate to comprehensively describe the dose dependence of the cellular response to instantaneous photon irradiation or ion irradiation with varying LET. Furthermore, with the GLOBLE model for photon radiation, it has been shown that the assignment of two repair time scales to the two lesion classes allows to adequately reproduce time-dose effects after photon irradiation with an arbitrary constant dose-rate.

In this work, the results of four projects that strengthen the mechanistic consistency and the practical applicability of the LEM and GLOBLE model will be presented. First, it was found that the GLOBLE model is applicable to describe time-dose effects in the cellular response to two split photon doses and in the occurrence of deterministic radiation effects. Second, in a comparison of ten models for the temporal course of DSB rejoining, it was revealed that a bi-exponential approach, as suggested by the LEM and GLOBLE model, finds a relatively large support by 61 experimental data sets. Third, in a comparison of four kinetic photon cell survival models that was based on fits to 13 dose-rate experiments, it was shown that the GLOBLE model performs well with respect to e.g. accuracy, parsimony, reliability and other factors that characterize a good approach. Last but not least, the dynamic concept of two time scales of cellular repair was introduced in the LEM. The consistency of predictions with this new kinetic model for ion radiation effects was verified and an agreement with experimental data was detected. In summary, the theoretical evidence that the time-dose-LET-dependence of the cellular response to radiation is explicable with radiation-characteristic damage distribution patterns on micrometer-scale was affirmed.

Zusammenfassung

Diese Arbeit ist der Aufklärung des Einflusses gewidmet, den die Zeit, die Dosis und gegebenenfalls der lineare Energietransfer (LET) auf die zelluläre Reaktion auf Photonen- oder Ionen-Bestrahlung haben. Insbesondere wurde das gemeinsame Konzept des Giant Loop Binary Lesion (GLOBLE) Modells und des Local Effect Models (LEM), welches Zell-Überlebenswahrscheinlichkeiten mit einer Anhäufung von DNA Doppelstrangbrüchen (DSB) in Mikrometer-Strukturen der DNA erklärt, hinsichtlich zeitlicher Aspekte untersucht. In vorhergehenden Studien wurde mit dem LEM und GLOBLE Modell bereits demonstriert, dass die Definition von zwei Schadenskategorien, die sich durch einzelne oder gehäufte DSB in einem DNA "giant loop" auszeichnen, und von zwei zugehörigen Reparatur-Zuverlässigkeiten geeignet ist, um die Dosisabhängigkeit in der zellulären Reaktion auf instantane Photonen- und Ionen-Bestrahlung mit variablem LET übergreifend zu beschrieben. Zudem wurde mit dem GLOBLE Modell für Photonen-Bestrahlung gezeigt, dass die Zuordnung von zwei Reparatur-Zeitskalen zu den zwei Schadenskategorien es ermöglicht, Zeit-Dosis-Effekte in der zellulären Reaktion auf Photonen-Bestrahlung mit beliebiger konstanter Dosisrate angemessen zu reproduzieren.

In dieser Arbeit werden vier Projekte präsentiert werden, die die mechanistische Konsistenz und die praktische Anwendbarkeit des LEM und GLOBLE Modells bestärken. Erstens wurde festgestellt, dass das GLOBLE Modell für die Beschreibung von Zeit-Dosis Effekten anwendbar ist, die in der zellulären Reaktion auf zwei geteilte Dosen oder im Auftreten von deterministischen Strahlungseffekten beobachtbar sind. Zweitens wurde in einem Vergleich von zehn Modellen für DSB Reparatur festgestellt, dass ein bi-exponentieller Ansatz, wie ihn das LEM und GLOBLE Modell verfolgen, von 61 experimentellen Datensätzen relativ stark unterstützt wird. Drittens wurde in einem Vergleich von vier kinetischen Photonen-Zellüberlebensmodellen, die an 13 Dosisraten-Experimente angepasst wurden, gezeigt, dass das GLOBLE Modell seine Aufgabe hinsichtlich Kriterien wie Akkuratheit, Sparsamkeit mit freien Parametern und Zuverlässigkeit gut erfüllt. Zu guter Letzt wurde wurde das dynamische Konzept von zwei Reparatur-Zeitskalen für die zwei Schadensklassen auf das LEM übertragen. Die Konsistenz von Vorhersagen dieses neuen kinetischen Modells für Ionen-Bestrahlungs-Effekte wurde verifiziert und eine Übereinstimmung mit experimentellen Messungen festgestellt. Zusammenfassend wurde die theoretische Beweislage, dass Zeit-Dosis-LET-Effekte in der zellulären Reaktion auf Bestrahlung mit strahlungs-charakteristischen Schadensverteilungen auf Mikrometer-Ebene erklärt werden können, bekräftigt.

Contents

List of abbreviations

1st2ndO	First- and second-order
2ndO	Second-order
AIC	Akaike Information Criterion
AICc	Akaike Information Criterion for low sample size
BEIR	National Academy of Sciences Advisory Committee on the Biological Effects of Ionizing Radiation
BiExp	Bi-exponential
BiExpO	Bi-exponential with offset
cDSB	Clustered DSB
DDREF	Dose and dose-rate reduction factor
DLL	Directly lethal lesions
DNA	Deoxyribonucleic acid
DSB	Double-strand break
ExpExp	Mono-exponential with exponentially distributed decay rate
FUD	Fraction of unrejoined damage
GammaExp	Mono-exponential with gamma-distributed decay rate
GaussianExp	Mono-exponential with Gaussian-distributed decay rate
GCR	Galactic cosmic rays
GLOBLE	Giant Loop Binary Lesion
GSI	GSI Helmholtzzentrum für Schwerionenforschung GmbH
HR	Homologous recombination
ICRP	International Commission on Radiological Protection
iDSB	Isolated DSB
ISS	International Space Station
LC-LQ	Linear-Quadratic with Lea Catcheside fomalism
LEM	Local Effect Model
LET	Linear Energy Transfer
LQ	Linear-Quadratic
LQL	Linear-Quadratic-Linear
LPL	Lethal Potentially Lethal
MonoExp	Mono-exponential
MonoExpO	Mono-exponential with offset
NHEJ	Non-homologous end-joining
PFGE	Pulsed-field gel electrophoresis
PLL	Potentially lethal lesions
RBE	Relative Biological Effectiveness
RMR	Repair Misrepair
SSB	Single-strand break
TriExp	Tri-exponential
U-lesions	Uncommitted lesions

Publications related to this work

Peer-reviewed articles

(i) Herr L, Friedrich T, Durante M, Scholz M. A model of photon cell killing based on the spatio-temporal clustering of DNA damage in higher order chromatin structures. *PLoS ONE*, 9(1):e83923, 2014.

(ii) Herr L, Friedrich T, Durante M, Scholz M. Sensitivity of the Giant Loop Binary Lesion model on parameters characterising dose rate effects. *Radiation Protection Dosimetry*, doi: 10.1093/rpd/ncv150, 2015.

(iii) Herr L, Shuryak I, Friedrich T, Scholz M, Durante M, Brenner DJ. New insight into quantitative modeling of DNA double strand break rejoining. *Radiation Research*, accepted for publication, 2015.

(iv) Hufnagl A, Herr L, Friedrich T, Durante M, Taucher-Scholz G, Scholz M. The link between cell-cycle dependent radiosensitivity and repair pathways: a model based on the local, sister-chromatid conformation dependent switch between NHEJ and HR. *DNA Repair*, 27: 28–39, 2015.

(v) Herr L, Friedrich T, Durante M, Scholz M. A comparison of kinetic photon cell survival models. *Radiation Research*, under review, 2015.

(vi) Herr L, Friedrich T, Durante M, Scholz M. Investigation of time-dose relationships in the cellular response to ion irradiation with the Local Effect Model. In preparation.

Scientific reports

(i) Herr L, Friedrich T, Durante M, Scholz M. A sensitivity analysis of the Giant LOop Binary LEsion model. *GSI Scientific Report*, 237, 2013.

(ii) Herr L, Friedrich T, Durante M, Scholz M. Modeling time effects in the incidence of deterministic effects of radiation. *GSI Scientific Report*, 2014.

1 General introduction

Humans are exposed to ionizing radiation every day, e.g. to terrestrial radiation or to ingestion and inhalation of radioactive matter in the nutrition and air. Actually, this exposure causes an inevitable biological damage in the body of everyone. However, the fact that the major fraction of the population does not die because of radiation-induced diseases suggests that most of us tolerate daily radiation exposures very well. There are efficient cellular repair mechanisms that usually remove biological damage before it can lead to further harm.

On the other hand, there are non-natural radiation exposures which lead to a failure of cellular repair mechanisms and increase the risk for the incidence of diseases related to cellular misrepair or cell death. For instance, an accidental or occupational exposure may increase the risk for cancer, pneumonitis or the bone marrow syndrome. For the purpose of radiation risk assessments, it is therefore necessary to define relevant characteristics of radiation exposures, to identify their impact on the cellular radiation response and to quantify probabilities for the incident of diseases. Amongst others, the physical dose, the dose delivery schedule and the radiation quality in terms of photon or ion radiation with corresponding linear energy transfer are considered as major physical determinants of radiation effects. When these parameters can be controlled and corresponding effects on cells and tissues can be assessed, active processes of decision making regarding the handling of radiation risks are allowed for. As a first example, for radiation protection, it is aimed to identify threshold values which should guarantee acceptable excess risks for workers. As a second example, when it is expected that radiation-induced side effects are tolerable, one can even benefit from the harmful nature of radiation by maximization of destructive effects in tumors during radiotherapy.

In order to establish the relationship between radiation quality and cellular radiation response, experiments where e.g. in vitro cell survival and transformation probabilities are measured are of value. Furthermore, empirical studies which systematically screen factors impacting the radiation response provide a way to quantify excess risks in the occurrence of diseases. However, as soon as radiation effects should be determined for situations that have not yet occurred or that have not explicitly been investigated, adequate models are needed for extrapolations and predictions. Corresponding computations help to find recommendations for general limits of occupational exposures and optimal radiation treatment plans. Furthermore, when models for a radiation response are mechanistically motivated, i.e. when they suggest a causality between the radiation-induced biological damage, the cellular processing of it and the finally observed endpoint, they are instructive. By fits to empirically found or experimentally measured data, one can derive parameters for underlying mechanisms and thus gain insight into not directly observed events.

One model that is recognized for the prediction of the cellular response to ion radiation of varying dose and linear energy transfer is the Local Effect Model (LEM) [1][2][3][4][5][6][7]. It has been developed in the 1990ies during the preparation of a pilot study for heavy ion radiotherapy at the GSI in Darmstadt. Since then, it has successfully been used as an input for heavy ion radiotherapy treatment planning. Its complement for photon irradiation, the Giant Loop Binary Lesion (GLOBLE) model, is based on the same mechanistic concept that

explains cell survival probabilities with a clustering of biological damage on a micrometer-scale [8]. Briefly, it is assumed that DNA double-strand breaks (DSB) are the main determinant for radiation-related cell death and that two or more DSB (clustered DSB, cDSB) within a structural unit of the DNA, a giant loop, imply a higher risk for cell death than a single DSB (isolated DSB, iDSB). Consequently, the fractions of iDSB and cDSB induced by an instantaneous radiation determine cell survival probabilities in the LEM and GLOBLE model.

However, next to the dose, radiation quality and cellular characteristics, the schedule of dose delivery has in cases a crucial impact on radiation risks. For instance, when a photon dose is stretched over a longer time and DSB are induced with a temporal separation that allows for repair of some DSB before further DSB in vicinity might lead to a damage enhancement, one should expect that cell survival probabilities increase. In fact, it has already been demonstrated that with an introduction of two time scales of repair, one for iDSB and one for cDSB, the GLOBLE formulation of cell survival probabilities is adequate for the description of photon dose-rate experiments, where cell survival probabilities are recorded in dependence of the dose for varying dose-rates [9]. In continuation of this previous work, the purpose of the studies conducted for this thesis was to further explore time effects in the cellular response to radiation with the GLOBLE model and to transfer the temporal aspects to the LEM.

Four major projects were carried out and will be presented in the following. First, the GLOBLE model was tested with regard to its applicability in the description of photon split-dose experiments where two instantaneously given doses are temporarily separated and cell survival probabilities are recorded in dependence of this separation time. Moreover, it was investigated whether clinically observed time-dependencies in the risk for the incidence of deterministic radiation effects, denominating diseases as pneumonitis or the bone marrow syndrome, can be reproduced with the GLOBLE model.

Second, the performance of a bi-exponential approach for DSB rejoining, as suggested by the LEM and GLOBLE concept, was tested in a comparison to nine other models for DSB rejoining. The investigation comprised models for lesion repair that were proposed in other kinetic cell survival models and models for DSB rejoining that had not been explored in detail up to that point. All of the ten models were judged with regard to their accuracy and parsimony in fits to 61 experimental data sets found in literature.

Third, the GLOBLE model was compared to three other kinetic cell survival models. Data sets corresponding to 13 dose-rate experiments found in literature were used for the derivation of eight benchmarks that quantified the performance of the four models. Next to this quantitative comparison, the models were also distinguished with regard to their assumptions e.g. about the induction, repair and lethality of radiation-induced lesions.

Last but not least, the kinetic aspects presented in the GLOBLE model were transferred to the LEM. The introduction of an extension which accounts for the dynamics of damage induction and repair was thought to be beneficial especially for the assessment of time effects in prolonged heavy ion radiotherapy sessions and for the assessment of ion radiation risks related to low-dose and dose-rate exposures, as required for radiation protection.

In the following, the basics that are needed for the understanding of the presented studies will be explained. Then, the four just briefly presented projects will be motivated, evaluated and discussed in detail one by one. Finally, the common findings will be summarized and an outlook will reveal chances and challenges in the future research.

2 Basics

2.1 Ionizing radiation

In general, photon or ion radiation is considered to be ionizing when it carries sufficient energy to release electrons from the atoms or molecules of penetrated material. For the ionization of water molecules, the main constituents of the human body, about 33 eV have to be locally deposited. Consequently, radiation applied in medical imaging as X-ray and computerized tomography (CT) scans (5 - 150 keV) and in external radiotherapy (1 - 20 MeV for photons and up to 400 MeV/u for ions) and the major part of the radiation prevailing in outer space (in extreme cases about 1 TeV/u) is ionizing.

The fact that ionizing radiation locally deposits energy when it releases electrons or breaks molecular bonds indicates that not only the total energy of the radiation but as well its action within a target volume with a given density is characteristic for it. One measure for such considerations is the *macroscopic dose* (SI-unit Gray, $\mathrm{Gy} = \frac{\mathrm{J}}{\mathrm{kg}}$). It specifies the expected amount of energy deposited per unit of mass and thus - for a target with known density - the amount of energy deposited per volume.

The dependence of the macroscopic dose on the penetration depth of a beam in matter (longitudinal depth-dose profile, Figure 2.1.1A and B) results from the characteristic ways of interaction of the incoming photons or ions with the target particles. Photon- and ion-specific ways of interaction with matter also lead to different lateral energy deposition patterns on a microscopic scale, even when the macroscopic dose is equal (Figure 2.1.1C and D). Since microscopic energy deposition patterns and longitudinal depth-dose profiles are crucial for assessments of induced biological damage, as it will be explained later on, some traits of ionizing photon and ion radiation and the implied distinguishing features are shortly reviewed in the following. Further information can be found in [10] and [11].

2.1.1 Photon radiation

Ionizing photon radiation may interact with matter in three ways with the energy E of the beam implying the dominating interaction mode (corresponding energy ranges in parentheses):

(i) *Photoelectric effect* ($E \lesssim 100\,\mathrm{keV}$): An incoming photon is absorbed by a target atom or molecule and a secondary electron is released.

(ii) *Compton effect* ($100\,\mathrm{keV} \lesssim E \lesssim 10\,\mathrm{MeV}$): An incoming photon is scattered at a target atom or molecule, leaves the interaction site at a different angle and energy and releases a secondary electron.

(iii) *Pair production* ($E \gtrsim 10\,\mathrm{MeV}$): A highly energetic photon is converted into a positron and an electron in the field of a nucleus of a target atom.

Since each single photon typically ionizes only a single or a few target atoms or molecules before it is absorbed, photon radiation is denominated *indirectly ionizing radiation*. It is mainly the secondary electrons and not the incoming photons that deposit the energy in the target

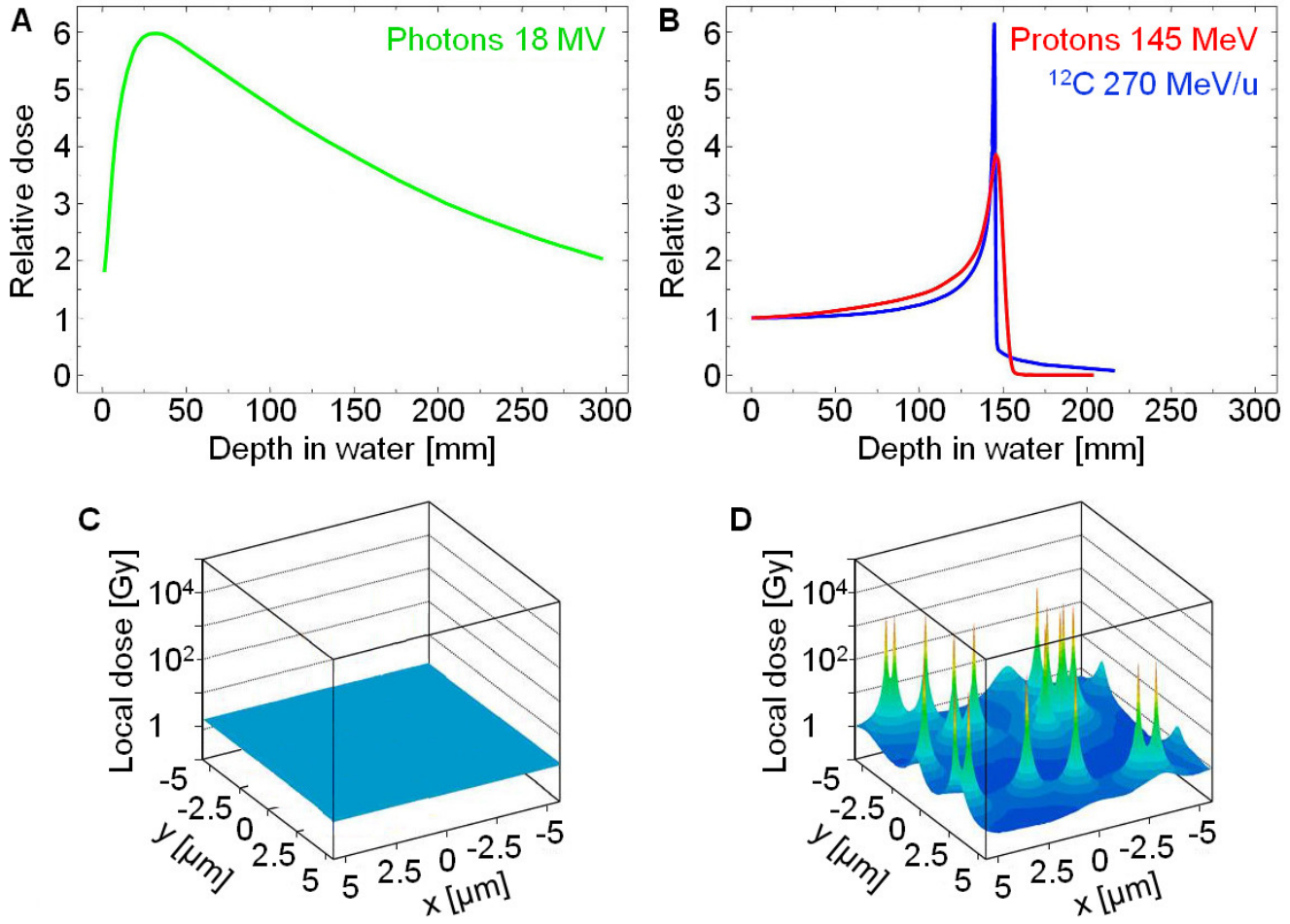

Figure 2.1.1: A) Depth-dose profile for 18 MV photon radiation. B) Depth-dose profile for 145 MeV proton and 170 MeV/u ^{12}C radiation. C) Lateral microscopic dose profile for photon radiation with average dose of 2 Gy [12]. D) Lateral microscopic dose profile for ^{12}C radiation with average dose of 2 Gy [12].

material. To assess the dependence of the longitudinal macroscopic dose on the penetration depth (Figure 2.1.1A), one has to account for the exponential decay of the number of initial photons in matter and for the movement of the secondary electrons. The largest number of secondary electrons is released close to the surface of the target but carries the energy some distance along the direction of the primary beam into the material. Therefore, one observes a little dose at the surface of the target and an increase up to a maximum dose deeper inside (*build-up effect*). Behind the maximum, the exponentially diminishing amount of initial photons and of released secondary electrons finally leads to an exponential decrease in the depth-dose profile.

Concerning the lateral energy deposition, photon radiation features an almost homogenous distribution pattern on a micrometer-scale (Figure 2.1.1C). Due to the fact that a vast amount of photons releases a huge amount of secondary electrons that are scattered in the material, one expects an almost even cross sectional dose.

2.1.2 Ion radiation

Unlike photon radiation, ion radiation is *directly ionizing*. Each single ion ionizes a significant amount of target atoms or molecules by *Coulomb interactions* along its track through the target material. Therefore, in contrast to the homogenous dose distribution of photon radiation with equal macroscopic dose, one usually observes discrete peaks in microscopic lateral dose profiles corresponding to single ions of a radiation beam (Figure 2.1.1D). Within the individual ion tracks, most of the energy is deposited by the released secondary electrons. In a first approach, it may be assumed that each ion track shows a *core* with a constant local dose resulting from energy depositions by the ion and by secondary electrons. In a *penumbra* around it, the radial dose decreases because a decreasing number of secondary electrons reaches corresponding radial distances to deposit energy. The maximum radius of an ion track depends crucially its energy which defines the maximum kinetic energy transfer and range of a secondary electron. A more detailed amorphous track structure model will be presented in section 2.3.3.2.

When an ion penetrates matter it loses more and more energy (E) by Coulomb interactions. Figure 2.1.1B visualizes the longitudinal macroscopic dose which is relatively low in the region where an ion enters the target material with high energy. The slower the ion becomes by loss of kinetic energy, the larger becomes the deposited energy. Finally, an ion loses the largest portion of its energy while coming to rest at the so-called *Bragg peak*. The *Linear Energy Transfer* (*LET*) which describes the expected incremental lateral energy deposition is assessable with the Bethe Bloch formula:

$$LET_{\infty} = -\frac{dE}{dx} = \frac{4\pi e^4}{m_e c^2}\frac{Z_{eff}^2}{\beta^2} N_A \rho_t \frac{Z_t}{A_t}\left[\ln\frac{2m_e c^2\beta^2}{I(1-\beta^2)} - \beta^2\right]. \tag{2.1.1}$$

with:

x: Coordinate along the ion's path.
e, m_e: Electron charge and mass.
c: Speed of light in vacuum.
Z_{eff}: Effective charge of the ion.
β: Relativistic velocity of the ion.
N_A: Avogadro number.

ρ_t: Target density.
Z_t, A_t: Atomic number and atomic mass of the target.
I: Mean ionization potential.

The Bethe Bloch formula indirectly implies that particles of a given species penetrate further in matter when their initial kinetic energy is increased and the corresponding *LET* in the entrance channel is decreased. Furthermore, it is predicted that at the same energy, particles with a lower effective charge have a lower *LET* which again results in a longer range. This explains for instance the dose deposition beyond the Bragg peak that can be seen in the depth-dose profile of heavy ions (^{12}C in Figure 2.1.1B). It is due to the longer range of lighter fragments.

2.1.3 Radiation sources and radiation exposures

On earth, *radioactive elements and isotopes*, e.g. ^{222}Rn, ^{14}C and ^{40}K, constitute the majority of the natural radiation sources. Their energetically unstable nuclei emit α(^{4}He ion), β^-(electron), β^+(positron) or γ(photon) radiation in order to reach states with lower energy and eventually stability. On average, a human receives around 2 mSv (milli-Sievert, unit for the radiation-weighted equivalent dose) per year.

Another natural source is cosmic radiation. Of special relevance for e.g. astronauts in outer space are *galactic cosmic rays* (GCR) and *solar particle events* (SPE) [13]. GCR are produced outside the heliosphere and are therefore present at all times, with some variations in the intensity. They consist of protons ($\approx$ 80%), alpha particles ($\approx$ 12%) and heavy ions that have been accelerated to high kinetic energies (up to 1 TeV/u). Despite the low occurrence, heavy ions with their high *LET* contribute significantly to the dose that a human receives during space flight. Therefore, there is a special interest in the investigation of the biological effects of e.g. C, N and O at around 30 keV/μm and Fe at around 150 keV/μm. In contrast to GCR, SPE occur rather irregularly when the sun erupts and mainly releases protons with up to 1 GeV and a very high fluence. It has been estimated that during a mission on the ISS, an astronaut gets an average dose of 72 mSv which is about 28.9 mGy [14].

For gamma irradiation of cell cultures, one often uses ^{60}Co or less frequently ^{137}Cs sources. On the main decay chain of the radioactive isotope ^{137}Cs, 662 keV photons are released and during the decay of ^{60}Co, higher energetic 1.17 MeV and 1.33 MeV photons are emitted. By adjusting the mass of the radioactive substrates and the distance to the source, one can regulate the dose that is given to the target. For cell survival experiments (section 2.3.1) one usually applies up to 30 Gy.

During external radiotherapy, one irradiates patients most frequently with X-rays. In a linear accelerator, electrons are accelerated and then focused on a target material where they are stopped. During the stopping process "Bremsstrahlung" (X-ray photons) and relatively few gamma rays are produced which then can be collimated to optimally hit the patient. The applied dose can be regulated by the current at the electron producing cathode, by the accelerating voltage and by the distance to the patient. The range of doses is usually up to 80 Gy, depending on the type of tumor and the schedule of the dose delivery. More information about photon radiotherapy and corresponding techniques can be found in [15], [16], [17].

Last but not least, for the irradiation of patients or of cell cultures with ions [18] [19], one needs *particle accelerators* which - at least in the case of heavy ions (atomic number > 4) - consume a comparably large space. The requested ion species is produced in an ion source and

typically pre-accelerated in a linear accelerator system [20][21]. The heavy ion beam is then injected into a synchrotron and brought to a requested energy before the beam is extracted and deflected to hit the patient. Two examples for heavy ion treatment facilities are the Heidelberg Ion-Beam Therapy Center [22] in Germany and the National Institute of Radiological Science (NIRS) in Chiba, Japan. The particle accelerator at NIRS is basically able to deliver beams with an energy up to 800 MeV/u. However, for the carbon ion treatment of more than 8000 patients since 1994 [23], the chosen energy was typically between 200 MeV/u and 400 MeV/u, depending on the depth of the tumor location. At HIT, carbon ions are accelerated up to 430 MeV/u before a gantry with a weight of 670 t optimally guides the beam 360° around the patient.

2.2 Cellular aspects

2.2.1 The DNA structure

Figure 2.2.1 sketches the structure of a mammalian cell. Of all the indicated structural elements that might be damaged by radiation, the cellular nucleus containing *deoxyribonucleic acid* (DNA) is considered as most relevant target [24][25]. Although the shape of a mammalian cellular nucleus varies with the cell type and cell cycle stage, a diameter around 10 μm constitutes a reasonable generalization.

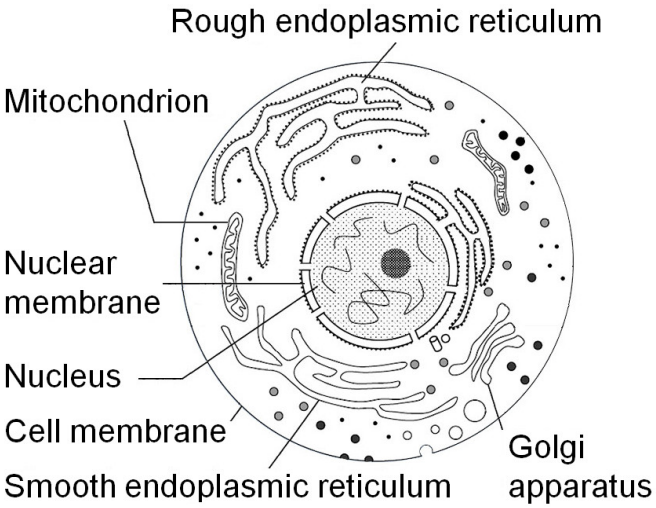

Figure 2.2.1: The structure of a cell. Only the most prominent components are labeled. Taken from [26] and modified.

The DNA in the cellular nucleus encodes the genetic information that is eventually needed for the maintenance of the cellular metabolism and for cell replication. Therefore, the integrity of the DNA is crucial for the prevention of cell mutations and cell death. With regard to the DNA structure, the "genetic code" is enclosed in two winding sugar-phosphate backbones in form of a sequence of pairs of four alternating nucleobases. Figure 2.2.2A explains the build-up of the DNA in more detail. The cross sectional width of the double helix is about 2 nm and the total genomic content (genome) of a human with about 3.2 billion base pairs stretches over 1 m. Usually, human cells are diploid meaning that in an unreplicated state, there are two copies of the genome. This huge amount of base pairs is apportioned on two times 23 *chromatids*.

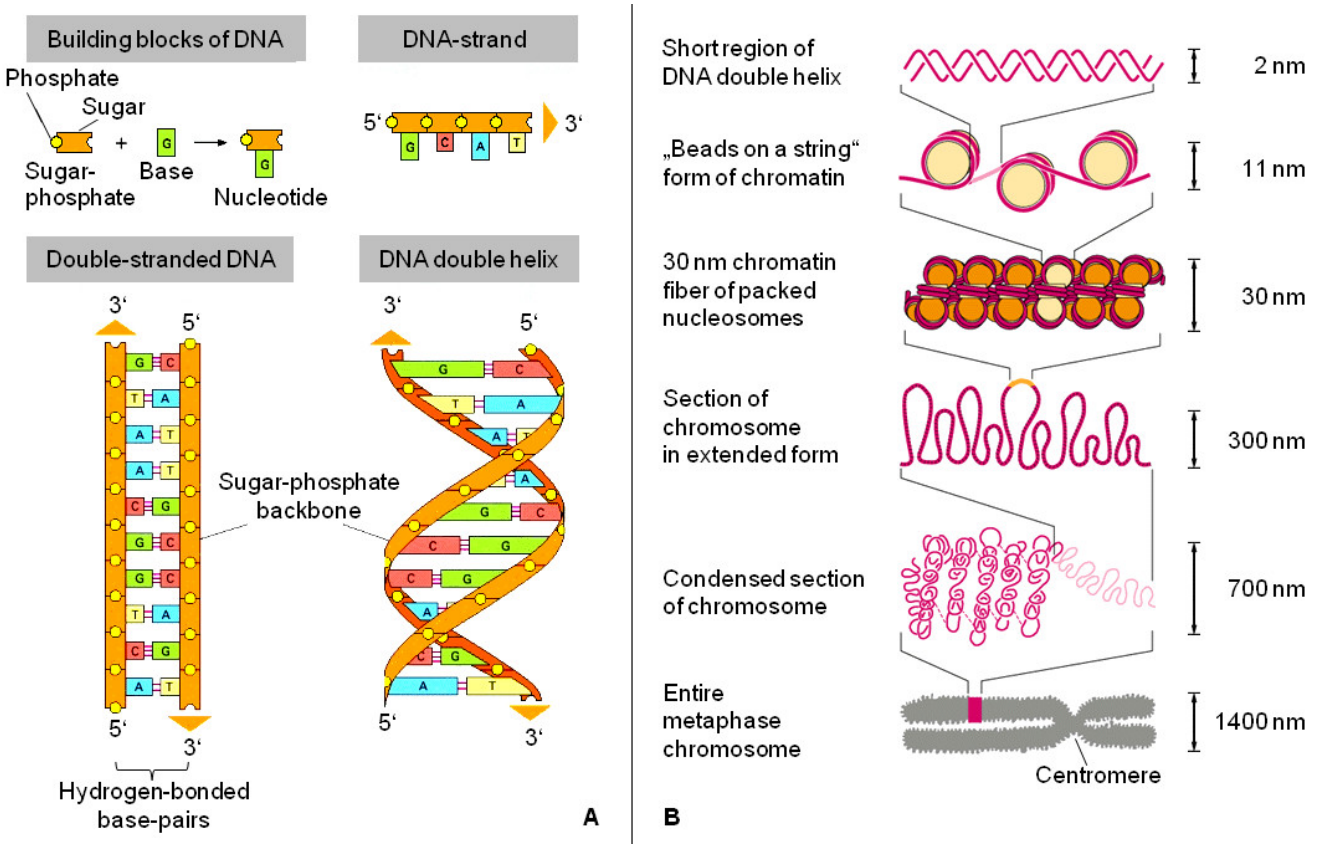

Figure 2.2.2: A) Graphical explanation of the build-up of the DNA read from from top-left to bottom-right. B) Graphical explanation of the compactification of the DNA. The illustrations were taken from [27] with permission and modified.

In order to store the whole DNA in the relatively small nuclear volume, it has to be highly compacted. Figure 2.2.2B shows how the DNA double-strand is tightly packed to *chromatin* in complexes with proteins. On a first level, the DNA is wrapped around core histones for the formation of nucleosomes. Sections of the DNA which are frequently transcribed remain in this relative relaxed *euchromatic* state which looks like "beads on a string". Regions of the DNA which are rather inactive are further compacted to 30 nm fibers of nucleosomes, the *heterochromatin*. Only during mitosis, the cell cycle stage in which the cell is dividing (section 2.2.2), the chromatin is condensed and finally forms *chromosomes*, where two sister-chromatids are bound together at the so-called centromere.

During all other stages of the cell cycle, which means most of the time, the organization of the chromatin is more flexible than in mitosis. For the G1- and G0-phase, experiments recording the random walk behavior of the chromatin revealed that there are two organizational substructures of the DNA on a scale > 100 kilo base pairs [28]. It was suggested that there are relatively free moving DNA *giant loops* with a size of about 2 mega base pairs (Mbp) whose ends are attached to a kind of less flexibly moving backbone (Figure 2.2.3A). Further experiments revealed the existence of the random walk/giant loop organization of the chromatin also in S-phase cells [29] and theoretical computations strengthened the hypothesis of the existence of giant loops fixed in a core region (micelle, Figure 2.2.3B) [30]. For this thesis, the organization of the chromatin in giant loops will be of special relevance and the 2 Mbp subunits will be simplified as cubes with side length of 0.54 μm.

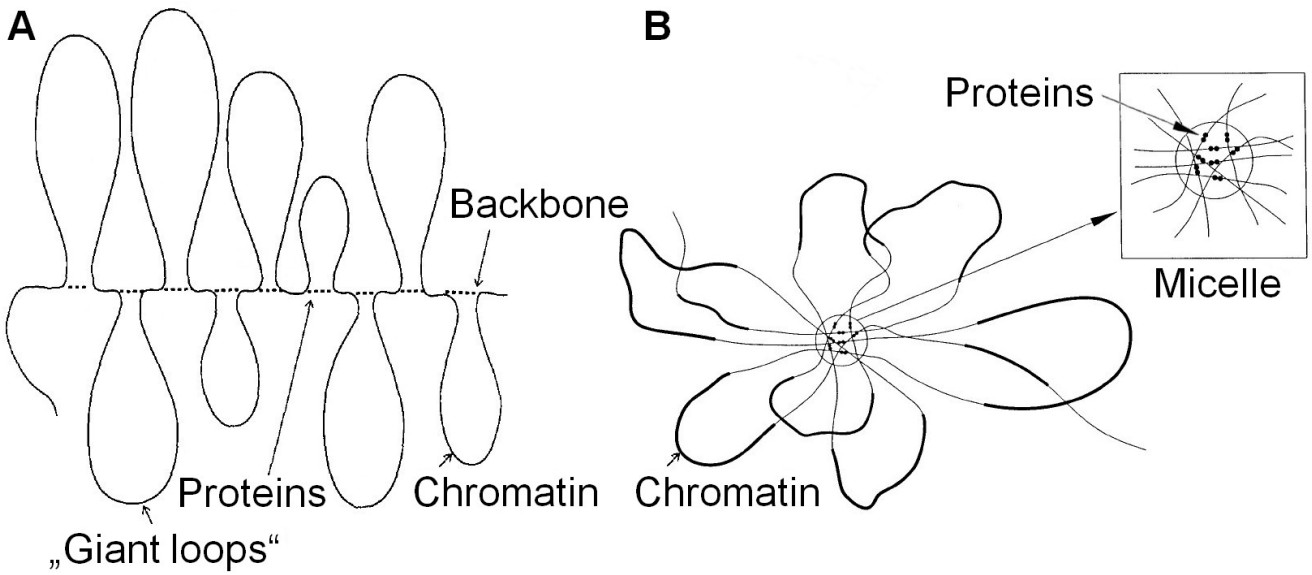

Figure 2.2.3: Sketch of the giant loop (size ≈2 Mbp) organization of the chromatin. A) The randomly moving loops are attached to a kind of backbone (taken from [28] with permission and modified). B) The loops are fixed with protein complexes in a core region, the micelle (taken from [30] and modified). In both Panels, the usually randomly coiled giant loops and in A) additionally the backbone are drawn smoothly for the sake of visibility.

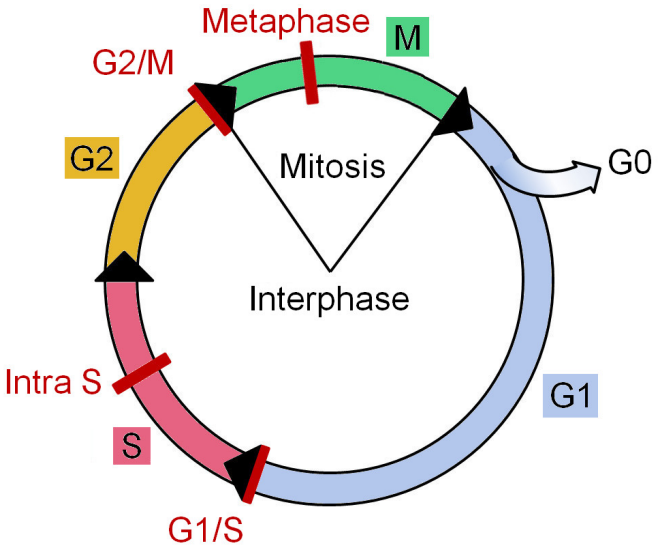

Figure 2.2.4: The various stages of the cell cycle. Cell cycle checkpoints are highlighted in red.

2.2.2 The cell cycle

For self-renewal and growth of an organism, a part of its constituent cells has to replicate (proliferate). Proliferating cells run through a cell cycle consisting of several stages of preparation (interphase) for the final division in mitosis (Figure 2.2.4). After the division of its parental cell, a clone enters the gap1-(G1-)phase where it produces functional elements and grows. In the subsequent synthesis-(S-)phase the DNA content is duplicated. Finally, after some last steps in the gap2-(G2-)phase, the cell enters mitosis where the chromosomes condense, are split and separated into two halves of the cell and where the two daughter cells emerge. The total cell cycle time is around 12-24 h for mammalian cells in vitro and the G1-phase with about 8-10 h usually consumes most of it. As an alternative to the progression in the cell cycle, a cell might become quiescent (G0-phase).

For the regulation of cell growth and the securing of the integrity of a proliferating cell, there are four cell cycle *checkpoints* [31][32]. In general, the G1-, S- and G2-/M-checkpoints ensure that cells with DNA damage do not progress in the cell cycle. At the G1-checkpoint it is additionally tested if cells have grown enough and if there is enough space and nutrition before synthesis is started. At the metaphase-checkpoint in mitosis it is verified that the chromosomes are correctly aligned before they are torn apart. A functioning cell is delayed or arrested in the cycle until detected errors have been removed. In case of failures it undergoes cell death (apoptosis) or is silenced.

For the purpose of some experiments it is crucial that all the cells of an investigated culture are in the same cell cycle stage. There are several ways to achieve such a cell *synchronization* some of which exploit cell cycle arrests [33]. By addition of drugs to the culture medium cells are blocked at a defined cell cycle checkpoint and by letting cells grow densely or by deprivation of nutrition they accumulate at the G1/G0-phase. Furthermore, one can use the lose attachment of mitotic cells to culture dishes to harvest only the cells at this defined stage.

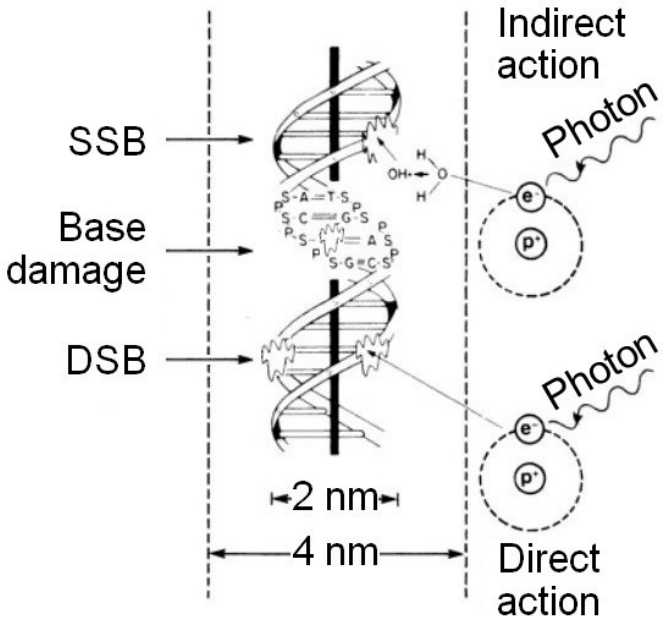

Figure 2.2.5: Illustration of direct and indirect actions of radiation and of three kinds of DNA damage (taken from [11] with permission and modified). Here, a DNA base damage, single strand break (SSB) and double-strand break (DSB) are sketched as single lesions. Usually, radiation induces combinations of them. Furthermore, in the figure, a direct action of radiation consists in the modification of the DNA by a secondary electron that has been released in an atom or molecule nearby. An indirect action of radiation is sketched as the interaction of the DNA with a radiation-induced hydroxyl radical (OH·). The dotted lines indicate a cylinder with 4 nm diameter in which induced free radicals live long enough to reach the DNA in the center (diameter around 2 nm) by diffusion.

Ionizing radiation may cause biological damage in two ways as illustrated in Figure 2.2.5:

(i) *Direct actions* of radiation: biological molecules as the DNA are ionized by incoming primary particles or photons and corresponding secondary electrons.

(ii) *Indirect actions* of radiation: biological molecules are modified by free radicals produced by the radiation nearby.

Figure 2.2.5 also sketches three important kinds of radiation-induced DNA lesions: *base damages*, *single strand breaks* (SSB) and *double-strand breaks* (DSB). At least at doses $\lesssim 100\,\mathrm{Gy}$, the number of these lesions is proportional to the applied dose and relatively independent of the cell type [34]. Although the exact values slightly vary with the temperature, pH of the culture medium and other factors, the orders of magnitudes of the yields for a mammalian cell with unreplicated DNA content are 1000-2000 Gy^{-1} for base damages, 500-1000 Gy^{-1} for SSB and only about 20-50 Gy^{-1} for DSB [35]. When it comes to cell mutations and death, DNA double-strand breaks have to be considered as most effective despite the relatively low occurrence [36][37][38].

To prevent mutations and death, cells have developed repair mechanisms for a removal of DSB. Depending on the cell cycle stage, the two most frequently running processes are the

non-homologous end-joining (NHEJ) and *homologous recombination* (HR) (Figure 2.2.6) [38]. The HR is only applicable when there is a matching copy of the section of DNA where a DSB occurred - that is in late S- and G2-phase of the cell cycle. After resection of the site where the DSB occurred, one strand of the damaged piece of DNA invades the matching double helix on the sister-chromatid. The missing sequence on the two damaged strands is restored in this "Holliday junction" by using the intact strands as templates. This way of copying the genetic information usually implies an accurate removal of DSB. In contrast, the repair of DSB with NHEJ, mainly during G1-phase, is linked with a low fidelity. After an optional degradation of the two pieces of DNA around the DSB, the lose ends are simply joined together. Consequently, genetic information might get lost and when multiple DSB occur in vicinity, it might happen that wrong ends are brought together.

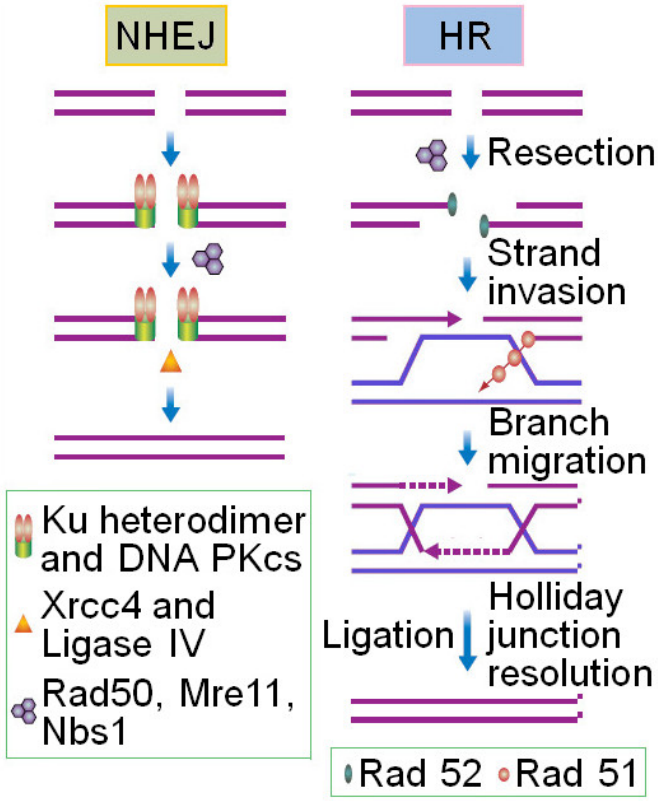

Figure 2.2.6: Sketch of the sequence of the two major DSB repair pathways: non-homologous end-joining (NHEJ) and homologous recombination (HR). The figure has been taken from [38] with permission and was modified.

When the ends of DNA around a DSB cannot be rejoined or when there is misrejoining between multiple DSB, *chromosomal aberrations* might result, e.g. deletions, insertions or translocations of genetic material between chromosomes [39][40]. Depending on the severity of the damage, concerned cells might come to a rest in the cell cycle and undergo apoptosis or they might die during a "mitotic catastrophe".

2.2.4 Temporal course of DSB rejoining

There are several methods to assess the temporal progress in the cellular rejoining of radiation-induced DSB, e.g. *neutral filter elution*, *pulsed-field gel electrophoresis* (PFGE) and the decay of *γH2AX foci* [41] [42]. Depending on the assay, measured DSB rejoining might slightly vary and since the current data base is the largest for experiments involving PFGE, it will be focused on this method in section 3.2. During PFGE, the DNA of irradiated cells is radioactively labeled or stained and loaded onto a gel. Under application of an alternating and pulsed electric field, polarized fragments of the DNA are drawn into the gel with the distance depending on the molecular weight. The amount of present DSB can be computed from the fraction of radioactivity or glowing dyes measured in the gel. At this stage it should be emphasized that PFGE measures only DSB *rejoining* and not whether the connection of two ends of DNA was correct (no loss of genetic material, no linking of wrong ends, etc.).

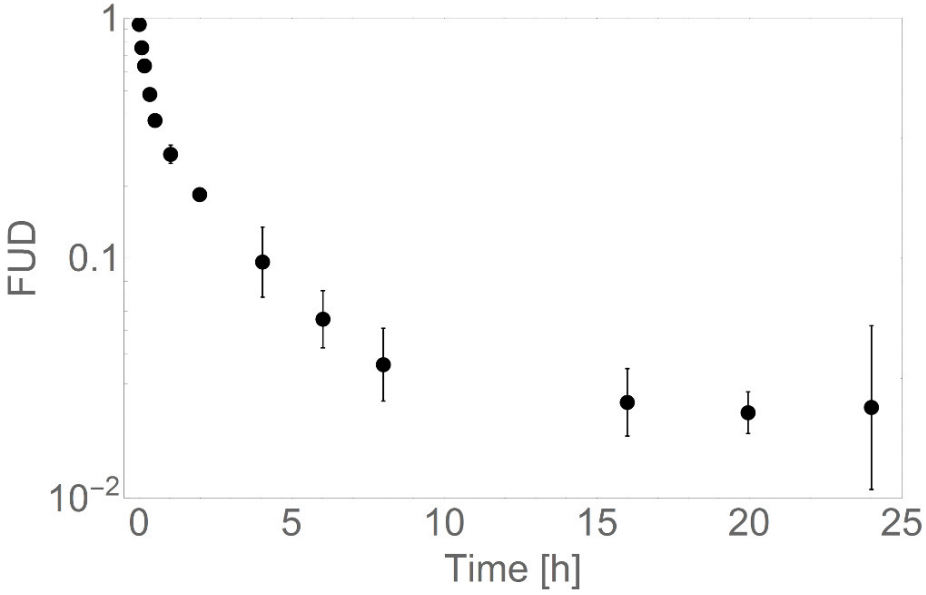

Figure 2.2.7: A DSB rejoining curve recorded for the NFHH cell line after application of 40 Gy photon radiation. The fraction of unrejoined damage *FUD* is plotted in dependence of the time after irradiation. Data taken from [43].

Figure 2.2.7 shows an example for a DSB rejoining curve recorded after high-dose-rate photon irradiation with 40 Gy. The fraction of the number of unrejoined DSB compared to the number of initial DSB (*FUD*) is plotted over time. A first general observation is that there are "rejoinable" DSB vanishing in time and "residual" DSB that remain even after 24 h. There are four plausible origins for the convex shape of DSB rejoining curves which might take effect in combination [44]:

(i) Different repair mechanisms (e.g. NHEJ and HR).
(ii) Different classes of DSB (e.g. with regard to their spatial or chemical complexity).
(iii) Different locations of DSB (e.g. hetero- or euchromatin).
(iv) Different modes of DSB rejoining (e.g. intra- and inter-lesion rejoining).

Especially with regard to points i-iii, DSB might be characterized by the repair mechanism they are processed with, by their belonging to a class or by their location. The denotation

"DSB categories" will comprehensively be used to count the numbers of DSB repair mechanisms and/or a certain number of DSB classes and/or a certain number of different DSB locations that underlies the shape of rejoining curves in the following. The categorization of DSB with respect to point iv is not as straight forward. On the one hand, one might define two DSB categories on the hand of the finally realized mode of rejoining (intra- or inter-lesion). On the other hand, when *initial* DSB should be categorized, there is not necessarily an ab initio criterion that decides whether a DSB will undergo an interaction or not. Therefore, it might be the best to state that all initial DSB are considered to belong to a single category in the context of different modes of rejoining - as it is done in several cell survival models (sections 2.4.4, 2.4.5).

Actually, it is often assumed that the fraction of unrejoined DSB follows a bi-exponential decay:

$$F_{BiExp} = Ae^{-k_1 t} + (1-A)e^{-k_2 t}. \tag{2.2.1}$$

A bi-exponential decay means that one fraction (A) of DSB is rejoined with fast kinetics (rate k_1) and another fraction with slow kinetics (rate k_2). It supports the hypotheses of two dominant repair mechanisms, two classes of DSB or two distinct locations of DSB - of two DSB categories. The validity of the bi-exponential model will be tested in a comparison to other models for DSB rejoining as part of this thesis (section 3.2).

The general shape of DSB rejoining curves does not change when high-*LET* ion radiation is applied. However, the fractions of lesions that are rejoined with slow kinetics and the residual damage usually increase [45][46][47].

Concerning the link between DSB rejoining and the higher-order chromatin structure, it has been found that the slow component of DSB rejoining goes in hand with multiple breaks in DNA giant loops whereas single DSB in giant loops are repaired relatively quickly [48][49]. An agreement of the concept of the Local Effect Model, which involves DNA giant loops (section 2.3.3), with DSB rejoining after photon and ion irradiation was demonstrated by Tommasino et al. [50]. In a detailed study where DSB rejoining curves were recorded with the decay of γH2AX foci, the authors revealed that a definition of two lesion classes based on the number of DSB in giant loops allows for an accurate reproduction and for a mechanistic interpretation of the data. Furthermore, Löbrich et al. showed that the slow component of DSB rejoining is linked to an increased probability for misrejoining [51]. All of these observations will be of importance for a consideration of time-effects in cell survival probabilities with the Giant Loop Binary Lesion model and the Local Effect model, introduced in sections 2.4.3 and 3.4.

2.3 Measuring and modeling of clonogenic cell survival

2.3.1 Measuring clonogenic cell survival

The goal of radiation therapy is not only the killing of tumor cells in terms of disintegration via apoptosis or necrosis but also their sterilization. To assess the dose dependence of *clonogenic cell death* of varying cell lines, in vitro cell "survival" experiments may be conducted. Of course, in vitro experiments hardly reflect in vivo tissue effects that might strongly impact the cellular response to radiation, but at least they provide a good starting point to categorize cell lines with respect to their *radiosensitivity*.

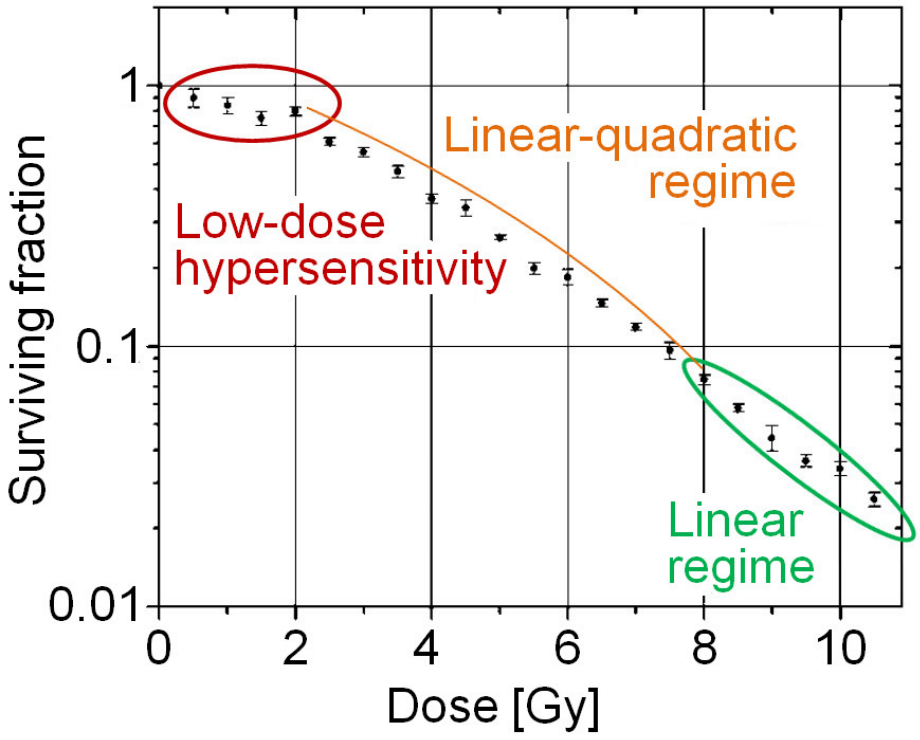

Figure 2.3.1: Example for a typical photon cell survival curve measured for the U373MG cell line. The regime of low-dose hypersensitivity, linear-quadratic bending and linear flattening are highlighted. The illustration was taken from [54] with permission and modified.

In cell survival experiments, several cell cultures are irradiated for each requested dose point (including samples with zero dose as controls) before or after seeding them into dishes to grow [52]. After several cell cycle times (about 14 days), in each dish, the cell colonies containing 50 or more cells are counted and scored as progeny of one surviving cell. The number of surviving cells in a dish is then divided by the number of initially seeded cells to obtain a raw fraction of surviving cells. However, these measured raw fractions are not yet final survival probabilities since even without irradiation, not all cells seeded into a dish start to grow. Therefore, for the final derivation of dose-dependent cell survival probabilities, all measured points (including the controls) are used to find the intercept at zero dose by fitting e.g. a linear-quadratic model (section 2.3.2) with offset to them. The raw fractions are then normalized with this offset, the so-called plating efficiency *PE*, to yield cell survival probabilities *S(D)* [53]. One usually plots the means of the dose-specific measured samples with the standard error as *cell survival curve*.

Typically, acute photon cell survival curves, recorded after high-dose-rate irradiation, are linear-quadratic on a logarithmic scale between about 2 Gy and 8 Gy [54]. At higher doses, a transition to a linear dependence can be observed meaning that a linear-quadratic function would overestimate the radiosensitivity of the cell line. At lower doses, a hyper-sensitivity in terms of an initial very steep decline in survival probabilities and a subsequent recovery is sometimes observed. Figure 2.3.1 shows an example for a survival curve measured for the U373MG cell line [54].

Actually, the radiosensitivity of cells changes significantly with the cell cycle stage - with the exception of very radiosensitive cells that have severe repair deficiencies (Figure 2.3.2). Cells

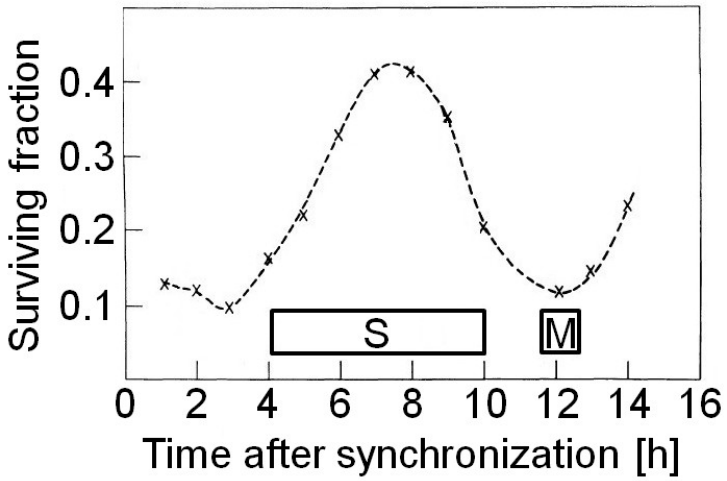

Figure 2.3.2: Radiosensitivity of Chinese Hamster cells through the cell cycle. The cells have been synchronized at time zero and their survival probabilities after irradiation with 6.6 Gy photon radiation have been recorded. The illustration was taken from [55] and [11] with permission and modified.

in late S-phase usually show the highest survival probabilities at a defined dose, supposedly due to the availability of the reliable HR pathway. In late G2-phase and mitosis, cells are most radiosensitive since small perturbations might lead to fatal errors in the cell division. During the other stages of the cell cycle, they show an intermediate behavior.

Cell survival curves measured after high-*LET* ion radiation are usually linear on a logarithmic scale. Depending on the ion species and the (high) LET of the radiation, this linear slope varies for a given cell line. When the LET of an instantaneous ion irradiation is sufficiently lowered, a quadratic bending begins to appear in recorded survival curves on a logarithmic scale and a "photon-like" behavior emerges. In conclusion, cell survival probabilities do not only depend on the dose of an applied radiation but also on the type of radiation in terms of photon or ion exposure and if applicable, the LET and the ion species.

The differences between biological effects measured after acute photon radiation and ion radiation with varying LET are usually quantified with the *relative biological effectiveness* (*RBE*). It is defined as the ratio between the photon dose and the ion dose leading to the same considered biological endpoint (e.g. 10% cell survival). Figure 2.3.3A provides an example for how to derive the *RBE*. In order to determine the *RBE* for 10% survival probabilities, one has to find the photon dose and the ion dose corresponding to this required endpoint. The quotient of the photon and the ion dose defines the *RBE*. Figure 2.3.3B shows an example for the dependence of the *RBE* on the LET of ^{12}C radiation. Mechanistic reasons for the enhanced effectiveness of ion radiation will be presented in the introduction of the Local Effect Model below (section 2.3.3).

2.3.2 The Linear-Quadratic model

As a very good first approximation, one commonly describes cell survival curves $S(D)$ with the Linear-Quadratic (LQ) model:

$$S(D) = e^{-(\alpha D + \beta D^2)}. \tag{2.3.1}$$

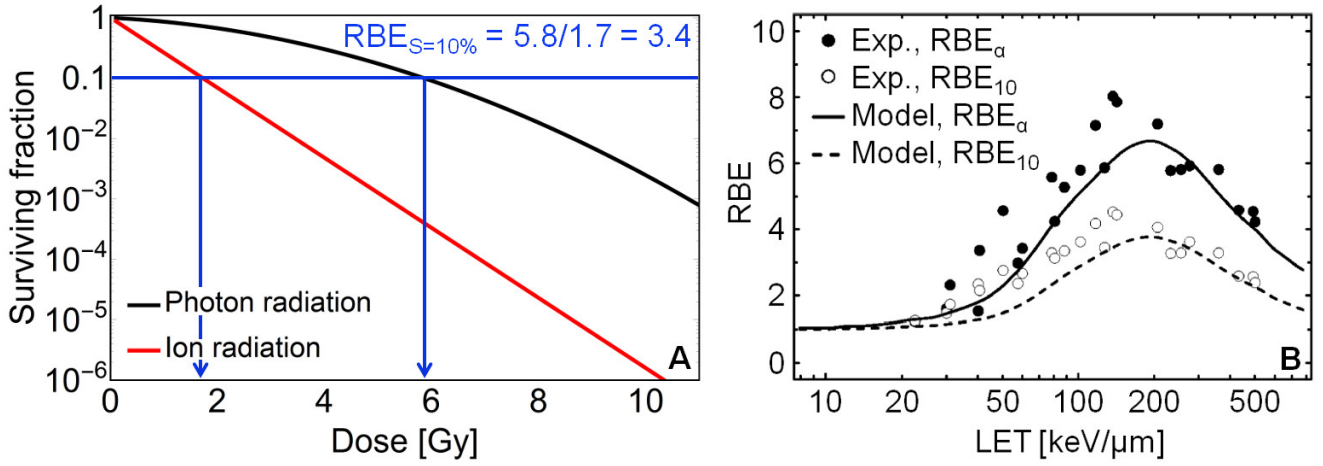

Figure 2.3.3: A) Example for a calculation of the relative biological effectiveness RBE. A linear-quadratic-linear photon cell survival curve for an abstract cell line with α = 0.1 Gy^{-1}, β = 0.05 Gy^{-2} and D_t = 8 Gy and a corresponding survival curve for ^{12}C ion radiation with LET = 200 keV/μm are plotted. B) Plot of the RBE over the LET for ^{12}C irradiation of V79 cells. RBE_α denotes the RBE corresponding to a comparison of the initial slopes of cell survival curves measured for photon and ion radiation and RBE_{10} denotes the RBE for 10% survival probabilities. The experimental data were taken from [56] and the model predictions were computed with the Local Effect Model. The plot was taken from [7] with permission and modified.

Referring to a Poisson distribution, $S(D)$ represents a probability for no event. The corresponding negative exponent, denominated effect $Eff(D)$ with

$$Eff(D) = -\ln[S(D)] = \alpha D + \beta D^2 \tag{2.3.2}$$

can be interpreted as the expected number of radiation-induced lethal events and graphs of $Eff(D)$ are denoted as *dose effect curves*. Usage of the effect *Eff(D)* in computations avoids the logarithmic calculus and to guarantees a higher stability of predictions. Actually, the LQ parameters α and β are often employed to characterize the radiation response of cell lines or even of tissues in clinical studies.

However, as already pointed out, the LQ model neglects low-dose hypersensitivity and the linear regime at higher doses [54]. Several approaches overcoming one or both of these problems have been suggested [57] [58]. For the investigations presented in this thesis, where the high-dose regime is of special importance, the linear-quadratic-linear (LQL) model will be employed [2]:

$$Eff(D) = \begin{cases} \alpha D + \beta D^2 & D < D_t \\ (\alpha + 2\beta D_t)D - \beta D_t^2 & D \geq D_t. \end{cases} \tag{2.3.3}$$

The LQL model pragmatically features a threshold dose D_t from which on cell survival curves are linear on logarithmic scale and thus eliminates the shortcoming of the pure LQ model at high doses.

2.3.3 The Local Effect Model

In section 2.3.1 it has already been pointed out that cell survival curves measured after photon and high-*LET* ion radiation differ in their shape. For a given cell line, one could pragmatically describe photon cell survival curves with a LQ approach and high-*LET* survival curves with a linear approach. However, this would ultimately mean that for this considered cell line, a different parametrization in terms of α and β had to be used for photons, different ion species and different values of the *LET*. It would actually be preferable to have a fixed "characteristic" set of parameter values for each considered cell line because of several reasons, amongst others:

(i) Characteristic parameter values allow the comparison of different cell lines amongst each other.

(ii) Adjusting parameter values during computations is very inconvenient and time-consuming when the cellular response to a variety of radiation modalities is needed.

(iii) For some radiation modalities there are no experiments available which might be used to derive corresponding parameter values. When predictions for such modalities are needed, no extrapolation from known data is feasible.

The last two points are especially relevant for heavy ion radiotherapy, where treatment plans require the calculation of tissue responses for a variety of employed *LET*.

Therefore, during the preparation of a pilot study for heavy ion radiotherapy at the GSI in Darmstadt in the 1990ies, a mechanistic model which allows to predict *RBE* values for a variety of ion species and LET was developed: the Local Effect Model (LEM). It does not only overcome the shortcomings i-iii of empirical approaches but also helps to better understand cellular characteristics that lead to observed radiation responses. In fact, it has turned out that the LEM has a strong predictive power and therefore, it has continuously been used as an input for heavy ion treatment planning even after the end of the pilot study at the GSI, e.g. at HIT in Heidelberg. Since the 1990ies, the model has undergone several amendments [1][2][3][4][5][6] and the most recent version will be presented in the following [7]. This version is only valid for acute (high-dose-rate) irradiation and has been extended to include dynamic effects as part of this thesis (section 3.4). Furthermore, since the LEM is applicable for a variety of endpoints and since there are many options in the computational procedures, the subsequent descriptions will be restricted to the methods needed here.

2.3.3.1 The general idea

As stated in the name, the Local Effect Model is based on the idea that equal spatial damage patterns should lead to equal biological effects - independent of the radiation modality. In particular, the approach focuses on the spatial distribution of DSB, which are considered to be the main reason for radiation-induced cell death [36][37]. With reference to the giant loop structure of the chromatin [28][29][30], it is suggested that a single DSB in a loop (*isolated DSB*, iDSB) will be repaired with high fidelity since the ends of the loop remain attached to a kind of backbone or micelle. Two or more DSB in a loop (*clustered DSB*, cDSB) allow for the diffusion of fragments and are expected to be harmful to a cell - independent of the exact number of DSB per loop [7][48][59][60]. Consequently, the ratio between the number of cDSB (N_{cDSB}) and the total number of lesions ($N_{iDSB} + N_{cDSB}$) is a measure for the severity of radiation-induced damage in the LEM. It is denominated *cluster index* (C):

$$C = \frac{N_{cDSB}}{N_{iDSB} + N_{cDSB}}. \tag{2.3.4}$$

For photon radiation with homogenous dose distribution, C can be derived with Poisson statistics. For the computations, giant loops are simplified as cubic target volumes with side length of 0.54 μm [6]. A cellular nucleus with a volume of about 500μm^3 contains about $N_L = 3175$ so-called *domains*, consequently. When the expected number of DSB in a mammalian cell is assumed to be proportional to the applied dose D_γ with factor α_{DSB} (usually set to 30 Gy^{-1} for a mammalian cell [6]), the expected number of DSB per domain becomes

$$\lambda = \frac{\alpha_{DSB} D_\gamma}{N_L} \tag{2.3.5}$$

and the expected numbers of iDSB and cDSB after photon irradiation are:

$$\begin{aligned} N_{iDSB}(D_\gamma) &= N_L \lambda e^{-\lambda} \\ N_{cDSB}(D_\gamma) &= N_L (1 - \lambda e^{-\lambda} - e^{-\lambda}). \end{aligned} \tag{2.3.6}$$

The numbers $N_{iDSB}(D_\gamma)$ and $N_{cDSB}(D_\gamma)$ imply C. With an inverse computational procedure, a photon dose D_γ can be derived from a given C and a corresponding effect $Eff(D_\gamma)$ can be determined when the photon cell survival curve is known.

This inverse procedure is exploited for the calculation of cell survival probabilities after ion irradiation with the LEM (compare with Figure 2.3.4). After simulation of $N_{iDSB}(D_{Ion})$ and $N_{cDSB}(D_{Ion})$ for ion radiation with given LET and dose D_{Ion}, C is computed and an equivalent photon dose D_γ^{eq} leading to the same value of C is derived. With a linear-quadratic-linear parametrization (α, β and D_t), the corresponding photon effect $Eff(D_\gamma^{eq})$ is found. By scaling of the effect with the absolute numbers of lesions corresponding to the ion and photon radiation, the ion effect results from:

$$Eff(D_{Ion}) = \frac{N_{iDSB}(D_{Ion}) + N_{cDSB}(D_{Ion})}{N_{iDSB}(D_\gamma) + N_{cDSB}(D_\gamma)} Eff(D_\gamma^{eq}). \tag{2.3.7}$$

The way how to simulate $N_{iDSB}(D_{Ion})$ and $N_{cDSB}(D_{Ion})$ for ion radiation will be presented in the following.

As a summary of the idea behind the LEM, it should be emphasized again that the specific clustering of DSB on micrometer-scale explains the variations in the response of a given cell line to different radiation modalities. At a given dose, the low spatial density of DSB after loosely ionizing photon radiation results in a much lower cluster index than the concentration of DSB along the tracks of high-*LET* radiation. Consequently, photon cell survival probabilities are generally increased in comparison to high-*LET* ion radiation.

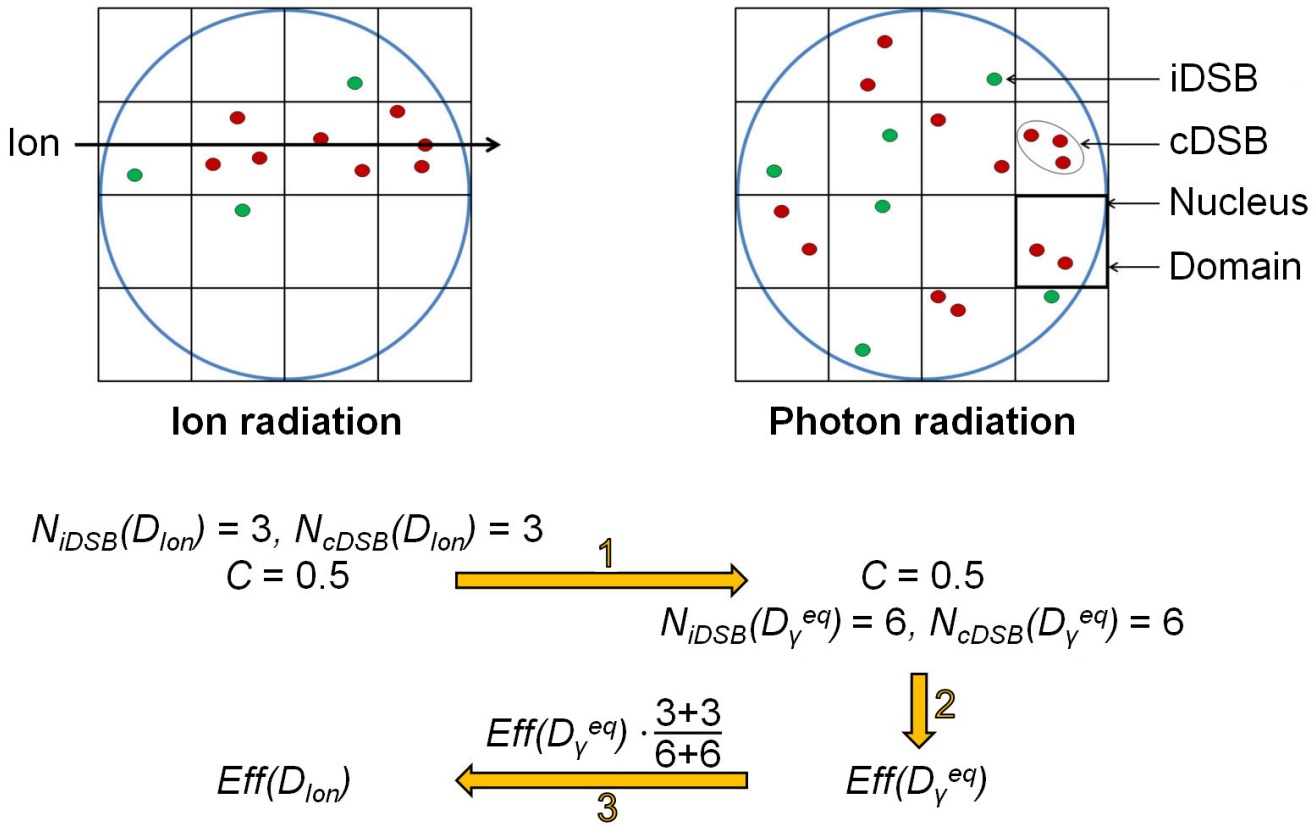

Figure 2.3.4: Principle of the Local Effect Model. After simulation of the numbers of isolated and clustered DSB ($N_{iDSB}(D_{Ion})$ and $N_{cDSB}(D_{Ion})$) for a given ion radiation with dose D_{Ion}, the implied cluster index *C* is calculated. An equivalent photon dose D_γ^{eq} leading to the same value of *C* is derived and the corresponding effect $Eff(D_\gamma^{eq})$ is computed. After rescaling for the absolute number of lesions, the effect for the requested ion radiation $Eff(D_{Ion})$ has been found. Note that this two-dimensional plot and that the given numbers of iDSB and cDSB are simplifications for more complex distributions of iDSB and cDSB in three dimensions.

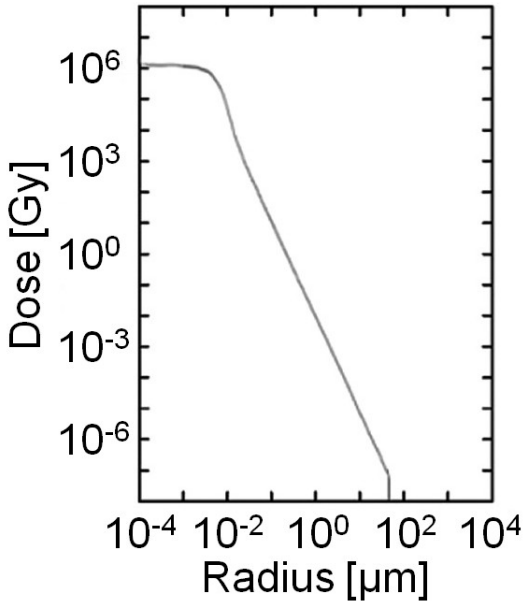

Figure 2.3.5: Example for a radial dose distribution in ion tracks as assumed in the Local Effect Model. The Figure was taken from [5] with permission and modified.

2.3.3.2 The amorphous track structure model

For the simulation of the ion radiation-induced spatial distribution of DSB, one has to assess the dose distribution corresponding to individual ion tracks penetrating a cell. In the LEM, it is assumed that the energy of an ion remains constant while it is traversing the nucleus with a length of roughly 6.5 μm. Furthermore, as a simplification for actually random energy depositions, the dose along an ion track is taken as uniform at defined radial distances R from the track center. In radial direction, the model divides the ion track into two regions: a core and a penumbra around it. Their outer radii (in μm) are energy-dependent (E is the energy in MeV/u and β is the relative velocity of the ion)[5]:

$$\begin{aligned} R_{core} &= \beta \cdot 0.0065 \mu m \\ R_{track} &= 0.062 [\frac{\mu m}{MeV^{1.7}}] \cdot E^{1.7}. \end{aligned} \tag{2.3.8}$$

When radical diffusion is neglected, there is a constant dose deposition in the cylinder that corresponds to the core region of the track and a quadratic fall-off of the radial dose D in the penumbra until no dose is deposited beyond the rim of the track. When R is the radius and λ_{norm} a constant that ensures the reproduction of the LET in the radial integral, the corresponding formulas are:

$$\begin{aligned} D &= \frac{\lambda_{norm}}{R_{core}^2} && R < R_{core} \\ D &= \frac{\lambda_{norm}}{R^2} && R_{core} \leq R \leq R_{track} \\ D &= 0 && R_{track} < R. \end{aligned} \tag{2.3.9}$$

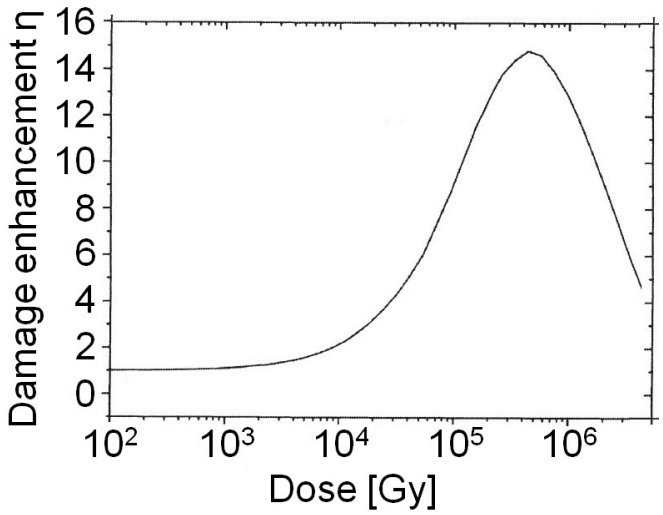

Figure 2.3.6: Dose-dependence of a DSB enhancement factor which accounts for clustering of SSB on nanometer-scale. Figure taken from [4] with permission and modified.

In a last step, it is assumed that radical diffusion modifies the initial dose deposition with regard to events that might lead to DNA modifications (indirect actions of radiation). Therefore, the radial dose defined in equation 2.3.9 is convoluted with a Gaussian distribution with a width (standard deviation) of 4 nm. Figure 2.3.5 shows an example for the resulting radial dose that is finally used for the simulation of the radiation-induced biological damage in the LEM.

2.3.3.3 Simulation of the spatial DSB distribution

The spatial distribution of DSB and eventually the numbers of iDSB and cDSB are simulated by means of the Monte Carlo method in the LEM code. In the track of every single ion traversing a cellular nucleus, there is a random induction of DSB. To draw a realization of the spatial DSB distribution pattern corresponding to a single ion, the volume around the center of the track is subdivided into several hollow cylinders with increasing radii. With the amorphous track structure model, the mean dose prevailing in each hollow cylinder is computed. Especially close to the center of the ion track, the doses are so high that there is a non-negligible probability that two single-strand breaks are produced so close to each other ($\lesssim$ 25 base pairs) that a cell will hardly be able to distinguish them from a DSB [4]. This DSB enhancement on a nanometer-scale is accounted for by multiplying the mean dose in each hollow cylinder with a dose-dependent factor ($\eta(D)$) that is visualized in Figure 2.3.6. With this enhanced dose, the expected number of initial DSB (proportionality $\alpha_{DSB} = 30\,\mathrm{Gy}^{-1}$) is derived for each hollow cylinder. By employment of a Poisson distribution around this finally expected number of DSB, realized numbers of DSB within the hollow cylinders are drawn and each DSB is assigned with a random position using a uniform distribution. Thus, a realization of the random DSB induction in a single ion track traversing a nucleus has been found.

However, it is in general not a single ion but a random number of ions that cause DSB in a considered cellular nucleus. For an expected total dose D (in Gy) that is deposited in the nucleus with area A (in cm^2) and density ρ (in g/cm^3) by ion radiation of a defined LET (in keV/μm),

the expected number $< N_{Dir} >$ of ions traversing the nucleus (direct hits) can be calculated with:

$$< N_{Dir} >= 0.63 \cdot 10^9 \cdot A \cdot D \cdot LET^{-1} \cdot \rho. \tag{2.3.10}$$

The expected number $< N_{Ind} >$ of ions that pass by a nucleus with radius R_N and touch it with a part of the penumbra (indirect hits) is:

$$< N_{Ind} >= 0.63 \cdot 10^9 \cdot [\pi(R_{track} + R_N)^2 - \pi R_N^2] \cdot D \cdot LET^{-1} \cdot \rho. \tag{2.3.11}$$

As a very good approximation, it may be assumed that the density ρ in a cellular nucleus equals the density of water with 1 g/cm^3. The actually realized number of ions directly hitting a nucleus is crucial for the deposited dose, the amount of induced damage and finally for the survival probability of a considered cell. Therefore, the LEM code employs the stratified sampling method by introduction of "hit classes" which are defined by the number of ions directly hitting a cell. There are enough hit classes around $< N_{Dir} >$ to ensure that the most probable numbers of hits per cells are reflected in the computations. Then, for every hit class, the corresponding effectiveness in cell killing is simulated separately as follows:

(i) A random number of indirectly hitting ions is drawn from a Poisson distribution with mean $< N_{Ind} >$ (indirect hits).
(ii) Each ion (direct and indirect hits) is assigned with a random spatial DSB distribution pattern as described above.
(iii) Each ion is assigned with a random position in (direct hits) or outside (indirect hits) the nucleus and the positions of the DSB are moved accordingly.
(iv) The numbers of initial DSB induced in individual cubes of a grid representing the domains in the nucleus are counted.
(v) The corresponding numbers of iDSB and cDSB are scored and the cluster index C is calculated.
(vi) With the equivalent photon dose leading to an equal value of C and the photon dose-response curve (section 2.3.3.1), the ion effect is derived.

These computational steps are repeated until the average ion effect from all simulations matches a required accuracy. After the ion effect has been derived for all hit classes, the final cell survival probability for the ion radiation is calculated as a weighted mean. The weights for the survival probabilities of the individual hit classes are implied by the Poisson distribution with expected value $< N_{Dir} >$. Figure 2.3.7 visualizes the steps of the LEM code in the computational order.

2.3.4 The Giant Loop Binary Lesion model

In the LEM, the classification of DSB and the supposed severity of the lesions strongly suggests a direct link to cell survival probabilities. This link between damage distribution patterns and cell survival probabilities was established in the Giant Loop Binary Lesion (GLOBLE) model for photon irradiation ([8]).

The GLOBLE model adapts the definition of iDSB and cDSB on the hand of single or multiple DSB within a DNA giant loop. Thus, after acute photon irradiation of a mammalian cell, the expected numbers of iDSB and cDSB ($N_{iDSB}(D)$ and $N_{cDSB}(D)$) can be derived as described above (equations 2.3.6). The assumption that cDSB are much more likely to lead to cell death suggests

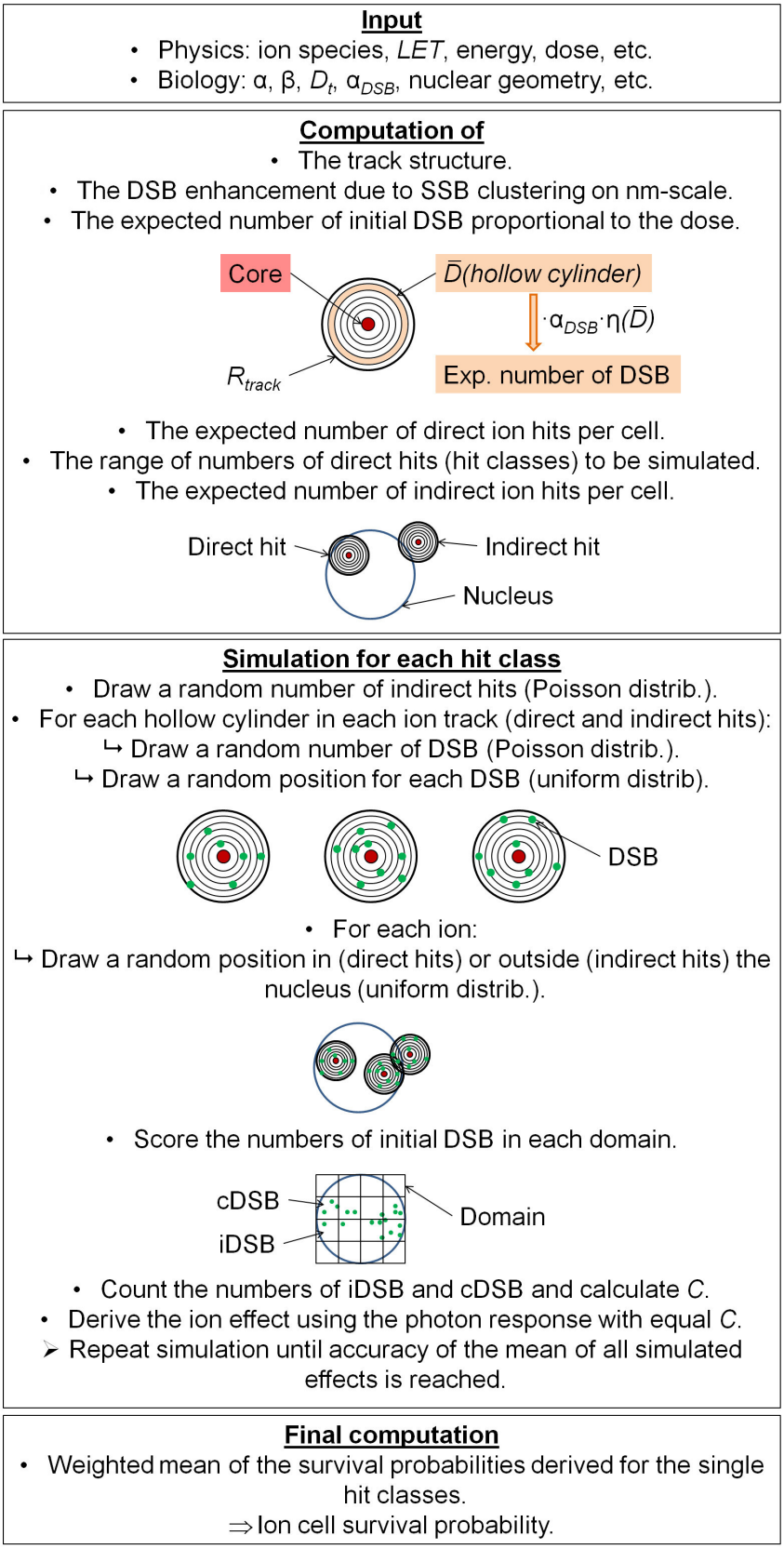

Figure 2.3.7: The major steps in the LEM code needed for the investigations in this thesis. The sketches of ion track structures and corresponding DSB are strongly simplified and do not reflect actual orders of magnitude (e.g. the size of DSB in comparison to track sizes).

that there is a probability ϵ_c for at least one lethal event after a cDSB which is much larger than the respective probability for a lethal event after an iDSB (ϵ_i). With the knowledge of $N_{iDSB}(D)$ and $N_{cDSB}(D)$, the employment of ϵ_i and ϵ_c as model parameters already implies the expected number of lethal events after photon radiation - which is the requested radiation effect *Eff(D)*:

$$Eff(D) = \epsilon_i N_{iDSB} + \epsilon_c N_{cDSB}. \tag{2.3.12}$$

The corresponding cell survival probability is the Poisson probability for no lethal event:

$$S(D) = e^{-(\epsilon_i N_{iDSB} + \epsilon_c N_{cDSB})}. \tag{2.3.13}$$

When the linear component of the GLOBLE effect for $D \to 0$ is identified with the linear-quadratic parameter α and half of the second-order term of a Taylor expansion with respect to the dose is identified with β, one finds that [8]:

$$\begin{aligned} \epsilon_i &= \frac{\alpha}{\alpha_{DSB}} \\ \epsilon_c &= 2\frac{N_L\beta + \alpha_{DSB}\alpha}{\alpha_{DSB}^2}. \end{aligned} \tag{2.3.14}$$

These conversion formulas will be used several times during subsequent investigations.

Several extensions of the GLOBLE model have successfully been introduced to account for cell cycle effects [61], ultrasoft X-ray radiation [62] or dynamic effects [63]. The dynamic extension will be of special relevance for this thesis and therefore be explained in detail in section 2.4.3. Furthermore, for the subsequent parts of this thesis, it should be emphasized that the lethalities of iDSB and cDSB (ϵ_i and ϵ_c) have only been proven to be appropriate parameters for the description of photon cell survival curves with the GLOBLE model. In the LEM for ion radiation, the different severity of iDSB and cDSB is still used to motivate the derivation of a cluster index and an equivalent photon dose with the LQL model. However, a transfer of the two lethalities to the LEM would allow to directly compute the effect implied by the numbers of iDSB and cDSB induced by ion radiation. Consequently, such a modification of the LEM is in progress, but it has not been finished, yet.

2.4 Time-dose effects

The cellular response to radiation does not only depend on the total dose and on the *LET* but also on the schedule of its delivery. When photon irradiation is protracted over time by lowering the *dose-rate* or when it is split into multiple *fractions*, the number of induced DSB, which is implied by the total dose, remains constant but the generation of the single lesions is separated in time. Thus, cells are given the opportunity to repair some of the induced damage before further damage arises. When one e.g. assumes that clustering of DSB is decisive for the severity of the radiation effect, as it is done in the LEM and GLOBLE model, Figure 2.4.1 helps to understand the temporal aspects. Instead of four severe cDSB (red) and six rather harmless iDSB (green) after acute irradiation, only two cDSB and ten iDSB are observed during and after protracted photon irradiation because spatially close initial lesions have been separated in time. The same principle holds true when a dose is fractionated into several acute doses. During each

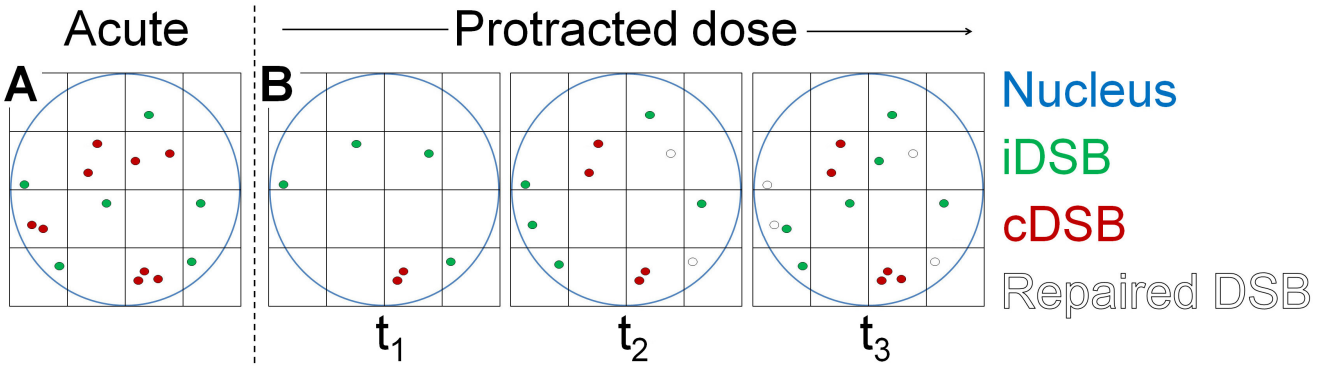

Figure 2.4.1: Visual explanation of the effect of dose protraction in the framework of the LEM and GLOBLE model. When a total dose is protracted over the time (three discrete time points t between start and end of irradiation are shown in Panel (B)), the initially induced DSB are temporarily separated in contrast to acute irradiation (A). Thus, a cell might repair some of the DSB before other DSB occur in the same domain and lead to more severe types of damage (cDSB).

radiation break cells are given time to repair and the severity of the induced damage is reduced, consequently.

Obviously, there are two temporal limiting cases for the protraction of doses: when photon doses are applied in a short amount of time there is hardly a chance for simultaneous cellular repair and when doses are protracted to infinity, no severe lesions occur since all DSB are temporarily separated. The time scale of the transition between these two limits depends crucially on the time scale of cellular repair. When cellular repair interferes with the induction of lesions, an intermediate lesion pattern with an intermediate radiation effectiveness has to be expected.

Beyond photon radiation, an interesting question which has hardly been investigated is the interplay between the irradiation schedule and the *LET* of the radiation. With the dimension of the *LET*, two additional limiting cases occur next to low-*LET* + short protraction times and low-*LET* + large protraction times: high-*LET* + short protraction times and high-*LET* + large protraction times. When the clustering of DSB is again considered to be decisive for the radiation response, it should be expected that severe damage is induced in both high-*LET* limits due to the spatial density of DSB within single ion tracks. However, in the transition from high- to low-*LET* ion radiation, more and more time effects should become observable. This not yet well-explored transition will be examined as part of this thesis (section 3.4).

2.4.1 Observing time-dose effects

There are mainly two experimental setups measuring time-dose effects in cell survival probabilities: *dose-rate experiments* and *split-dose experiments*. In split-dose experiments [64][65], a total dose is split into two parts which are applied with a separation time T_{sep}. At $T_{sep} = 0$ the acute cell survival probability is measured and at $T_{sep} \to \infty$ the cell survival probability is maximally increased. The transition happens up to around $T_{sep} = 3\,\mathrm{h}$. Figure 2.4.2A shows an example.

In dose-rate experiments [64][66][67][68], cell survival curves are recorded under the application of several requested dose-rates. For high dose-rates, the acute cell survival curve is observed and for extremely low dose-rates one measures linear curves on a logarithmic scale

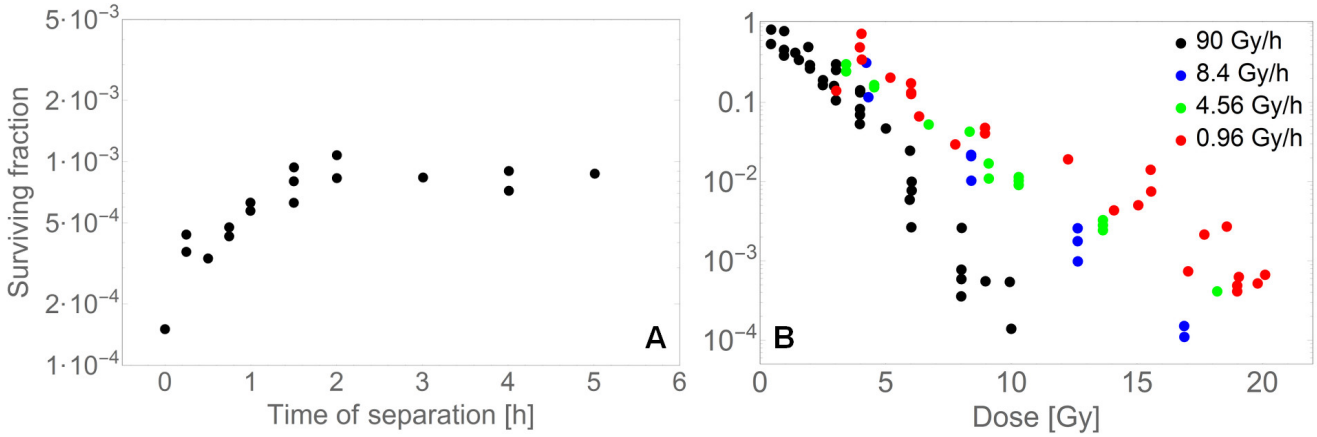

Figure 2.4.2: A) Photon split-dose experiment measured with the LL cell line. Two times 2.5 Gy were applied and the survival probability was recorded in dependence of the separation time. B) Photon dose-rate experiment conducted with the same cell line. Cell survival curves for specific dose-rates (different colors) were recorded. The experimental data was taken from [64].

with the slope usually corresponding to the initial linear slope of the acute curve. In the transition from instantaneous irradiation to extremely low-dose-rate irradiation, the curvature of the recorded survival curves diminishes. In the LEM and GLOBLE framework this observation can be explained with the fractions of iDSB and cDSB. At low doses, the fraction of iDSB is much larger than the fraction of cDSB, independent of the dose-rate. Therefore, the low lethality of iDSB (ϵ_i) dominates the shape of cell survival curves and a corresponding linear slope is recorded. Under application of high dose-rates, the fraction of cDSB increases with the dose and a transition from the dominating low lethality of iDSB to the high lethality of cDSB (ϵ_c) results in a bending of survival curves, consequently. However, when the dose-rate is lowered, ever less cDSB are produced even at high doses so that the bending of survival curves becomes less pronounced until it completely vanishes at extremely low dose-rates. Figure 2.4.2B shows an example for a dose-rate experiment.

One last observation of time-dose effects is of interest for this thesis: the decrease of incident probabilities of *deterministic radiation effects* with a decreasing dose-rate. Deterministic radiation effects are clinically observed after radiation exposure with sufficiently high dose and comprise amongst others the bone marrow syndrome, gastrointestinal syndrome, pneumonitis and cartaracts. The dose-dependence of the fraction of patients suffering from symptoms of a considered disease shows a quasi-threshold around which the incidence probability increases rapidly from 0% to 100%. A Weibull-function has empirically been shown to describe this dose-dependence adequately (Figure 2.4.3, blue curve) [69]. When the dose-rate $\dot{D}$ of the exposure is lowered, it has empirically been observed that the dose D_{50} at which 50% of the patients show symptoms decreases inversely proportional (Figure 2.4.3, red curve):

$$D_{50}(\dot{D}) = \theta_\infty + \frac{\theta_1}{\dot{D}}. \tag{2.4.1}$$

The parameters θ_∞ which equals D_{50} after acute exposure and θ_1 which implies the strength of the impact of the dose-rate on D_{50} are characteristic for a considered disease. For pneumonitis

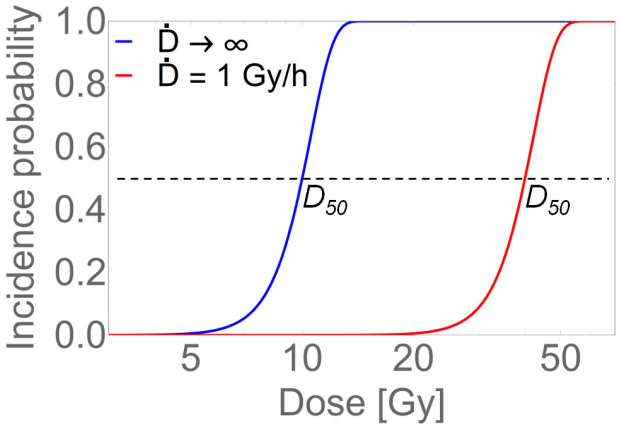

Figure 2.4.3: Dose-dependence of the incidence probability of pneumonitis. When the dose-rate $\dot{D}$ is lowered (red curve), the dose D_{50} at which 50% of the patients show symptoms increases. Empirical formula and parameters taken from [69].

$\theta_\infty = 10\,\mathrm{Gy}$ and $\theta_1 = 30\,\mathrm{Gy^2h^{-1}}$ are reported and for the bone marrow syndrome $\theta_\infty = 3\,\mathrm{Gy}$ and $\theta_1 = 0.07\,\mathrm{Gy^2h^{-1}}$ [69]. Thus, large dose-rate effects should be expected for pneumonitis whereas the impact of the dose-rate on the incidence of the bone marrow syndrome should be much lower. Since deterministic radiation effects are suspected to be closely linked to cell survival, the observed time-dose effects might be predictable with kinetic cell survival models, as the GLOBLE model, as it will be shown in this thesis (section 3.1).

2.4.2 The kinetic extension of the LQ model

In order to describe time-dose effects with the Linear-Quadratic model, Lea and Catcheside introduced a kinetic extension [70][71]. The authors based their work on studies of chromatid breaks and assumed that they are induced proportionally (yield ξ) to the dose. In reference to this proportionality, repair involving single lesions (restitution) was considered to be responsible for the linear component of cell survival curves on a logarithmic scale. Since the probability for inter-lesion repair (exchange) increases quadratically with the number of present lesions, exchanges were thought to be responsible for the quadratic bending. Furthermore, Lea and Catcheside suggested that the major fraction of chromatid breaks will be restituted after irradiation with rate r and that the kinetics of chromatid exchanges will be negligible in the overall dynamics, consequently. With that, the time-dependence of the number n of chromatid breaks during irradiation with dose-rate $\dot{D}$ is defined by:

$$\begin{aligned} \frac{dn}{dt} &= \xi\dot{D} - rn, \quad n(0) = 0, \\ n(t) &= \frac{\xi\dot{D}}{r}(1 - e^{-rt}). \end{aligned} \tag{2.4.2}$$

When the radiation is protracted until time T, the number of chromatid exchanges n_{ex} formed during and after irradiation is:

$$n_{ex} = \int_0^T \tilde{\beta}[\frac{\xi\dot{D}}{r}(1 - e^{rt})]^2 dt + \int_T^\infty \tilde{\beta}[\frac{\xi\dot{D}}{r}(1 - e^{-rT})]^2 e^{-2r(t-T)} dt = \beta G(T) D^2 \tag{2.4.3}$$

with the LQ model parameter $\beta = 0.5\xi^2\tilde{\beta}r^{-1}$, the dose $D = \dot{D}T$ and the dose-protraction factor

$$G(T) = 2\frac{rT + e^{-rT} - 1}{(rT)^2}. \tag{2.4.4}$$

The dose-protraction factor "interpolates" between a full quadratic bending of cell survival curve at short protraction times and no bending at long protraction times. The corresponding protraction-time-dependent radiation effect is:

$$Eff(D,T) = \alpha D + \beta G(T) D^2. \tag{2.4.5}$$

For split-dose experiments with two instantaneously applied equal doses (total dose D), one has to calculate the number of chromatid exchanges during the irradiation break T_{sep} and after the second fraction. Since this computation is lengthy, only the result is presented here:

$$Eff(D,T_{sep}) = \alpha D + \frac{1}{2}\beta D^2(1 + e^{-rT_{sep}}). \tag{2.4.6}$$

2.4.3 The kinetic extension of the GLOBLE model

In the kinetic extension of the GLOBLE model [63], the temporal development of the fractions of domains without a DSB (f_0), with an iDSB (f_i) and with a cDSB (f_c) is crucial. It implies the fractions of domains that will eventually suffer lethal events after iDSB (l_i) and cDSB (l_c) and with that the radiation effect an infinite amount of time after the irradiation:

$$Eff = N_L[l_i(t \to \infty) + l_c(t \to \infty)]. \tag{2.4.7}$$

The theoretical derivation of cell survival probabilities an infinite amount of time after a radiation exposure can be identified with a derivation of cell survival probabilities after complete repair [72].

In order to describe the temporal development of f_0, f_i, f_c, l_i and l_c, differential equations reflecting the dynamics involved in damage induction and repair are employed. Figure 2.4.4 helps to understand the formulation of the kinetic extension of the GLOBLE model by visualizing the processes and corresponding rates that were accounted for. For the induction of damage, it is assumed that there is a stepwise transition of domains from the group without DSB to the group of domains with iDSB and, in case that this first DSB is not repaired before a next DSB arises in the same domain, the transition into the group of domains with cDSB. The rate of induction of DSB in a cell is assumed to be proportional to the applied dose-rate, in agreement with the proportionality between the number of induced DSB and the dose α_{DSB}. With that, the expected number of DSB induced per unit of time in a domain is:

$$\dot{\lambda}(\dot{D}) = \frac{\alpha_{DSB}\dot{D}}{N_L}. \tag{2.4.8}$$

For the repair of DSB, kinetics that are in agreement with the binary concept of iDSB and cDSB in DNA giant loops were adapted. The basic GLOBLE (and LEM) concept suggests that iDSB

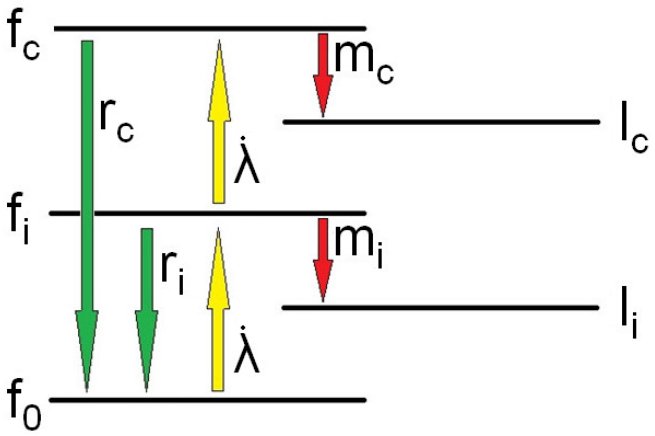

Figure 2.4.4: Transitions between the fractions of domains without DSB (f_0), with iDSB (f_i), with cDSB (f_c), with lethal event after iDSB (l_i) and with lethal event after cDSB (l_c). Corresponding transition rates are written next to the arrows. Figure taken from [63] with permission and modified.

are repaired relatively quickly because the ends of a concerned giant loop remain attached to the nuclear matrix and because the broken ends of the DNA can hardly leave their original site. In contrast, the repair of cDSB is supposed to take much longer since fragments might part from the loop and since such complex lesions might involve a more complex repair machinery. Actually, experiments have shown evidence for an increase of misrejoining events [51] and for an involvement of multiple DSB in giant loops [48][49] during the so-called slow phase of DSB rejoining. Consequently, a bi-phasic repair of lesions with a short half-life time HLT_i for the repair of iDSB and a long half-life time HLT_c for the repair of cDSB was introduced in the GLOBLE model. The total corresponding repair rates ($\ln(2)/HLT_x$, $x = i,c$) are constituted of the rates for repair with lethal event and without lethal events. Since the lethalities of iDSB and cDSB (ϵ_i and ϵ_c) imply the fractions of domains which eventually suffer lethal events, they are reflected in the rates for the incidence of lethal events (m_x, $x = i,c$) in damaged domains:

$$m_x = \epsilon_x \frac{\ln(2)}{HLT_x}. \tag{2.4.9}$$

The remaining damaged domains which do not suffer lethal events return to the state without DSB with rates

$$r_x = (1-\epsilon_x)\frac{\ln(2)}{HLT_x}. \tag{2.4.10}$$

Since it seems unlikely that a last DSB, potentially remaining after repair of the other DSB of a cluster, is suddenly treated with the high-fidelity repair mechanism corresponding to iDSB, domains with cDSB do not migrate back to the group with iDSB.

With the rates for the induction and repair of iDSB and cDSB, the coupled differential equations for the temporal development of the fractions of domains without DSB, with iDSB, with cDSB, with lethal event after iDSB and with lethal event after cDSB become:

$$
\begin{aligned}
\frac{df_0}{dt} &= -\dot{\lambda} f_0 + r_i f_i + r_c f_c \\
\frac{df_i}{dt} &= \dot{\lambda} f_0 - (\dot{\lambda} + r_i + m_i) f_i \\
\frac{df_c}{dt} &= \dot{\lambda} f_i - (r_c + m_c) f_c \\
\frac{dl_i}{dt} &= m_i f_i \\
\frac{dl_c}{dt} &= m_c f_c .
\end{aligned}
\tag{2.4.11}
$$

With initial conditions reflecting the schedule of dose delivery, the solutions of l_i and l_c at an infinite time after irradiation imply the cell survival probability. It is the Poisson probability for no lethal event:

$$
S(D, \dot{D}) = e^{-N_L[l_i(t\to\infty)+l_c(t\to\infty)]}. \tag{2.4.12}
$$

For dose-rate experiments one has to evaluate the differential equations only at time T where the irradiation ceases. The total number of lethal events an infinite amount of time after the irradiation is implied by the number of lethal events that have happened up to that point in time plus the number of iDSB and cDSB that will be misrepaired afterward:

$$
Eff_{dose-rate}(D, \dot{D}) = N_L[l_i(T) + l_c(T) + \epsilon_i f_i(T) + \epsilon_c f_c(T)]. \tag{2.4.13}
$$

The kinetic extension of the GLOBLE model has already been successfully validated on the hand of several dose-rate experiments in [9]. The application to split-dose experiments and to deterministic radiation effects will be presented in this thesis (section 3.1).

2.4.4 The Repair Misrepair model

One well-accepted approach for the description of time-dose effects in cell survival probabilities after photon irradiation is the Repair Misrepair (RMR) model. In the original publication from 1980, Tobias et al. [73] present the most general concept of the mechanistically motivated model and many examples for how to apply it in special cases. However, with regard to the relevance for investigations in this study, only the formulation for dose-rate experiments will shortly be summarized in the following.

In the basic RMR approach, only one class of radiation-induced lesions is considered to be decisive for cell survival probabilities: the "uncommitted lesions" (U-lesions). U-lesions might represent any specific molecular lesion as long as there is a consistency between model predictions and experimental observations. As a first approximation, in each cell, U-lesions are induced proportionally with yield α to the applied dose-rate $\dot{D}$. This yield α should not be confused with the linear-quadratic parameter.

Depending on the proximity to other U-lesions, U-lesions might either undergo a linear repair process with rate λ which means intra-lesion repair or a quadratic repair process with rate κ which means a pairwise interaction. With these assumptions about damage induction and

repair, the subsequent differential equation for the temporal development of U-lesions can be set up:

$$\frac{dU}{dt} = \alpha\dot{D} - \lambda U - \kappa U^2. \tag{2.4.14}$$

The yield of U-lesions that have been linearly repaired in a cell is denominated R_L in the RMR model and the corresponding yield for quadratically repaired U-lesions is called R_Q. Consequently, at time t after the beginning of a radiation exposure where $R_L(0) = R_Q(0) = 0$, there are the following numbers of linearly or quadratically repaired U-lesions in a cell:

$$\begin{aligned} R_L &= \int_0^t \lambda U(\tilde{t})d\tilde{t} \\ R_Q &= \int_0^t \kappa U^2(\tilde{t})d\tilde{t} \end{aligned} \tag{2.4.15}$$

When the fractions (1-ϕ) and (1-δ) lead to lethal events after linear or quadratic repair, respectively, the radiation effect Eff predicted with the RMR model is:

$$Eff = (1-\phi)R_L + (1-\delta)R_Q. \tag{2.4.16}$$

In the special case of a protracted irradiation from time 0 to T, where T and a given dose D imply the dose-rate $\dot{D} = D/T$, the effect an infinite amount of time after the irradiation can be calculated with:

$$Eff(D,T) = 0.5[\lambda\epsilon_m + 2(1-\delta)\alpha\dot{D} - \epsilon_m\lambda_a]T - \ln\left[\epsilon_m\left(1 + \frac{\kappa\alpha\dot{D}(\lambda_a - \lambda)(1-e^{\lambda_a T})}{\lambda^2(\lambda_a + \lambda) + 4\kappa\lambda\alpha\dot{D}}\right)\right] \tag{2.4.17}$$

and

$$\epsilon_m = \frac{\lambda(\phi - \delta)}{\kappa}, \quad \lambda_a = \sqrt{4\kappa\alpha\dot{D} + \lambda^2}. \tag{2.4.18}$$

This formulation of the RMR model was used for the description of dose-rate experiments during subsequent investigations.

2.4.5 The Lethal Potentially Lethal model

The last mechanistically motivated kinetic cell survival model for photon radiaton that is of relevance for this thesis is the Lethal Potentially Lethal (LPL) model by Curtis [74]. It was introduced in 1986 and is conceptually related to the RMR model with some distinctive features, though, which will be pointed out in the comparison of kinetic cell survival models in section 3.3. Again, only those parts of the setup of the LPL model which will be used in subsequent analysis will be explained in the following.

In the LPL model, there are two classes of lesions which are likely to be identified with specific forms of DSB. First, there are directly lethal lesions (DLL) which are induced proportionally to the applied dose-rate $\dot{D}$ with yield η_L per cell. They do not undergo transformations in the course of time and are directly identified with lethal events in the mathematical setup of the LPL

model. Second, there are potentially lethal lesions (PLL) which are also induced proportionally to the dose-rate, but with yield η_{PL} per cell. PLL are either repaired in a linear process with rate ϵ_{PL} involving a single lesion only or in a quadratic process with rate ϵ_{2PL} involving the interaction of two lesions. All interactions lead to lethal events in the LPL model whereas lethal events never happen during intra-lesion repair processes. The presented assumptions about the dynamics of damage induction and repair in the LPL model allow to formulate the following differential equations for the numbers of PLL n_{PL} and lethal events n_L in a cell:

$$\begin{aligned} n_{PL} &= \eta_{PL}\dot{D} - \epsilon_{PL} n_{PL} - \epsilon_{2PL} n_{PL}^2 \\ n_L &= \eta_L \dot{D} + \epsilon_{2PL} n_{PL}^2. \end{aligned} \tag{2.4.19}$$

When a cell is exposed to a protracted dose from time 0 to T and there is no damage before the irradiation, there are the following numbers of PLL and lethal events at time T:

$$\begin{aligned} n_{PL}(T) &= \frac{2\eta_{PL}\dot{D}(1-e^{-\epsilon_0 T})}{\epsilon_0 + \epsilon_{PL} + (\epsilon_0 - \epsilon_{PL})e^{-\epsilon_0 T}} \\ n_L(T) &= \eta_L D + \frac{\epsilon_{PL}}{\epsilon_{2PL}} \ln\left[\frac{2\epsilon_0}{\epsilon_0 + \epsilon_{PL} + (\epsilon_0 - \epsilon_{PL})e^{-\epsilon_0 T}}\right] + \frac{(\epsilon_0 - \epsilon_{PL})^2 T}{4\epsilon_{2PL}} - n_{PL}(T) \end{aligned} \tag{2.4.20}$$

with

$$\epsilon_0 = \sqrt{\epsilon_{2PL}^2 + 4\epsilon_{2PL}\eta_{PL}\dot{D}}. \tag{2.4.21}$$

When survival probabilities are evaluated at infinite amount of time - identifiable with complete repair - the corresponding effect for a protracted irradiation is:

$$Eff(D,T) = n_{PL}(T) + n_L(T) - \frac{\epsilon_{PL}}{\epsilon_{2PL}} \ln\left[1 + \frac{n_{PL}(T)}{\epsilon_{PL}/\epsilon_{2PL}}\right]. \tag{2.4.22}$$

After substitution of T by $\dot{D} = D/T$, this formulation of the LPL was used for the description of dose-rate experiments.

2.5 Quantitative measures for model comparisons

In a comparison of models which are designed to describe experimental measurements, it is not only important to determine the model which provides the highest accuracy in fits to the available data. With a sufficient number of free parameter values, one can reproduce almost every dependency and thus, models with high numbers of free parameters would often be favored. However, the good performance of complex models might to some degree be due to the fact that they capture random fluctuations of the data points better than simple models although the simple models might be closer to the dependency that is actually underlying the observations. Therefore, in a comparison, one has to find the model which describes the available data points adequately with a reasonable amount of parameter values, also known as the *principle of parsimony*. There are several quantitative measures for a parsimonious model comparison and especially when the data situation is not perfect, the question which measure to choose becomes philosophical. Two of the measures which will be used for investigations in this thesis will be explained in the following. For further reading [75] and [76] is suggested.

2.5.1 The reduced chi-squared

The reduced chi-squared measure is popular for model comparisons, perhaps due to the simplicity of its calculation and its direct applicability to data which are presented as the mean of several samples with measurement errors. In general, the chi-squared value for a model $M(\vec{x}, \vec{P})$ with parameters $\vec{P}$, which describes N determined mean values $\bar{y}_i$ (i = 1,2,...,N) with variances σ_i^2 in dependence of $\vec{x}$, is defined as:

$$X^2 = \min_{\vec{P}} \left[\sum_{i=1}^{N} \left(\frac{(M(\vec{x}_i, \vec{P}) - \bar{y}_i)^2}{\sigma_i^2} \right) \right]. \tag{2.5.1}$$

The errors of the determined mean values have to originate from a Gaussian distribution to allow for the calculation of X^2. In practice, the measurement errors are gained from the fluctuations of the original measurements underlying $\bar{y}_i$ and are thus only realizations of some random error distribution themselves. However, distributions for the errors are not accounted for in the derivation of X^2 and realized measurement errors are considered as deterministic ones.

In order to account for the complexity of models, X^2 is normalized with the number of degrees of freedom K that was used to derive it. The result is the reduced chi-squared measure which can be used to compare models:

$$X_{red}^2 = \frac{X^2}{K}. \tag{2.5.2}$$

As a rule of thumb, the closer X_{red}^2 is to 1, the better is a model. The number of degrees of freedom K corresponds to the number of data points N minus the effective number of free parameter values - that means the number of parameter values adjusted for any correlations between them. Actually, the derivation of K might be challenging for non-linear models and thus constitutes a first drawback in the application of X_{red}^2. In summary, the most important drawbacks are:

(i) Difficulties in the derivation of the number of degrees of freedom for non-linear models.
(ii) Measurement errors have to originate from a Gaussian distribution.
(iii) When no measurement errors are given, X_{red}^2 is far from 1.
(iv) For non-nested models, there is no direct way to derive the significance of differences in the performance of several models.
(v) The difference between two values derived for two models has no intuitive meaning.

On the other hand, a selection of advantages of the reduced chi-squared measure are:

(i) Simple to calculate.
(ii) Due to the additivity of the terms for the single data points, weights can easily be assigned to them.
(iii) Data presented as mean values ± standard error can easily be evaluated.

2.5.2 The Akaike Information Criterion

The Akaike information criterion (*AIC*) is an information-theoretic approach allowing for multimodel inference. As such, it intuitively allows to rank models with respect to their support

by the investigated data. Furthermore, after distinction of the best approximating model, it provides a way to assess the the relative evidence for alternative models.

For the derivation of the *AIC* one has to set up the likelihood function for the observation of the available measurements y with a given model M. The model parameter values $\tilde{\vec{P}}$ which maximize the likelihood of observing the data with the model are optimal. With the corresponding *maximum-likelihood* $L(\tilde{\vec{P}}|y,M)$, the *AIC* is defined as:

$$AIC = -2\ln[L(\tilde{\vec{P}}|y,M)] + 2K. \tag{2.5.3}$$

Here, K is the number of estimable parameters. The smaller the value of *AIC*, the larger is the support for a model that can be extracted from the given data.

As a simplification, it is often assumed that the errors in the measurements originate from the same distribution. Then, in case of uncorrelated observations, the likelihood function is simply the product of several probability distributions where the given residuals are inserted. In case that a Gaussian distribution underlies the residuals, the maximum-likelihood can be gained from the residual sum of squares (all denotations have been adopted from section 2.5.1):

$$RSS = \min_{\vec{P}}\left[\sum_{i=1}^{N}((M(\vec{x}_i,\vec{P}) - y_i)^2)\right]. \tag{2.5.4}$$

With RSS one can calculate *AIC* as:

$$AIC = -2\ln[RSS/N] + 2K. \tag{2.5.5}$$

The number of estimable parameters K corresponds to the number of free model parameters plus one for the variance in the case of a Gaussian distribution.

However, when data sets are presented in the form of mean values ± standard errors, it becomes difficult to set up the likelihood function because the evidences for non-equal distributions of the residuals have to be accounted for. In that case, the computation of the actual *AIC* becomes computationally challenging.

When experiments with small numbers of measurements should be used for a model comparison, there is a correction term to the *AIC* which allows for a more reliable evaluation of the model performances:

$$AICc = -2\ln[RSS/N] + 2K + \frac{2K(K+1)}{N-K-1}. \tag{2.5.6}$$

Since the *AICc* converges to the *AIC* in the limit of large data sets and has no further drawbacks, its usage is generally recommended [75]. Another convenient property of the *AIC(c)* is the intuitive interpretation of differences found in the performance of several models. When $AICc^{min}$ corresponds to the model which approximates the data the best, the inverse *evidence ratio* tells how likely it is that another model with $AICc^i$ is actually closer to the data generating process:

$$ER = e^{\frac{AICc^{min} - AICc^i}{2}}. \tag{2.5.7}$$

In summary, the *AIC(c)* has amongst others the following advantages:

(i) Multiple non-linear and non-nested models can be ranked with respect to their support by the data.
(ii) The inverse evidence ratio intuitively tells how likely it is that an alternative model is more appropriate than the one that has been found to approximate the data the best.
(iii) The residuals between measurements and model predictions do not have to follow a specified distribution.
(iv) The *AICc* allows for reliable judgements even when there are relatively few measurements.

On the other hand, some of its shortcomings are:
(i) The computational effort might be high when no special case can be exploited.
(ii) It is hard to include weights or measurement errors for the data points in the computations.
(iii) There is no way to assess the absolute performance of a model. If all models describe the data badly one cannot infer it from the *AIC(c)*.

3 The projects with corresponding results and discussions

3.1 Applications of the GLOBLE model

3.1.1 Motivation

The concept of the Giant Loop Binary Lesion (GLOBLE) model suggests that it is applicable to describe cell survival probabilities after photon irradiation with arbitrary dose delivery schedule [8][63]. In preceding studies [9] it has been shown that the model approximates data recorded in photon dose-rate experiments, where dose-dependent cell survival curves are measured for varying dose-rates, very well. However, referring to its setup, the GLOBLE model should also be usable to provide descriptions to other observations that involve time-dose effects after photon irradiation. A first example is represented by split-dose experiments where two instantaneously applied doses are temporarily separated and cell survival probabilities are recorded in dependence of this separation time. Such split-dose experiments reflect the capacity of an investigated cell line to repair induced biological damage between the two exposures and to reduce the radiation effectiveness. For practical purposes as for photon radiotherapy, they consequently allow to assess time scales where the dose delivery schedule has an impact on the finally achieved radiation response.

Another very useful field of application of the GLOBLE model is the assessment of time-dose effects in the clinically observed incidence of deterministic radiation effects. Deterministic radiation effects denominate diseases as pneumonitis or the bone marrow syndrome that are thought to be closely related to radiation-induced cell death. It has empirically be observed that the dose where 50% of the patients show symptoms of such diseases increases when the dose-rate is lowered. Due to the fact that the GLOBLE model can reproduce time-dose effects in cell survival probabilities, it was tested whether this applicability also concerns time-dose effects in related deterministic radiation effects.

In the following, the investigation of the GLOBLE model with regard to its adequacy in the description of split-dose experiments and the prediction of time-dose effects in deterministic radiation effects will be presented. The corresponding results were published in [63].

3.1.2 Materials and methods

3.1.2.1 GLOBLE formulation for split-dose experiments

The basic setup of the GLOBLE model with regard to underlying assumptions and the formulation of differential equations that describe the dynamics of damage induction and repair during

irradiation was presented in sections 2.3.4 and 2.4.3. In order to apply the GLOBLE model to split-dose experiments, an expression for cell survival probabilities after two temporarily separated acute exposures had to be derived.

According to equation 2.3.6, when a first dose D_1 is instantaneously given, the expected numbers of domains in a cellular nucleus with no DSB (N_0), an iDSB (N_{iDSB}) or a cDSB (N_{cDSB}) are:

$$\begin{aligned} N_0(0^+) &= N_L e^{-\lambda_1} \\ N_{iDSB}(0^+) &= N_L \lambda_1 e^{-\lambda_1} \\ N_{cDSB}(0^+) &= N_L(1-\lambda_1 e^{-\lambda_1} - e^{-\lambda_1}) \end{aligned} \tag{3.1.1}$$

with

$$\lambda_1 = \frac{\alpha_{DSB} D_1}{N_L}. \tag{3.1.2}$$

Here, t = 0^+ denominates the time directly after the first exposure, N_L the number of domains and α_{DSB} the DSB yield. Referring to equations 2.4.11 with $\dot{\lambda} = 0$, after a time T_{sep} has gone by, a part of the iDSB and cDSB has been repaired. Corresponding domains either join the group of domains without DSB or are scored as domains with lethal event after iDSB (L_{iDSB}) or cDSB (L_{cDSB}). That means at time T_{sep}^-, shortly before the second exposure, it holds that:

$$\begin{aligned} N_0(T_{sep}^-) &= N_0(0^+) + (1-\epsilon_i) N_{iDSB}(0^+)(1-e^{-(r_i+m_i)T_{sep}}) \\ &\quad + (1-\epsilon_c) N_{cDSB}(0^+)(1-e^{-(r_c+m_c)T_{sep}}) \\ N_{iDSB}(T_{sep}^-) &= N_{iDSB}(0^+) e^{-(r_i+m_i)T_{sep}} \\ N_{cDSB}(T_{sep}^-) &= N_{cDSB}(0^+) e^{-(r_c+m_c)T_{sep}} \\ L_{iDSB}(T_{sep}^-) &= \epsilon_i N_{iDSB}(0^+)(1-e^{-(r_i+m_i)T_{sep}}) \\ L_{cDSB}(T_{sep}^-) &= \epsilon_c N_{cDSB}(0^+)(1-e^{-(r_c+m_c)T_{sep}}). \end{aligned} \tag{3.1.3}$$

Again, the total rates of repair $r_x + m_x$ ($x = i, c$) are defined by the half-life times of iDSB and cDSB HLT_x with $r_x + m_x = \ln(2)/HLT_x$. Directly after an instantaneous application of the second dose at time T_{sep}, the numbers of domains with no DSB, an iDSB or a cDSB are:

$$\begin{aligned} N_0(T_{sep}^+) &= N_0(T_{sep}^-) e^{-\lambda_2} \\ N_{iDSB}(T_{sep}^+) &= N_{iDSB}(T_{sep}^-) e^{-\lambda_2} + N_0(T_{sep}^-) \lambda_2 e^{-\lambda_2} \\ N_{cDSB}(T_{sep}^+) &= N_{cDSB}(T_{sep}^-) + N_0(T_{sep}^-)(1-\lambda_2 e^{-\lambda_2} - e^{-\lambda_2}) \\ &\quad + N_{iDSB}(T_{sep}^-)(1-e^{-\lambda_2}) \end{aligned} \tag{3.1.4}$$

with

$$\lambda_2 = \frac{\alpha_{DSB} D_2}{N_L}. \tag{3.1.5}$$

At an infinite amount of time after the irradiation, which mathematically represents a complete processing of the damage, all these occurring iDSB and cDSB are either repaired with viable outcome or they have lead to a lethal event - the corresponding fractions are ϵ_i and ϵ_c. Therefore, the total number of lethal events induced by the split-dose irradiation, which is equated with the radiation effect is:

$$Eff = L_{iDSB}(T_{sep}^{-}) + L_{cDSB}(T_{sep}^{-}) + \epsilon_i N_{iDSB}(T_{sep}^{+}) + \epsilon_c N_{cDSB}(T_{sep}^{+}). \tag{3.1.6}$$

The corresponding survival probability is the probability for no lethal event

$$S = e^{-Eff}. \tag{3.1.7}$$

For the subsequent investigations, the GLOBLE effect Eff for split-dose irradiation was used to describe the negative logarithm of experimentally measured data. In agreement with previous studies [8][9], the number of domains N_L was set to 3000 and the DSB yield α_{DSB} to 30 Gy^{-1}. Furthermore, since it has been shown in [77] that the value of the half-life time of cDSB, HLT_c, has little impact on final cell survival probabilities, it was fixed to 5 h for the computations. Thus, ϵ_i, ϵ_c and HLT_iconstituted the three free fit parameters.

3.1.2.2 Experimental split-dose data

In order to test if the GLOBLE model matches cell survival probabilities measured in split-dose experiments, five data sets were selected from literature. Table 3.1.1 lists the original publications, the irradiated cell lines and the applied photon doses in Columns 1-3. Since the data sets were graphically presented in the original publications, as data points representing the mean of several measurements, they were read in and digitized with "GetData Graph Digitizer" [78]. Unfortunately, the graphical data sets contained no error bars or error bars that were too small to be noticeable. Therefore, the statistical power to derive absolute measures for the quality of the GLOBLE model in the description of these data sets (e.g. in terms of a reduced chi-squared) was limited.

To find the best fit of the GLOBLE model to the experimental data, the sum of squares between the data points y (on a negative logarithmic scale) and model predictions Eff was minimized.

Cell line	**Publication**	**Doses [Gy]**	ϵ_i	ϵ_c	HLT_i **[h]**
CHO 10B2	Stackhouse and Bedford [65]	8+8	0.00387	0.140	1.34
MT	Stephens et al. [64]	5+5; 6+6	0.00958	0.119	0.288
LL	Stephens et al. [64]	5+5	0.0179	0.267	0.548
B16	Stephens et al. [64]	5+5	0.00771	0.180	0.146
HX34	Stephens et al. [64]	5+5	0.0121	0.193	1.10

Table 3.1.1: Experimental data used for fits of the GLOBLE model to split-dose experiments. The cell lines, original publications and the two temporarily separated doses applied in the experiment are listed. Furthermore, Columns 4-6 provide the best-fit parameter values derived for the GLOBLE model in fits to these experiments.

Since one data set comprised measurements in dependence of the separation time T_{sep} for two different total doses D (MT cell line [64]), the residual sum of squares RSS implying the best-fit parameters $\tilde{\tilde{P}}_{glob}$ was generally defined as:

$$RSS = \sum_{i=1}^{N_D} \left[\sum_{j=1}^{M_i} (Eff(T_{sep,i,j}, D_i, \tilde{\tilde{P}}_{glob}) - y_{i,j})^2 \right]. \tag{3.1.8}$$

Here, N_D denominates the number of doses applied in an experiment and M_i the number of data points corresponding to the dose-specific survival curve i.

3.1.2.3 Deterministic radiation effects

As a benchmark for observations of time-dose effects in the incidence of deterministic radiation effects, the empirical formulation presented in section 2.4.1 (equation 2.4.1) was employed [69]. Briefly, it predicts that the dose D_{50} where 50% of the patients start to show symptoms of a clinical disease increases inversely proportional to the applied dose-rate. The disease-specific parameters θ_∞ and θ_1 reflect D_{50} for acute exposure (infinitely large dose-rates) and the increase in D_{50} with a decrease of the dose-rate, respectively.

Two extreme cases were used for the compatibility check with the GLOBLE model. First, for pneumonitis with $\theta_\infty = 10\,\mathrm{Gy}$ and $\theta_1 = 30\,\mathrm{Gy^2h^{-1}}$, large time-dose effects are expected and second for the bone marrow syndrome with $\theta_\infty = 3\,\mathrm{Gy}$ and $\theta_1 = 0.07\,\mathrm{Gy^2h^{-1}}$, comparably small time-dose effects are predicted [69] - as already explained in section 2.4.1.

In order to reproduce these effects with the GLOBLE model, information about the lethality of cDSB in comparison to iDSB, that is typical for the clinically observed endpoint, had to be collected. Actually, already the ratio ϵ_i/ϵ_c defines the reduction of radiation effectiveness when cDSB are substituted by iDSB due to a lowering of the dose-rate. Absolute values of the two lethalities are thus not required when only changes in the radiation effect with the dose-rate and not absolute values of the radiation effect should be predicted - as it was the case in the current study. In literature, linear-quadratic α-β-ratios for pneumonitis ($\alpha/\beta = 3\,\mathrm{Gy}$ [79]) and the bone marrow syndrome ($\alpha/\beta = 8\,\mathrm{Gy}$ [80]) are provided. With equations 2.3.14 and a reasonable choice of the absolute value of ϵ_i, the following parameter values were employed for GLOBLE computations: $\epsilon_i = 0.00333$, $\epsilon_c = 0.229$ for pneumonitis and $\epsilon_i = 0.00333$, $\epsilon_c = 0.09$ for the bone marrow syndrome. As equivalents for D_{50} in the GLOBLE model, the isoeffective doses that lead to the same radiation effect Eff as instantaneously applied 10 Gy (for pneumonitis) and 3 Gy (for the bone marrow syndrome) were derived.

3.1.3 Results

3.1.3.1 Description of split-dose experiments

The best fits of the GLOBLE model to the five investigated split-dose experiments are visualized as solid graphs in Figure 3.1.1. Clearly visible, there is a very good agreement between the computed and the measured cell survival probabilities. For example, when the experiment

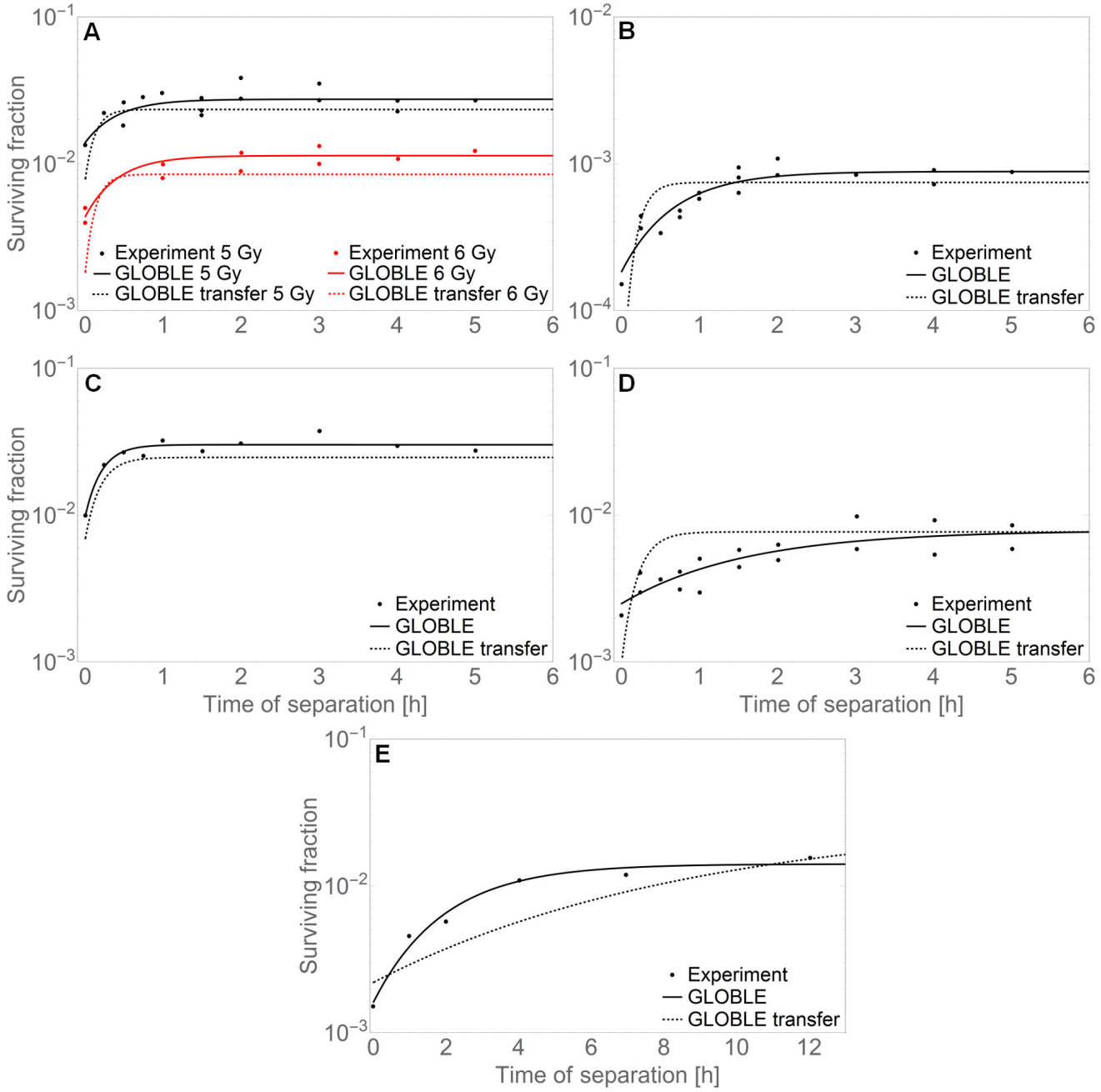

Figure 3.1.1: Five split-dose experiments with best-fits of the GLOBLE model drawn as solid lines. The dashed lines represent GLOBLE predictions for the cell line with parameter values that were derived in dose-rate experiments (transfer). A) MT cell line irradiated with 5+5 Gy and 6+6 Gy [64]. B) LL cell line irradiated with 5+5 Gy [64]. C) B16 cell line irradiated with 5+5 Gy [64]. D) HX34 cell line irradiated with 5+5 Gy [64]. E) CHO 10B2 cell line irradiated with 8+8 Gy [65].

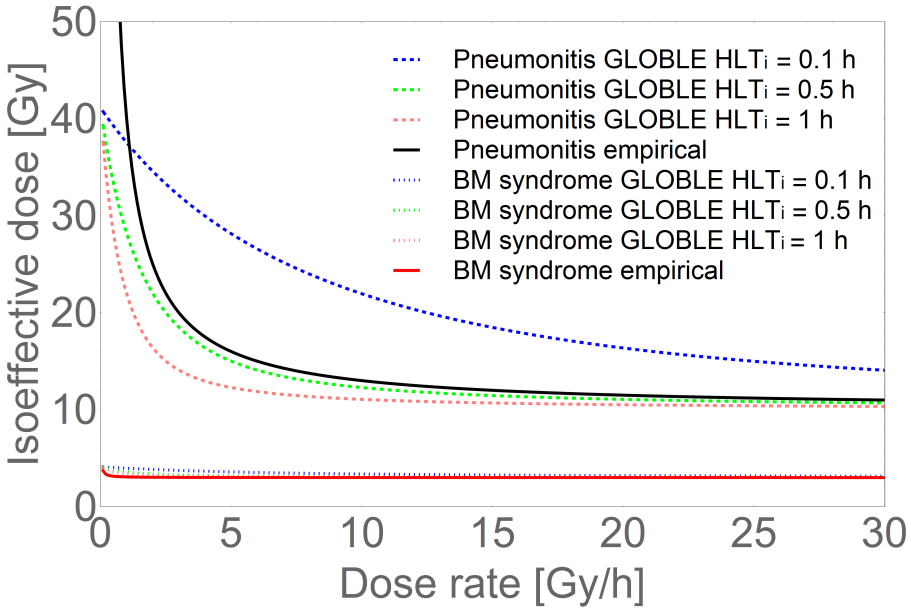

Figure 3.1.2: Predictions of the dose-rate-dependence of the dose (isoeffective dose) where 50% of the exposed persons show clinical symptoms of pneumonitis or the bone marrow syndrome. GLOBLE predictions with varying half-life times of iDSB are compared to predictions with an empirical formula [69]. Figure taken from [63] with permission and modified.

with the MT cell line (Panel A) is considered, one observes a distinct increase in cell survival probabilities up to separation times T_{sep} around 1 h and then a convergence to the maximum survival probability achievable. As expected, at a given separation time, the survival probability for a smaller total dose (10 Gy) is higher than for a larger total dose (12 Gy). Actually, both dose-specific survival curves are described with one single set of parameters for the investigated MT cell line. Obviously, global sets of parameter values that are specific for a given cell line can be used to describe the cellular response to different types of radiation exposures, consequently. All of these observations verify the agreement between the mechanistic explanation of the cellular response to split doses with the GLOBLE concept and actual measurements.

The parameter values corresponding to the best model fits are listed in Table 3.1.1, Columns 4-6. The fact that all of the values are in the order of magnitude that one would expect with regard to their meaning, although no constraints were set during the fit procedure, further supports the good applicability of the GLOBLE model. For instance, the median of the derived half-life times of iDSB is 0.46 h and thus in the range of half-life times found for the fast component of a bi-exponential model in DSB rejoining experiments [81].

3.1.3.2 Prediction of deterministic radiation effects

Figure 3.1.2 shows predictions of time-dose effects in the incidence of deterministic radiation effects with the GLOBLE model and with the empirical formula 2.4.1. Obviously, the GLOBLE model captures very well the large dose-rate effects empirically observed for pneumonitis and the small dose-rate effects corresponding to the bone marrow syndrome. Especially when a half-life time of iDSB $HLT_i = 0.5$ h is employed, which is in agreement with the fast component of

	Best-fit split-dose exp.			Best-fit dose-rate exp.			
Cell line	ϵ_i	ϵ_c	HLT_i **[h]**	ϵ_i	ϵ_c	HLT_i **[h]**	$T_{1/2}$ **[h]**
CHO 10B2	0.00387	0.140	1.34	0.00130	0.162	6.10	1.17
MT	0.00958	0.119	0.288	0.00865	0.178	0.0859	0.33
LL	0.0179	0.267	0.548	0.0114	0.543	0.0954	0.61
B16	0.00771	0.180	0.146	0.00781	0.203	0.131	0.16
HX34	0.0121	0.193	1.10	0.00893	0.320	0.133	0.97

Table 3.1.2: For each listed cell line, Columns 2-4 provide the best-fit parameter values derived for the GLOBLE model in a fit to a split-dose experiment. Additionally, Columns 5-7 contain GLOBLE parameter values that have been derived for the same cell line in a fit to a dose-rate experiment presented in the same original publication. The last Column lists the half-life times $T_{1/2}$ that have been determined with recovery fits to the split-dose experiments in the original publications (explanation in the text).

DSB rejoining and the investigation of split-dose experiments above, the empirical approach and the GLOBLE model hardly deviate down to dose-rates about 3 Gy/h. Therefore, it can be stated that the GLOBLE model, which is in first instance thought to describe cell survival probabilities, can be used to predict even clinical phenomena, in a very limited area of application, though. Differences to the empirical approach will be discussed below.

3.1.4 Discussion

3.1.4.1 Reported repair half-life times in comparison to values derived with the GLOBLE model

In the results section it was demonstrated that the GLOBLE model is applicable to describe split-dose experiments. The graphs corresponding to best-fits of the GLOBLE model match the described experimental split-dose data very well and the derived parameter values are in the right order of magnitude. Actually, in the original publications of the investigated split-dose experiments, half-times $T_{1/2}$ for the increase of cell survival probabilities with an increase of the separation time were derived. The authors used an empirical exponential recovery equation for "split-dose recovery" and found $T_{1/2}$ by corresponding fits to the experimentally recorded data. The results are listed in the last Column of Table 3.1.2. For the MT cell line, the mean of the two values of $T_{1/2}$ provided in the original publication is given.

Obviously, the half-life times of iDSB derived with the GLOBLE model are in a very good agreement with the empirically derived half-life times. The deviations are around 10%. Thus, the GLOBLE approach allows to reliably find characteristic time scales of an experiment and to mechanistically interpret the origin of this typical time scale at the same time.

3.1.4.2 Prediction of deterministic radiation effects

The investigation of the dose-rate-dependence of the dose D_{50} where 50% of exposed persons show clinical symptoms of a deterministic radiation effect has revealed a good agreement of

empirical predictions and GLOBLE predictions down to dose-rates about 3 Gy/h (Figure 3.1.2). When lower dose-rates are decreased, the GLOBLE approach suggests that the isoeffective dose increases less than expected referring to the empirical approach. Actually, at infinitely low dose-rates, the GLOBLE model converges to finite values of the dose where 50% of exposed persons show clinical symptoms whereas the empirical formula suggests that this dose increases to infinity. This divergence of the two approaches is reasoned with the two different concepts.

In the empirical description, it is assumed that D_{50} is inversely proportional to the dose-rate which indirectly means that the effect of a given dose is always reduced when the dose-rate is lowered. A divergence in the limit of low dose-rates is inevitable, consequently. In contrast, the GLOBLE model suggests that there is a limit in the reduction of radiation effects at low dose-rates. At extremely low dose-rates, only iDSB are induced by the radiation exposure. A further lowering of the dose-rate cannot reduce the severity of the damage, because the number of iDSB, which is implied by the total dose only, and their lethality remains constant. Thus, at very low dose-rates, GLOBLE predictions of an isoeffective dose converge.

The question whether the empirical approach or the GLOBLE approach is more appropriate for the prediction of the impact of the dose-rate on the incidence of deterministic radiation effects is hard to be answered rigorously. Carruthers et al. provide a good overview over clinical studies investigating the impact of the dose-rate on the incidence of pneumonitis [82]. Whereas a reduction of a "high" dose-rate above around 3 Gy/h to any distinctively lower value seems to be clearly advantageous for the prevention of pneumonitis, a reduction of dose-rates within the range below 3 Gy/h does not reveal any statistical benefit. This might carefully be taken as an argument for a limited reduction of radiation effects in the low dose-rate regime as predicted with the GLOBLE model, although even the GLOBLE model would then overestimate corresponding time-dose effects. Moreover, a good overview over D_{50} found for pneumonitis and the bone marrow syndrome in more systematic mouse studies is provided by Down et al. [83]. The presented experimental data do not indicate a saturation of D_{50} for decreasing dose-rates down to 1.2 Gy/h and 0.6 Gy/h, respectively. This would rather argue for the empirical approach. Nevertheless, also Down et al. suggest the usage of a model which predicts finite values of D_{50} for vanishing dose-rates in their presented studies. This would again argue for the GLOBLE approach.

To conclude, the GLOBLE model and the empirical formulation are equivalent in the range of dose-rates above 3 Gy/h where the impact of the dose-rate on the incidence of deterministic radiation effects is little controversial. In the lower range of dose-rates which is less well explored, there are arguments for the one or the other approach. Anyway, considering the range of dose-rates that is usually involved when deterministic radiation effects occur, the general demand for predictions at very low dose-rates might be of a rather theoretical nature.

3.1.4.3 Derivation of cell line specific sets of parameter values

In the results section it was stated that one is able to derive cell line specific sets of parameter values when the GLOBLE model is fitted to split-dose experiments, even when several dose-specific survival curves were recorded. With that in mind, the question arises, if these sets of parameter values can be used to predict the response of a given cell line in a completely different experimental setup and vice versa. In fact, in the original publications of the split-dose experiments, simultaneously conducted dose-rate experiments were presented. In Columns 5-7 of Table 3.1.2, the GLOBLE parameters derived in fits to these dose-rate experiments are

listed. Obviously, there are larger deviations between two respective parameters when they were extracted from different experimental setups. Especially the half-life time of iDSB fluctuates strongly, usually around 80% and in one extreme case around 350%. However, in this extreme case, represented by the experiments conducted with the CHO 10B2 cell line, an unusually large value of HLT_i was found for the dose-rate experiment indicating that the source of the problem lies already in the description of this special experiment.

Figure 3.1.1 visualizes deviations between measurements and predictions (dashed lines) when GLOBLE parameter values that were derived a in fit to a dose-rate experiment are used to describe a split-dose experiment conducted in the same cell line. In the experiments where the B16 and LL cell lines were irradiated, the predicted maximum survival probabilities are approached faster than observed because of the lower half-life times of iDSB found in dose-rate experiments. For the experiment with the CHO 10B2 cell line, the opposite holds true. The pure dynamics in the experiments with the MT and HX34 cell lines are generally well reproduced by the values of HLT_i from corresponding dose-rate experiments. Concerning the prediction of the maximum level of cell survival probabilities reached at large values of T_{sep}, there is a slight underestimation compared to the experimental data recorded for the MT, LL and B16 cell lines. Furthermore, there is a general underestimation of survival probabilities at $T_{sep} = 0\,\mathrm{h}$ which means at the exposure to a single acute dose.

These discrepancies between parameter values derived from dose-rate experiments and split-dose experiments do not only occur when the GLOBLE model is used but also when the Lethal Potentially Lethal model is employed as done by Stephens et al. in their original study [64]. Concerning the deviations of repair half-life times, the authors observe the same systematics that have been presented here and provide possible explanations. According to them, the most likely reason for the disagreements is the fact that, despite great efforts, the temperature could not be well controlled during the split-dose experiments. The reductions in temperature during the split-dose experiments could slow down cellular repair processes. Consequently, the differing parameter values derived in fits of the GLOBLE model to dose-rate and split-dose experiments do not necessarily reflect shortcomings of the model but might be due to experimental difficulties.

3.1.4.4 Critical review of the GLOBLE concept

Since the GLOBLE model is supposed to be a biologically motivated approach, its assumptions about cellular characteristics and their impact on cell survival probabilities have to be justified. The fact that the GLOBLE model has been shown to provide accurate descriptions of dose-rate and split-dose experiments at least does not falsify the mechanisms that are thought to be decisive for cell death.

Damage clustering on micrometer- and nanometer-scale

Actually, the concept of two lesion classes, iDSB and cDSB, which are defined exclusively by the spatial and temporal coexistence of initial DSB in DNA giant loops, is one of the most distinctive features of the GLOBLE approach in comparison to other cell survival models. A more detailed comparison of kinetic photon cell survival models will be presented below in section 3.3. However, already at this stage, the special idea that it is not directly the dose but rather the damage distribution pattern that determines the cellular radiation response should be emphasized. In most of the published cell survival models, a given combination of dose, dose-rate and cellular

parameter values implies a constant cell survival probability, independent of the spatial dose distribution. In contrast, the GLOBLE model allows for varying cell survival probabilities when varying local and temporal damage distributions result after the application of two different radiation qualities. This is usually the case for ion compared to photon radiation and thus, the GLOBLE model promises a universal applicability in connection with the conceptually equal Local Effect Model which covers aspects related to ion radiation.

Since the definition of iDSB and cDSB on the hand of the multiplicity of DSB in a giant loop is crucial for the GLOBLE model, one has to carefully evaluate evidences for the impact of DNA giant loops on the cellular radiation response. On the one hand, there are several investigations that confirm the importance of sub-structural units of the DNA which are in the order of magnitude of 2 Mbp or a few μm, respectively. Johnston et al. conducted a whole series of experiments, where a modified neutral filter elution technique allowed to maintain the higher-order chromatin structure during the elution of radiation-induced fragments. Consequently, only those fragments that resulted from multiple DSB within giant loops were extracted. Amongst others, the authors found support for the following hypotheses:

(i) Looped higher-order chromatin structures are the critical target for the induction of DSB [59].
(ii) The number of DSB within higher-order chromatin structure might impact their repair [48].
(iii) Radiosensitive cell lines have deficiencies in the repair of multiple DSB within higher-order chromatin structures [48].
(iv) Single DSB within higher-order chromatin structures are repaired with fast kinetics and multiple DSB with slow kinetics [48].
(v) The relevant size of the higher-order chromatin loops is about 1.6 Mbp [59].

In another study, Gauter et al. analyzed the compatibility of experimentally measured DNA fragment sizes 4 h after irradiation with a random DSB induction and rejoining process which is independent of the spatial distribution of initial DSB [49]. The authors revealed that compared to randomness, there are too many fragments in the order of 2-3 Mbp remaining at long times after irradiation. They support the hypothesis that multiple breaks within giant loops are rejoined with slow kinetics. Furthermore, Löbrich et al. have developed an assay which allows to study fractions of correctly rejoined and misrejoined DSB in the course of time after a radiation exposure [51]. With this innovative approach they revealed that most of the correct rejoining events are detected at less than about 2 h after irradiation and that misrejoining mainly happens in the longer time range between 2-24 h.

All of these studies confirm the hypothesis that DNA giant loops are determinants of the cellular radiation response and that the assumptions behind the GLOBLE model are reasonable. On the other hand, it has been demonstrated that damage clustering on a nanometer-scale, which is not explicitly accounted for in the GLOBLE approach, impacts the radiation effectiveness. Damage clusters on a nanometer-scale denominate combinations of DSB, SSB and base damages within small volumes (diameter around 4 nm [84]) and more complex combinations of these lesions are supposed to lead to a damage enhancement. Ward has published a broad overview over studies that support the hypothesis that "locally multiply damaged sites" are decisive for the cellular radiation response [85]. He comes to the conclusion that not only DSB but also other forms of radiation-induced lesions have to be accounted for when cellular radiosensitivities are derived. In a computational study, Ottolenghi et al. found a higher fraction of complex DSB (which are DSB in combination with other DSB or forms of biological damage) for high-LET

than for low-LET radiation [86]. The authors even were able to detect a correlation between two spatially close DSB and cell killing. Moreover, a large series of track structure studies by Goodhead, Nikjoo and co-workers (e.g. [87][88]) confirms the increasing complexity of DSB on nanometer-scale when the LET of the radiation is increased. Inherent relationships between local DSB complexity and radiation effectiveness are pointed out in [89].

However, it is important to notice that the major increase of the complexity of DSB on nanometer-scale is detected for ion radiation with increasing LET or for ion radiation in comparison to photon radiation. Thus, a damage enhancement on nanometer-scale can help to explain the LET-dependence of the radiation effectiveness but hardly the photon dose-dependence when e.g. a higher photon dose is compared to a lower one. First, in the range of photon doses usually applied in cell survival experiments, little damage enhancement on nanometer-scale due to overlapping electron tracks should be expected. Second, since electron tracks after photon irradiation (with a defined energy) feature a typical local damage induction pattern that is independent of the dose, the curvature of acute photon cell survival curves observed already at doses around 2 Gy cannot be explained with an enhancement effect due to an increased complexity of damage on nanometer-scale [90]. Consequently, for a mechanistic explanation of the shape of photon dose-response curves, the paradigm of damage clustering on micrometer-scale, as it is used in the GLOBLE model, might be more appropriate.

At this stage, it should be emphasized that the weight on damage clustering on micrometer-scale in the GLOBLE model does not exclude damage enhancements on a nanometer-scale. It is only supposed that - at least in the case of photon radiation - the impact of damage clustering on nanometer-scale is dominated by the events on larger scales and therefore neglected in a first approximation. Actually, the Local Effect Model which is conceptually related to the GLOBLE model features a component dedicated to a very special form of damage enhancement on nanometer-scale. When two SSB occur within 25 base pairs, they are counted as a DSB and thus might lead to an increased severity of the biological damage. Such considerations could be transferred to the GLOBLE model without changing the general idea. However, as shown in Figure 2.3.6, a damage enhancement due to SSB clustering is expected only at very high photon doses and a negligence seems to be justified, consequently. In conclusion, the fact that the GLOBLE model does not explicitly account for damage enhancement on nanometer-scale should not generally deny its importance. It might be suggested that the two levels of damage clustering are complementary and that their relative importance depends to a certain degree on the considered endpoint.

Concerning simplifications and assumptions

During the presented investigations of the GLOBLE model, only three parameters were left open for the derivation of cellular responses: the two lethalities ϵ_i and ϵ_c and the half-life time of iDSB HLT_i. In previous investigations it was shown that these three parameters are sufficient for an accurate reproduction of dose-rate experiments and here it was additionally demonstrated that split-dose experiments and time effects in the incidence of deterministic radiation effects are well described. Due to this good accuracy and since a parsimonious number of free parameters is beneficial, the usage of only three parameters seems to be reasonable.

However, the GLOBLE model features three further parameters that might have an impact on predictions: the half-life time of cDSB HLT_c, the number of giant loops N_L and the double-strand break yield α_{DSB}. In [77] it has been shown that variations of HLT_c imply negligible changes

in survival probabilities calculated with the GLOBLE model. It is the pure existence of a slow component of repair but not its exact value which is decisive for predicted outcomes. Therefore, a fixation of this parameter seems to be reasonable.

Reported DSB yields α_{DSB} for a mammalian cell are in the range of $25\,\mathrm{Gy}^{-1}$ [91] to $60\,\mathrm{Gy}^{-1}$ [92] whereas a fixed value of $30\,\mathrm{Gy}^{-1}$ was assumed here in reference to previous investigations. Actually, a variation of α_{DSB} leads to observable changes in cell survival probabilities predicted with the GLOBLE approach. Yet, since the yield of DSB induction is supposed to be relatively independent of the cell line [34], such a variation of α_{DSB} would concern all investigated cell lines (under the assumption of the same genomic content) and therefore not be characteristic for a particular radiosensitivity. As a consequence of the low specificity of α_{DSB}, it is reasonable to set this parameter to a fixed value and to save one free parameter.

Last but not least, the impact of varying numbers of giant loops N_L represented as domains in the GLOBLE model was investigated in a master's thesis [93]. Motivated by the observation that the giant loops in a cellular nucleus usually have varying sizes, effects of domain size distributions on cell survival probabilities were explored. It was found that such domain size distributions have a noticeable impact on the predicted cellular response. The question if accounting for varying domain sizes enhances the performance of the GLOBLE model in the description of time-dose effects has not been finally answered, yet. However, since one already achieves a good accuracy with $N_L = 3000$, the additional benefit of another free parameter might be challenged.

A last point that should be discussed with regard to assumptions made for the computations is the negligence of cell cycle effects. Actually, there is a way to account for varying radiosensitivities in dependence of the cell cycle stage with the GLOBLE model. In [61] it was demonstrated that a cell cycle dependent variation of the genomic content and a choice of two repair pathways according to the homology of the chromatin loops is adequate for the reproduction of the observed cell cycle radiosensitivities of a given cell line. Thus, in the framework of the GLOBLE model, the cell cycle is indeed expected to impact cellular responses to radiation exposure significantly. However, in the investigated split-dose experiments, an obvious bias due to cell cycle effects could not be detected. In the experiment where the CHO 10B2 cell line was exposed, the cells were synchronized in G1-phase and therefore featured a uniform radiosensitivity. In the experiments with the other four cell lines, such a statement is not as straightforward because no synchrony was given. Yet, cell cycle effects in split-dose experiments are usually detected by a "dip" in the plateau of cell survival probabilities [11]. In a heterogeneous cell population, the first of the two applied doses typically kills more cells in a radiosensitive cell cycle stage than in a resistant stage. When the time between the two exposures is elongated, the initially resistant cells move on in the cell cycle and reach a radiosensitive cell cycle stage themselves. The application of the second dose at that point in time causes a decreased survival probability compared to the survival probability measured before. This results in the mentioned "dip". Such an obvious bias due to cell cycle effects could not be observed in the four split-dose experiments by Stephens et al. Consequently, the assumption of a cell cycle-averaged radiosensitivity in the presented applications of the GLOBLE model seems to be well-justified with regard to parsimony in the selection of parameters.

3.1.5 Conclusion

In this study it was demonstrated that the kinetically extended GLOBLE model is applicable for the description of split-dose experiments and the prediction of time-dose effects in the incidence of deterministic radiation effects. The supposed mechanisms underlying the cellular radiation response are apparently compatible with experimental and in a limited range with clinical observations and thus, the concept of the GLOBLE model is strengthened. In comparison to other kinetic photon cell survival models, the exclusive definition of two lesion classes on the hand of the multiplicity of DSB in a giant loop distinguishes the GLOBLE approach. Instead of the dose it is rather the damage pattern that implies the radiation effect. The consequent compatibility of the GLOBLE (and LEM) concept with photon and ion radiation responses constitutes a clear advantage. With regard to the modeling of the repair of lesions and finally with regard to predicted cell survival probabilities, it needs to be tested whether the binary concept entails benefits.

3.2 Comparison of models for DSB rejoining

3.2.1 Motivation

The temporal course of DSB rejoining is of special interest for the assessment of time effects in the cellular response to radiation. Next to the dose and *LET* of the radiation, the dose delivery schedule might strongly impact e.g. cell survival probabilities as explained in section 2.4. Therefore, accurate and nevertheless simple models are needed for the description of DSB rejoining. In connection to more sophisticated approaches, as presented with the GLOBLE model, they might help to provide better predictions of radiosensitivity which might become especially important in treatment planning for protracted or highly fractionated radiotherapy.

One common approach for the description of DSB rejoining is a bi-exponential model (BiExp), as pointed out in section 2.2.4. It supports the idea of two DSB categories defined by e.g. the chosen repair pathway, the spatial or chemical complexity of the damage or the location of a DSB in hetero- or euchromatin. However, the hypothesis that a bi-exponential model is superior to other mathematical formulations of DSB rejoining has never been ultimately tested. A mono-exponential (MonoExp) or a tri-exponential (TriExp) model might be alternatives suggesting similar interpretations. A mono-exponential model implies a single DSB category and a tri-exponential three of them. Furthermore, for the evaluation of experiments, residual DSB are sometimes subtracted from the fraction of unrejoined damage before a model is fitted to the data. To capture this additional quasi-parameter, a constant offset might be introduced in a mono-exponential (MonoExpO) or bi-exponential (BiExpO) model. For a tri-exponential model, an offset in addition to the already large number of five free parameters should be suspected to lead to a strong overfitting of the data.

Other possible approaches for the description of DSB rejoining data involve continuously distributed DSB rejoining rates. This means, that there are no discrete DSB categories, but that every DSB is processed with respect to its individual appearance. Such approaches have been suggested at several occasions [94] but never been rigorously tested. Therefore, fitting models with continuously distributed DSB rejoining rates to experimental data and comparing their performance to more established models was considered to be instructive. As candidate distributions of DSB rejoining rates, a Gaussian distribution (GaussianExp), an exponential distribution (ExpExp) and a gamma distribution (GammaExp) were taken into account. A Gaussian distribution implies that all DSB are rejoined with a rate fluctuating closely around a mean rate (with standard deviation σ). In contrast, an exponential distribution allows for a wider and asymmetric spread of rejoining rates around the mean; the fractions of DSB rejoined with rates faster or slower than the mean are fixed, though. A more flexible alternative to the exponential distribution is provided with the gamma distribution which can capture fast and slowly rejoined damage with varying fractions.

One last and with regard to the modeling of cell survival very important approach for the description of DSB rejoining is a second-order process [95]. The idea behind it is that the probability for interactions of DSB is the highest shortly after irradiation due to the relatively large number of DSB close together. With increasing time, more and more DSB interact and consequently, the probability for such inter-lesion rejoinings decreases over-proportionally. Mathematically, this process is formulated with a second-order differential equation; a first-order process meaning intra-lesion rejoining might be added. The performance of first- and second-

order (1st2ndO) or pure second-order (2ndO) processes has never been investigated by fitting the models to experimentally measured data and by comparing them to e.g. multi-exponential approaches. However, first- and second-order processes have often been employed to model the decay of lesions in kinetic cell survival models as in the Repair Misrepair Model [73] or the Lethal Potentially Lethal model [74]. Therefore, a comparison of second-order DSB rejoining models to e.g. the bi-exponential model which is exploited in the GLOBLE model [63] might provide important insight about which assumptions behind kinetic cell survival models might be most appropriate.

All the arguments stated above motivated the detailed comparison of ten models for DSB rejoining. Their performance was tested on the hand of fits to 61 DSB rejoining data sets, including photon and ion radiation experiments, and compared by using the corresponding $AICc$ values. The methods, the results and the discussion are presented in the following and in a corresponding publication [96].

3.2.2 Materials and methods

3.2.2.1 The models

As stated in the motivation, ten models for DSB rejoining were investigated with regard to their accuracy and complexity. Their mathematical formulations of the fractions F of unrejoined DSB at time t after instantaneous irradiation are:

(i) Mono-exponential model with constant rejoining rate k (MonoExp):

$$F_{MonoExp}(t) = e^{-kt}. \tag{3.2.1}$$

(ii) Mono-exponential model with constant rejoining rate k and a fraction of unrejoined DSB A (MonoExpO):

$$F_{MonoExpO}(t) = A + (1-A)e^{-kt}. \tag{3.2.2}$$

(iii) Bi-exponential model with two constant rejoining rates k_1 and k_2 and a fraction of fast rejoined DSB A (BiExp):

$$F_{BiExp}(t) = Ae^{-k_1 t} + (1-A)e^{-k_2 t}. \tag{3.2.3}$$

(iv) Bi-exponential model with two constant rejoining rates k_1 and k_2, a fraction of fast rejoined DSB A_1 and a fraction of unrejoined DSB A_2 (BiExpO):

$$F_{BiExpO}(t) = A_2 + (1-A_2)[A_1 e^{-k_1 t} + (1-A_1)e^{-k_2 t}]. \tag{3.2.4}$$

(v) Tri-exponential model with three constant rejoining rates k_1, k_2 and k_3 and fractions of fast and medium-speed rejoined DSB A_1 and A_2 (TriExp):

$$F_{TriExp}(t) = A_1 e^{-k_1 t} + A_2 e^{-k_2 t} + (1-A_1-A_2)e^{-k_3 t}. \tag{3.2.5}$$

(vi) Solution of a pure second-order process with rejoining rate k (2ndO, differential equation and solution are provided):

$$\begin{aligned} \frac{dB_{2ndO}}{dt} &= -kB_{2ndO}^2, \quad B_{2ndO}(0) = B_{2ndO}^0, \\ F_{2ndO}(t) &= \frac{B_{2ndO}(t)}{B_{2ndO}^0} = \frac{1}{1+\tilde{k}}. \end{aligned} \tag{3.2.6}$$

For the fits, kB_{2ndO}^0 was substituted by $\tilde{k}$ which is a rate per unit of time instead of a rate per unit of time and per lesion as k is. Furthermore, the number of unrejoined breaks after time t, $B_{2ndO}(t)$, was normalized with B_{2ndO}^0 to yield a fraction of unrejoined DSB.

(vii) Solution of a first- and second-order process with rejoining rates k_1 and k_2 (1st2ndO, differential equation and solution are provided):

$$\begin{aligned} \frac{dB_{1st2ndO}}{dt} &= -k_1 B_{1st2ndO} - k_2 B_{1st2ndO}^2, \quad B_{1st2ndO}(0) = B_{1st2ndO}^0, \\ F_{1st2ndO}(t) &= \frac{B_{1st2ndO}(t)}{B_{1st2ndO}^0} = \frac{k_1 e^{-k_1 t}}{k_1 + \tilde{k_2}(1-e^{-k_1 t})}. \end{aligned} \tag{3.2.7}$$

For the fits, $k_2 B_{1st2ndO}^0$ was substituted by $\tilde{k_2}$ which is a rate per unit of time instead of a rate per unit of time and per lesion as k_2 is. Furthermore, the number of unrejoined breaks after time t, $B_{1st2ndO}(t)$, was normalized with $B_{1st2ndO}^0$ to yield a fraction of unrejoined DSB.

(viii) Exponential model with Gaussian-distributed rejoining rate (GaussianExp, mean rate μ, standard deviation σ, error function *Erf*):

$$\begin{aligned} F_{GaussianExp}(t) &= \left(\int_0^\infty \frac{1}{\sqrt{2\pi\sigma^2}} e^{-\frac{(\mu-k)^2}{2\sigma^2}} dk \right)^{-1} \int_0^\infty e^{-kt} \frac{1}{\sqrt{2\pi\sigma^2}} e^{-\frac{(\mu-k)^2}{2\sigma^2}} dk \\ &= \frac{e^{-(\mu-0.5\sigma^2 t)t} \left[1 + Erf\left(\frac{\mu-\sigma^2 t}{\sqrt{2}\sigma}\right) \right]}{1 + Erf\left(\frac{\mu}{\sqrt{2}\sigma}\right)}. \end{aligned} \tag{3.2.8}$$

Since the Gaussian distribution was only evaluated for positive k, it was re-normalized accordingly.

(ix) Exponential model with exponentially distributed rejoining rate (ExpExp, mean rate $\mu = \frac{1}{\lambda}$, rate parameter of the distribution λ):

$$F_{ExpExp}(t) = \int_0^\infty e^{-kt} \lambda e^{-\lambda k} dk = \frac{1}{1+\mu t}. \tag{3.2.9}$$

(x) Exponential model with gamma-distributed rejoining rate (GammaExp, mean rate $\mu = \alpha\theta$, shape parameter α, scale parameter θ):

$$F_{GammaExp}(t) = \int_0^\infty e^{-kt} \frac{k^{\alpha-1} e^{-\frac{k}{\theta}}}{\theta^\alpha \Gamma(\alpha)} dk = \frac{\alpha^\alpha}{(\alpha+\mu t)^\alpha}. \tag{3.2.10}$$

All of the ten models are restricted to the calculation of the time-dependence of the fraction of unrejoined DSB only. They feature the simplest formulations - in terms of minimal sets of free parameters - for testing the hypotheses whether DSB are rejoined with discrete or continuously distributed rates or in a second-order process. Therefore, apart from the time, all other physical or biological factors impacting the cellular radiation response, e.g. dose, *LET*, culture condition, cell cycle stage, etc. are neglected. As a consequence, the ExpExp and the 2ndO model mathematically coincide. Furthermore, different sets of parameter values (especially rejoining rates) might be derived for one cell line, due to different experimental conditions.

Table 5.1.1 in the appendix (section 5.1) lists all of the ten models with the corresponding free parameters and - to provide a feeling for the orders of magnitude - median values that have been derived in fits to photon and ion DSB rejoining experiments as it will be explained in the following. The provided median parameter values should be interpreted with caution since insignificant parameter values were not excluded in their calculation due to the generally low number of significant parameter values in ion experiments. Moreover, Figure 3.2.1 visualizes the distributions of DSB rejoining rates that correspond to the ten investigated models. For the sake of visibility, the height of the graphs was chosen arbitrarily - only the peaks corresponding to discrete rates of first-order exponential models reflect the fractions of DSB rejoined with the respective kinetics. The drawn distributions actually underlie the graphs fitted to the rejoining experiment with 40 Gy photon irradiation of CHO-K1 cells shown in Figure 3.2.2 later on.

It should be noted that there are more sophisticated models for the explanation of DSB rejoining which consider e.g. enzymatic reactions [97] or which are based on Monte Carlo simulations [98] . However, the aim of this study was to investigate the compatibility of DSB rejoining data with a certain number or with a continuum of DSB rejoining rates and with corresponding DSB categories. Furthermore, the simplicity of the tested models allowed to draw some links to kinetic cell survival models which usually employ such basic time-dependencies and not highly complex formulations. Consequently, DSB rejoining models including detailed biological or physical mechanisms were not considered in the following.

3.2.2.2 Experimental data

For the assessment of the compatibility of the models with measured data, 61 DSB rejoining experiments recorded after high-dose-rate irradiation ($\geq$ 45 Gy/h) were selected from literature. Table 5.1.2 in the appendix (section 5.1) lists the publications, cell lines and some experimental conditions. All data sets were graphically presented in the original publications and therefore read in with "GetData Graph Digitizer" [78].

For photon radiation, there is a broad published data base which allowed for the choice of data according to three relatively stringent criteria ensuring a high statistical power (i, ii) and a large data base with high quality of the measurements (iii):

(i) The fraction of unrejoined DSB had to be measured at at least seven time points after irradiation.
(ii) Every data point had to represent a mean value of several experiments ± standard error.
(iii) Only experiments employing a gel electrophoresis method were chosen.

In total, 46 photon radiation experiments fulfilling these criteria were found. The data situation for DSB rejoining after ion radiation is unfortunately much worse. To at least roughly assess the performance of the tested models in the description of ion radiation experiments, criterion ii was discarded and criterion i was relaxed to six data points. With that, 12 DSB rejoining

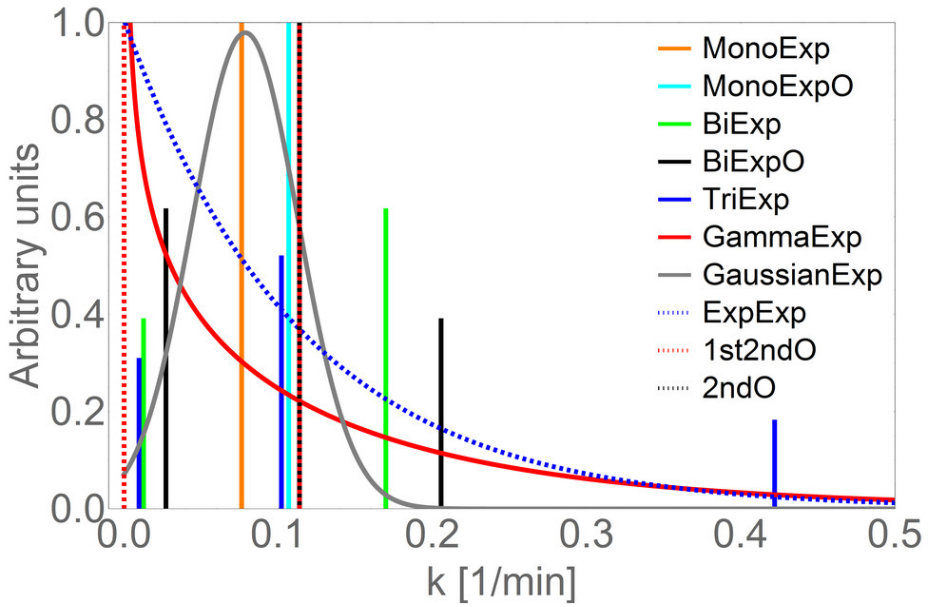

Figure 3.2.1: Distribution of DSB rejoining rates (all denominated as k) derived in fits of the ten investigated models to an experiment where CHO-K1 cells grown in monolayer were exposed to 40 Gy photon radiation [99]. For the sake of clarity, the distributions are plotted with arbitrary height with exception of the peaks corresponding to the first-order exponential models which reflect the fractions of DSB rejoined with respective kinetics. The plot was published in [96].

data sets for ion irradiation were selected. These 12 data sets were accompanied by five photon radiation data sets in the original publications of which two had already been chosen before. The other three were included in the investigations for the sake of completeness.

In all of the finally chosen 61 experiments, the irradiation of cells was executed below 4°C and the subsequent incubation was at 37°C. Apart from that, the data sets comprise measurements in various cell lines (rodent and human, normal and tumor tissue, etc.) and were taken under diverse experimental conditions (varying dose, *LET*, culture conditions, etc.). This was suggested to allow for the designation of the model which is most suitable to capture a wide range of possible radiation responses.

3.2.2.3 Quantification of the model performances

For the quantitative comparison of the ten models in the description of the selected DSB rejoining data, the *AICc* was employed. Due to the fact that some data sets comprised only few more measurements than the maximum number of free model paramters (five), the existence of a small-sample correction term was considered to be especially advantageous e.g. in comparison to X^2_{red}. In order to account for measurement errors of the data points that were presented as the mean ± standard error of x measurements in the original publications, every data point was re-transformed into x synthetic measurements reflecting the implied Gaussian distribution. When the number of samples underlying a data point was not specified in an original publication, this number was set to three because three was in the range of samples specified in almost all of the publications.

For the computation of the $AICc$ it was assumed that the residuals between the synthetic measurements and model predictions follow the same Gaussian distribution. Thus, equation 2.5.6 could be exploited. For all the calculations, "Wolfram Mathematica 10" [100] was used and during the minimization of the sum of squares with the pre-programmed routine "NonlinearModelFit" it was demanded that all parameter values are ≥ 0 and that fractions of damage (A, A_1, A_2) are ≤ 1. In order to distinguish plausible and rather implausible models after fits to a given data set, the inverse evidence ratio ER was used. When the relative support for another model than the best performing one was lower than 5% ($ER < 5\%$), it was supposed to be inadequate for the reproduction of the data.

3.2.3 Results

3.2.3.1 Visual inspection and general observations

A first qualitative assessment of the performance of the ten models in the description of DSB rejoining data was gained by visual inspection. Columns 2 and 3 in Table 5.1.3 in the appendix (section 5.1) give the percentages of the 49 photon and 12 ion experiments where the graphs of a considered model showed larger deviations from the corresponding data points. A two-sided Fisher's exact test never rejects the null-hypothesis that a given model performs equally good or bad in the description of photon or ion irradiation data (p-value 0.05, Column 4). This finding might certainly reflect the extremely poor statistical power of the few ion irradiation experiments. However, since the present data situation does not allow the distinction of results for photon and ion radiation, they will be pooled in the following (Column 5).

Figure 3.2.2 gives a typical example for the systematics that can be observed in a comparison of the fitted graphs with the experimental data. The MonoExp and GaussianExp model predict a much faster rejoining of DSB after around 20 min than actually measured. In the given data set one might object that there are much more data points recorded at short times than at long times after irradiation (compare with inlay) and that these short time data points might bias the findings. However, it can generally be noticed that the MonoExp and GaussianExp model are not compatible with measured DSB rejoining data because of a systematic underestimation of the unrejoined damage in the long time range in 96.7% and 91.8% of the 61 data sets. If data points in the short time range biased the behavior in the long time range and the single rate or the rate with a symmetrical distribution were generally adequate for the description of whole DSB rejoining curves, one should expect random deviations in the range with few data points which is not the case. Due to the systematic mismatch between measurements and the quick vanishing of DSB in the MonoExp and GaussianExp model, these two models might be rejected as candidate models for the description of DSB rejoining.

Actually, the MonoExp and GaussianExp model feature comparable (mean) DSB decay rates in 77.0% of the 61 investigated data sets and they even coincide in 42.6% of the cases when the GaussianExp model features no significant standard deviation. Therefore, the relatively simple MonoExp model can be employed as a very good approximation of a GaussianExp model.

The introduction of an offset reflecting unrejoinable DSB in the MonoExpO model hardly constitutes an improvement in comparison to the pure MonoExp model. Figure 3.2.2 exemplarily shows that the MonoExpO model underestimates the fraction of rejoined damage in the region with highest curvature and overestimates the fraction of residual damage at long times after

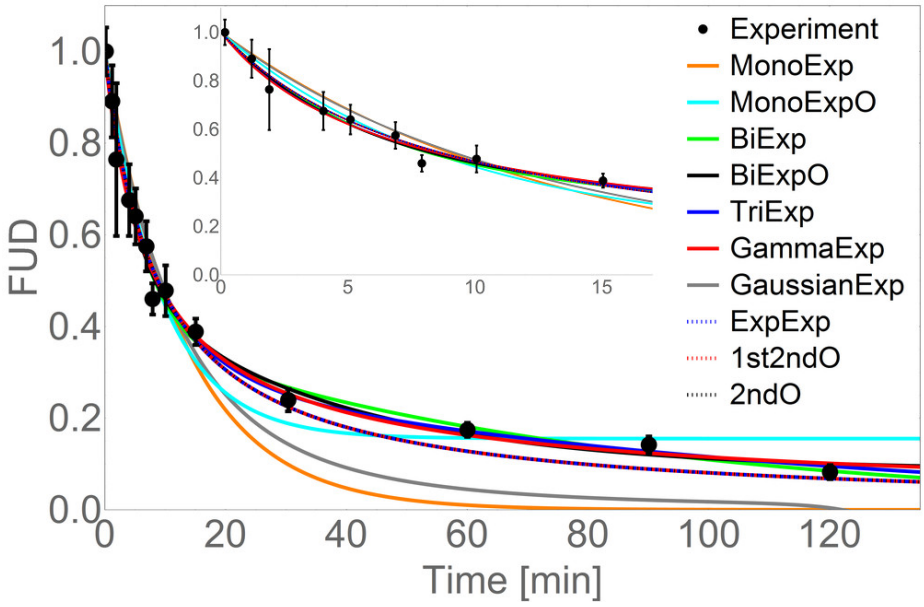

Figure 3.2.2: Comparison of DSB rejoining measured after 40 Gy photon irradiation of CHO-K1 cells grown in monolayer [99] with corresponding fits of the ten investigated models. The fraction of unrejoined damage (FUD) is plotted in dependence of the time after irradiation. For a better visibility, the inlay enlarges the range of short times after exposure. Especially in this short-time region, the graphs partly overlap. The plot was published in [96].

irradiation. This observation systematically runs like a thread through most of the 48 data sets (78.7%) where the model fails to approximate DSB rejoining data well.

Figure 3.2.2 also visualizes a similar performance of the 2ndO, ExpExp and 1st2ndO model whose graphs overlap (as already mentioned, the first two are equivalent). In fact, the 2ndO and 1st2ndO model coincide in 72.1% of the 61 cases when the linear rate in the 1st2ndO model becomes zero. In Figure 3.2.2 the 2ndO, ExpExp and 1st2ndO model visually describe the DSB rejoining data quite well as it is the case in 27.9% and 44.3% of the cases, respectively. There is no systematic trend with respect to over- or underestimations of special parts of DSB rejoining curves and therefore, these three models might be judged as quite accurate in the description of DSB rejoining.

However, there are four models which visually match DSB rejoining data better than the 2ndO, ExpExp and 1st2ndO model: the GammaExp, BiExp, BiExpO, and TriExp model. They reproduce the investigated data well in 78.7%, 85.2%, 95.1% and even 100% of the 61 cases. Figure 3.2.2 thus presents only one example for many good performances. Actually, the TriExp and BiExpO model are equivalent in 47.5% of the cases which means that one fraction of DSB in the TriExp model is not rejoined and assigned with rate zero. The TriExp and BiExp model coincide in 37.7% of the cases when two of the three DSB fractions in the TriExp model are assigned with equal rejoining rates in the optimal fit. Furthermore, the BiExpO and BiExp model are equivalent in 31.1% of the cases when no significant fraction of residual DSB is detected with the BiExpO model. All these equivalences between the BiExp, BiExpO, and TriExp model already indicate that there might be parameter redundancies in the BiExpO, and TriExp model and that two

fractions of DSB - as given in the BiExp model - might be sufficient for an accurate reproduction of DSB rejoining curves. This aspect will be investigated in the next paragraph.

3.2.3.2 Significance of parameter values

The finding that the BiExp, BiExpO, TriExp and GammaExp model accurately describe DSB rejoining data does not imply that they are statistically the most appropriate models. With regard to the principle of parsimony, they also have to feature a sufficiently small number of model parameters. The final trade-off between accuracy and complexity will be executed on the hand of inverse evidence ratios in the next section. However, for these four models with a known good accuracy, one might detect overfittings with a large occurrence of insignificant parameter values and thus already guess adequate models for DSB rejoining by reasoning power. A parameter value will be considered to be insignificant when its error is larger than half of its own value in the following.

In Columns 6 and 7 of Table 5.1.3 in the appendix (section 5.1), the percentages of the 49 photon and 12 ion experiments where at least one insignificant parameter value was derived for a given model are listed. With one exception, the GaussianExp model, a two-sided Fisher's exact test did not reject the hypothesis of equal performances for photon and ion radiation (Column 8). Therefore, all results will be pooled in the following (Column 9).

As suspected with regard to equivalences between the BiExp, BiExpO, and TriExp model in the last paragraph, the TriExp and BiExpO model feature at least one insignificant parameter value in 100% and 88.5% of the 61 cases. This suggests that these two models catch random fluctuations in the data very well and that they do not necessarily reflect the mechanisms underlying the true data generating process. In general, the predictive power of models which often show insignificant parameter values is rather low and therefore, the TriExp and BiExpO model might be inadequate for the description of DSB rejoining. The performance of the BiExp and GammaExp model is better with 54.1% and only 21.3% of the 61 cases where insignificant parameter values occur. Consequently, these two models might turn out to be most appropriate for describing DSB rejoining in the final judgment with inverse evidence ratios.

Of course, it is reasonable to assume that it is rather the relation between the number of data points in an experiment and the number of free model parameters than the number of parameters alone that leads to an overfitting. Therefore, it was expected that more insignificant parameter values would be derived in fits to the investigated ion irradiation data where the number of data points per experiment was generally much lower than for the investigated photon irradiation data. However, due to the low number of available ion irradiation experiments, the statistical power to detect such effects was not given as described above.

To nevertheless test the impact of small sample size data sets, the 26 DSB rejoining curves with less than 10 data points (no matter if ion or photon radiation) were selected and investigated in separate. It turned out that the percentages of these 26 cases where the BiExpO, BiExp and GammaExp model featured at least one insignificant parameter value increased to 96.2%, 76.9% and 38.5%, respectively. With a two-sided Fisher's exact test, no significant difference could be detected in the performance of the BiExpO model in small (< 10 data points) or large (≥ 10 data points) sample data sets ($p = 0.222$). Obviously, the number of free parameter values is generally too large in this model and - not to forget - in the TriExp model which always produces insignificant values. In contrast, the choice of small and large sample data sets has a significant impact on the derivation of significant parameter values with the BiExp ($p = 0.0039$)

and GammaExp model ($p = 0.006$). Consequently, the GammaExp model might have a small advantage over the BiExp model since its lower number of free parameters increases the chance to derive significant parameter values even when the number of data points is relatively low.

3.2.3.3 Model selection with the inverse evidence ratio

The final distinction of models that are plausible or rather implausible for the description of the selected DSB rejoining data was made using the inverse evidence ratio (ER, equation 2.5.7). After fitting all models to a given data set, the models with $ER < 5\%$ were considered to be unfavorable and excluded from the group of supported models. As listed in Columns 10 and 11 of Table 5.1.3 in the appendix (section 5.1), the percentages where models were excluded differ little in the 49 photon data sets and the 12 ion data sets. Only for the BiExpO and TriExp model, there is a significantly worse performance in the ion experiments. The penalty for a relative large number of free parameters compared to the number of data points seems to be effective and the related issue of data selection will be raised in the discussion (section 3.2.4.1).

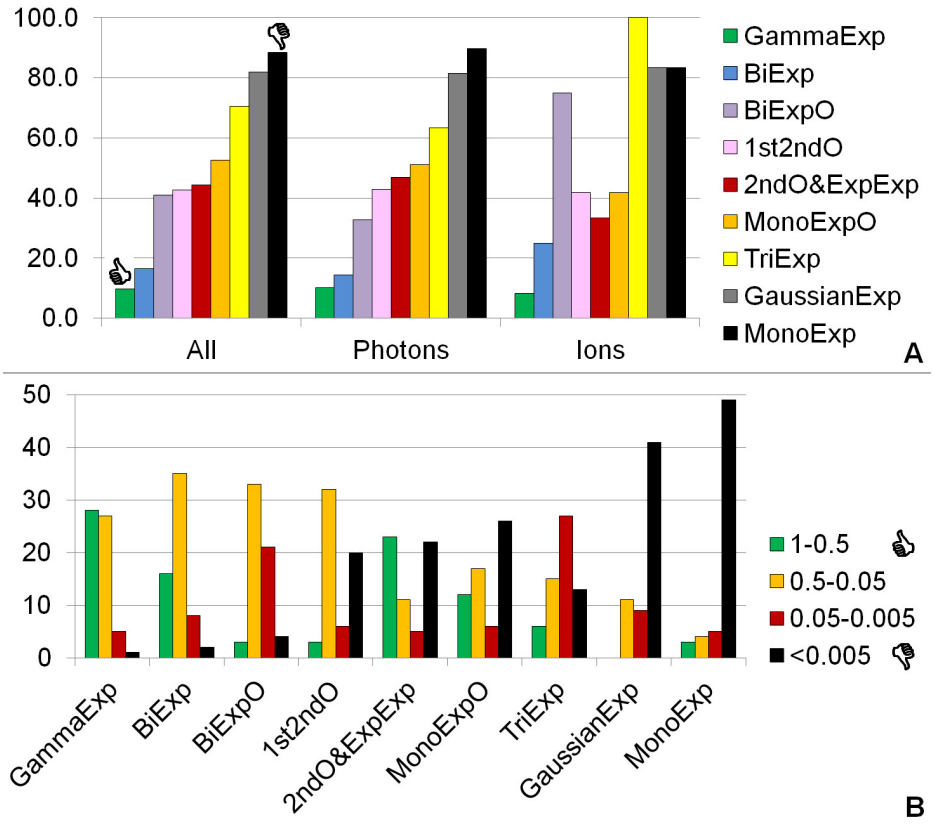

Figure 3.2.3: A) Ranking of the ten investigated models with respect to the percentages where they were excluded from the group of supported models (inverse evidence ratio $ER < 5\%$). The rankings are provided for the evaluation of 49 photon and 12 ion data sets and the pool of them (all). B) Binned distribution of ER derived for each of the ten investigated models in fits to the 61 DSB rejoining experiments. The red and black color indicate that the cases where a model was considered to be not supported by a given data set ($ER < 5\%$). The graphic was published in [96] and modified.

Figure 3.2.3A shows an overview over the percentages of exclusion as listed in Table 5.1.3 and thus provides a visual ranking of the ten investigated models. As expected, the GammaExp and BiExp model are always on position one and two - no matter if results for photon or ion experiments are considered separately or pooled. In fact, the GammaExp model is excluded from the group of supported models in only 10.2% of the 49 photon data sets, in 8.3% of the 12 ion data sets and in total in 9.8%. For the BiExp model the corresponding percentages are 14.3%, 25.0% and 16.4%. Especially with regard to the results for photon data and the pool of ion and photon data (where the photon experiments constitute the majority), the GammaExp and BiExp model clearly distinguish from the next best model, the BiExpO model which is excluded in 32.7% and 41.0% of the 49 and 61 experiments, respectively. In the case of the 12 ion data sets, the distinction of the BiExp model from the next best models, the 2ndO and ExpExp model (33.3% of exclusions), is not as pronounced but still present.

An interesting observation concerning differences between the performances of the GammaExp and of the BiExp model can be made when the distribution of inverse evidence ratios is roughly assessed. Figure 3.2.3B illustrates the number of extremely good, good, bad an extremely bad values of ER in four bins for each model. Obviously, the GammaExp model features inverse evidence ratios $> 50\%$ in almost half of the 61 cases and thus often shows an excellent performance compared to the other models. In contrast, the BiExp model rather performs sufficiently good ($5\% < ER < 50\%$) in comparison to the other models and gains its plausibility for the reproduction of DSB rejoining from this constant adequacy. The 1st2ndO, ExpExp and 2ndO model obviously are excluded from being a plausible model because of increased fractions of extremely bad performances ($ER < 0.5\%$) and the GaussianExp and MonoExp model almost exclusively perform extremely bad. The BiExpO and TriExp model mostly show intermediate values of ER around the important threshold of 5%.

As a conclusion from the last three paragraphs, the GammaExp and BiExp model seem to unify best an accuracy and parsimony in the description of DSB rejoining data and are thus the favorite approaches. This statement holds true for the given data situation and the consideration of the temporal aspects of DSB rejoining only (no dependence on dose, cell cycle, culture condition, etc.). The discussion (section 3.2.4.1) will pick up related aspects concerning the data and model selection.

3.2.3.4 Distinction of the GammaExp and BiExp model in the long time range

In order to better differentiate between the applicability of the GammaExp and the BiExp model, very basic characteristics of these two approaches were exploited. The BiExp model with two constant decay rates must capture slowly rejoined DSB and unrejoined DSB with one rate and is therefore expected to predict a relatively quick disappearance of all DSB in the long time range. In contrast, in the GammaExp model with a potentially wide distribution of decay rates, extremely small rates can represent fractions of unrejoined damage even after long times. Thus, it should be expected that the behavior of these two models in the long time range might indicate advantages for the one or the other approach.

To investigate the behavior of the GammaExp and BiExp model in the long time range, an out-of-sample study was conducted. From the 61 DSB rejoining curves those with more than eight data points of which at least one was recorded later than 12 h after irradiation were selected. They are highlighted in gray in Table 5.1.2 in the appendix (section 5.1). From these 22 data sets, the measurements after 12 h were deleted and the GammaExp and BiExp model were fitted

to the remaining data. With the resulting optimal parameter values P_{red}, the graphs predicted with the GammaExp and BiExp model were plotted and compared to the whole corresponding experiments - including the previously deleted long time observations. Figure 3.2.4 provides three examples: in Panel A both models describe the long time data points similarly good or bad, in Panel B the GammaExp model looks better and in Panel C the BiExp model.

In the three Panels in Figure 3.2.4 it becomes obvious that the BiExp model generally predicts a faster DSB rejoining in the long time range than the GammaExp model. Consequently, the BiExp model might be favorable when the fraction of unrejoined DSB actually vanishes quickly as in Panel C. Otherwise, the GammaExp model which apparently has the potential to capture the whole distribution of rejoining rates even in the short time range might be preferable (Panel B).

A visual inspection of all 22 considered data sets reveals that the GammaExp model is indeed a better approach for the prediction of long time DSB rejoining when data are measured only in the short time range. In 45.5% of the 22 cases it approximates previously deleted data points well whereas the BiExp model is close to the long time data points in only 27.3%. A quantitative analysis supports this finding. When the residual sum of squares RSS of model predictions and the previously deleted long time range data points is computed, the GammaExp model goes in hand with smaller values of RSS in 14 of the 22 cases (63.6%). Only when RSS is calculated over the whole DSB rejoining curves - with parameters P_{red} but all data points - the BiExp model does better with a smaller values of RSS in 10 of the 22 cases but is still inferior to the GammaExp model.

Furthermore, it can be attested that the BiExp model systematically underestimates fractions of unrejoined DSB in the long time range when it is fitted to short time range data. The null-hypothesis that the model underestimates data points with 50% probability was tested with a binomial distribution and it was confirmed with $p = 0.26$. In contrast, the GammaExp model leads to no significant underestimation of fractions of unrejoined DSB in the long time range ($p = 4.3 \cdot 10^{-4}$).

It might be objected that the choice of the 22 data sets already implied the better performance of the GammaExp model in the long time range. With regard to the inverse evidence ratio derived in the fits to the whole curves (section 3.2.3.3), this model was not supported in only four of the 22 experiments whereas the BiExp model was excluded seven times. To ensure that there is no bias by data selection, only those 11 of the 22 DSB rejoining data sets which previously supported both models were commonly evaluated. However, the general picture remains the same as before. The GammaExp model approximates omitted long time range data points visually good in 45.5% of the 11 cases whereas the BiExp model matches in only 27.3%. This is confirmed by the RSS derived with P_{red} for the long time range data points which is lower for the GammaExp model in 63.6% of the cases.

In summary, the GammaExp model has advantages over the BiExp model when it comes to the prediction of fractions of unrejoined damage long times after irradiation, when data points have been recorded in the short time range only.

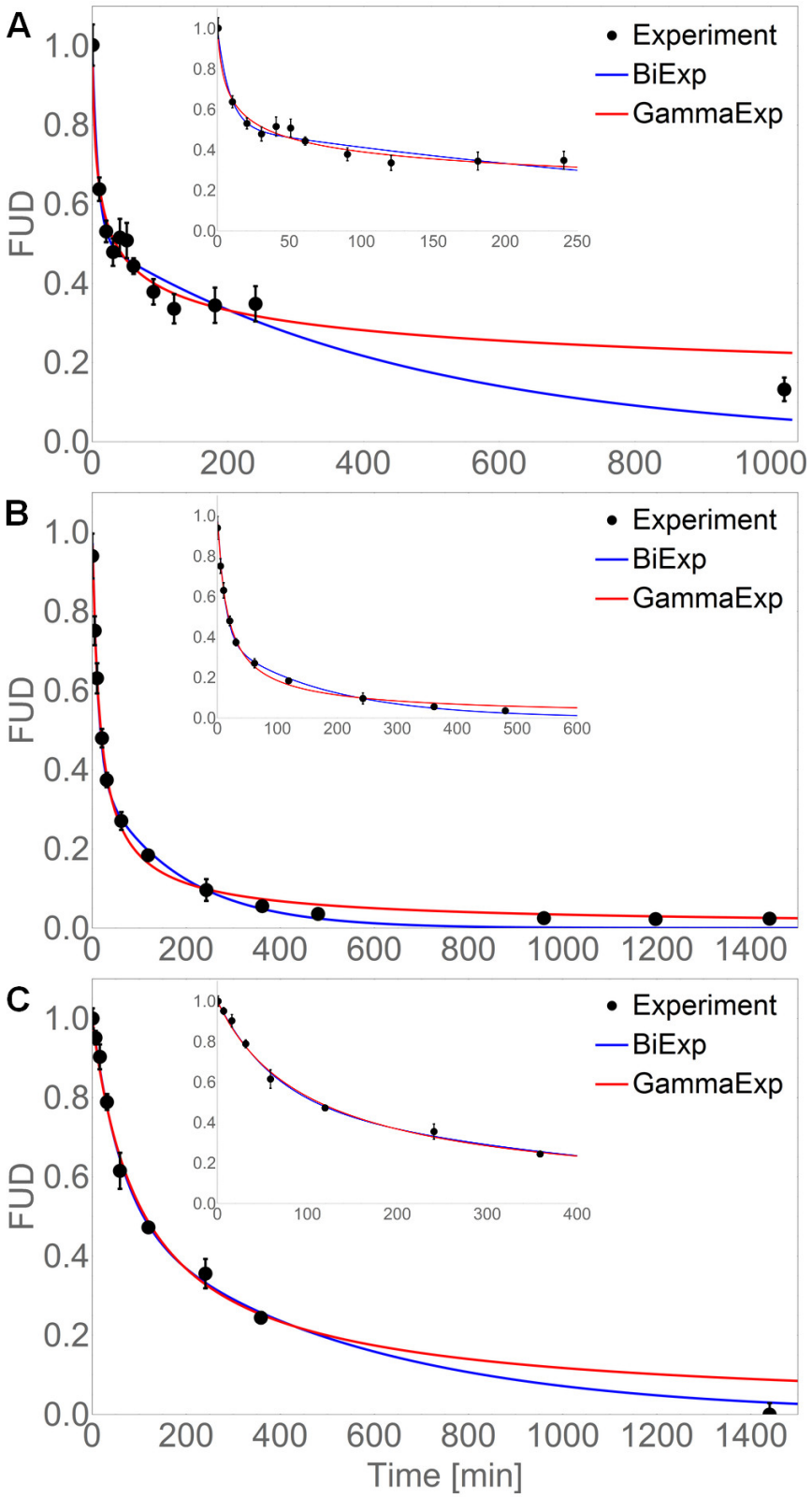

Figure 3.2.4: Three examples for the long time behavior of the BiExp and GammaExp model in an out-of-sample test as explained in the text. The inlays magnify the short time ranges. A) XR-V15B cells exposed to 20 Gy photon radiation [101]. B) NFHH cells exposed to 40 Gy photon irradiation [43]. C) HF19 cells exposed to 30 Gy photon irradiation [102]. This figure was presented in [96] in a modified version.

3.2.3.5 Description of DSB rejoining data after ion irradiation with the GammaExp and BiExp model

As it has been pointed out before, the GammaExp model might have slight advantages in comparison to the BiExp model when it comes to the description of DSB rejoining data sets with small sample sizes. Thus, the GammaExp model is supposed to be especially valuable for the evaluation of the few available ion irradiation data sets where the number of measurements is usually low. Of the 12 ion experiments investigated here, 11 have less than 10 data points. In fact, when the corresponding five photon experiments are included, fits of the "popular" BiExp model result in at least one insignificant parameter value in 70.6% of the 17 cases. This prevents any meaningful comparison of low- and high-LET data with regard to changes in e.g. the fraction of fast or slowly rejoined damage or the magnitude of the rejoining rates.

However, the GammaExp model features insignificant parameter values in only 35.3% of the 17 cases. This means that with this rather "uncommon" approach, differences in the cellular response to ion and photon irradiation become better assessable. Since the GammaExp model has never been used for the interpretation of photon and ion DSB rejoining curves, and since the approach is not as intuitive as a bi-exponential lesion rejoining, a short example will be presented in the following.

Table 3.2.1 provides the parameter values that have been derived for the GammaExp model in fits to rejoining data for the GM38(A) cell line [46][51][103]. With exception of the GM38 120 keV/μm data, there is no change in the mean life-time μ of DSB and therefore, this magnitude does not seem to reflect LET-dependent changes in the rejoining of DSB. Moreover, the shape parameter α does not provide an intuitive feeling for changes in the radiation response. However, with the GammaExp model, one can also evaluate fractions of rather fast or slowly rejoined DSB by integration over the distribution of decay rates derived for a given data set. When the maximum half-life time of the 25% of DSB which are rejoined the fastest (T_{fast}) is computed, one observes no LET-dependence, but the minimum half-life time of the 25% of DSB which are rejoined the slowest (T_{slow}) distinctly changes with the LET and ion species. Admittedly, there are no systematics that can be extracted from the variation of T_{slow} with the LET and ion species, but there is an evident increase of this magnitude from photon to ion exposure. Besides, a feeling for residual DSB predicted with the GammaExp model might be gained by

Cell line	**Radiation quality**	**Mean LT (μ) [min]**	**Shape (α)**	T_{fast} **[min]**	T_{slow} **[min]**	**% DSB /w LT > 12 h**
GM38	Photon	35.1 ± 6.4	1.21 ± 0.36	25.4	102.4	2.9
GM38	150 keV/μm Fe	30.8 ± 5.3	0.54 ± 0.054	24.8	577.9	23.0
GM38	70 keV/μm He	37.9 ± 3.0	0.75 ± 0.054	23.0	262.5	14.8
GM38	120 keV/μm He	81.9 ± 6.8	0.55 ± 0.040	27.5	184.1	9.4
GM38A	32 keV/μm Ne	31.1 ± 11.7	0.39 ± 0.12	61.0	662.4	23.9

Table 3.2.1: Parameter values of the GammaExp model (mean life-time μ and α) derived in fits to DSB rejoining data of the GM38(A) cell line [46][51][103]. Other magnitudes that can be deduced from the corresponding gamma distribution are provided, as explained in the text.

derivation of the fraction of DSB with a life-time larger than a specified threshold (e.g. 12 h in Table 3.2.1).

3.2.4 Discussion

3.2.4.1 Data selection

All results of the presented model comparison depend on the selection of the experimental data. As it has been shown, the selection of supported models is impacted by the sample size of the data sets in relation to the number of free parameters of a considered model. Thus, complex models (e.g. a multi-phasic exponential model) which might actually be the closest to the data generating process might be ruled out in comparison to a simpler model (e.g. a mono-exponential model). Furthermore, when only special cases of the whole truth are measured, complex models which are able to reproduce the whole dependence might be less supported than models which are applicable to this special case. For example, if DSB rejoining was truly bi-exponential and only the fast component of rejoining was measured, a bi-exponential model would have disadvantages against a mono-exponential model.

It was intended to minimize such systematic favoritism of the one or the other model by choosing measurements with most diverse features: different numbers and ranges of data points, a variety of cell lines, culture conditions, doses, LET, etc. By having no confinement in the data selection with regard to what a "typical" DSB rejoining curve should look like, all the investigated models had a relatively equal chance to perform well. Under the premise of a random choice of some DSB rejoining curve, it has turned out that the GammaExp and the BiExp model are most likely to provide a decent fit. This finding holds as long as the current data situation reflects sufficiently all of the faces that DSB rejoining curves might show. If there will be a larger amount of newly measured data in future, which demands for more complex models than these two by featuring e.g. a distinct third phase of rejoining, an update of the model comparison would be required.

3.2.4.2 Implications on the categorization of DSB

One aim of this study was to gain insight into which categorization of DSB is indirectly supported by the available experimental data. As already pointed out, the mono- bi- and tri-exponential model suggest that there are one, two or three discrete categories of rejoinable DSB. An additional offset in the mono- or bi-exponential model represents another category, the residual DSB. DSB corresponding to a certain category are supposed to feature distinctive characteristics which are decisive for the final speed with which they are processed. Other characteristics must be inferior in that respect. For example, it might be the number of DSB in a target volume which determines the rate of rejoining and it does hardly matter if there are base damages around or not - as it is assumed in the GLOBLE model and the LEM.

Of course, approaches with discrete DSB rejoining rates might be approximations for more complex distributions of rates. However, to be justified, approximations must also lead to a reasonable description of experimental data and therefore, the MonoExp, BiExp, TriExp, MonoExpO and BiExpO model have to compete standing alone.

The good performance of the BiExp model in the model comparison suggests that two categories of rejoinable DSB treated with two distinct rates are compatible with the experimental observations. With regard to the low accuracy of the MonoExp and MonoExpO model, a single rejoining rate is insufficient for the description of DSB rejoining data and it does not matter if there is a fraction of residual DSB or not. Furthermore, the fact that the BiExpO and TriExp model generally overfit the data leads to the conclusion that a third category of DSB is not supported enough to justify an own model parameter.

The GaussianExp, ExpExp and GammaExp model suggest that DSB are not categorized but that every DSB is processed according to its individual appearance. Thus, the speed of rejoining of a DSB is influenced by the exact number of other DSB around it, on neighboring SSB or base damages, on the exact location, etc. Depending on the model, there are different weights on the fractions of DSB which are rejoined with relatively slow or relatively fast kinetics. Figure 3.2.1 provides a helpful visualization.

In the GaussianExp model, all DSB are rejoined with rates which are comparably close to the mean rate μ (about 95% are rejoined within $\mu \pm \sigma$). Even though a cut-off and renormalization was executed to eliminate negative rates, this statement is justifiable because of generally low values of σ compared to μ. Due to the quasi-symmetry of the distribution, the fractions of DSB which are rejoined faster or slower than the mean are approximately equal and thus, there is no way to assign unequal weights to slowly and fast rejoined damage. As the model comparison has shown, the symmetrical and narrow fluctuation of decay rates around a mean rate is hardly supported by the experimental data.

The ExpExp model constitutes an improvement compared to the GaussianExp model with regard to its asymmetrical distribution of decay rates. It allows to assign unequal fractions to the DSB rejoined faster or slower than with the mean rate. Moreover, due to its comparably slow convergence to zero in the limit of large decay rates and no convergence to zero in the limit of short decay rates, it can capture larger amounts of damage rejoined with much faster or slower kinetics than the mean. These suspected advantages of the ExpExp model over the GaussianExp model are confirmed by its better performance in the model comparison. However, the ExpExp model is quite rigid since the mean decay rate already defines the median of the distribution and thus the rate where 50% of the DSB are rejoined faster or slower. This lack in flexibility constitutes a clear disadvantage e.g. in comparison to the GammaExp model. Consequently, the ExpExp model is quite accurate and parsimonious in the description of DSB rejoining experiments, but not accurate enough.

The optimal balance between accuracy and parsimony in the description of DSB rejoining data seems to be achieved with the GammaExp model. Additionally to the asymmetric distribution of rates around the mean rate and to the capability to capture a significant amount of very slow and fast rejoined damage, it allows to assign varying fractions to fast and slowly rejoined DSB with the shape parameter. Apparently, this flexibility is needed to find support by the experimental data. Certainly, it does not necessarily have to be a gamma distribution that underlies the rates of DSB rejoining - any asymmetric and very flexible distribution with few parameters could work. Yet, the gamma distribution gives a hint to what characteristics an adequate distribution of rejoining rates might have.

Last but not least, the 2ndO and 1st2ndO model as implemented here feature a single DSB category which is finally rejoined in two different modes - as explained in section 2.2.4. The presented model comparison suggests that the introduction of a linear rejoining of lesions with a corresponding rate in the 1st2ndO model leads to no major improvement in comparison to the

2ndO model. Actually, it has been shown that these two models often coincide. In comparison to the BiExp and GammaExp model, it might be concluded that the single lesion category in the 1st2ndO and 2ndO model is not supported by the investigated DSB rejoining experiments and that even the introduction of a second DSB rejoining rate cannot amend the finding. In fact, during the work on this project, some inconsistencies in the 1st2ndO and 2ndO model were noticed which make these approaches even less favorable. Section 3.2.4.3 is dedicated to this issue.

The following statements summarize the implications of the presented model comparison on DSB rejoining rates and DSB categories:

(i) Models that feature a *single decay rate* or a decay rate that shows small deviations from an expected value reproduce DSB rejoining with low accuracy.
(ii) Models that are *unable to cover at least two varying rejoining rates with flexible weights* on faster or slower rejoined DSB result in an inaccurate description of DSB rejoining curves.
(iii) Models that explain DSB rejoining with *first- and second-order kinetics* reproduce DSB rejoining with a low accuracy.
(iv) Models with a *single DSB category* lack in accuracy.
(v) Models with *at least three discrete DSB categories* are too complex for the description of DSB rejoining curves.
(vi) A *bi-exponential model* with two discrete decay rates and a *mono-exponential model with gamma-distributed decay rate* are most suitable for the description of DSB rejoining.

3.2.4.3 Shortcomings in the first-second-order and the second-order approach

The presented model comparison has revealed that the linear intra-lesion rejoining in the 1st2ndO model leads only to small performance advantages over the pure 2ndO model. Actually, it was found that the linear component is even redundant in many cases. Consequently, it is safe to state that in the 1st2ndO and 2ndO model, interactions of DSB represented by second-order differential equations are predominantly responsible for the convex shape of predicted DSB rejoining curves. At short times after an acute irradiation, the number of unrejoined DSB in proximity is the highest and with that the corresponding probability of interactions. In the course of time, ever more DSB have disappeared and the probability for two unrejoined DSB in vicinity decreases over-proportionally. Therefore, there is a steep decline in predicted DSB rejoining curves at short times after irradiation which flattens out the more time has passed.

However, this mechanistic explanation of the origin of the shape of DSB rejoining curves is in disagreement with experimental observations [51]. It is much more plausible that the fastest component of DSB rejoining is constituted by intra-lesion rejoining since the broken ends of a single DSB are usually quickly fixed and closer together than the ends of two different DSB. Furthermore, intra-lesion rejoining goes in hand with a higher fidelity than inter-lesion rejoining and less complex and time-consuming processes might be involved, consequently. The paradigm of the 1st2ndO and 2ndO model is in a clear contrast to these experimental evidences and considerations and therefore, the mechanisms behind these two models might be questioned. The intermediate performance of the two models in the model comparison also suggests the usage of alternative models.

3.2.4.4 Implications on kinetic cell survival models

Two of the ten investigated DSB rejoining models are reflected in kinetic cell survival models: the BiExp model serves as basis for the repair of lesions in the GLOBLE model [63] and the 1st2ndO model is employed in the RMR model [73] and LPL model [74]. It is important to stress that the three kinetic cell survival models consider *repair* in *abstract lesion classes* and not directly the *rejoining* of *DSB*.

Concerning repair and rejoining, the repair of lesions might still take place after two ends of a DSB have been rejoined e.g. because several repair proteins are still attached to the site. Alternatively, one might consider repair to be finished when a single end of a DSB is ultimately fixed and remains unrejoined. However, in a rough assessment, the general trend in the kinetics of rejoining and repair might be comparable.

Concerning lesion classes and DSB, abstract lesion classes employed in kinetic cell survival models do not have to represent DSB categories one to one. Yet, in the GLOBLE and LPL model, one can argue that iDSB and cDSB one the one hand and DLL and PLL on the other hand are defined on the basis of DSB. Consequently, temporal characteristics of the lesion classes should reflect characteristics of DSB. In the RMR model such a direct link between lesions and DSB is unfortunately not given since the authors retain the possibility to include a variety of biological damage in the class of "uncommitted lesions". However, due to the strong involvement of DSB in radiation-induced cell killing, any mechanistic cell survival model with a low impact of DSB would directly be questionable. Therefore, the temporal development of U-lesions in the RMR model might carefully be compared to the kinetics in DSB rejoining. Having all these caveats in mind, one can finally draw the link between the performance of DSB rejoining models and the adequacy of lesion repair models employed in kinetic cell survival models.

The presented model comparison has revealed that experimental data support the bi-exponential model for DSB rejoining more often than the first-second-order model. Consequently, the bi-exponential approach in the GLOBLE model might be more adequate than the first-second-order approach in the RMR and LPL model. Furthermore, in section 3.2.4.3 it has been explained why first- and second-order kinetics might be in conflict with experimental observations and considerations about DSB interactions. Since the GLOBLE model is based on an alternative approach where intra-lesion repair dominates the short time range after irradiation and inter-lesion repair the long time range, the GLOBLE model might have an advantage over the RMR and LPL model also in that respect.

Radivoyevitch and co-authors conducted a study which supports the conclusions which have been drawn here with respect to the adequacy of the 1st2ndO approach in the RMR and LPL model [104]. The authors did not only investigate the compatibility of the 1st2ndO approach with DSB rejoining data but also with data which reflect the temporal course of misrejoining events. They find that, compared to the experiments, the kinetics in the RMR and LPL model go in hand with too many misrejoining events in the short time range and conclude that this might constitute a shortcoming for the two models.

Concerning the Linear-Quadratic model with Lea-Catcheside formalism (LC-LQ model) [70][71], the link between the underlying kinetics and DSB rejoining is hard to establish. There is currently no mechanistic and biologically consistent interpretation that allows to derive the LC-LQ model from DSB induction and rejoining. Therefore, it is questionable if the approach is discussable here. When the dynamic interpretation of the LQ model as proposed by Lea and

Catcheside is related to DSB rejoining nevertheless, it corresponds to a first-second-order approach, although Lea and Catcheside consider the temporal aspects of inter-lesion repair to be negligible in comparison to intra-lesion repair. Consequently, it could be stated that the kinetics underlying the LC-LQ model find less support by the experimental DSB rejoining data than e.g. bi-exponential kinetics.

An ultimate conclusion about the adequacy of the RMR, LPL and GLOBLE model with respect to their actual purpose, the prediction of cell survival probabilities, is naturally not feasible on basis of the presented comparison of DSB rejoining models. Assumptions about the induction or lethality of lesions might make up for deficiencies in the repair of lesions. Consequently, a comparison of kinetic cell survival models investing their performance in the description of e.g. dose-rate experiments should considered to be highly interesting. Such a comparison was conducted as part of this thesis and will follow in the next section.

3.2.5 Conclusion

The presented comparison of ten models for DSB rejoining on the hand of fits to 61 experimental data sets showed a strong support for a bi-exponential approach and a mono-exponential approach with gamma-distributed decay rate. Models with a single DSB rejoining rate and models which involve second-order kinetics lack in accuracy when it comes to the reproduction of the data. Furthermore, models involving second-order kinetics are questionable with regard to the impact of interactions at short times after irradiation. A tri-exponential model and a bi-exponential model with offset lead to an overfitting of the data.

The bi-exponential model and the mono-exponential model with gamma-distributed decay rate distinguish in their predictions of DSB remaining long times after irradiation. In an out-of-sample test, the bi-exponential model systematically underestimates fractions of unrejoined damage in contrast to the other model. Moreover, the model with gamma-distributed decay rate has some advantages over the bi-exponential model in the application to small sample size data sets because of one free parameter less. On the other hand, the interpretation of results found with the model with gamma-distributed decay rate to experimental data is much less intuitive than the interpretation of results found with the bi-exponential model where fractions of fast and slowly rejoined damage with corresponding rates are directly assessable.

Concerning the categorization of DSB, the presented results support either two categories, characterized by two predominant features of DSB, or a continuum of DSB categories, i.e. an individual processing of the lesions depending on their appearance.

Finally, the better performance of the bi-exponential model compared to the first-second-order model suggests that kinetic cell survival models with bi-exponential lesion repair as the GLOBLE model might have advantages over models involving second-order dynamics as the RMR and LPL model.

3.3 Comparison of kinetic cell survival models

3.3.1 Motivation

Next to the delivered dose and the LET of an applied radiation, the schedule of the dose delivery has a potential impact on the cellular response. Especially for photon radiation, there is a large data base of experiments investigating time-dose effects when doses are protracted or split into several fractions. It has e.g. been found that cell survival probabilities generally increase when dose-rates are lowered roughly between 25 Gy/h and 0.5 Gy/h. The role of kinetic cell survival models describing such observations is threefold.

First, for the explanation of causes of time-dose effects, mechanistically motivated cell survival models might be *instructive*. For instance, in section 2.4, the framework of the GLOBLE model and LEM has been employed to better understand plausible reasons for an increase of cell survival probabilities with a decrease of intermediate dose-rates. With an abstract and simple definition of lesion classes with corresponding lethalities and repair characteristics, the main features of more complex biological processes become intuitively perceivable. Second, kinetic cell survival models provide a *link* between measured damage induction and rejoining on the one hand and observed cell survival probabilities on the other hand. For example, a meaningful combination of experimentally derived DSB induction rates and DSB rejoining rates in a mathematical formalism allows to predict in which range of dose-rates changes in cell survival probabilities should be expected. And third, *predictions* of cell survival probabilities after high- and low-LET radiation are useful, e.g. for treatment planning in heavy ion radiotherapy where usually an increased RBE of particles has to be accounted for. When the dose delivery in a session takes some time due to complex treatment techniques, changes in the RBE might be expected not only in dependence of the LET and dose but also in dependence of the actual schedule. However, for this third purpose of a kinetic cell survival model, it has to be applicable to low- and high-LET radiation, which is not always the case.

Since the 1940ies there have been cell survival models accounting for time-dose effects, e.g. the Lea-Catcheside (LC-LQ) formalism [70] [71]. Two other very popular models, the Repair Misrepair (RMR) model [73] and the Lethal Potentially Lethal (LPL) model [74], followed in the 1980ies. After introduction of the kinetic extension of the GLOBLE model in 2014, it was naturally questioned which advantages or disadvantages this new approach might have in comparison to the well-established ones. In the previous section 3.2 it was already asserted that the kinetics behind the GLOBLE model might be more appropriate than the kinetics behind the RMR and LPL model with regard to DSB rejoining. However, possible shortcomings in the formulation of lesion repair might be fixed when there is an adequate representation of lesion induction and of lethalities in a cell survival model. Therefore, a qualitative and quantitative model comparison was dedicated to the investigation of this issue.

In the following, the LC-LQ, RMR, LPL and GLOBLE model will be tested with respect to their accuracy and parsimony in the description of 13 photon dose-rate experiments. Some further benchmarks will be used to assess other qualities of a good model - some of which have been proposed by Fertil et al. [105]. These quantitative results will be complemented by qualitative arguments about advantages and disadvantages in the discussion. The corresponding findings have been published in [106].

3.3.2 Materials and methods

3.3.2.1 The models

As motivated, four models were tested in this model comparison: the LC-LQ model [70][71], the RMR model [73], the LPL model [74] and the GLOBLE model [63]. All of them have been introduced in sections 2.4.2, 2.4.3, 2.4.4 and 2.4.5. Therefore, only some remarks concerning model adjustments for the fit procedures will be made here.

In order to reduce the number of free parameter values in the four models, some biologically well-founded assumptions were made. The lesion (double-strand break) yields in the RMR and GLOBLE model (α and α_{DSB}) were set to $30\,\mathrm{Gy}^{-1}$ [6]. Such a fixation of lesion yields was not feasible in the LPL model since it is unknown what fraction of DSB has to be considered as "directly" or "potentially" lethal. In the LC-LQ model, there is no fit parameter reflecting a lesion yield. Furthermore, the number of giant loops (domains) and the half-life time of cDSB in the GLOBLE model were set to $N_L = 3000$ and $HLT_c = 5\,\mathrm{h}$, respectively. The low sensitivity of survival probabilities predicted in the GLOBLE model on HLT_c was shown in [77] and therefore, at least the fixation of this parameter should be well-justified. Nevertheless, for the sake of consistency, HLT_c was increased to 10 h after the half-life time of iDSB was larger than 5 h in the fit to one experiment. This change in HLT_c did not change any further parameter value in the optimal fit, though. An overview over the free model parameters that were used can be gained in the headlines of Table 5.2.2 in the appendix (section 5.2). Furthermore, already at this stage, their order of magnitude can be assessed by having a look at the average values (last Row) that were derived in the global fits as explained below.

3.3.2.2 The experimental data

For the comparison of the four models, photon cell survival experiments which demand for the usage of kinetic approaches were needed and it was decided to test the models on the hand of their performance in the description of dose-rate experiments. After searching the literature, 13 dose-rate experiments with at least three different applied dose-rates were chosen. The requirement for at least three dose-rates was based on the intention to execute a robustness test where one of the dose-rate-specific curves of an experiment was removed and fits to the remaining curves were performed, as explained below. Since the survival curves were presented graphically in the original publications, the data points were read in with "GetData Graph Digitizer" [78]. Unfortunately, with one exception, the data points represented the mean of several measurements but no error bars were provided. This inevitably lowered the statistical power of the investigation. Table 5.2.1 in the appendix (section 5.2) lists all of the selected experiments with corresponding publications and setups.

3.3.2.3 The fit procedure

The optimal fit of the four models to a given dose-rate experiment was determined by minimization of the sum of squares over all available data points. That means that for each model, a global fit was derived over all dose-rate-specific survival curves of the experiment. The mini-

mum (residual) sum of squares RSS is therefore defined with the best-fit parameters $\tilde{\vec{P}}_{glob}$ of a model as:

$$RSS = \sum_{i=1}^{N_d} \left[\sum_{j=1}^{M_i} (f(D_{i,j}, \dot{D}_i, \tilde{\vec{P}}_{glob}) - y_{i,j})^2 \right]. \tag{3.3.1}$$

Here, N_d denotes the number of dose-rates applied in an experiment. M_i is the number of data points recorded for the survival curve corresponding to the dose-rate $\dot{D}_i$. The respective experimentally determined effects are denoted by $y_{i,j}$ and the best-fit model predictions by $f(D_{i,j}, \dot{D}_i, \tilde{\vec{P}}_{glob})$.

For the minimization of the sum of squares, the pre-programmed routine "NonLinearModelFit" in "Wolfram Mathematica 8.0" [100] was used. To ensure that the global minimum for a given model and experiment is reliably found, the search methods hat to be adjusted. For the LC-LQ, RMR and GLOBLE model "DifferentialEvolution" was selected and for the LPL model "NelderMead" was chosen.

For the sake of stability, the two probabilities for lethal events in the RMR model ϕ and δ were substituted by their complements $\tilde{\phi}$ = 1-ϕ and $\tilde{\delta}$ = 1-δ. Moreover, to prevent inconsistent results in the RMR and LPL model, the restrictions that all parameter values should be larger than zero and that $\tilde{\phi}$ and $\tilde{\delta}$ in the RMR model should be smaller than one had to be set. No restrictions on parameter values were needed in fits of the LC-LQ and GLOBLE model - the best-fit results were always reasonable. Last but not least, to provide a higher reliability in the derivation of optimal parameter values, the mathematical formulations of the effects $Eff(D, \dot{D})$ = -ln($S(D, \dot{D})$) of the models were employed in all computations and not the survival probabilities themselves.

3.3.2.4 Setup of a robustness test

For the assessment of the predictive power of the four models in benchmarks that will be introduced below, a robustness test was conducted. In each experiment, its N_d dose-rate-specific survival curves were removed in turns from the corresponding data set. That means that e.g. for an experiment with three dose-rate-specific survival curves, there were three reduced data sets: one where the data points recorded for the highest dose-rate were deleted, one where the medium dose-rate data points were discarded and the same for the lowest dose-rate. To each of these reduced data sets, the four models were fitted by minimization of the sum of squares to yield N_d new best-fit parameter sets $\tilde{\vec{P}}_{red,i}$ (i = 1,2,...N_d) for each model.

3.3.2.5 Definition of a measure for relative fluctuations

One last tool needed for the calculation of the decisive benchmarks below is the coefficient of median absolute deviation $CMAD$. It is applicable to quantify relative fluctuations in a small set of distributed values $\tilde{p}$ as suggested by Fertil et al. [105]. (One might roughly compare it to a low-sample-size standard deviation.) When the indices k and l run over the number of values $\tilde{p}$, the $CMAD$ is defined as:

$$CMAD = \frac{median_k(|\tilde{p}_k - median_l(\tilde{p}_l)|)}{median_l(\tilde{p}_l)}. \tag{3.3.2}$$

The meaning of the values $\tilde{p}$ will be defined case-specifically when needed.

3.3.2.6 Benchmarks for the quantitative model comparison

Eight measures were defined in order to quantify the performance of the four investigated models with respect to various endpoints that distinguish a good model. Due to the fact that the statistical characteristics of these measures generally depend on the investigated experiment, a direct common evaluation of a measure over all the experiments, e.g. the derivation of its mean value for each model, was not feasible. Therefore, rankings of the models were employed for each measure as follows:

(i) In a given experiment, the measure was derived for each model.
(ii) In the given experiment, the models were ranked with respect to the value of this measure.
(iii) Such a ranking was generated for each experiment (13 rankings).
(iv) For each model, the average of its ranks was taken over all of the 13 experiments.
(v) The four average rankings corresponding to the considered measure were taken as benchmarks for the comparison of the models.
(vi) The significance of the differences in the four benchmarks was tested pairwise with a Wilcoxon-Mann-Whitney test.

Only one measure (the resolution power) was computed comprehensive for all the experiments, as it will be explained below, and therefore directly employed as benchmark. Finally, the eight benchmarks considered in the model comparison are:

i) The global accuracy and parsimony

As a first measure of a model's performance, its global accuracy and parsimony in the description of an experiment was derived. Since there were no measurement errors provided in the original publications, the calculation of a reduced chi-squared value was not feasible and a comparable measure was introduced. It will be denominated as normalized residual sum of squares in the following and is defined as:

$$RSS_{norm} = \frac{RSS}{N-K}. \tag{3.3.3}$$

Here, N is the total number of data points corresponding to a given experiment and K is assumed to be the number of free parameters of a considered model. The normalization of RSS by the number of degrees of freedom $(N-K)$ acts as punishment for larger numbers of free parameters and thus, RSS_{norm} is the smallest for the most accurate and parsimonious model. As motivated above, the average of the 13 rankings of the models with regard to RSS_{norm} was taken as benchmark for the final comparison.

It was chosen to use a measure comparable to the reduced chi-squared because it allows to define "individual" normalized sums of squares by assigning weights to dose-rate-specific curves of an experiment, as it will be explained in the next point. The usage of the $AIC(c)$ for the comparison of the accuracy and parsimony of the four models would be as compromised as the

usage of the reduced chi-squared value due to the lack of original measurements or at least of error bars corresponding to their means in the original publications. Nevertheless, to ensure that a model selection on the hand of the $AIC(c)$ does not lead to contradictory results, models were also ranked with regard to this value and the results for the average rankings were compared to the results that were gained with RSS_{norm}. For the computations of the $AICc$, it was assumed that all mean data points were original measurements and the the residuals follow a Gaussian distribution.

ii) The individual accuracy and parsimony

When a model is globally fitted to a dose-rate experiment, it might happen that the model systematically approximates some dose-rate-specific curves well and other ones badly (e.g. high versus low dose-rates). The global RSS_{norm} does not necessarily reflect such biases since they might be compensated in the average. To assess the homogeneity of the four models in the description of the dose-rate-specific survival curves after derivation of a global fit, the individual normalized residual sum of squares was taken for each curve ($i = 1,2,...,N_d$):

$$RSS_{indiv,i} = \frac{1}{M_i - K\frac{M_i}{N}} \sum_{j=1}^{M_i} [f(D_{i,j}, \dot{D}_i, \tilde{\vec{P}}_{glob}) - y_{i,j}]^2. \tag{3.3.4}$$

The weights $(M_i - K\frac{M_i}{N})^{-1}$ assign that fraction of degrees of freedom to a considered dose-rate-specific survival curve that is implied by its number of data points in relation to the total number of data points in the experiment.

After all the $RSS_{indiv,i}$ were derived in a given experiment for a considered model, the corresponding average was computed. Then, still within the given experiment, the models were ranked with respect to these averages. Finally, the decisive benchmark was again derived by averaging the 13 ranks for a given model.

iii) Reliability

Ideally, mechanistic cell survival models should allow for an extrapolation from experimental observations to cellular responses at other doses and dose-rates. Consequently, parameter values derived for a considered cell line should depend as little as possible on the data selection. Only when a set of parameter values that has been derived for a given cell line in a sub-sample of available data is adequate for the reproduction of further available data, the model can be judged as reliable.

To quantify the reliability of the four investigated models, a robustness test was performed as explained in section 3.3.2.4. For a given model and cell line which was exposed in an experiment, the robustness test provided N_d sets of parameter values - one for each reduced data set where a dose-rate-specific survival curve was omitted. So together with the global best-fit parameters, there were N_d+1 sets of model-specific parameter values derived for one cell line. The model-specific global sets of parameter values did not enhance the statistical power of the investigations but were included for the sake of completeness.

In order to derive the relative fluctuation of model-specific parameter values derived for one and the same cell line, the $CMAD$ (equation 3.3.2) was employed. For each model-specific parameter $\tilde{p}$, the $CMAD$ was computed over all the available N_d+1 values (l and k

$= 1,2,...,N_d+1$). Then, the mean of the $CMAD$ corresponding to the parameters of a specified model was calculated (Mean of MAD/Median, MMM). The models were ranked with regard to this measure in each cell line. Thus, 13 rankings were derived and could be averaged over the cell lines to yield the final benchmark.

iv) Resolution power

To assess the ability of a model to predict characteristic responses for a given cell line rather than an appropriate generic response, a resolution power was defined. In a kind of "signal to noise" ratio it quantifies the specificity of a set of model parameters that is supposed to characterize a given cell line.

As a measure for the "noise", the relative fluctuation of model-specific parameter values was quantified across cell lines. For a single parameter corresponding to a considered model, its $CMAD$ (equation 3.3.2) was calculated over the 13 values derived in the global fits. The mean of these $CMAD$ derived for all of the parameters corresponding to the considered model was taken as its cell line comprehensive parameter noise.

The parameter noise should be compared to relative parameter fluctuations within cell lines. Accordingly, relative fluctuations of parameter values derived in fits to different experimental data sets recorded for one cell line were taken as "signal". Corresponding computations have already been executed in the assessment of a model's reliability in terms of the MMM for a given cell line. Therefore, the mean of the 13 cell line specific MMM was calculated for each model to yield its parameter signal. The ratio of signal and noise was considered as resolution power of a model. Since this measure is already unique for each model, it was directly taken as benchmark (without the necessity to compute average rankings).

v-viii) Relative fluctuation of predicted isodoses and survival probabilities

For practical applications it is instructive to provide measures for the relative fluctuation of model predictions and not only of model parameter values. For instance, predicted doses (isodoses) that are needed to achieve a fixed radiation effect Eff are of interest because they might be employed as reference for the calculation of an RBE. Similarly, one might consider predictions of survival probabilities at fixed doses. In the subsequent investigations, the relative fluctuations of isodoses needed to achieve an effect corresponding to 50% and 10% survival probabilities and the relative fluctuations of survival probabilities at 2 Gy and 5 Gy will be quantified.

After the global fit and the robustness test, there were N_d+1 sets of parameter values derived for each cell line and model. For a given cell line and model, these parameter values were used to derive corresponding predictions of isodoses and survival probabilities for all dose-rates that had been applied in the respective experiment. Then, for each considered endpoint (two isodoses and two survival probabilities) the subsequent steps were made. For a given cell line, model and dose-rate, a relative fluctuation of the endpoint was computed in terms a $CMAD$. That means when e.g. survival probabilities at 2 Gy should be evaluated for the given cell line, model and dose rate, $\tilde{p}$ in equation 3.3.2 has to be identified with the N_d+1 ($k, l = 1,2,...,N_d+1$) corresponding predictions of cell survival probabilities at 2 Gy. For the given cell line and dose-rate, the models were ranked with respect to their $CMAD$. Then, the average ranking over all

dose rates and cell lines was calculated for each model. Thus, one MMM resulted for each model under the considered endpoint which could be used as benchmark for the comparison.

3.3.3 Results

3.3.3.1 Visual inspection

Already a visual inspection of the best-fit global model predictions in comparison to the measured data points reveals that there are small differences in the accuracy of the LC-LQ, RMR, LPL, and GLOBLE model. Figure 3.3.1 gives an example for most of the investigated cell lines. The four panels highlight the measured dose-rate-specific survival curves with corresponding graphs (global best-fits). All of the four kinetic cell survival models approximate the data reasonably well. However, especially at the highest dose-rate (Panel A), one notices that the LC-LQ and GLOBLE model show a more pronounced curvature in the corresponding survival curves than the LPL model. The graph produced with the RMR model shows almost no bending after a sharp initial kink. The models predict equivalent extents in the increase in cell survival probabilities with a decrease of the dose-rate. Finally, at the lowest dose-rate, the RMR model suggests higher survival probabilities than the other models.

Similar observations can be made in plots created for the other 12 cell lines. Compared to the LPL model, there is a tendency for a higher curvature in the GLOBLE model and for the highest curvature in the LC-LQ model (8 of 13 cases) and a tendency for a decreased curvature in the RMR model (11 of 13 cases). Such differences in the curvature do not always imply that the one or the other model is less accurate - depending on the cell line an increased or decreased curvature might be favorable.

However, when it comes to the RMR model, the number of cases where a severe underestimation of acute survival probabilities at low doses and an overestimation of acute survival probabilities at high doses can be noticed is relatively high (4 out of 13). Figure 3.3.2 provides an extreme example on the hand of an acute survival curve recorded for the CHO 10B2 cell line. There are no systematics that could explain why the model has some shortcomings in the description of the one or the other considered cell line. Thus, together with several under- and over-estimations of survival probabilities recorded at intermediate or low dose-rates, the findings suggest a comparably low accuracy of the RMR model.

For the LC-LQ and GLOBLE model, one can systematically distinguish the cases where these two models show deficiencies. When radiosensitive cell lines with a straight acute survival curve exhibit a dose-rate effect, the two models are by construction not able to reproduce the data. This issue will be picked up in the discussion. In the current investigation, there are 3 out of 13 cases where the LC-LQ and GLOBLE model lead to a low accuracy and Figure 3.3.3 gives a corresponding example. With exception of these special cases, the LC-LQ and GLOBLE model generally provide reasonable fits to all dose-rate-specific survival curves and therefore, a good accuracy should be expected. Due to a slight stronger bending of curves produced with the LC-LQ model at higher doses, the GLOBLE model might prove to approximate the data better.

The LPL model describes almost all investigated survival curves well - independent of the dose-rate. However, in comparison to the LC-LQ and GLOBLE model, it features one free fit parameter more and consequently has an advantage which has to be accounted for. The usage

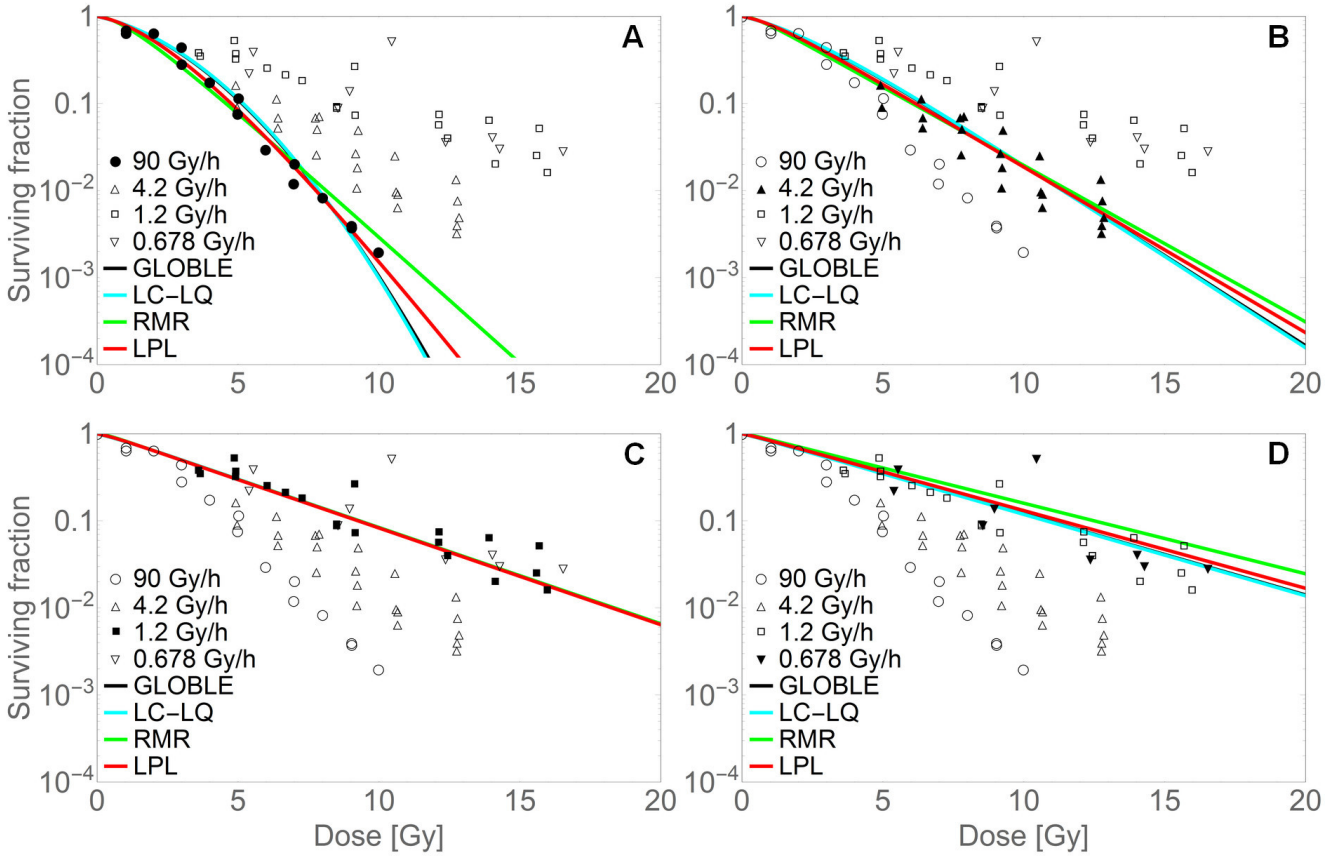

Figure 3.3.1: Global fits of the four investigated models to survival curves recorded for the IN859 cell line [68]. The global best-fit parameters were derived by minimization of the sum of squares including all data points. The different Panels visualize the description of highlighted dose-rate-specific curves. The graphs corresponding to the LC-LQ and GLOBLE model overlap. The figure was presented in [106] in a modified version.

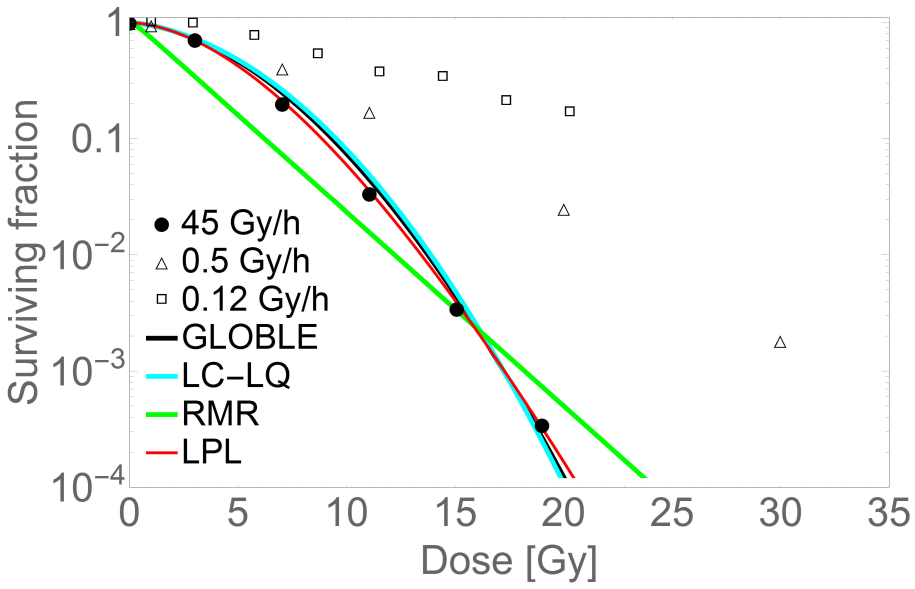

Figure 3.3.2: Global fits of the four investigated models to a dose-rate experiment recorded with the CHO 10B2 cell line [65]. Although the best-fit parameter values were derived by a global fit including all dose-rate-specific survival curves, only the graphs describing the acute curve are shown. The RMR model severely underestimates measured survival probabilities at low doses and overestimates them at high doses. The figure was presented in [106] in a modified version.

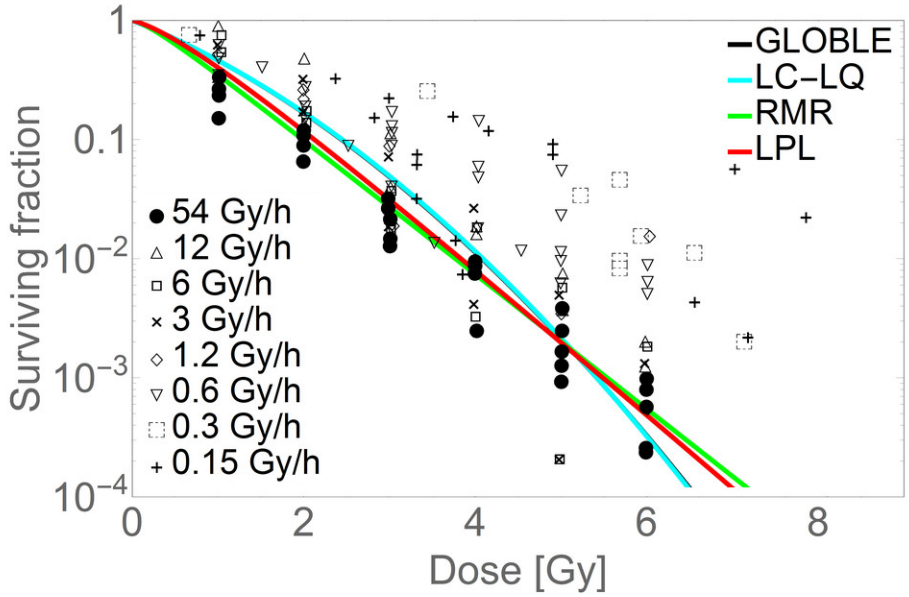

Figure 3.3.3: Global fits of the four investigated models to a dose-rate experiment recorded with the radiosensitive HX138 cell line [107]. Although the best-fit parameter values were derived by a global fit including all dose-rate-specific survival curves, only the graphs describing the acute curve are shown. Due to an over-pronounced curvature, the LC-LQ and GLOBLE model overestimate survival probabilities at low doses and underestimate them at higher doses. Their graphs overlap. The figure was presented in [106] in a modified version.

Model	Av. rank RSS_{norm}	Av. rank RSS_{indiv}	Av. rank reliability	Resolution power	Av. rank survival 2 Gy	Av. rank survival 5 Gy	Av. rank isodose 50%	Av. rank isodose 10%
GLOBLE	1.92	2.12	1.77	0.18	2.28	2.46	2.24	2.25
LQ	2.69	2.10	1.31	0.17	2.33	2.38	2.21	2.48
LPL	1.88	2.60	3.15	0.43	2.19	2.12	2.19	2.04
RMR	3.5	3.18	3.77	0.66	3.22	3.04	3.37	3.23

Table 3.3.1: Results of the quantitative comparison of the LC-LQ, RMR, LPL and GLOBLE model. The models were judged with respect to the eight listed benchmarks. The group of best-performing models (statistically equivalent performance) is colored in green, intermediate models are indicated with the color yellow and the significantly worst performing model is highlighted in red. ("Av." abbreviates "average".)

of the normalized global and individual residual sums of squares in the next section will ensure a model selection not only by accuracy but also by parsimony.

3.3.3.2 Accuracy and parsimony

As a first benchmark for the comparison of the LC-LQ, RMR, LPL and GLOBLE model, their global accuracy and parsimony was computed using RSS_{norm} (equation 3.3.3). Column 2 in Table 3.3.1 provides the corresponding average rankings of the models over the 13 experiments. The results confirm the impressions gained in the visual inspection. The LPL model describes the measured data best, closely followed by the GLOBLE model and the LC-LQ model. The RMR model has some obvious drawbacks with respect to its accuracy and parsimony. Actually, the null-hypothesis that the LPL, GLOBLE and LC-LQ model have statistically the same average ranking cannot be rejected in pairwise Wilcoxon-Mann-Whitney tests ($p > 0.05$). However, the average ranking of the RMR model is always significantly different from the other rankings ($p < 0.05$).

The fact that the LPL model is judged as one of the best models on the basis of RSS_{norm} suggests that the additional free parameter is justified by an increase in accuracy compared to the LC-LQ and GLOBLE model. To confirm this finding on the basis of another statistical measure, the average ranking of the models with respect to the $AICc$ derived in the global fits to the 13 experiments was calculated. Obviously, the $AICc$ punishes complex models slightly more than RSS_{norm} because the average rankings of the LPL and RMR model drop to 2.08 and 3.77, respectively. In contrast, the average rankings of the GLOBLE and LC-LQ model increase to 1.69 and 2.38, respectively. Thus, the GLOBLE and LPL model swap their position in the order with respect to accuracy and parsimony. However, there is again no significant pairwise difference between the average rankings of the GLOBLE and LPL model on the one hand and the LPL and the LC-LQ model on the other hand. The RMR model performs significantly worse. Thus, despite significantly different average rankings of the GLOBLE and LC-LQ model, the judgment of the models on the hand of the $AICc$ is comparable to their judgment on the hand of RSS_{norm}.

To quantify the homogeneity of the four models in the description of the individual dose-rate-specific survival curves of an experiment after a global fit, a benchmark for the individual accuracy and parsimony was defined. The average rankings on the hand of $RSS_{indiv,i}$ (equation

3.3.4) derived for each of the i=1,2,...,N_d dose-rate-specific survival curves in each of the 13 experiments are provided in Column 3 of Table 3.3.1. Obviously, the LC-LQ model allows for the most homogenous approximation of the data recorded with any given dose-rate in an experiment, followed by the GLOBLE model and the LPL model. However, the null-hypothesis that the average rankings of these three models are equal is only rejected in a pairwise test of the GLOBLE and LPL model ($p < 0.05$). Furthermore, no systematics can be discerned with regard to which dose-rate-specific curves (e.g. high or low dose-rate) are likely to be better or worse described than other ones in a given experiment by e.g. the LPL model. Consequently, the performance of the LC-LQ, GLOBLE and LPL model should be considered as equivalent with respect to the considered benchmark. The RMR model shows again a significantly worse performance than the other three models.

3.3.3.3 Reliability and resolution power

A low fluctuation of model parameter values derived in fits to different selections of experimental data sets for one and the same cell line was considered to characterize a "reliable" model. The average rankings of the four models with respect to the MMM of parameter values derived for the 13 cell lines (section 3.3.2.6) were used as benchmarks and are presented in Column 4 of Table 3.3.1. Obviously, the LC-LQ model provides most stable sets of parameter values for an investigated cell line, closely followed by the GLOBLE model and the LPL model. The null-hypothesis that the LC-LQ and GLOBLE model feature the same average ranking is not rejected ($p > 0.05$), however, the average ranking of the LPL model is significantly different. Furthermore, the worst average ranking of the RMR model is statistically verified in pairwise comparisons with the other three models.

When the relative fluctuation of parameter values in different selections of data sets for a given cell line is compared to the relative fluctuation of parameter values across different cell lines, one gets the "resolution power" of a model (section 3.3.2.6). Column 5 of Table 3.3.1 provides the values of this benchmark derived for the four investigated models. The LC-LQ model features the highest resolution power with only a small prominence in comparison to the GLOBLE model. The distance to the next best model, the LPL model is larger and the RMR model shows a comparably low resolution power. There is no way to derive the statistical significance between these four values - the distinct superiority of both, the LC-LQ and GLOBLE model, in comparison to the other two models is very meaningful, though.

3.3.3.4 Prediction of isodoses and survival probabilities

In practice, the four kinetic cell survival models should provide stable predictions of survival probabilities and isodoses independent of the selection of data sets that was used to derive the characteristic parameter values for the considered cell line. Thus, relative fluctuations of the models in the prediction of four endpoints, cell survival probabilities at 2 Gy and 5 Gy and isodoses implying the effect corresponding to 50% and 10% survival probabilities, were calculated (section 3.3.2.6). The four corresponding average rankings were taken as the last decisive benchmarks. Columns 6-9 of Table 3.3.1 present the respective values.

For all endpoints, the LPL model provides the most stable predictions. In the prediction of survival probabilities at 2 Gy and of isodoses needed to achieve an effect of 10% survival, the

GLOBLE model is next best followed by the LC-LQ model. For survival probabilities at 5 Gy and isodoses needed to achieve an effect of 50% survival, these two models swap their position. In almost all of the cases, the null-hypothesis that the average rankings of the three models are equal in a pairwise comparison is not rejected ($p > 0.05$). Only in the prediction of 10% survival probabilities, the difference in the average rankings of the LPL and LC-LQ model is significant ($p < 0.05$). The RMR model shows again the worst performance and its average ranking is always significantly different from the rankings of the three other models.

3.3.4 Discussion

3.3.4.1 Brief discussion of the quantitative results

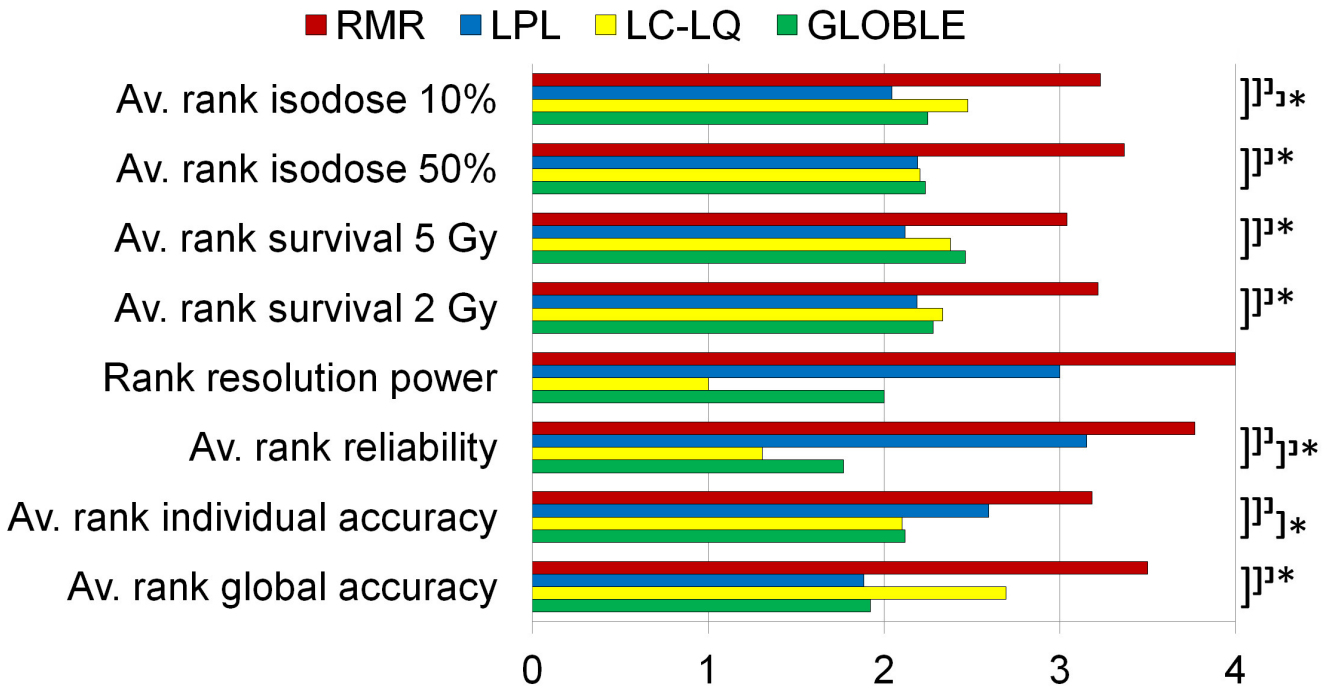

Figure 3.3.4: Results of the quantitative comparison of four kinetic cell survival models with respect to eight investigated benchmarks. Pairwise significantly different performances are indicated with a star. The figure was presented in [106] in a modified version.

As a summary of the findings presented in the last section, Figure 3.3.4 illustrates the performance of the models with respect to the eight considered benchmarks. Two distinctive statements can be made on the basis of these results. First, the RMR model shows deficiencies in the description of dose-rate experiments. Independent of the investigated benchmark, the model performs significantly worse than the other models and thus seems to be less recommendable. Second, the LC-LQ, LPL and GLOBLE model generally approximate dose-rate experiments equivalently well. With few exceptions, no statistical differences can be detected when respective benchmarks of the models are compared. Consequently, for the evaluation of experiments or for the prediction of requested endpoints, all of the three models are likely to

provide adequate information. Advantages or disadvantages of the models must be discerned on the basis of qualitative arguments about the appropriateness of mechanistic assumptions behind the models.

Concerning the methods of the quantitative model comparison one has e.g. to discuss the usage of a normalized residual sum of squares as measure for accuracy and parsimony. Unfortunately, the data points of the dose-rate experiments published in literature were presented as means of several measurements without error. This prevented a meaningful usage of any statistical measure for model comparisons. None of them had any clear advantage or disadvantage with regard to the quantification of accuracy and parsimony. However, with regard to the feasibility of modifications, the normalized residual sum of squares provided the advantage to define individual measures for accuracy and parsimony (RSS_{indiv}) by assignment of weights to sums of squares of dose-rate-specific survival curves. Thus, the usage of the normalized residual sum of squares should be well justified.

Moreover, one might argue about the role of varying numbers of free model parameters in the derivation of the reliability. Models with a relatively low number of free parameters, here represented by the LC-LQ and GLOBLE model, might exhibit smaller fluctuations of parameter values when different selections of data sets are employed to derive cell line specific fits. In contrast, models with a relatively large number of parameters might adapt more sensitively to the new situation. Consequently, in terms of the reliability defined in this study, models with a lower number of model parameters might have an advantage. However, it was the purpose of the benchmark "reliability" to actually quantify parameter fluctuations regardless of the number of free parameters of a model in order to identify possible overfits by parameter uncertainty. Therefore, the findings based on this benchmark should be meaningful as they are.

Anyway, the good performance of the LPL model in the prediction of isodoses and survival probabilities shows that despite larger fluctuations of intended cell line characteristic parameter values, the model provides stable results. Supposedly, there is a correlation between its fit parameters such that changes in one value can be compensated by changes in another one.

Last but not least, the "noise" defined in the introduction of the resolution power should be questioned critically. The whole spectrum of possible fluctuations in model parameters can only be covered when a wide range of radiation responses is reflected by the different cell lines used for the comprehensive derivation. Actually, the 13 cell lines investigated in the current study represent a good cross-section over various characteristics (radiosensitive or -resistant, human or rodent, normal tissue or tumor, etc.). In consequence, they should offer a good basis for the computation of "noise".

3.3.4.2 Comparison to other published studies

The usage of the global accuracy and parsimony, reliability and resolution power as benchmarks for a model comparison was already suggested by Fertil et al. [105]. These authors compared six radiation action models, amongst others the LQ, RMR and LPL model, with respect to their description of acute survival curves. Due to the reduction of the kinetic cell survival models to static versions, other formalisms than the ones defined in the present study were employed. The RMR formulation comprised two and the LPL formulation three free parameter values. Moreover, the robustness test for the assessment of fluctuations of cell line specific parameter values did obviously not involve the omission of dose-rate-specific survival curves. Instead, in a single acute survival curve, data points recorded at either low or high doses were deleted before

the fit procedures. Thus, only 2+1 instead of N_d+1 different sets of parameter values were derived.

In fact, the findings of Fertil et al. partly deviate from the results presented here. With regard to the global accuracy and parsimony, the LPL model performs worst in comparison to all of the other models whereas the LQ and RMR model show equivalently good approximations. Furthermore, the RMR model leads to a relatively high reliability which is in contrast to the findings above. An agreement between both studies can be found in the low resolution power of the RMR and LPL model; Fertil et al. assign a higher resolution power to the RMR model, though. Finally, the high reliability and resolution power of the LQ model is consistent in both model comparisons.

There is at least a possible explanation for the increased reliability of the RMR model compared to the LPL model in the investigation of Fertil et al. Apparently, the models with the least number of free parameters have an advantage in the derivation of this benchmark and since the RMR model features one parameter less than the LPL model, this might reason the better performance. Apart from that, the sources for the differences in the global accuracy and parsimony must be searched in the different underlyings of the investigations (acute survival curves vs. whole dose-rate experiments) and the corresponding model formulations.

Another comparison of kinetic cell survival models employing a comparable measure for accuracy and parsimony as the one used here was presented by Sontag [108]. He investigated the performance of six models in the description of six delayed plating experiments, amongst others the RMR and LPL model. Since he did not fix the lesion induction rate in the RMR model, the model was defined with one free parameter more compared to the current study. Nevertheless, concerning the RMR model, he comes to the same conclusion as drawn above: it lacks in accuracy and parsimony. This lack in accuracy and parsimony is significant in comparison to the other models that he investigated with one exception: the LPL model performed equivalently bad. The latter finding is in contrast to the results that have been presented here.

A last published investigation of kinetic cell survival models that should be mentioned was published by Brenner et al. [109]. The authors theoretically suggested that the concepts of the LC-LQ, RMR and LPL model should lead to similar predictions of time-dose effects at low doses and dose-rates when repair is completed at the time of the derivation of the survival probabilities. In the present analysis, theoretical commonalities in the LC-LQ, RMR and LPL approaches will be discussed below. However, already at this stage, it can be stated that the slight differences in the concepts of these three models potentially lead to significant differences in the description of experimental data as e.g. shown with the bad performance of the RMR model.

3.3.4.3 Qualitative comparison

Induction of radiation damage

One of the major tasks in the setup of mechanistically motivated kinetic cell survival models is the appropriate definition of lesion classes. With corresponding lethalities and temporal characteristics they must imply cell survival probabilities that are in agreement with experimental observations. Due to the fact that DSB are considered to be the main reason for radiation-induced cell killing [36][37], a close relation between lesion classes and DSB should be given. A failure of a model to reflect characteristics of DSB might question its biological adequacy.

For the (LC-)LQ model, which was originally explained on the hand of chromosome breaks, Chadwick and Leenhouts suggested a mechanistic interpretation based on DSB. Referring to their molecular theory, the linear component of cell survival curve reflects DSB induced by single electron tracks. The quadratic bending is motivated by the formation of DSB from two SSB produced in overlapping electron tracks - the corresponding probability increases quadratically with the dose. However, this concept is in a disagreement with experimentally observed DSB and SSB yields and therefore, the (LC-)LQ model rather remains an empirical approach for the prediction of cell survival curves. The kinetic LC-LQ formalism does not explicitly involve a lesion induction rate anyway and therefore, a reflection of DSB induction rates is not imperative.

In the first publications of the LPL and GLOBLE model, is was explicitly declared that the corresponding lesion classes (DLL, PLL and iDSB, cDSB) reflect distinct characteristics of DSB. Therefore, an agreement of the two models with observed qualities of DSB should be given. At least in the GLOBLE model, one indirectly finds a reasonable compliance with DSB induction yields since setting α_{DSB} to $30\,\mathrm{Gy}^{-1}$ allows for reasonable fits to experimentally measured cell survival data.

In the LPL model, such a compliance with DSB induction rates is harder to detect because it is unknown how many DSB constitute DLL and PLL, respectively. Therefore, there is no fixed relation between $\eta_L + \eta_{PL}$ and a DSB induction rate. However, the average values of η_L and η_{PL} that were derived in the global fits of the LPL model (last Row of Table 5.2.2) sum up to $3.5\,\mathrm{Gy}^{-1}$. This means that the number of DLL and PLL induced at a given radiation dose is only about one tenth of the initial number of DSB. Consequently, the supposed relation between DLL, PLL and DSB must be of a rather complicated nature.

The establishment of a link between DSB and "uncommitted lesions" in the RMR model is less straight forward than in the LPL and GLOBLE model. Uncommitted lesions might represent any uniform kind of radiation-induced damage which does not necessarily include DSB. However, as explained, a negligence of DSB would directly question the concept and therefore, induction rates of U-lesions should not be contradictory to DSB induction rates. In fact, during the previous investigations, the yield of induction of U-lesions (α) was set to the value for DSB induction ($30\,\mathrm{Gy}^{-1}$) in order to reduce the number of free parameter values. It was verified that a relaxation of this parameter does not lead to improvements of the model's accuracy and parsimony in comparison to the other three models. Although the mean values of the four usually employed parameters changed quite strongly (compare $\lambda = 2.45\,\mathrm{h}^{-1}$, $\kappa = 0.91\,\mathrm{h}^{-1}$, (1-$\phi$) = 0.162 and (1-$\delta$) = 0.807 to the average values provided in Table 5.2.2), the fit quality of the model did not improve a lot and therefore, one free parameter less was considered to be beneficial. The mean value of α derived in these global fits with five free parameters was $1.5\,\mathrm{Gy}^{-1}$. Therefore, the shape of U-lesions must be of a quite complex nature such that about 20 DSB correspond to one of them.

Repair of lesions and rejoining of DSB

Another interesting point of discussion is the number of lesion classes with corresponding repair characteristics defined in the four investigated models. The comparison of ten DSB rejoining models (section 3.2) has revealed that different numbers of DSB categories and different modi of rejoining (first- vs. second-order) find a varying relative support by experimental data. A bi-exponential rejoining model was favored compared to a first- and second-order model.

When the repair of abstract lesion classes is carefully related to DSB rejoining, this argues for the GLOBLE model. In the GLOBLE model, there is a bi-phasic repair implied by two classes of lesions (iDSB and cDSB) which are processed independently of each other with two distinct rates.

In contrast, the dynamics RMR and LPL model involve a single lesion class (U-lesions and PLL) undergoing either linear (intra-lesion) or quadratic (inter-lesion) repair processes. In section section 3.2, this first- and second-order repair has been shown to be not supported by observations in DSB rejoining experiments because of three reasons. First, such repair processes do not approximate DSB rejoining data well in comparison to e.g. a bi-exponential approach. Second, it was found that second-order processes dominate over linear processes in the description of DSB rejoining. However, it should be expected that interactions are much less frequent than the restitution of lesions. Third, first- and second-order processes are in conflict with the paradigm that most of the interactions happen at long times after irradiation. In first-second-order model, the large probability for lesions in vicinity implies most interactions directly after the irradiation.

The LC-LQ model in the interpretation of Lea and Catcheside is actually based on similar assumptions about intra- and inter-lesion rejoining as the RMR and LPL model. Therefore, the dynamics in the LC-LQ model are compatible with a first- and second-order approach. However, as explained above, a mechanistic interpretation involving the induction and repair of DSB or of classes of them has not been established. A DSB-related explanation of shapes of cell survival curves is hardly feasible and a link to DSB rejoining experiments is hard to find. Consequently, the LC-LQ model will be excluded in the subsequent discussion.

After all, it is not DSB rejoining that should be described with the four investigated models but cell survival probabilities. With regard to the good performance of the LPL model in the investigations above, this model obviously compensates potential drawbacks in the repair of lesions with assumptions about their induction and lethalities.

In fact, a comparison of parameter values derived in the investigation of DSB rejoining curves (Table 5.1.1) to parameter values derived from dose-rate experiments (Table 5.2.2) reveals that DSB rejoining can indeed not fully be equated with lesion repair. The mean linear repair rate found with the RMR and LPL model is $3.77\,\mathrm{h}^{-1}$ and $3.08\,\mathrm{h}^{-1}$, respectively, whereas the median linear repair rate found with the first-second-order model for DSB rejoining (photon radiation) is usually not significantly different from zero. Furthermore, the quadratic rates in the two survival models are distinctively lower than the corresponding rate in the DSB rejoining approach (compare $\kappa = 0.416\,\mathrm{h}^{-1}$ and $\epsilon_{2PL} = 0.306\,\mathrm{h}^{-1}$ to $k_2 = 1.78\,\mathrm{h}^{-1}$). Thus, the rates derived with the RMR and LPL model for first- and second-order processes in survival experiments do not contradict the hypothesis that intra-lesion repair should typically dominate the dynamics after irradiation. Only the disagreement with the paradigm that interactions should mainly happen in the long time range remains.

The average half-life time of iDSB in the GLOBLE model ($HLT_i = 1.085\,\mathrm{h}$) is distinctively higher than the median value found for the fast component of a bi-exponential DSB rejoining in photon experiments (0.21 h). Under the hypothesis that iDSB reflect a fraction of quickly rejoined DSB this suggests that repair processes in the GLOBLE model are not finished when ends of a DSB are joined. One might speculate that the site of a just removed damage remains prone to damage enhancement for a longer time e.g. as long as it takes to remove proteins. In other words, the GLOBLE suggests that the time scale where lesions have an impact on cell

survival probabilities is longer than the life-time of a DSB. Of course, such speculations remain to be proven.

One last point of discussion concerning lesion repair in the four investigated model is the existence of residual damage. Only the LPL model explicitly accounts for lesions that do not vanish in the course of time in terms of DLL. In the RMR and GLOBLE model, all lesions mathematically disappear the sooner or later and so do PLL in the LPL. However, the existence of DLL in the LPL does not necessarily mean that corresponding biological damage is not processed by a cell in the course of time - it is only implied that it leads to lethal events. Similarly, the repair of U-lesions, iDSB, cDSB and PLL is not in conflict with e.g. residual DSB. Damage fixations might be considered as lethal events and thus, corresponding lesions are not counted as U-lesions, PLL, iDSB or cDSB any longer. The fractions of U-lesions, PLL, iDSB or cDSB that actually correspond to residual damage are not defined in the models and therefore, a validation or falsification by comparison with experimentally measured residual damage is not feasible.

Temporal development of the dose-rate effect

After having discussed the induction and repair of lesions in the four investigated models, the question about corresponding implications on the time scale of dose-rate effects observed in cell survival probabilities needs to be answered. Actually, it has been remarked in the visual inspection of the model fits that all of the approaches evenly describe the increase of cell survival probabilities with a decrease of the dose-rate (section 3.3.3.1). No matter if the individual dose-rate-specific curves were reproduced better (LC-LQ, LPL and GLOBLE model) or worse (RMR model), the temporal course of the dose-rate effect seemed to be comparable.

In fact, there is a mathematical explanation for this observation. In the LC-LQ model, an increase of cell survival probabilities is achieved by a decrease of the quadratic component. The full value of β derived for instantaneous irradiation is effectively lowered according to the dose-protraction factor G (equation 2.4.4) until only the linear component of the model remains at very low dose-rates (large protraction times). In the RMR, LPL and GLOBLE model, the decrease of the quadratic bending of corresponding survival curves dominates over changes in higher-orders of the dose when dose-rates are lowered at sufficiently low doses. Actually, it could be proven [73][74] that the G-factor and its equivalents in the RMR (x = RMR) and LPL (x = LPL) model

$$G_x(T) = \frac{1}{2\beta_x}\frac{d^2(-\ln(S))}{dD^2}(D \to 0) \tag{3.3.5}$$

exactly coincide for $r = \lambda = \epsilon_{PL}$. Similarly, equating $\ln(2)/r$ with HLT_i, it has been shown that the G-factor and its GLOBLE equivalent (x = GLOBLE) deviate less than a few percent over a wide range of lethalities (ϵ_i and ϵ_c) which is usually not exceeded in cell survival experiments [63]. Figure 3.3.5 illustrates that no difference can be noticed when the G-factor is plotted together with the corresponding formulations of the RMR, LPL and GLOBLE model.

The fact that all of the four models mainly reproduce dose-rate effects by a reduction of the quadratic component of dose-effect curves theoretically implies shortcomings when radiosensitive cell lines with a small bending of acute survival curves exhibit a strong dose-rate effect. In practice, the visual inspection of fits of the LC-LQ, RMR, LPL and GLOBLE model to such dose-rate experiments (section 3.3.3.1) revealed that only the LC-LQ and GLOBLE model show

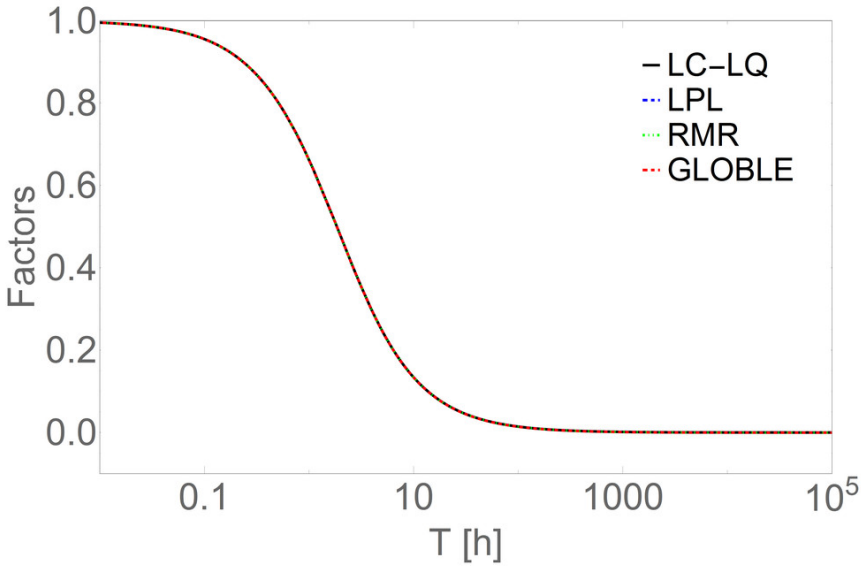

Figure 3.3.5: Comparison of the G-factor and its equivalents from the RMR, LPL and GLOBLE model. No difference is noticeable. For the derivation of the factor corresponding to the GLOBLE model, ϵ_i was set to 0.01 and ϵ_c to 0.35. For a wide range of these two lethalities, the same time-dependence is produced, though.

systematic deviations from the data (Figure 3.3.3). In order to capture the increase of cell survival probabilities with a decrease of the dose-rate, the two models predict an over-pronounced curvature for actually linear high-dose-rate effect curves in a relatively wide range of doses. This curvature then carries a potential for a straightening when the dose-rate is lowered. In contrast, the RMR and LPL model produce acute dose effect curves with a relatively strong initial bending confined to very low doses and a subsequent quick flattening. Thus, they approximate most of the data points accurately. Obviously, the fourth free parameter in the RMR and LPL model provides an advantage in comparison to the LC-LQ and GLOBLE model in this special case.

Relationships to the Linear-Quadratic model

Having asserted that the G-factor and its equivalents in the RMR, LPL and GLOBLE model coincide for sufficiently low doses, the demonstration of other similarities between the LC-LQ approach and the other ones might help to understand plausible reasons for a conformity or divergence in predictions. Furthermore, since linear-quadratic parameters are often used to characterize radiation responses, equivalent expressions derived from the RMR, LPL and GLOBLE model are of interest.

The LQ parameter α describes the linear slope of cell survival curves for dose $D \to 0$ (on a negative logarithmic scale). In [73][74][8] it has been shown that corresponding expressions in the RMR, LPL and GLOBLE model are:

$$\begin{aligned} \alpha_{RMR} &= \tilde{\alpha}(1-\phi) \\ \alpha_{LPL} &= \eta_L \\ \alpha_{GLOBLE} &= \alpha_{DSB}\epsilon_i. \end{aligned} \tag{3.3.6}$$

In the definition of α_{RMR}, the original lesion yield α of the model is confusable with the LQ parameter and consequently was substituted with $\tilde{\alpha}$ here and in the following.

Despite of different definitions of lesion classes and lethalities in the four models, the initial slope of cell survival curves has a common trait: it reflects the least amount of lethal damage inducible per unit of dose. When doses are protracted over long times, all of the four approaches assume that there is no temporal and spatial coexistence of multiple lesions and that a dose-dependent enhancement of the radiation effect by interactions (LC-LQ, RMR and LPL model) or cDSB (GLOBLE model) cannot occur. Consequently, corresponding cell survival curves are linear on a logarithmic scale with slopes equivalent to the LQ parameter α.

In the LQ and RMR model, α and α_{RMR} might be interpreted as the number of lethal intra-lesion repair processes. Since intra-lesion repair never leads to a lethal event in the LPL model, α_{LPL} reflects only the number of DLL. In the GLOBLE model, α_{GLOBLE} is the number of iDSB leading to lethal events when all of the α_{DSB} induced DSB per unit of dose actually are iDSB.

The LQ parameter β defines the quadratic component of acute dose-effect curves (half of the second derivative with respect to the dose) for $D \to 0$. Its equivalents in the RMR, LPL and GLOBLE model are [73][74][8]:

$$\begin{aligned} \beta_{RMR} &= \frac{\tilde{\alpha}^2 \kappa}{2\lambda}(\phi - \delta) \\ \beta_{LPL} &= \frac{\eta_{PL}^2 \epsilon_{2PL}}{2\epsilon_{PL}} \\ \beta_{GLOBLE} &= \frac{\alpha_{DSB}^2}{2N_L}(\epsilon_c - 2\epsilon_i). \end{aligned} \tag{3.3.7}$$

Comparably, the LQ, RMR and LPL model define the quadratic component as the yield of pairwise induced lesions that interact and lead to a lethal event. Whereas β is comprehensive, the pairwise yield of coexistent lesions are represented by $\tilde{\alpha}^2$ and η_{PL}^2 in the RMR and LPL model. The relative fractions of interactions compared to linear repair are κ/λ and $\epsilon_{2PL}/\epsilon_{PL}$, respectively. In the LPL model these interactions fully enhance the radiation effect with a lethality of 1 compared to the lethality of 0 for intra-lesion repair. In the RMR model the interactions enhance the radiation effect with $\phi - \delta$. Finally, in the GLOBLE model such a deduction is less straightforward. However, also in this approach, a pairwise lesion induction yield α_{DSB}^2 and the damage enhancement $\epsilon_c - 2\epsilon_i$ can be found. The pairwise lesion induction yield does not directly refer to iDSB and cDSB but to the underlying biological damage, DSB, though.

The similarities between the four models discussed up to now reason comparable shapes of predicted acute cell survival curves - at least for equivalent parameter values. Differences have to be expected when higher than second-orders in the dose, i.e. the fourth, fifth etc. term of a Taylor expansion around $D = 0$, are analyzed. For the LQ model, there are no higher-order terms - as already stated in the name. Therefore, the slope (first derivative with respect to the dose) of the LQ effect Eff is a linear function with intercept α at $D = 0$ and an increase of 2β per unit of dose. In the RMR, LPL and GLOBLE model, the third-order components of acute dose-effect curves (γ) are negative and flatten out the quadratic bending at higher doses. The three corresponding formalisms are:

$$\gamma_{RMR} = -\frac{\tilde{\alpha}^3 \kappa^2}{3\lambda^2}(\phi - \delta)$$
$$\gamma_{LPL} = -\frac{\eta_{PL}^3 \epsilon_{2PL}^2}{3\epsilon_{PL}^2} \tag{3.3.8}$$
$$\gamma_{GLOBLE} = -\frac{\alpha_{DSB}^3}{6N_L^2}(2\epsilon_c - 3\epsilon_i).$$

In order to visualize the impact of higher-order terms in the RMR, LPL and GLOBLE model, Figure 3.3.6 shows the slopes of acute dose-effect curves predicted with the LC-LQ and GLOBLE model. In contrast to the RMR and LPL model, the GLOBLE model has the same number of free parameters as the LC-LQ model and was therefore used for the demonstration. From the LC-LQ parameter values chosen for the plot ($\alpha = 0.2\,\mathrm{Gy}^{-1}$, $\beta = 0.02\,\mathrm{Gy}^{-2}$ and $r = (\ln(2)/0.5)\,\mathrm{h}^{-1}$), equivalents for the GLOBLE model could be derived ($\epsilon_i = 0.00667$, $\epsilon_c = 0.147$ and $HLT_i = 0.5\,\mathrm{h}$). In fact, the RMR and LPL model behave comparably to the GLOBLE model. However, since the additional free parameter did not allow to find exact equivalences with the LC-LQ model, these models were omitted.

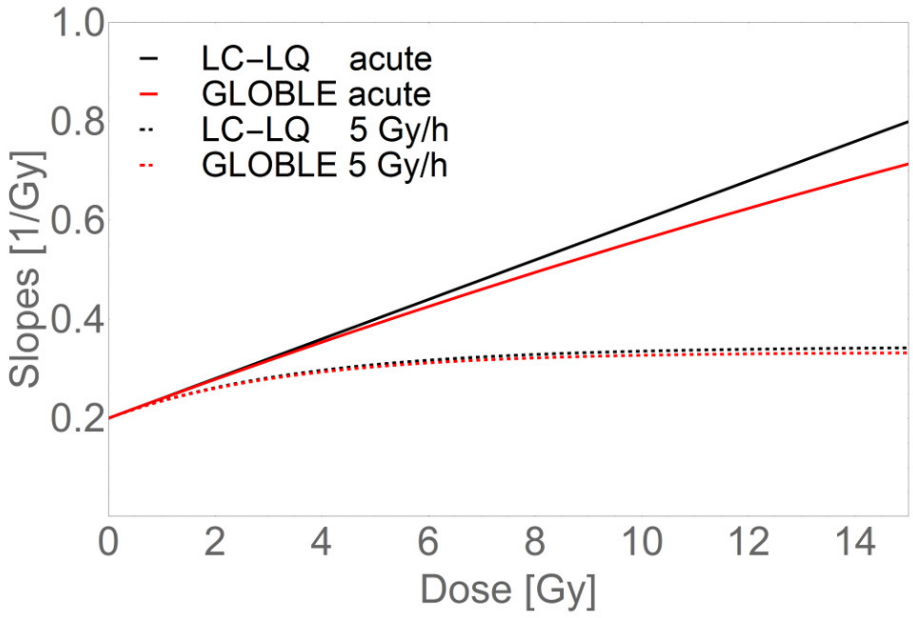

Figure 3.3.6: Comparison of the slopes of effects predicted with the LC-LQ and GLOBLE model with equivalent parameter values ($\alpha = 0.2\,\mathrm{Gy}^{-1}$, $\beta = 0.02\,\mathrm{Gy}^{-2}$, $r = (\ln(2)/0.5)\,\mathrm{h}^{-1}$ and $\epsilon_i = 0.00667$, $\epsilon_c = 0.147$, $HLT_i = 0.5\,\mathrm{h}$). At higher dose-rates, a distinct flattening of effect curves predicted with the GLOBLE model can be noticed whereas this difference to the LC-LQ model diminishes when the dose-rate is lowered.

As Figure 3.3.6 clearly shows, the slope of acute GLOBLE predictions becomes ever smaller than the one corresponding to acute LC-LQ predictions with an increase of the dose. This means a flattening of GLOBLE survival curves at higher doses in comparison to LC-LQ survival curves. Yet, Figure 3.3.6 also demonstrates that the difference between the two models diminishes when the dose-rate is lowered. Due to the reduced quadratic bending of survival curves at lower dose-rates, the deviations observable within the range of doses usually applied in cell

survival experiments become smaller. Actually, this constitutes a drawback for the distinction of kinetic cell survival models. At low dose-rates, clear differences between theoretic model predictions come to bear only at relatively high doses. However, due to extensive irradiation times, experimental low-dose-rate measurements can hardly be executed at such high doses. Consequently, the potential to detect significant differences between kinetic cell survival models on the hand of dose-rate experiments is not as high as for static models and experiments with instantaneous irradiation.

Spatial aspects in the lethality of lesions

The potentially most important difference between the concepts of the LC-LQ, RMR and LPL model on the one hand and the GLOBLE model on the other hand are spatial aspects in the lethality of lesions. In the GLOBLE model, the spatial and temporal coexistence of DSB in a giant loop with defined size is the only criterion for the assignment of a corresponding lethality. A single DSB (iDSB) in a giant loop is directly assigned with a low expected lethality and two or more DSB (cDSB) go in hand with a high lethality. For the derivation of the numbers of iDSB and cDSB, one can potentially employ any radiation quality specific dose distribution (a unification with the conceptually related Local Effect Model for ion radiation needs to be made). Thus, the radiation response predicted with the GLOBLE model is not directly photon-dose-dependent but rather dependent on the corresponding spatio-temporal damage distribution pattern.

The inherent contrast to the LC-LQ, RMR and LPL model is threefold. First, in the LC-LQ, RMR and LPL model, there is no defined volume in which two lesions might lead to a damage enhancement. The three models rather consider lesions "in vicinity" to be candidates for an interaction. Second, even when two lesions occur in vicinity, they might interact or not and thus, their lethality is not defined ex ante. And third, for the derivation of the probability that two lesions occur "in vicinity", one has to assume a Poisson-distributed damage pattern as given after photon radiation. Only when the probability of finding a lesion within a certain volume in the nucleus is homogeneously proportional to the dose, the probability of finding two lesions in vicinity leads to the typical quadratic dose-dependence. Consequently, the severity of a radiation-induced damage pattern is directly dependent on the photon radiation dose in the LC-LQ, RMR and LPL model.

The employment of a Poisson distribution in the LC-LQ, RMR and LPL model leads to drawbacks when these models should be applied in the prediction of cell survival probabilities after high-LET radiation which does not lead to a homogeneous distribution of lesions [72]. Due to the missing link between ab initio characteristics of induced lesions and final lethalities, consistent mechanistic explanations for the increased effectiveness of high-LET radiation are not feasible. Naturally, the three models can be employed to describe high-LET cell survival experiments nevertheless. Tobias et al. [73] suggested a LET-dependence of yields and of misrepair probabilities for U-lesions and Curtis [74] similarly presented an LET-dependent yield for DLL. However, since the values of lesion yields for varying LET and ion species remain unknown without a reference experiment, an extrapolation from one radiation type to another one is difficult.

Contrarily, the GLOBLE model suggests a radiation quality comprehensive applicability in overlap with the LEM. Due to the decisiveness of the spatio-temporal damage pattern for the radiation response, one can use the approach to predict the effectiveness of any radiation modality as long as corresponding dose and DSB distributions are assessable. Only the transfer of the two

lethalities ϵ_i and ϵ_c to the LEM has still to be made. However, already at this stage, the global mechanistic consistency of the GLOBLE/LEM approach with respect to the binary lesion system certainly constitutes its major advantage.

Further model features and credit to other models

In the presented model comparison, the LC-LQ, RMR, LPL and GLOBLE model were only applied for the description of dose-rate experiments. However, they are also apt to predict radiation responses after split-dose exposures or a variety of other radiation schedules. Furthermore, cell survival probabilities were evaluated an infinite amount of time after the (protracted) irradiation in the current study. The assumption that corresponding predictions reflect the cellular response finite times after radiation is justified when the time scale of repair processes is much shorter than the time scale of the cell cycle [72]. Then, the limit of large times represents fully completed repair processes. In contrast to that, the models can moreover be used to predict the usually increased radiation effectiveness when only a part of the induced damage could be repaired. In the original publications of the RMR [73] and LPL [74] model, the effect of lesion fixation at a given time after exposure was explicitly regarded. In the GLOBLE model, lesion fixation can be accounted for by an appropriate evaluation of the differential equations 2.4.11.

Besides, the investigated formulations of the LC-LQ, RMR, LPL and GLOBLE model do not explicitly account for many biological factors that have been shown to have an impact on the radiation response. For instance, all of the employed approaches do not reflect the variation of radiosensitivity in dependence of the cell cycle stage. However, at least for the GLOBLE model, an extension of the static version which includes cell cycle effects has already been proposed [61] and corresponding kinetic formulations will follow.

Furthermore, the explored LC-LQ, RMR, LPL and GLOBLE formalisms do not consider a possible diminution of repair capacities e.g. in terms of a reduction of repair proteins during irradiation. A time-dependent decrease of e.g. repair rates might improve the accuracy of descriptions on the one hand but would lead to more free fit parameters on the other hand. Thus, the benefit of an introduction of saturable repair kinetics at least in the LC-LQ, LPL and GLOBLE model cannot be assessed. Only for the RMR model, a corresponding extension was proposed [73] - without rigorous testing of the accuracy and parsimony, though. Despite from that, there are saturable repair models which explicitly account for such processes [110].

Other models for the prediction of time effects in photon cell survival probabilities that should be named here are the Two-Lesion Kinetic (TLK) model [111] and the generalized LQ (gLQ) model [112]. The TLK model allows to discriminate much more biological endpoints after radiation exposure of a cell than it can explicitly be done with the LC-LQ, RMR, LPL and GLOBLE model. It e.g. accounts for mutations after linear or quadratic repair, for the corresponding fractions of viable and non-viable outcomes, etc. Consequently, the approach features 16 free parameters and its parsimony might be questioned. A large number of free parameters might lead to accurate descriptions of data points but the usually involved high parameter uncertainty does often not allow for distinct statements about the endpoints under investigation. Therefore, and because it would have been hard to argue which of the parameters could be reasonably fixed, the TLK was excluded from the model comparison.

As stated in the name, the gLQ model is a modification of the LQ model which compensates for shortcomings at higher doses. Although the authors provide a mechanistic interpretation for their approach, the biological adequacy remains questionable. Especially the claim that SSB

were sublethal and DSB lethal lesions is questionable and corresponding lesion yields are not in agreement with experimental observations. Franken and Barendsen addressed this issue in a note [113]. Consequently, the gLQ was not included in the current study.

Last but not least, especially with respect to the above stated global applicability of the GLOBLE/LEM approach, the Microdosimetric-Kinetic Model (MKM) should be honored [114]. Comparable to the LEM at the GSI, it was introduced in Japan for ion radiotherapy treatment planning. It also allows to assess the radiation response for varying radiation modalities and the kinetic properties were re-analyzed recently [115].

3.3.5 Conclusion

In this study, the Linear-Quadratic model with Lea-Catcheside formalism, the Repair Misrepair model, the Lethal Potentially Lethal model and the Giant Loop Binary Lesion model have been compared quantitatively and qualitatively. On the hand of eight quantitative benchmarks derived after fits to 13 dose-rate experiments, it was revealed that the LC-LQ, LPL and GLOBLE model perform comparably in most of the cases. The RMR model is significantly worse with respect to all investigated endpoints. Small advantages for the RMR and LPL model can only be noticed in the description of radiosensitive cell lines which exhibit dose-rate effects. However, with regard to the highest probability for interactions of lesions directly after irradiation, the RMR and LPL concept of lesion repair might be less supported by experimental observations than the bi-phasic repair in the GLOBLE model.

In general, the finding of the comparison of DSB rejoining models that a bi-exponential approach has a higher support by measurements than a first-second-order approach has no noticeable impact on the relative performance of e.g. the GLOBLE model in comparison to the LPL model. Obviously, potential deficiencies in assumptions about lesion repair can be compensated by appropriate assumptions about lesion induction and lethalities.

Finally, in the qualitative comparison of the four investigated models, many similarities were highlighted. However, the GLOBLE model crucially distinguishes from the other approaches in terms of its universal applicability. Since the cellular radiation response depends on the spatio-temporal damage distribution pattern rather than on the photon dose, the GLOBLE model can theoretically be used to predict radiation effects after exposure to any radiation quality in connection with the LEM. Based on the concept of the kinetic extension of the GLOBLE model, the introduction of temporal aspects in the LEM code is therefore of note.

3.4 Dynamic extension of the Local Effect Model

3.4.1 Motivation

The Local Effect Model (LEM) [1][2][3][4][5][6][7] has turned out to be a powerful tool for the prediction of the cellular response after ion irradiation. Especially for the purpose of heavy ion treatment planning, the LEM is recognized for its predictions of the RBE. In its current version, the LEM is applicable for instantaneous radiation exposures. However, there is a recent trend for hypofractionated treatments in clinical practice [19][23]. During such treatments, relatively large doses are applied in each session and the patient is carefully re-positioned when the radiation fields are applied from different angles. These procedures alone are already time-consuming. Additional respiratory gating techniques [116] which mitigate undesired effects due to breathing movements even prolong the total irradiation time including the breaks in a session. Having in mind that cellular time-dose effects come into action when photon dose-protraction times or the time between split photon doses are larger than about 15 min, one should expect that time effects also affect hypofractionated heavy ion radiotherapy [115]. Consequently, it might be recommendable that predicted RBE do not only reflect dose- and LET-dependencies but rough radiation schedules as well.

Next to the radiotherapy community, the radiation protection community has an interest in predictions of time-dose-LET effects related to heavy ion exposures. However, the doses and dose-rates usually considered in this context are in a different order of magnitude, as motivated in section 2.1.3. For instance, for the protection of astronauts in outer space, it is asked whether it is justified to assign a decreased radiation effectiveness to heavy ions occurring with low dose-rate in galactic cosmic rays (GCR). Commissions for radiation protection as the ICRP [117][118] or BEIR [119] recommend universal dose and dose-rate effectiveness factors (DDREF) of 2 and 1.5, respectively, to extrapolate from high-dose and dose-rate data to low-dose and dose-rate responses. Although the DDREF refers to cancer induction and has mainly been derived with photon radiation data, a comparison with the decrease in radiation effectiveness predicted for ion radiation and cell survival probabilities might be instructive.

Having the challenges in radiotherapy and radiation protection in mind, there is a high demand for the introduction of an adequate model for the calculation of time-dose-LET effects in the cellular response to ion radiation. Since the experimental and clinical experience with ion radiation is much smaller than for photon radiation, extrapolating model predictions might be extremely useful. It has been shown that the dynamic extension of the Giant Loop Binary Lesion (GLOBLE) model for photon radiation accurately describes time-dose effects in cell survival probabilities, also in comparison to other available kinetic cell survival models. Due to the same mechanistically plausible concept for radiation action, a corresponding extension of the LEM seems promising.

In the following, the dynamic extension of the LEM will be introduced. It will be used to assess time-dose-LET-dependencies in cell survival probabilities and thus answer the questions when and in what extent reductions of the ion radiation effectiveness should be expected. The impact of these findings on heavy ion radiation therapy and radiation protection in outer space will be discussed. All the findings will be published in [120].

3.4.2 Materials and methods

3.4.2.1 Implementation of the dynamic extension

In order to calculate the effect of protracted or fractionated ion radiation doses, the static version of the LEM code as described in section 2.3.3 underwent three main changes: first, the simulation of the damage induction was modified, second, the repair of lesions was included and third, the counting of iDSB and cDSB was adjusted. Since all of the steps prior to the actual simulation basically remained the same, that is the upper two Panels in Figure 2.3.7 (section 2.3.3), the following explanation will start with the simulation for each hit class. As a short reminder, since the radiation response of a cell often depends crucially on the number of ions traversing it, radiation effects are simulated separately for each plausible number of direct ion hits, denominated as hit classes, in the LEM. The expected response of a cell population is finally calculated as weighted mean of the hit class responses.

For the simulation of damage induction after instantaneous irradiation in the LEM code, a random number of ions indirectly hitting a cellular nucleus is drawn for each hit class (step i) in section 2.3.3.3). For each of the directly and indirectly hitting ions, a realization of the distribution of initial DSB within its track is drawn and each ion is assigned with a random position in or around the cellular nucleus - as defined in steps ii) and iii) in section 2.3.3.3. The resulting total spatial DSB distribution pattern can then be evaluated. However, when ion doses are protracted or fractionated, the considered ions do not hit the cellular nucleus simultaneously but approximately uniformly distributed over the irradiation time or the fractions. For a protracted dose this is between time 0 and T and for a x-times fractionated dose this is within the x dose applications which might be arbitrarily short. Correspondingly, in the extended LEM code, each considered ion is not only assigned with a random DSB distribution pattern and position but also with a random "hit time". The "hit time" of an ion directly implies the induction time of the associated initial DSB. Each initial DSB thus features a spatial and temporal position. For all further considerations, the DSB are ordered with respect to their induction time.

With regard to the counting of DSB which spatially and temporarily coexist in a domain (comparable to step iv) in section 2.3.3.3), the locations and induction times of the initial DSB do not provide sufficient information. In order to detect temporal overlaps, one additionally has to know the life span of each DSB. Corresponding assumptions about cellular repair were adopted from the concept of the kinetic GLOBLE model (section 2.4.3). According to that, the life span of iDSB follows an exponential distribution with a relatively short half-life time HLT_i. In contrast to that, the exponential distribution of life spans of cDSB is characterized by a long half-life time HLT_c. The value of HLT_c will be fixed to 5 h in the following, in agreement with previous investigations.

In the modified LEM code, each initial DSB is first considered as an iDSB and is assigned with a random life span drawn from an exponential distribution with mean value HLT_i. Thus, the temporarily ordered iDSB induced sometime in a given domain can be compared with respect to their temporal overlap between induction and end of repair. When a temporal coexistence of two subsequent iDSB in a domain is detected, they are unified and scored as one cDSB and a new random life time is drawn - this time from an exponential distribution with mean value HLT_c. The induction time of this cDSB is defined by the induction time of the second iDSB. Every further iDSB joining an already existent cluster does not change the induction time or life

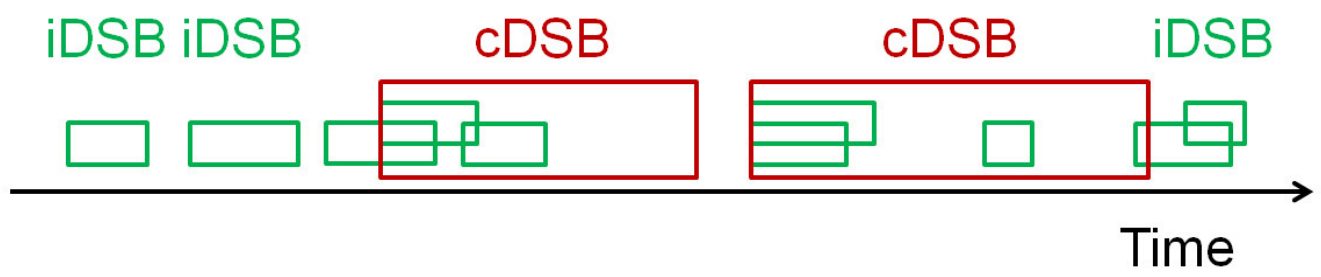

Figure 3.4.1: Example for the scoring of iDSB and cDSB in a given domain. As soon as two iDSB along the time axis overlap, they initiate a new cDSB. The induction time of the cDSB corresponds to the induction time of the second iDSB and its life span is drawn from an exponential distribution with mean HLT_c. The induction of further iDSB during the occurrence of a cDSB does not change the characteristics of the cDSB. Only after a cDSB has been repaired, new iDSB or cDSB might be detected in the domain. The elevation of some iDSB in the illustration is for the sake of visibility.

time of the cDSB, it is just deleted from the list of iDSB. After testing all possible spatial and temporal overlaps of DSB, the numbers of iDSB and cDSB simulated in the given run are found. Figure 3.4.1 gives an example for the scoring of iDSB and cDSB in a considered domain.

Due to the distinct impact of the numbers of iDSB and cDSB on cell survival probabilities in the LEM, the abort criterion for the simulation of each hit class was adapted in the dynamic extension of the LEM. For every hit class, the simulations are now repeated until required accuracies in the numbers of iDSB and cDSB are reached and not until a required accuracy in the effect is reached.

In summary, in the kinetic version of the LEM, the following steps are executed for each hit class until the required accuracies in the numbers of iDSB and cDSB are reached:

(i) A random number of indirectly hitting ions is drawn from a Poisson distribution (indirect hits).

(ii) Each ion (direct and indirect hits) is assigned with a random spatial DSB distribution pattern.

(iii) Each ion is assigned with a random position in (direct hits) or outside (indirect hits) the nucleus and the positions of the DSB are moved accordingly.

(iv) Each ion is assigned with a random "hit time" which defines the induction time of associated initial DSB. The initial DSB are ordered with respect to their induction time.

(v) Each initial DSB is assigned with a random short life span.

(vi) The temporal overlap of DSB is tested in each domain. In case that two subsequent initial DSB coexist, they are scored as one cDSB and a corresponding random long life span is drawn. The induction time of the cDSB is equated with the induction time of the second initial DSB. Each further initial DSB joining the cluster is only deleted from the list of iDSB.

(vii) The resulting numbers of iDSB and cDSB are scored.

Changes in comparison to the list presented in section 2.3.3.3 are highlighted in red.

3.4.2.2 Assessment of dose-rate effects for ion radiation

For the assessment of dose-rate effects associated with ion radiation, predicted effects Eff for protracted irradiation (from time 0 to T) were compared to those predicted for instantaneous

irradiation. In particular, with the dose-rate $\dot{D} = D/T$, relative changes in the effect were defined as:

$$\Delta Eff = \frac{Eff(\dot{D}_{low}) - Eff(\dot{D}_{high})}{Eff(\dot{D}_{high})}. \tag{3.4.1}$$

In order to investigate the changes in the effect in dependence of single impacting parameters while keeping all of the other parameters fixed, the following standard setting was defined:

Ion species	^{12}C.
Dose	5 Gy.
High dose-rate	10000 Gy/h.
Low dose-rate	0.0001 Gy/h.
HLT_i	0.5 h.
HLT_c	5 h.
α	0.1 Gy^{-1} or 0.5 Gy^{-1}.
β	0.05 Gy^{-2}.
D_t	8 Gy or 14 Gy.

The ion species ^{12}C was chosen for the study due to its relevance in heavy ion treatments and 5 Gy were considered to be high enough to detect possible dose-rate effects even when survival curves feature little bendings. The high and low dose-rates will be used as an approximation for limiting cases (instantaneous irradiation and infinite protraction) only. Furthermore, the half-life times of iDSB and cDSB were fixed according to values applicable for photon radiation and the linear-quadratic-linear (LQL) parameters α, β and D_t should cover a wide range of radiosensitivities.

3.4.2.3 Comparison to experimental data

In order to verify that the dynamic extension of the LEM adequately describes observed time-dose effects in exposures to ion radiation, experimental data requiring for the usage of kinetic ion cell survival models were searched for. Regrettably, there are only few experiments investigating time-dose-LET effects in literature, as it will be discussed in section 3.4.4.3. However, one excellent experiment was published by Inaniwa et al. [115] and was used for a performance test of the LEM, consequently. In a split-dose experiment, the authors measured survival probabilities of the HSG cell line after irradiation with two times 2.5 Gy ^{12}C radiation with an energy of 290 MeV/u in dependence of the separation time T_{sep}. Unfortunately, no simultaneous experiment was conducted with photon radiation [121] and the spread of reported linear-quadratic parameter values (α, β) for HSG cells is relatively large. Values of α range from 0.19 Gy^{-1} [122][123] to 0.313 Gy^{-1} [56] and β ranges from 0.044 Gy^{-2} [124] to 0.0615 Gy^{-2} [56].

Therefore, in a first step, the half-life time of iDSB (HLT_i) needed as an input for the LEM was derived based on the following consideration. It will be shown below that the temporal aspects in the cellular response to ion and photon radiation are governed by HLT_i alone and not by the radiation characteristics (section 3.4.3.1). Consequently, as a good approximation and in accordance with the linear-quadratic parametrization of the photon response in the LEM, the linear-quadratic model with Lea-Catcheside formalism (equation 2.4.6) was fitted to the

split-dose data. By equating HLT_i with $\ln(2)/r$, a value of 0.17 h was found. Then, with this value for HLT_i and a half-life time of 5 h for cDSB, LEM survival probabilities were calculated for the experimental radiation settings and for varying combinations of α and β in the range of plausible values. In the range between 0.19 Gy^{-1} and 0.32 Gy^{-1}, α was evaluated in steps of 0.01 Gy^{-1} and in the range between 0.04 Gy^{-2} and 0.065 Gy^{-2}, β was evaluated in steps of 0.005 Gy^{-2}. The required input value D_t was always derived from α and β with the empirical formula $D_t = 4 + 1.1\alpha/\beta$ [44]. After having found LEM predictions of survival probabilities for various combinations of α and β, the corresponding chi-squared value X^2 with respect to the measured data was computed. The smallest value of the derived X^2 was taken as an indicator for the appropriate combination of α and β.

3.4.3 Results

The dynamic extension of the LEM provides predictions of the existence and extent of time-dose-LET effects in ion radiation on the one hand and the framework for the mechanistic interpretation of these findings on the other hand. To clearly structure various computational results and common mechanistic explanations, only quantitative aspects of LEM predictions will be presented in this result section. The reasons for the observations will be explained in the discussion together with a critical acclaim of the LEM concept (sections 3.4.4.1 and 3.4.4.2).

3.4.3.1 Impact of the protraction time

With the dose-protraction factor G for photon radiation in mind (section 2.4.2), one intuitive way to assess the existence and extent of ion dose-rate effects is the investigation of the impact of protraction times. For the standard setting defined above, relative changes of the ion effect ΔEff were computed in dependence of protraction times T between 0.001 h and 10^5 h. As a reference for acute irradiation, $T_{short} = 0.0005$ h was taken, in agreement with $\dot{D}_{high} =$ 10000 Gy/h and a total dose of 5 Gy. Panels A and B in Figure 3.4.2 illustrate the results for a variation of the LET between 25 keV/μm and 100 keV/μm. To allow for a comparison of responses corresponding to different cellular radiosensitivities, Panel A shows the results for α = 0.1 Gy^{-1}, β = 0.05 Gy^{-2}, D_t = 8 Gy and Panel B for α = 0.5 Gy^{-1}, β = 0.05 Gy^{-2}, D_t = 14 Gy.

Obviously, dose-rate effects inherent to 5 Gy ^{12}C radiation become observable below a LET of about 100 keV/μm. The extent of relative changes of the effect becomes stronger with a decrease of the LET. For example, the maximum reduction of the radiation effect is about 20% for 50 keV/μm whereas it is over 50% for 25 keV/μm for the abstract cell line with α/β = 2 Gy (Panel A). Furthermore, the extent of the reduction of the radiation effectiveness depends on the LQL parameters characterizing the investigated cell line. For the abstract cell line with α/β = 10 Gy, the the maximum reduction of the radiation effect for 25 keV/μm is only about 25% (Panel B).

However, the general sigmoid shape of the decrease of the radiation effectiveness with an increase of the protraction time always remains the same. When ΔEff corresponding to 5 Gy photon radiation (predicted with the LC-LQ model with equal values of α and β and r = $(\ln(2)/0.5)\,h^{-1}$) is plotted for the sake of comparison as a black line in Figure 3.4.2A and B, one observes a distinct agreement with ion radiation. Only the extent of the reduction of radiation effectiveness is higher for photon than for ion radiation. Panels C and D in Figure 3.4.2

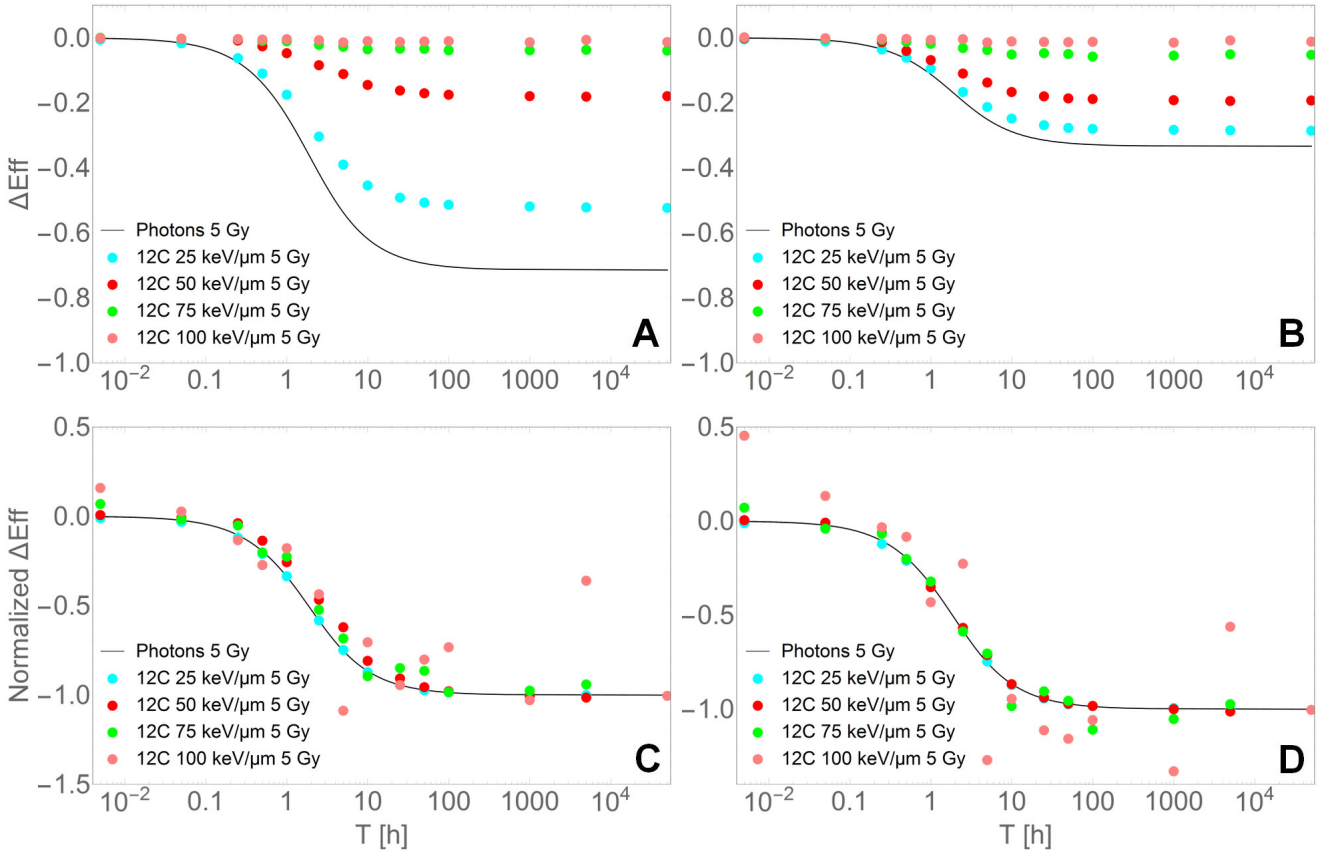

Figure 3.4.2: Relative change of the radiation effect ΔEff predicted for 5 Gy ^{12}C radiation with varying LET in dependence of the protraction time T of the dose. The abstract cell line in Panels A and C is characterized by α/β = 2 Gy and in Panels B and D by α/β = 10 Gy. In Panels A and B, the original LEM predictions of ΔEff are plotted. In Panels C and D these predictions are normalized by the maximum reduction of the radiation effect seen for each LET in Panels A and B. In all Panels, a LC-LQ prediction of ΔEff for photon radiation with equal biological parameter values and dose are shown for the sake of comparison.

verify the finding that the shape of the reduction of radiation effectiveness is independent of the radiation quality. When all analytically calculated and simulated curves are normalized with the maximum reduction of the radiation effect, they overlap. Only for the curves corresponding to 100 keV/μm, the fluctuations of simulated data points are in a comparable order of magnitude as ΔEff and therefore, no agreement with the other curves can be detected. In conclusion, for a sufficiently low LET, the shape of the protraction-time-dependent reduction of the radiation effectiveness is independent of the radiation quality and of the LQL parameters of the cell line. Only the order of magnitude of relative changes of the effectiveness is impacted by these two determinants. For a better resolution, the dependence of ΔEff on the LET and LQL parameters will be explicitly investigated two sections below. In the next section, the range of protraction times where the incremental decrease of ion radiation effects is the strongest will be explored.

3.4.3.2 Impact of the short half-life time

Since the shape of the dose-protraction factor G for photon radiation depends on the rate of linear repair r and since it has been shown that this rate is equivalent to $\ln(2)/HLT_i$ (section 3.3.4.3), it might be suggested that the decrease of the ion radiation effectiveness with an increase of the protraction time depends on HLT_i. To verify this hypothesis, relative changes of the effect were simulated for varying HLT_i and for protraction times T between 0.001 h and 10^5 h, keeping the rest of the parameters fixed as defined in the standard setting. The LET of the ^{12}C radiation was chosen to be 25 keV/μm.

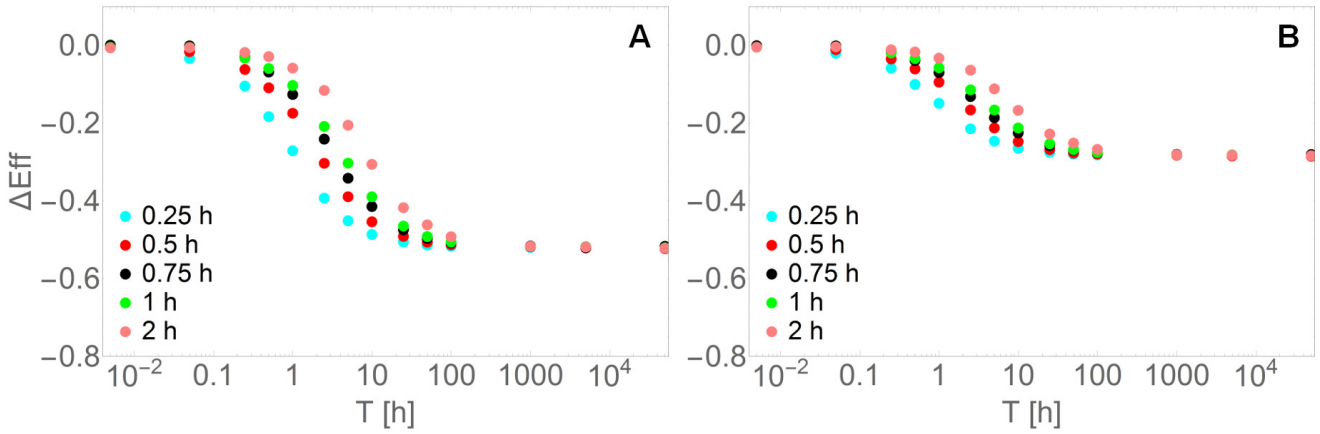

Figure 3.4.3: Relative change of the radiation effect ΔEff predicted for 5 Gy ^{12}C radiation with 25 keV/μm in dependence of the protraction time T of the dose. The individual curves are characterized by varying values of the half-life time of iDSB, HLT_i. The abstract cell line in Panel A is characterized by α/β = 2 Gy and in Panel B by α/β = 10 Gy.

The results shown in Figure 3.4.3 confirm the impact of HLT_i on the range of protraction times where the transition from maximum to minimum radiation effectiveness happens. Moreover, by comparison of Panel A and B in Figure 3.4.3 it is confirmed that the maximum reduction of the radiation effectiveness is only implied by the cellular parameters α and β and not by HLT_i. A section in the discussion (3.4.4.1) will be dedicated to the mechanistic explanation of these findings.

3.4.3.3 Impact of the LET

After having noticed that the existence and extent of an ion dose-rate effect depends crucially on the LET of the radiation, the corresponding relationship was explicitly investigated. For the standard settings defined above, ΔEff was computed in dependence of the LET between 10 keV/μm and 300 keV/μm. Figure 3.4.4 illustrates the results found for variations of the low dose-rate that was compared to the high dose-rate $\dot{D}_{high} = 10000$ Gy/h. Again, the simulations were executed for the two abstract cell lines with $\alpha/\beta = 2$ Gy (Panel A) and $\alpha/\beta = 10$ Gy (Panel B).

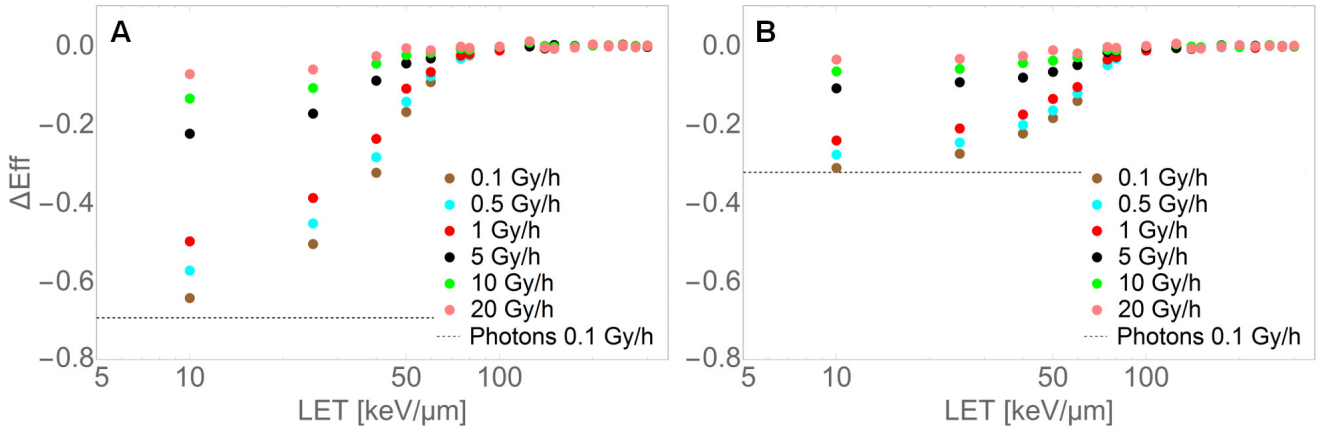

Figure 3.4.4: Relative change of the radiation effect ΔEff predicted for 5 Gy ^{12}C radiation and varying dose-rates in dependence of the LET. The abstract cell line in Panel A is characterized by α/β = 2 Gy and in Panel B by α/β = 10 Gy. Corresponding LC-LQ predictions of ΔEff for 5 Gy photon radiation applied with 0.1 Gy/h are shown for the sake of comparison.

As Figure 3.4.4 demonstrates, no dose-rate effects should be expected for 5 Gy ^{12}C radiation when the LET is roughly above 100 keV/μm. With a decrease of the LET, the radiation effectiveness generally decreases. However, there are two factors that distinctly impact the curves shown in Figure 3.4.4. First, the extent of the reduction of the radiation effectiveness at a given LET depends on the dose-rate. For the abstract cell line with $\alpha/\beta = 2$ Gy (Panel A) and a LET of 10 keV/μm, one might compare 15% to 65% for dose applications with $\dot{D}_{low} = 10$ Gy/h and $\dot{D}_{low} = 0.1$ Gy/h, respectively. This finding is in agreement with the observations presented in the previous section. Second, ΔEff is again dependent on the LQL parameters of a cell line. For $LET = 10$ keV/μm and $\dot{D}_{low} = 0.1$ Gy/h, the abstract cell line with $\alpha/\beta = 10$ Gy (Panel B) features a reduction of the radiation effect of only about 30% compared to the 65% detected for the cell line with $\alpha/\beta = 2$ Gy (Panel A).

In order to provide an orientation mark for the maximum decrease of ΔEff when 5 Gy are applied with 0.1 Gy/h, the corresponding relative change in the photon radiation effect is plotted in Figure 3.4.4. The photon predictions in Panels A and B were again determined with the LC-LQ model, with α and β set to the values used for the prediction of the ion response and $r = (\ln(2)/0.5)\,\mathrm{h}^{-1}$. The horizontal lines representing ΔEff for photon radiation are drawn across the whole panels for the sake of visibility and should not indicate any LET-dependence.

Especially in case of the abstract cell line with $\alpha/\beta = 10\,\mathrm{Gy}$, the comparison of the LET-dependence of ΔEff for ion radiation applied with 0.1 Gy/h with ΔEff predicted for photon radiation reveals an asymptotic behavior in the limit of low-LET. This supports the hypothesis that ion radiation effects become more and more similar to photon radiation effects in the limit of low-LET. A section in the discussion (section 3.4.4.2) will be dedicated to this topic.

3.4.3.4 Impact of linear-quadratic-linear parameters

In order to finally provide an overview over the impact of linear-quadratic-linear parameters on relative changes in the radiation effect, as it has already been indicated several times, ΔEff was computed in dependence of the LET between $10\,\mathrm{keV}/\mu\mathrm{m}$ and $300\,\mathrm{keV}/\mu\mathrm{m}$ for varying values of α, β and D_t. Again, the standard setting was used for the fixation of the rest of the factors impacting the radiation response. It should be emphasized that the plotted relative changes of the effect correspond to the maximum relative reductions achievable due to the comparison of acute ($\dot{D}_{high} = 10000\,\mathrm{Gy/h}$) to extremely protracted ($\dot{D}_{low} = 0.0001\,\mathrm{Gy/h}$) doses.

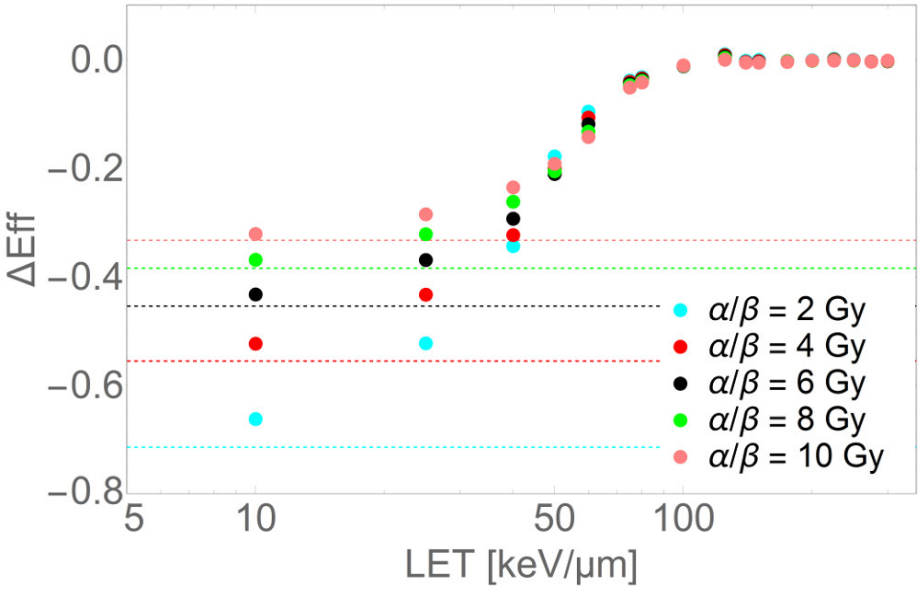

Figure 3.4.5: Relative change of the radiation effect ΔEff predicted for 5 Gy ^{12}C radiation and varying linear-quadratic-linear parameters in dependence of the LET. The absolute parameter values α, β, D_t corresponding to the given values of α/β are: $\{0.1, 0.05, 8\}$, $\{0.2, 0.05, 9.5\}$, $\{0.3, 0.05, 11\}$, $\{0.4, 0.05, 12.5\}$ and $\{0.5, 0.05, 14\}$. For all α/β, LC-LQ predictions of ΔEff for 5 Gy photon radiation are shown for the sake of comparison.

Figure 3.4.5 illustrates that the extent of relative changes in the radiation effectiveness at a given LET is larger for cell lines with a lower α-β-ratio, as it would be expected for photon radiation. The simulations in Figure 3.4.5 confirm that similar considerations seem to be true for ion radiation with sufficiently low LET. For the sake of comparison, ΔEff corresponding to 5 Gy photon radiation (instantaneous compared to extremely protracted irradiation) is plotted for all α-β-combinations in Figure 3.4.5. For the predictions, the LC-LQ model with $r = (\ln(2)/0.5)\,\mathrm{h}^{-1}$ was used. Again, the continuous lines are for the sake of visibility and should

not indicate a LET-dependence. Clearly noticeable, the simulations for ion radiation characterized by a defined α-β-ratio approach ΔEff calculated for corresponding photon irradiations in the limit of low-LET. As stated above, corresponding mechanistic interpretations will be provided in sections 3.4.4.1 and 3.4.4.2.

3.4.3.5 Impact of the ion species

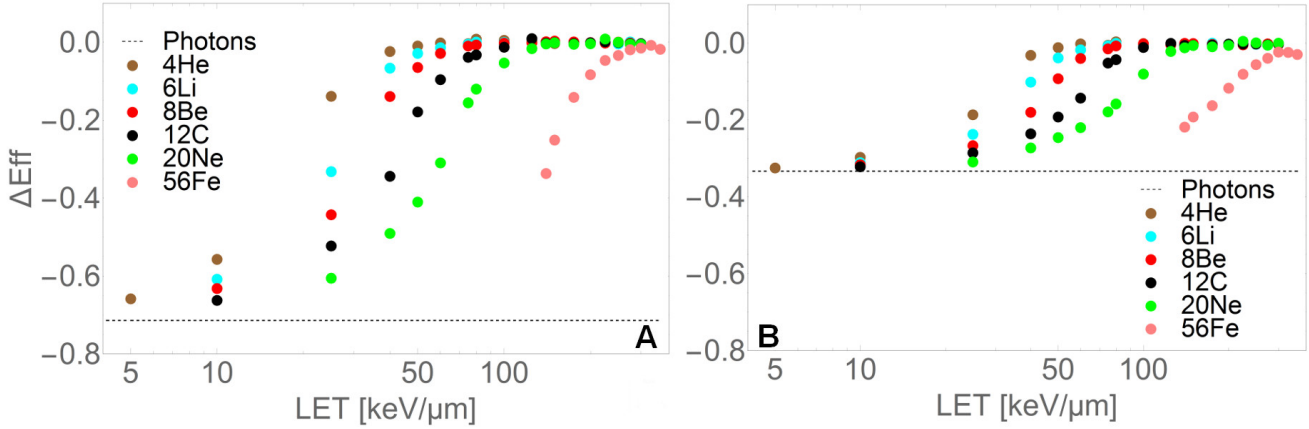

Figure 3.4.6: Relative change of the radiation effect ΔEff predicted for varying ion species in dependence of the LET. For each exposure, the total dose is 5 Gy. The abstract cell line in Panel A is characterized by α/β = 2 Gy and in Panel B by α/β = 10 Gy. LC-LQ predictions of ΔEff for 5 Gy photon irradiation are shown for the sake of comparison in both Panels.

In all of the previous investigations of the LET-dependence of dose-rate effects, carbon ions were used for the computations. However, the combination of ^{12}C and a LET already implies the energy of the particle. For different ion species, the LET-dependence of ΔEff should deviate, consequently. Figure 3.4.6 visualizes the results when the LET-dependence of ΔEff is simulated for varying particle species, keeping the rest of the parameters fixed according to the standard setting. Considering the sigmoid shape of ΔEff plotted over the LET only, the predictions look similar for all ion species: there is an asymptotic approximation of ΔEff to 0 in the limit of high-LET and an asymptotic convergence of ΔEff to the maximum reduction of the radiation effect achievable in the limit of low-LET. The maximum reduction of the radiation effect does not depend on the ion species but only on the LQL parameters of the cell line as a comparison of Panel A and B reveals. This statement is verified by a comparison of the asymptotic behavior of the simulated curves at $LET \rightarrow 0$ with predictions of ΔEff for photon radiation - which supposedly defines the lower boundary. The black lines in Figure 3.4.6 are calculated with the LC-LQ model under usage of α-β-combinations which are equal to those used for the simulations and $r = (\ln(2)/0.5)\,\mathrm{h}^{-1}$.

The range of LET where the transition from no reduction to a maximum reduction of the radiation effect happens shifts with the weight of the considered ion species. When the LET of the radiation is lowered, dose-rate effects have to be expected earlier, at higher LET, when heavier ions are given. Complementary, when the LET is decreased even further, heavier ions approach the maximum reduction of the radiation effectiveness already at higher LET. For ^{20}Ne

it is predicted that changes of the radiation effect occur at a LET lower than about 125 keV/μm whereas for ^{4}He changes should be expected at values lower than about 60 keV/μm. In the discussion (section 3.4.4.2), an explanation for different LET ranges involved in the reduction of the radiation effectiveness of varying particle species will be provided on the hand of track structures.

3.4.3.6 Impact of the dose

Due to the fact that the computations were made with a fixed dose of 5 Gy so far, the impact of dose variations on relative changes of the ion effect will be considered as a complement in the following. Figure 3.4.7 shows the LET-dependence of ΔEff for varying doses. For the computations, the standard setting was employed with $\alpha/\beta = 2$ Gy in Panel A and $\alpha/\beta = 10$ Gy in Panel B. At a given LET, the reduction of the radiation effectiveness obviously increases with the dose. When the abstract cell line with $\alpha/\beta = 2$ Gy is irradiated with 2 Gy of 10 keV/μm carbon ions, the radiation effect is reduced by about 45% when the dose is extremely protracted instead of instantaneously given. In contrast, the corresponding reduction of the radiation effect is about 80% when a dose of 10 Gy is applied.

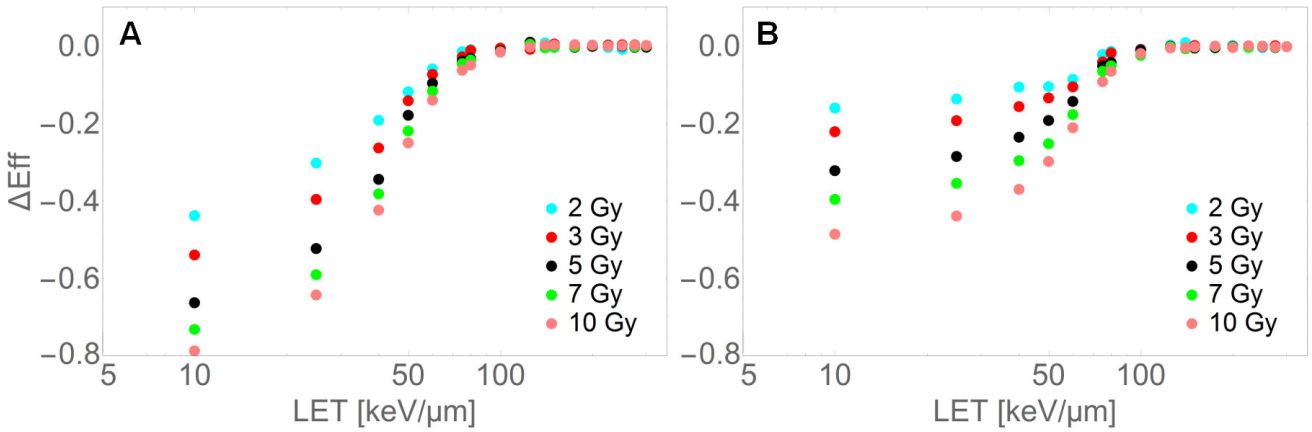

Figure 3.4.7: Relative change of the radiation effect ΔEff predicted for ^{12}C radiation and varying doses in dependence of the LET. The abstract cell line in Panel A is characterized by α/β = 2 Gy and in Panel B by α/β = 10 Gy.

Actually, the dose-dependence of protraction-time-related reductions in the ion radiation effect are of special relevance for radiation protection in outer space. In order to derive an extrapolation from a measured high-dose and high-dose-rate response to a low-dose and low-dose-rate response, one needs appropriate model predictions. In the current study, ΔEff provides a relative measure for the reduction of the radiation effect when high dose-rates ($\dot{D}_{high} = 10000$ Gy/h) are substituted by extremely low dose-rates ($\dot{D}_{low} = 0.0001$ Gy/h). The value ΔEff in the limit of low doses should therefore give insight into the dose- and dose-rate-related reduction of the radiation effectiveness. To investigate this issue, ΔEff was simulated in dependence of the dose between 0.01 Gy and 10 Gy for a selection of ion species and corresponding LET relevant in outer space.

Panels A and B in Figure 3.4.8 demonstrate that based on the assumptions behind the LEM, no reduction of the ion radiation effect should be expected up to doses of about 0.1 Gy for cell lines with low α-β-ratio (Panel A) and up to about 0.25 Gy for cell lines with high α-β-ratio

(Panel B). For further increasing doses, 30 keV/μm ^{16}O radiation entails a stronger reduction of the radiation effectiveness than 30 keV/μm ^{14}N and 30 keV/μm ^{12}C radiation. ^{56}Fe radiation with a LET of 150 keV/μm is linked to comparably low reductions of the radiation effect. The reductions are even hardly noticeable at the just mentioned 0.1 Gy in Panel A and 0.25 Gy in Panel B. Nevertheless, the shape of ΔEff is roughly comparable for all investigated ion species with defined LET.

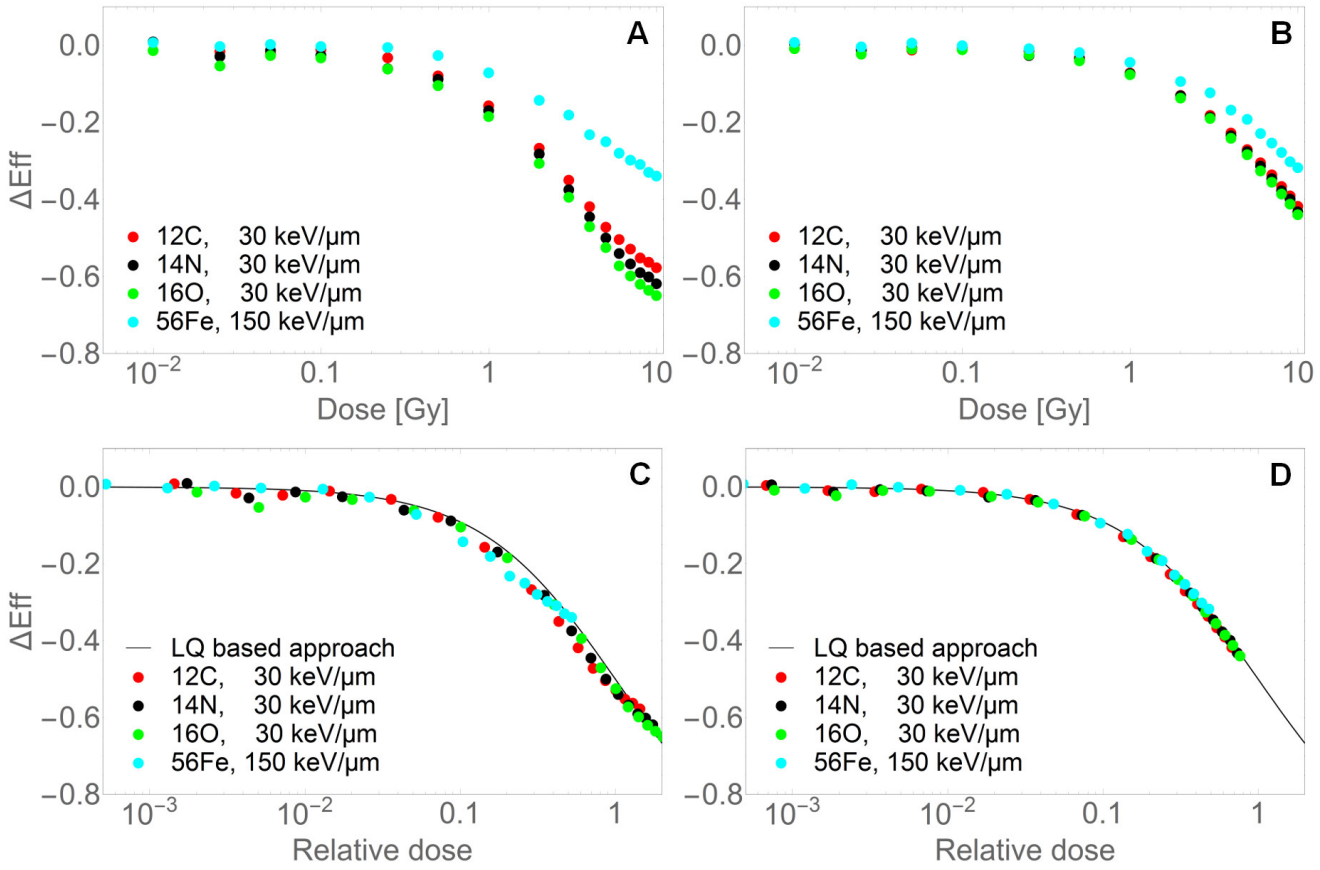

Figure 3.4.8: Relative change of the radiation effect ΔEff for varying ion species and LET. Panels A and B show ΔEff in dependence of the absolute dose. In Panels C and D, the doses of each each ion-specific curve have been normalized with the dose implied by the ratio α_I/β_I which was derived in linear-quadratic-linear fits to the acute ion cell survival curve. A LQ-based approach (black line) describes the dependence of ΔEff on this normalized dose very well (explanation in the text). The abstract cell line in Panel A and C is characterized by α/β = 2 Gy and in Panel B and D by α/β = 10 Gy.

Actually, there is a conceptual reason for the similar shapes of the curves plotted in Figure 3.4.8A and B. In the framework of the Linear-Quadratic model for photon radiation (or LQL model with sufficiently high D_t), one expects that only the linear component of an originally linear-quadratic curve remains after an application of doses with extremely low dose-rates. Consequently, extremely low dose-rates reduce the predicted acute radiation effect by 50% at the dose where the impact of α on the survival curve equals the impact of β. This dose is defined by the α-β-ratio. In fact, when acute cell survival curves are simulated for the given ion species and LET values, and the Linear-Quadratic-Linear model is fitted to them for the derivation of

α_I and β_I, one finds that the curves shown in Figure 3.4.8A cross ΔEff = -50% at the dose α_I/β_I.

This motivated the generation of Panels C and D where ΔEff is not explicitly plotted in dependence of the dose but in dependence of a relative dose D_{rel} normalized by the α_I-β_I ratio derived for each investigated modality. Obviously, on this scale, the simulated data points overlap, indeed. The analytical formulation for the observed dependence can be gained from:

$$\Delta Eff = \frac{\alpha_I D - (\alpha_I D + \beta_I D^2)}{\alpha_I D + \beta_I D^2} = \frac{1}{1 + \frac{\alpha_I}{\beta_I}/D} = \frac{1}{1 + \frac{1}{D_{rel}}}. \tag{3.4.2}$$

This analytical formula for ΔEff was added as a black graph in Figure 3.4.8C and D. The good agreement with the simulations will be discussed below.

3.4.3.7 Description of experimental data

The compatibility of the LEM with measurements that require the usage of a kinetic ion cell survival model was tested by the computation of predictions for a split-dose experiment published by Inaniwa et al. [115]. As explained above, HLT_i = 0.17 h was derived as relevant time parameter and α, β and D_t were chosen in the range of values that are plausible with regard to published studies on HSG cells. It was found that α = 0.25 Gy^{-1}, β = 0.055 Gy^{-2} and D_t = 9 Gy provide the best match of the LEM predictions and the measurements.

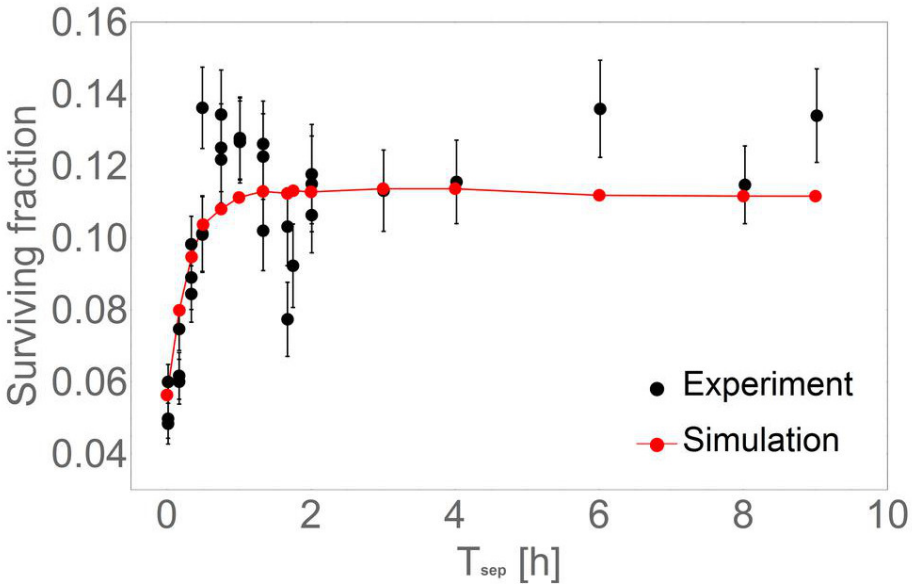

Figure 3.4.9: Comparison of LEM predictions and experimental data. The black points represent cell survival probabilities recorded by Inaniwa et al. in a split-dose experiment with two times 2.5 Gy ^{12}C ion radiation (E = 290 MeV/u) [115]. A corresponding simulation produced with the LEM is shown in red.

Figure 3.4.9 shows the LEM simulations together with the experimental data. Obviously, the good performance of the approach is supported by a visual inspection. The simulations distinctively match the data. One might detect a small underestimation of the maximum survival

probability that is reached in the limit of large separation times where two data points (at T_{sep} = 6 h and T_{sep} = 9 h) are above the simulations. However, these two data points in the long time range have a relatively low weight in comparison to the majority of data points up to T_{sep} = 2 h and therefore, they had only little impact during the derivation of the smallest X^2. Moreover, since a "dip" in the recorded split-dose survival curve is visible, it seems that cell cycle effects biased the results [115]. Since the LEM in its current version does not account for cell cycle dependent radiosensitivities, a slight mismatch might be expected. In conclusion, the slight underestimation of two data points that one finds in a comparison of LEM predictions and experimental observations can be explained and considered to be tolerable. The generally good performance finally argues for the applicability of the model.

3.4.4 Discussion

3.4.4.1 Similarities in the cellular response to ion and photon radiation

In the static version of the Local Effect Model, the relatively large experimental and clinical experience with biological responses to photon radiation is exploited for predictions of ion radiation responses. In fact, the basic assumption that equivalent biological damage patterns should lead to equivalent biological responses has proven to be a powerful tool e.g. for the assessment of the RBE for treatment planning studies. With regard to distinctive features of photon and ion radiation, the LEM suggests that only physical properties in terms of different energy deposition patterns lead to different radiation effects. Cellular characteristics as repair fidelities of iDSB and cDSB are not affected by the type of the exposure.

In this respect, the dynamic extension of the LEM pursues the idea of its parental version. It retains the concept of iDSB and cDSB as the decisive lesion categories for cell survival probabilities and their definition on the hand of the numbers of initial DSB within a giant loop - independent of the radiation quality. However, next to the spatial component, it accounts for a temporal component by assigning half-life times to iDSB and cDSB which can be used to derive life spans of individual lesions and thus to detect temporal coexistences. In agreement with the rest of the LEM concept, these half-life times are independent of the radiation quality and only defined by the repair characteristics of the considered cell line. Consequently, it should not be surprising that those parts of time-dose-LET effects in the cellular response to radiation that are governed by cellular characteristics are comparable for photon and ion radiation in the LEM predictions.

A first example for an agreement of observations for different radiation types was provided in the investigation of the protraction-time-dependence of relative changes of the radiation effect ΔEff. At the given settings (^{12}C, D = 5 Gy, α/β = 2 Gy or 10 Gy) and for $LET < 100\,\mathrm{keV}/\mu\mathrm{m}$, the general sigmoid shape describing the reduction of the radiation effectiveness with an increasing protraction time T is comparable for photon and ion radiation of varying LET (Figure 3.4.2A and B). Concerning photon radiation, the mechanistic reason for this sigmoid shape has already been explained within the framework of the GLOBLE model which is conceptually related to the LEM. Due to the proportionality between the total number of initial DSB and the total applied dose, a protraction of the dose only separates initial DSB in time. On the one hand, in the limit of protraction times that are much shorter than HLT_i, initial lesions are induced at a frequency which is too high to allow for cellular repair in the interim time. Single DSB within

a giant loop cannot be removed before the induction of a next DSB which implies a cDSB and thus a damage enhancement. On the other hand, in the limit of protraction times that are much larger than HLT_i, the temporal separation of the initial lesions is almost always sufficient to allow for a complete repair before a damage enhancement might take place. Consequently, the photon radiation effectiveness is supposed to decrease the most around HLT_i.

The computations presented in Figure 3.4.2A and B suggest that similar considerations hold true for ion radiation with sufficiently high dose and low LET. Actually, when the magnitude of the reduction of radiation effects is left outside, and only temporal aspects are considered, as visualized in Panels C and D, there is a perfect agreement between photon and ion radiation (within the resolution power). This leads to the conclusion that the dynamic LEM approach consistently reflects cell line characteristic time scales of dose-rate effects, implied by HLT_i.

This hypothesis was verified by the investigation of the impact of HLT_i on the protraction-time-dependence of ΔEff (Figure 3.4.3). For 5 Gy ^{12}C radiation with $LET = 25\,\mathrm{keV}/\mu\mathrm{m}$, the range where ΔEff decreases the most consistently shifts to larger protraction times when HLT_i is increased.

Concerning different orders of magnitudes of ΔEff detected in the investigation of the dependence on the protraction time, there are two impacting factors: first at a given α-β-ratio, the differences in the magnitude of dose-rate effects between photon and ion radiation of varying LET must originate from the physical properties of the respective radiation type. This issue will be discussed in the next section. Second, it was revealed that the maximum reduction of radiation effects is lower for the abstract cell line with $\alpha/\beta = 10\,\mathrm{Gy}$ then for the cell line with $\alpha/\beta = 2\,\mathrm{Gy}$. This observation can be explained with the mechanistic concept of the LEM and provides a second example for how cellular characteristics are reflected consistently in the response to varying radiation exposures.

In Figure 3.4.5, it was shown that when all other determinants of a cellular radiation response are fixed, the extent of observable dose-rate effects systematically decreases with an increasing α-β-ratio of a cell. That means that the abstract cell line which features the largest bending of acute photon survival curves, relative to the corresponding linear slope, profits the most when dose-rates of an ion exposure are lowered at sufficiently large doses and low LET.

In order to explain this phenomenon, it is instructive to start with empirical evidences for photon radiation. In the linear-quadratic framework which is employed in the LEM, one assumes that the maximum radiation effect is implied by acute irradiation which defines the parameters α and β. The minimum photon radiation effect is implied by a straight survival curve on a logarithmic scale with slope α. Consequently, when a cell line features only a relatively little quadratic component β in acute survival curves, a reduction of this quadratic component with a decrease of the dose-rate hardly reduces the radiation effect. Much larger reductions of the radiation effectiveness have to be expected for cell lines with a small α-β-ratio.

However, this empirical finding cannot explain why similar observations should be feasible for ion radiation. Here, the LEM approach can be exploited as bridge between photon and ion radiation as follows: for a cell line with a large α-β-ratio, linear-quadratic photon cell survival curves are almost straight on a logarithmic plot. This means that an increased fraction of cDSB at higher photon doses (assessable with equation 2.3.6) hardly enhances the radiation effect. The severity of iDSB must be almost as high as the severity of cDSB, consequently. In contrast, the difference in the severity of iDSB and cDSB is large for cell lines with a pronounced quadratic component in comparison to the linear component. Therefore, when a change of the radiation exposure implies a lower fraction of cDSB, the reduction of radiation effectiveness is

stronger for cell lines with a small α-β-ratio than for those with large α-β-ratio. This statement is independent of photon and ion radiation and thus explains the observed α/β-dependence of the reduction of the radiation effect for both.

In conclusion, implications of the linear-quadratic parameters and of the half-life time that characterize a photon radiation response are consistently reflected in predictions of ion radiation effects with the LEM.

3.4.4.2 Differences in the cellular response to ion and photon radiation

In the previous section it was found that the LEM predicts no impact of the radiation quality on cellular characteristics , e.g. temporal aspects related to the reduction of the radiation effectiveness with a protraction of the dose. The range of protraction times where the transition from maximum to minimum radiation effect happens is determined by cellular repair rates. Apparently, it is rather the existence and the order of magnitude of dose-rate effects that is impacted by photon or ion radiation with varying LET. The fact that the characteristics of a beam in cases prevent any observable dose-rate effect indicates that the physical settings provide the constraints for a variety of biological responses. Therefore, the questions under which conditions dose-rate effects might be expected and why they are in a different order of magnitude for photon and ion radiation with varying LET will be answered in the following. It will be assumed that cellular characteristics allow for the observation of dose-rate effects, i.e. that the cells are not radiosensitive.

Referring to the LEM approach, dose-rate effects become detectable when there is a dose-rate-dependent shift in the fractions of iDSB and cDSB. For photon radiation there is only one determinant next to the dose-rate that has an impact on the scored numbers of iDSB and cDSB: the dose. At acute low doses, the expected number of cDSB in a cell (equation 2.3.6) is so small that a protraction of the dose can hardly lower the radiation effect by temporal separation of the initial DSB. In contrast, at acute extremely high doses, the fraction of cDSB in a nucleus is so high, that a protraction over moderate times does not noticeably change it. However, in the intermediate range of doses, which is usually applied in cell survival experiments, dose-rate effects are generally observable for photon radiation.

For ion radiation the whole problem is complicated by the existence of a third dimension next to time and dose: the LET. Almost all of the plots shown in the results section (3.4.2, 3.4.4, 3.4.5, 3.4.7) revealed that no determinant of the cellular response has an impact on dose-rate effects as long as the LET of the considered ion radiation is sufficiently high. When the LET is lowered, the extent of observable dose-rate effects increases until at very low LET a photon-like behavior is almost reached. This phenomenon can be explained with the track structure of a considered ion species. In the limit of very high LET, the kinetic energy of each single particle is extremely low. Consequently, due to the small kinetic energy and range of released secondary electrons, the corresponding dose in a cellular nucleus is deposited close to the track center.

This has two implications: first, even when there is a relatively large fluence of ions, which defines the expected number of particles traversing a nucleus, the narrow ion tracks hardly overlap. Therefore, each single particle track causes certain numbers of iDSB and cDSB which are independent of the damage induced in other particle tracks. A temporal separation of the ions in time does not decrease the total fraction of cDSB that will occur in the nucleus, consequently, and dose-rate effects should not be observed.

Second, even when narrow ion tracks spatially overlap after instantaneous irradiation of a nucleus, dose-rate effects are still not expected when the ions are distributed over the time in the limit of high-LET. Due to the confinement of all initial DSB to a very small volume, there is already a very large fraction of cDSB in each single ion track. In consequence, a temporal separation of two spatially overlapping tracks does not lower the fraction of cDSB and a reduction of the radiation effect by a decrease of the dose-rate is not given.

As a side remark: during the testing of the dynamic extension of the LEM it was verified that lower dose-rates do not lead to *increased* radiation effects. This might happen when the temporal separation of two spatially overlapping high-LET ion tracks entails two cDSB in some traversed domains instead of a single one. However, the test revealed that such events are negligible.

When the LET is lowered starting from the limit of extremely large values, the onset of observable reductions of the radiation effect depends on the ion species. In Figure 3.4.6 it was revealed that relative changes of the effect are detected at higher LET for heavier particles. This phenomenon can again be explained with the track structure of the ions. At a given dose and LET, the number of particles traversing a cellular nucleus is equal for all species. However, referring to equation 2.1.1, the larger effective charge of heavier particles implies a higher kinetic energy. Thus, the radius of the tracks of heavier ions is larger and especially the radial part which is assigned to the penumbra, in contrast to the core (compare R_{track} to R_{core} in equation 2.3.8), is over-proportionally increased in comparison to lighter ions. This is of special relevance since the highly increased volume of the penumbra gives rise to a region where secondary electrons are more and more "loosely ionizing".

The consequences are twofold: first, when single heavy particles are considered, the low (averaged) ionization density in the outer rim of the track increases the induced fraction of iDSB in comparison to a lighter particle. Second, the relatively large width of the tracks of heavy ions increases the probability for a spatial overlap of two tracks in a nucleus. Taking these two aspects together, one expects for heavier ions that a noticeable fraction of cDSB is created by the spatial coexistence of two initial DSB corresponding to two different tracks. Therefore, there is a potential to increase the fraction of iDSB and to decrease the fraction of cDSB by a temporal separation of the single ions, i.e. by a lowering of the dose-rate. At the same LET and dose, the implied reduction of the radiation effect cannot be achieved with lighter particles.

In the limit of low-LET, it has been demonstrated that dose-rate effects observed after ion radiation exposure approach those of photon radiation exposure. Each single ion track in the low-LET limit features a large volume of the penumbra and the corresponding distribution of initial DSB is almost homogeneous. Consequently, the overlap of a large number of tracks which is needed to achieve a given dose, produces a damage pattern which is comparable to photon radiation. The LEM predictions shown in Figure 3.4.6 are thus mechanistically consistent in the whole range of explored LET.

After the consistency of the LEM has been demonstrated with regard to time- and LET-related aspects, the consistency with dose-related aspects needs to be verified. In Figure 3.4.7 it was shown that the extent of dose-rate effects becomes lower when the dose of an exposure is decreased (while maintaining the ion species, LET and cellular parameters). A smaller dose at a given LET implies that the expected number of particles traversing a cellular nucleus decreases. Consequently, when the LET is sufficiently low to allow for the observation of dose-rate effects, the probability for an overlap of at least two ion tracks decreases. This entails a reduction of the

fraction of cDSB which are caused by initial DSB of different tracks. Thus, when the dose-rate is lowered and the single ions are temporarily separated, the fraction of cDSB which can convert to two or more iDSB is lower for exposures with lower dose. A smaller reduction of the radiation effect is the final consequence.

In conclusion, the dynamic extension of the LEM provides a consistent framework for the explanation of the impact of the time, dose and LET on the cellular response to ion radiation. Since its parental version has proven to describe experimental and clinical observations well, the same might be suggested for the new version. This topic will be discussed in the next section.

3.4.4.3 Agreement with experimental observations

A comparison of LEM predictions with experimental data published by Inaniwa et al. [115] provided evidence that temporal aspects in the cellular response to ion radiation can be reproduced adequately with the model. Consequently, the dynamically extended LEM is supposed to also describe other experimental and clinical observations requiring a kinetic model well. This hypothesis needs to be tested, though.

Unfortunately, the data situation for ion experiments in literature is extremely bad, perhaps due to the large costs that are involved in time-dose-LET experiments. There are e.g. some studies where dose fractionation experiments were conducted [125][126][127]. However, in these experiments, the radiation breaks stretched over 24 h so that only complete repair effects, but no time effects can be observed. In other publications, e.g. in reports by the Lawrence Berkeley Laboratory or in [128], heavy ion split-dose and dose-rate experiments were presented. Yet, the LET in the corresponding studies is too high to allow for a detection of reductions of the radiation effect. Therefore, from a theoretical point of view, it would be beneficial if more data were recorded for protracted or split ion radiations in the ranges of LET and protraction or separation times which require for the usage of kinetic models.

3.4.4.4 Implications on heavy ion radiotherapy

In cancer treatment with heavy ions, one exploits the advantageous property that ions deposit almost no energy in penetrated tissue up to a certain depth where a maximum energy is deposited (Bragg peak). By variation of the beam energy (for ^{12}C usually around 290 MeV/u) one cannot only adjust the position of a single Bragg peak to the tumor location but also cover the length of the tumor by an overlap of several Bragg peaks (spread-out Bragg peak). Thus, in first instance, one achieves a low physical dose in the normal tissue in the entrance region of the beam and a high dose in the tumor tissue in the Bragg peak region.

However, the sparing of the normal tissue compared to the tumor tissue is even enhanced when the relative biological effectiveness RBE of e.g. ^{12}C ion beams is accounted for. In the entrance region, the LET is around 10 keV/μm whereas it is around 50-80 keV/μm in the Bragg peak region [18]. Due to the higher LET in this range, one usually expects a larger RBE in the tumor than in the normal tissue. Consequently, treatment planning studies, which amongst others aim to maximize tumor control probabilities constrained on tolerable side effects in the normal tissue, have to account for both, the physical dose and biological weights. For the treatment planning studies at the GSI, the LEM is used to provide the required RBE predictions.

So far, the LEM did not comprise time effects in the calculation of the cellular response to ion radiation and in the corresponding prediction of RBE values. The computations in this

thesis have shown that referring to the LEM, the impact of time effects on the cellular response to ^{12}C radiation are negligible for dose-protraction times smaller than about 15 min (Figure 3.4.2), depending on the fast rate of cellular repair (Figure 3.4.3). Referring to the split-dose experiment by Inaniwa et al. and corresponding LEM predictions (Figure 3.4.9), separating two times 2.5 Gy of ^{12}C radiation with $LET = 13\,\mathrm{keV}/\mu\mathrm{m}$ by 10 min reduces the effect about 7% compared to instantaneous irradiation. This might be considered as a tolerable deviation. However, a separation time of 20 min already reduces the effect by 18% and this significant change might finally not be negligible.

In consequence, when the application of a dose during a radiotherapy session takes less than about 15 min, time effects should not come into action and treatment planning studies do not have to consider time-dependent changes in the RBE. This is usually the case when total doses are given in daily fractions of about 2 Gy to 5 Gy without many re-positionings of the patient or the employment of time-consuming treatment techniques. However, as soon as the treatment techniques get more complex, involve a larger number of treatment fields or a frequent re-positioning of the patient, 15 min are quickly exceeded. This concerns especially recent trends as e.g. treatments with respiratory gating [116] or hypofractionation schedules where larger doses are applied in fewer fractions [19][23].

For such cases, the dynamic LEM predicts a reduced radiation effect especially at a low LET as it is given in the entrance channel of a beam. Static calculations would overestimate the biological damage in the normal tissue, consequently. In contrast, the Bragg peak region, where there is a higher LET, is expected to be less concerned by time effects and the biological damage to the tumor is supposed to remain almost unchanged. Putting these arguments together, the kinetically extended LEM suggests that patients tolerate prolonged radiation sessions better than predicted with static models and that the desired tumor control is maintained, nevertheless. The success of hypofractionated treatments is at least not contradictory to this statement.

3.4.4.5 Implications on radiation protection

In comparison to radiotherapy, doses and dose-rates considered for the purpose of radiation protection are usually much lower, up to about 0.1 Sv and in the range of days or even years [119][117][118][129]. In fact, one of the major problems in radiation protection is the assessment of biological and clinical effects caused by low-dose and low-dose-rate exposure because in this range, statistically significant statements based on empirical observations are extremely hard to make. In the low-dose and dose-rate regime, the radiation caused excess risk for e.g. cancer induction is small in comparison to the general background risk. Thus, random fluctuations in the background risk itself, e.g. derived by evaluation of a control group, are in the same order of magnitude as a radiation-related excess risk. Huge sample sizes of exposed persons would be necessary to detect this little excess risk with significance, consequently [118]. In last instance, this is why the low-dose and dose-rate range is only vaguely elucidated by actual observations.

To nevertheless assess radiation-related risks for biological damage or clinical diseases in the low-dose and dose-rate regime, adequate models provide a good starting point. By extrapolation of high-dose and dose-rate data, insight into less well explored ranges might be gained. Especially in the case of heavy ion radiation, where there is less experience with low-dose and dose-rate effects than for photon radiation, a good approach for the estimation of radiation associated risks is valuable. Consequently, predictions with the dynamic extension of the LEM are

thought to provide useful information, even though cell survival probabilities and not cancer induction probabilities are investigated. Starting from high-dose and dose-rate data, which are needed to derive the model input parameters α and β, the LEM is applicable for assessments of relative changes of the radiation effect ΔEff as presented in the results section.

For the radiation protection of astronauts in outer space, one needs to estimate e.g. radiation effects caused by low-dose and dose-rate photons and ions occurring with a spectrum of LET in galactic cosmic rays (GCR). For instance, during a mission on the ISS, an astronaut is exposed to a total physical dose of 0.03 Gy in the average [14]. About 80% of the corresponding biologically weighted dose can be attributed to GCR. Furthermore, as an example for a quite extreme case, it has been estimated that the exposure during a mars mission would be much higher, with a physical dose of about 0.4 Gy [130]. In Figure 3.4.8, LEM predictions of the reduction of radiation effects were shown in dependence of the dose for a selection of relevant ion species and LET. Referring to the computations, negligible changes in the radiation effect should be expected when doses around 0.03 Gy are applied with very low dose-rates instead of in an instant. This finding is independent of the radiation type and therefore, without having to consider the different biological effectiveness of photons and ions of varying LET, the LEM suggests that no reduction of the total effect has to be accounted for in an extrapolation from high to low dose-rates. Consequently, at such low doses, risk assessments for endpoints that are closely related to cell survival do not have to reflect dose-rate related sparing effects. However, when astronauts are exposed to higher doses, e.g. to 0.4 Gy as estimated for mars missions [130], adjustments of cell survival related risk assessments with respect to dose-rate effects might be recommendable.

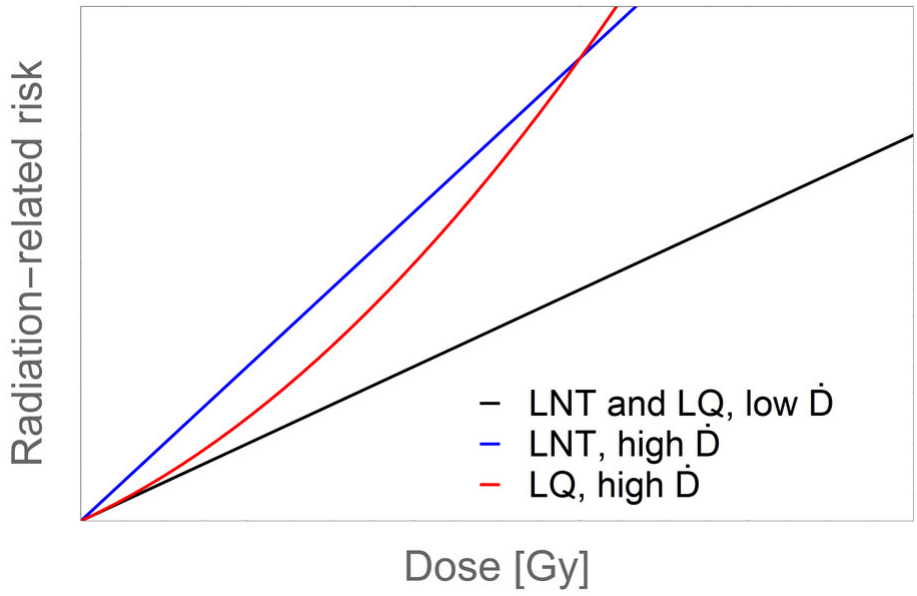

Figure 3.4.10: Visualization of differences between a linear-no-threshold (LNT) approach and a linear-quadratic approach for the assessment of low-dose and dose-rate radiation risks. In the whole dose range, the LNT approach predicts a reduction of the radiation risk of 50% when a very low instead of a very high dose-rate $\dot{D}$ is applied. In the low-dose regime, the LQ approach predicts a much smaller reduction of the radiation risk when the dose-rate is lowered.

For more general considerations of aspects related to radiation protection with the LEM, one important finding should be emphasized again: the LEM generally predicts a dose-dependent change of the radiation effect when extremely low instead of extremely high dose-rates are applied. Only below doses up to about 0.1 Gy, such changes become negligibly small. Consequently, the LEM does not support a generic factor for the extrapolation of high-dose and dose-rate risks to low-dose and dose-rate risks. This seems to be contradictory to the constant dose and dose-rate reduction factors (DDREF) proposed by BEIR [119] or ICRP[117][118]. Yet, one has to keep in mind that their approaches for the modeling of solid cancer induction clearly differ from the presented approach for cell survival. When the risk for radiation-induced cancer is assumed to be linear to the applied dose (linear-no-threshold model), and the cancer risk at a given dose is lower at low dose-rates than at high dose-rates, on gets two different dose-response curves. Even at low doses, there will be a noticeable relative difference between these two linear curves (Figure 3.4.10). However, when it is assumed that the linear dose- response curve for a low-dose-rate exposure has the same slope as the acute dose-response curve at low doses, as it is done in the linear-quadratic approach or in the LEM, a faster convergence of predictions at such low doses is implied. In consequence, in the assessment of reductions of radiation risks related to the change from high-dose and dose-rates to low-dose and dose-rates one has to account for both, the considered endpoint and the framework of the employed model. A large part of the BEIR VII phase 2 report [119] is dedicated to the discussion of alternative approaches for the extrapolation of radiation-related cancer risks. As a conclusion for the current study, the differences between LEM predictions and DDREF as presented here should not be interpreted as disagreements but as complementary information.

3.4.5 Conclusion

In this study, a mechanistically motivated kinetic extension of the Local Effect Model was proposed. Based on a dynamical simulation of DSB induction by ion radiation and a bi-phasic repair of iDSB and cDSB, consistent time-dose-LET effects are obtained. Furthermore, the kinetic LEM has been shown to provide an accurate description of experimental data. Thus, it should be expected that the LEM can be used for predictions of the cellular response to ion radiation with an arbitrary schedule and to simultaneously gain insight into potentially underlying cellular mechanisms. In the discussion it was explained that referring to the LEM, it might be advantageous to account for time effects in heavy ion radiotherapy when treatment sessions are prolonged. Furthermore, with regard to radiation protection, the LEM suggests that for endpoints that are closely related to cell survival probabilities, a reduction of radiation effects should not be expected in the limit of low doses and dose-rates. For an extrapolation from high-dose and dose rate to low-dose and dose-rate, a variety of factors have to be accounted for when the accuracy of predictions is the aim. Finally, in connection with the kinetic GLOBLE model, the LEM constitutes a universal tool for the assessment of radiation effects caused by photons and ions with varying LET and with protracted or fractionated dose delivery schedule.

4 Final conclusion and outlook

The four studies that have been conducted in preparation of this thesis were dedicated to the investigation of time-dose-LET effects in the cellular response to radiation. In particular, the impact of the spatial and temporal distribution of radiation-induced double-strand breaks in higher-order chromatin structures on the fidelity and time course of lesion repair was theoretically explored.

Preceding this work, during the establishment of the common framework of the Local Effect Model (LEM) for ion radiation and of the Giant Loop Binary Lesion (GLOBLE) model for photon radiation, it was demonstrated that the cellular response to instantaneous exposures is adequately described with a binary lesion system. By definition of two lesion classes on the hand of single (isolated) or multiple (clustered) DSB within DNA giant loops, and by assigning a higher severity to clustered DSB, a wide spectrum of dose- and LET-dependent radiation responses can be covered. Furthermore, in the Giant Loop Binary Lesion model, a kinetic extension was introduced where isolated DSB are assigned with a shorter repair half-life time than clustered DSB. With that, time-dose effects in the GLOBLE framework after protraction or fractionation of a given dose are explained by the inherent temporal separation of the initial DSB, a reduction of the coexistence of DSB within a considered giant loop due to interim repair processes and by the lower harmfulness of the increased fraction of isolated DSB.

In the first project presented in this thesis, it was demonstrated that the Giant Loop Binary Lesion model is applicable for the description of experimentally and clinically observed time-dose effects after photon irradiation. Not only cell survival probabilities recorded in split-dose experiments but also empirically found dose-rate dependent changes in the incidence of deterministic radiation effects can be assessed with the GLOBLE model. Actually, it was revealed that the GLOBLE approach does not only accurately reproduce these time-dose effects but that it also provides a consistent mechanistic explanation for the reasons underlying the final observations. Consequently, in the first project, experimental and empirical support for the GLOBLE concept was found.

The second study conducted for this thesis showed that the bi-exponential lesion repair that is implied in the binary concept of the Giant Loop Binary Lesion model and of the Local Effect Model finds indirect support by double-strand break rejoining experiments. In a comparison of ten models for DSB rejoining with regard to their accuracy and parsimony in the description of 61 published experiments, the bi-exponential model and a model with a gamma-distributed DSB rejoining rate performed the best. Models which explain DSB rejoining curves by interaction of breaks found less support by the experimental data. When DSB rejoining is carefully related to the repair of abstract lesion classes in kinetic cell survival models, this argues for the LEM and GLOBLE approach.

In the third project, four kinetic cell survival models were compared with respect to eight quantitative measures derived in fits to 13 dose-rate experiments and with respect to qualitative characteristics. Concerning the quantitative investigation, it was revealed that the GLOBLE model and two well-established kinetic approaches for photon cell survival probabilities, the Linear-Quadratic model with Lea-Catcheside formalism and the Lethal Potentially Lethal model,

perform equivalently well. Another approach, the Repair Misrepair model, performed worse. Thus, the GLOBLE model is able to keep up with recognized kinetic cell survival models from a mathematical point of view. When it comes to the qualitative comparison, the concept of the GLOBLE suggests even an advantage because it allows to explain the cellular response not only to photon but also to ion radiation in connection with the LEM.

Last but not least, in the fourth project, the Local Effect Model was kinetically extended. By adopting the idea that isolated DSB are expected to be repaired faster than clustered DSB from the GLOBLE model and by the introduction of temporal aspects in the simulation of damage induction by ion radiation, the LEM is now applicable for the prediction of time-dose-LET effects. Theoretical investigations have shown the consistency of the approach with regard to variations of the radiation effect in dependence of impacting radiation-related and cellular factors. Furthermore, the dynamic extension of the LEM was validated by comparison to a published experiment and implications on radiotherapy and radiation protection were discussed.

To summarize, the studies presented in this thesis support the idea that damage clustering in DNA giant loops is a determinant of the cellular radiation response. With the binary concept of two lesion classes with two severities and two time-scales of repair, one cannot only accurately predict the dependence of cell survival probabilities on the dose or the dose-rate for photon or for ion radiation with varying LET. One also finds plausible mechanistical explanations for the processes that underlie the final observations. Thus, the GLOBLE model and LEM might help to understand causalities leading to measured radiation effects.

One major project for the future work is the transfer of lethalities of isolated DSB and clustered DSB, which are used as parameters for the cellular response in the Giant Loop Binary Lesion model, to the Local Effect Model. With the two lethalities, one could directly derive cell survival probabilities after ion irradiation from the numbers of simulated isolated and clustered DSB, without the derivation of equivalent photon responses as it is done so far. However, the transfer of the two lethalities is not as straight-forward as one might think. There are several adjustments that have to be made in order to guarantee that the outputs of the current LEM, which have been shown to be adequate, are maintained. Nevertheless, there is a lot of confidence that the unification of the LEM and GLOBLE approach is feasible and will lead to a universal tool for the prediction of radiation effects.

5 Appendix

5.1 Tables for section 3.2

Parameter [unit]	Meaning	Median photon (range)	Median ion (range)
MonoExp			
k [h^{-1}]	Rate	1.02 (0.04, 4.77)	0.49 (0.18, 1.51)
MonoExpO			
k [h^{-1}]	Rate	2.10 (0.12, 8.08)	1.09 (0.41, 2.02)
A	Unrejoinable fraction	0.12 (0.03, 0.39)	0.17 (0.05, 0.39)
BiExp			
k_1 [h^{-1}]	Rate fast component	3.31 (0.96, 47.36)	1.90 (0.52, 3.83)
k_2 [h^{-1}]	Rate slow component	0.14 (0, 1.55)	0.07 (0, 0.21)
A	Fast rejoined fraction	0.62 (0.11, 0.95)	0.62 (0.29, 0.94)
BiExpO			
k_1 [h^{-1}]	Rate fast component	4.90 (1.04, 107.07)	2.57 (0.67, 4.70)
k_2 [h^{-1}]	Rate slow component	0.32 (0.03, 3.51)	0.24, (0.06, 1.53)
$A1$	Fast rejoined fraction	0.56 (0, 1)	0.56 (0, 0.77)
$A2$	Unrejoinable fraction	0.03 (0, 0.33)	0.09 (0, 0.39)
TriExp			
k_1 [h^{-1}]	Rate fast component	7.02 (0.96, 192.84)	2.36 (0.59, 4.70)
k_2 [h^{-1}]	Rate medium component	1.47 (0.29, 11.58)	0.28 (0.11, 2.54)
k_3 [h^{-1}]	Rate slow component	0.07 (0, 0.85)	0 (0, 0.1)
$A1$	Fast rejoined fraction	0.32 (0, 0.95)	0.49 (0, 0.75)
$A2$	Medium-speed rej. fraction	0.40 (0, 0.83)	0.32 (0.02, 0.94)
2ndO			
k_1 [h^{-1}]	Rate	2.12 (0.07, 8.21)	0.83 (0.32, 2.46)
1st2ndO			
k_1 [h^{-1}]	Linear rate	0 (0, 1.28)	0 (0, 0.38)
k_2 [h^{-1}]	Quadratic rate	1.78 (0.07, 8.21)	0.78 (0.13, 2.46)
GaussianExp			
μ [h^{-1}]	Mean rate	1.35 (0.02, 5.00)	0.51 (0.19, 1.54)
σ [h^{-1}]	Standard deviation	0.55 (0.05, 2.51)	0.26 (0.13, 0.46)
ExpExp			
μ [h^{-1}]	Mean rate	2.12 (0.07, 8.21)	0.83 (0.32, 2.46)
GammaExp			
α	Shape parameter	0.74 (0.14, 6.08)	0.57 (0.39, 6.73)
μ [h^{-1}]	Mean rate	3.43 (0.11, 18.37)	1.36 (0.50, 3.94)

Table 5.1.1: The ten investigated models and their fit parameters. Medians of the parameter values derived in fits to photon and ion DSB rejoining data are provided as an indication for their order of magnitude. Due to included insignificant values these specifications should be treated with caution.

Cell line	Publication	Cell cycle stage	Radiation quality	Dose	Irradiation in
HF19	Badie et al. [102]	Plateau	Gamma (^{137}Cs)	30 Gy	Monolayer
AT2	Badie et al. [102]	Plateau	Gamma (^{137}Cs)	30 Gy	Monolayer
180BR	Badie et al. [102]	Plateau	Gamma (^{137}Cs)	30 Gy	Monolayer
V79	Cheong et al. [131]	Plateau	X rays 250 kV	50 Gy	Monolayer
irs-1	Cheong et al. [131]	Plateau	X rays 250 kV	50 Gy	Monolayer
180BR	Kasten-Pisula et al. [43]	Plateau	X rays 200 kVp	40 Gy	Monolayer
LFS2800	Kasten-Pisula et al. [43]	Plateau	X rays 200 kVp	80 Gy	Monolayer
LFS2800	Kasten-Pisula et al. [43]	Plateau	X rays 200 kVp	40 Gy	Monolayer
AT3	Kasten-Pisula et al. [43]	Plateau	X rays 200 kVp	40 Gy	Monolayer
NFHH	Kasten-Pisula et al. [43]	Plateau	X rays 200 kVp	40 Gy	Monolayer
V79B	Kysela et al. [101]	79.7% G1	X rays 240 kVp	10 Gy	Agarose
V79B	Kysela et al. [101]	79.7% G1	X rays 240 kVp	20 Gy	Agarose
V79B	Kysela et al. [101]	79.7% G1	X rays 240 kVp	50 Gy	Agarose
XR-V15B	Kysela et al. [101]	72.5% G1	X rays 240 kVp	10 Gy	Agarose
XR-V15B	Kysela et al. [101]	72.5% G1	X rays 240 kVp	20 Gy	Agarose
XR-V15B	Kysela et al. [101]	72.5% G1	X rays 240 kVp	50 Gy	Agarose
CHO-10B	Metzger et al. [132]	Plateau	X rays 250 kV	50 Gy	Suspension
CHO-10B	Metzger et al. [132]	Exponential	X rays 250 kV	50 Gy	Suspension
CHO-10B	Metzger et al. [132]	G1	X rays 250 kV	50 Gy	Suspension
CHO-10B	Metzger et al. [132]	G1/S	X rays 250 kV	50 Gy	Suspension
CHO-10B	Metzger et al. [132]	Early S	X rays 250 kV	50 Gy	Suspension
CHO-10B	Metzger et al. [132]	Mid S	X rays 250 kV	50 Gy	Suspension
CHO-10B	Metzger et al. [132]	Late S	X rays 250 kV	50 Gy	Suspension
CHO-10B	Metzger et al. [132]	G2M	X rays 250 kV	50 Gy	Suspension
CHO-10B	Metzger et al. [132]	M	X rays 250 kV	50 Gy	Suspension
MCF-7 BUS	Núñez et al. [81]	Exponential	Gamma (^{60}Co)	45 Gy	Monolayer
MCF-7 BB	Núñez et al. [81]	Exponential	Gamma (^{60}Co)	45 Gy	Monolayer
T47D-B8	Núñez et al. [81]	Exponential	Gamma (^{60}Co)	45 Gy	Monolayer
T47D-B1	Núñez et al. [81]	Exponential	Gamma (^{60}Co)	45 Gy	Monolayer
EVSA-T	Núñez et al. [81]	Exponential	Gamma (^{60}Co)	45 Gy	Monolayer
RT-112	Núñez et al. [81]	Exponential	Gamma (^{60}Co)	45 Gy	Monolayer

AA8	Rothkamm et al. [133]	G1	X rays 95 kV	80 Gy	Monolayer
irs1SF	Rothkamm et al. [133]	G1	X rays 95 kV	80 Gy	Monolayer
V3	Rothkamm et al. [133]	G1	X rays 95 kV	80 Gy	Monolayer
CHO-K1	Stamato et al. [99]	Exponential	Gamma (^{137}Cs)	8 Gy	Monolayer
CHO-K1	Stamato et al. [99]	Exponential	Gamma (^{137}Cs)	20 Gy	Monolayer
CHO-K1	Stamato et al. [99]	Exponential	Gamma (^{137}Cs)	40 Gy	Monolayer
CHO-K1	Stamato et al. [99]	Exponential	Gamma (^{137}Cs)	8 Gy	Agarose
CHO-K1	Stamato et al. [99]	Exponential	Gamma (^{137}Cs)	20 Gy	Agarose
CHO-K1	Stamato et al. [99]	Exponential	Gamma (^{137}Cs)	40 Gy	Agarose
HX142	Whitaker et al. [134]	Exponential	Gamma (^{60}Co)	20 Gy	Monolayer
D283med	Whitaker et al. [134]	Exponential	Gamma (^{60}Co)	20 Gy	Monolayer
MGH-U1	Whitaker et al. [134]	Exponential	Gamma (^{60}Co)	20 Gy	Monolayer
HeLa	Whitaker et al. [134]	Exponential	Gamma (^{60}Co)	20 Gy	Monolayer
GM38	Löbrich et al. 1995 [51]	Confluent	X rays 225 kV	80 Gy	Mixed data
GM38	Löbrich et al. 1998 [46]	Confluent	150 keV/μm Fe	80 Gy	Monolayer
GM38	Löbrich et al. 1998 [46]	Confluent	70 keV/μm He	80 Gy	Monolayer
GM38	Löbrich et al. 1998 [46]	Confluent	120 keV/μm He	80 Gy	Monolayer
GM38A	Rydberg et al. [103]	Contact inh.	32 keV/μm Ne	80 Gy	Monolayer
GM5758	Stenerlöw et al. 2000 [135]	Confluent	Gamma (^{60}Co)	100 Gy	Monolayer
GM5758	Stenerlöw et al. 2000 [135]	Confluent	40 keV/μm He	100 Gy	Monolayer
GM5758	Stenerlöw et al. 2000 [135]	Confluent	80 keV/μm N	100 Gy	Monolayer
GM5758	Stenerlöw et al. 2000 [135]	Confluent	125 keV/μm N	100 Gy	Monolayer
GM5758	Stenerlöw et al. 2000 [135]	Confluent	175 keV/μm N	100 Gy	Monolayer
GM5758	Stenerlöw et al. 2000 [135]	Confluent	225 keV/μm N	100 Gy	Monolayer
V79	Stenerlöw et al. 1996 [45]	Exponential	Gamma (^{60}Co)	10 Gy	Monolayer
V79	Stenerlöw et al. 1996 [45]	Exponential	125 keV/μm N	10 Gy	Monolayer
U-343MG	Stenerlöw et al. 1996 [45]	Exponential	Gamma (^{60}Co)	10 Gy	Monolayer
U-343MG	Stenerlöw et al. 1996 [45]	Exponential	Gamma (^{60}Co)	20 Gy	Monolayer
U-343MG	Stenerlöw et al. 1996 [45]	Exponential	125 keV/μm N	10 Gy	Monolayer
U-343MG	Stenerlöw et al. 1996 [45]	Exponential	125 keV/μm N	20 Gy	Monolayer

Table 5.1.2: Information about the data used for the comparison of ten models for DSB rejoining (two pages). Data sets with more than eight data points and measurements later than 12 h after exposure are highlighted in gray.

	Visual inspection				Parameter significance				Inverse evidence ratio			
Model	**Photon**	**Ion**	**p-value**	**All**	**Photon**	**Ion**	**p-value**	**All**	**Photon**	**Ion**	**p-value**	**All**
GammaExp	22.4	16.7	1.000	21.3	20.4	25.0	0.707	21.3	10.2	8.3	1.000	9.8
BiExp	18.4	0.0	0.184	14.8	51.0	66.7	0.519	54.1	14.3	25.0	0.397	16.4
BiExpO	6.1	0.0	1.000	4.9	89.8	83.3	0.615	88.5	32.7	75.0	0.010	41.0
1st2ndO	55.1	58.3	1.000	55.7	85.7	100.0	0.327	88.5	42.9	41.7	1.000	42.6
2ndO & ExpExp	71.4	66.7	0.736	72.1	0.0	0.0		0.0	46.9	33.3	0.522	44.3
MonoExpO	79.6	75.0	0.707	78.7	8.2	16.7	0.588	9.8	51.0	41.7	0.749	52.2
TriExp	0.0	0.0		0.0	100.0	100.0		100.0	63.3	100.0	0.012	70.5
GaussianExp	91.8	91.7	1.000	91.8	34.7	75.0	0.020	42.6	81.6	83.3	1.000	82.0
MonoExp	98.0	91.7	0.357	96.7	0.0	0.0		0.0	89.8	83.3	0.615	88.5

Table 5.1.3: Results of the qualitative and quantitative model comparison in terms of percentages where the models were considered to be implausible for the description of DSB rejoining data. For every criterion (visual inspection, parameter significance and evidence ratio), photon and ion irradiation data were evaluated in separate and in a pool (all). The provided p-values correspond to a two-sided Fisher's exact test for the null-hypothesis that a model performs equally good or bad in the description of photon and ion experiments.

5.2 Tables for section 3.3

Cell line	Publication	Dose-rates [Gy/h]
HX118	Kelland and Steel [67]	90; 4.56; 0.96
RT112	Ruiz de Almodóvar et al. [136]	76.8; 30; 12; 6; 3; 1.2; 0.6
C3H 10T1/2	Wells and Bedford [66]	55.6, 24; 0.49; 0.29; 0.17; 0.06
CHO 10B2	Stackhouse and Bedford [65]	45; 0.5; 0.12
HX138	Holmes et al. [107]	54; 12; 6; 3; 1.2; 0.6; 0.3; 0.15
HX142	Holmes et al. [107]	54; 12; 1.2; 0.6; 0.3; 0.15
MT	Stephens et al. [64]	90; 24; 8.4; 4.56; 0.96
LL	Stephens et al. [64]	90; 8.4; 4.56; 0.96
B16	Stephens et al. [64]	90; 8.4; 4.56; 0.96
HX34	Stephens et al. [64]	90; 8.4; 4.56; 0.96
IN859	Yang et al. [68]	90; 4.2; 1.2; 0.678
IN1265	Yang et al. [68]	90; 4.2; 1.2; 0.678
SB	Yang et al. [68]	90; 4.2; 1.2; 0.678

Table 5.2.1: Information about the dose-rate experiments used for a comparison of four kinetic cell survival models.

	LC-LQ			RMR			
Cell line	α [Gy^{-1}]	β [Gy^{-2}]	r [h^{-1}]	λ [h^{-1}]	κ [h^{-1}]	1-ϕ	1-δ
HX118	0.326	0.039	2.84	5.79	0.770	0.0067	0.0225
RT112	0.163	0.025	1.41	1.58	0.010	0.0057	0.0247
C3H 10T1/2	0.122	0.012	0.28	0.34	0.001	0.0036	0.0200
CHO 10B2	0.044	0.021	0.11	3.12	0.983	0.0001	0.0139
HX138	0.659	0.116	0.58	1.65	0.408	0.0099	0.0456
HX142	0.855	0.108	0.64	1.84	0.885	0.0136	0.0481
MT	0.260	0.022	7.77	2.02	0.008	0.0072	0.0236
LL	0.344	0.074	7.05	9.55	0.154	0.0118	0.0399
B16	0.235	0.026	5.03	9.25	0.286	0.0065	0.0179
HX34	0.269	0.042	5.07	4.37	0.008	0.0086	0.0738
IN859	0.164	0.056	1.46	2.16	0.093	0.0003	0.0254
IN1265	0.275	0.028	1.22	1.87	0.008	0.0094	0.0352
SB	0.152	0.035	0.74	5.52	1.793	0.0000	0.0166
AVERAGE	0.297	0.046	2.63	3.77	0.416	0.0064	0.0313

	LPL				GLOBLE		
Cell line	η_L [Gy^{-1}]	η_{PL} [Gy^{-1}]	ϵ_{PL} [h^{-1}]	ϵ_{2PL} [h^{-1}]	ϵ_i	ϵ_c	HLT_i [h]
HX118	0.318	1.07	3.96	0.476	0.0108	0.297	0.236
RT112	0.156	3.16	1.45	0.009	0.0053	0.195	0.485
C3H 10T1/2	0.108	0.49	0.34	0.078	0.0040	0.096	2.594
CHO 10B2	0.024	1.28	0.13	0.005	0.0013	0.162	6.100
HX138	0.425	1.10	0.92	1.599	0.0218	0.851	1.184
HX142	0.723	1.10	0.78	0.597	0.0284	0.809	1.083
MT	0.260	10.07	7.90	0.004	0.0086	0.178	0.086
LL	0.336	1.91	9.83	0.692	0.0114	0.543	0.095
B16	0.234	3.93	5.40	0.020	0.0078	0.203	0.131
HX34	0.266	3.25	5.51	0.054	0.0089	0.320	0.133
IN859	0.123	1.17	1.85	0.352	0.0054	0.407	0.467
IN1265	0.275	12.68	1.24	0.000	0.0091	0.215	0.564
SB	0.107	1.05	0.73	0.091	0.0049	0.259	0.941
AVERAGE	0.258	3.25	3.08	0.306	0.0098	0.349	1.085

Table 5.2.2: Parameter values derived in global fits of the four investigated models to dose-rate experiments in 13 cell lines (the table has been split into two halves on this page).

5.3 Information about cell lines

Cell line	Description	Special characteristics
180BR	Human skin fibroblast	Derived from a radiosensitive patient who did not show symptoms of ataxia-telangiectasia. Defective of DSB repair (NHEJ).
AA8	Chinese hamster ovary	Derived from CHO-K1 cells.
AT2	Human skin fibroblast	Derived from a radiosensitive patient who showed symptoms of ataxia-telangiectasia. Defective in the ATM gene.
AT3	Human skin fibroblast	Derived from a radiosensitive patient who showed symptoms of ataxia-telangiectasia. Defective in the ATM gene.
B16	Murine melanoma	
C3H 10T1/2	Mouse embryo fibroblasts	
CHO-10B(2)	Chinese hamster ovary	
CHO-K1	Chinese hamster ovary	
D283med	Human medulloblastoma	
EVSA-T	Human breast cancer	
GM38(A)	Human skin fibroblast	
GM5758	GM5758	
HeLa	Cervical carcinoma	
HF19	Human skin fibroblast	
HSG	Human submandibular gland	The cell line is supposed to have been contaminated with HeLa cells.
HX118	Human melanoma xenograft	
HX138	Human neuroblastoma xenograft	Sensitive to high-dose-rate irradiation but exhibiting dose-rate effects.
HX142	Human neuroblastoma xenograft	Sensitive to high-dose-rate irradiation but exhibiting dose-rate effects.
HX34	Human melanoma xenograft	
IN1265	Human glioma	
IN859	Human glioma	
irs-1	Chinese hamster fibroblasts (lung)	Radiosensitive mutant of V79 cells.
irs1SF	Chinese hamster ovary	X-ray-sensitive mutant derived from AA8 cells.
LFS2800	Human fibroblast	Derived from patients showing the LiFraumeni syndrome.
LL	Murine Lewis lung carcinoma	

Cell line	Description	Special characteristics
MT	Murine mammary carcinoma	
MCF7 BB	Human breast cancer	
MCF7 BUS	Human breast cancer	
MGH-U1	Human bladder carcinoma	
NFHH	Human fibroblast	
RT-112	Human bladder carcinoma	
SB	Human glioma	Sensitive to high-dose-rate irradiation but exhibiting dose-rate effects.
T47D-B1	Human breast cancer	
T47D-B8	Human breast cancer	
U-343MG	Human glioma	
V3	Chinese hamster ovary	X-ray-sensitive, reduced expression of DNA-PKcs, defective for DSB repair.
V79	Chinese hamster fibroblasts (lung)	
XR-V15B	Chinese hamster fibroblasts (lung)	Radiosensitive mutant of V79 cells.

Bibliography

[1] Scholz M, Kraft G. Calculation of heavy ion inactivation probabilities based on track structure, x-ray sensitivity and target size. *Radiation Protection Dosimetry*, 52(1–4):29–33, 1994.

[2] Scholz M, Kraft G. Track structure and the calculation of biological effects of heavy charged particles. *Advances in Space Research*, 18(1/2):5–14, 1996.

[3] Scholz M, Kellerer AM, Kraft-Weyrather W, Kraft G. Computation of cell survival in heavy ion beams for therapy. *Radiation and Environmental Biophysics*, 36:59–66, 1997.

[4] Elsässer T, Scholz M. Cluster effects within the Local Effect Model. *Radiation Research*, 167(3):319–329, 2007.

[5] Elsässer T, Cunrath R, Krämer M, Scholz M. Impact of track structure calculations on biological treatment planning in ion radiotherapy. *New Journal of Physics*, 10:075005, 2008. CC-BY-NC-SA 3.0 license.

[6] Elsässer T, Kraft-Weyrather W, Friedrich T, Durante M, Iancu G, Krämer M, et al. Quantification of the relative biological effectiveness for ion beam radiotherapy: direct experimental comparison of proton and ion beams and a novel approach for treatment planning. *International Journal of Radiation Oncology*Biology*Physics*, 78(4):1177–1183, 2010.

[7] Friedrich T, Scholz U, Elsässer T, Durante M, Scholz M. Calculation of the biological effects of ion beams based on the microscopic spatial damage distribution pattern. *International Journal of Radiation Biology*, 88(1–2):103–107, 2012.

[8] Friedrich T, Durante M, Scholz M. Modeling cell survival after photon irradiation based on double-strand break clustering in megabase pair chromatin loops. *Radiation Research*, 178:385–394, 2012.

[9] Herr L. *The K-GLOBLE: A kinetic cell survival model*. Master thesis, J.W.Goethe Universität, Frankfurt, 2012.

[10] The International Commission on Radiation Units and Measurements. ICRU Report No. 85. Fundamental quantities and units for ionizing radiation. *Journal of the ICRU*, 11, 2011.

[11] Hall EJ, Giaccia AJ. *Radiobiology for the Radiologist*. Lippincott Williams and Wilkins, Philadelphia, 6th edition, 2006. ISBN: 0-7817-4151-3.

[12] Scholz M. Effects of ion radiation on cells and tissues. *Advances in Polymer Science*, 162:97–155, 2003.

[13] Durante M. Radiation protection in space. *La Rivista del Nuovo Cimento della Società Italiana di Fisica*, 25(8), 2002.

[14] Cucinotta FA, Kim MHY, Willingham V, George KA. Physical and biological organ dosimetry analysis for international space station astronauts. *Radiation Research*, 170:127–138, 2008.

[15] Connell PP, Hellman S. Advances in radiotherapy and implications for the next century: a historical perspective. *Cancer Research*, 69(2):383–392, 2009.

[16] Martin A, Gaya A. Stereotactic body radiotherapy: a review. *Clinical Oncology*, 22:157–172, 2010.

[17] Jeffray D, Kupelian P, Djemil T, Macklis RM. Review of image-guided radiation therapy. *Expert Reviews of Anticancer Therapy*, 7(2):89–103, 2007.

[18] Durante M, Loeffler JS. Charged particles in radiation oncology. *Nature Reviews Clinical Oncology*, 7:37–43, 2010.

[19] Okada T, Kamada T, Tsuji H, Mizoe JE, Baba M, Kato S, et al. Carbon ion radiotherapy: clinical experiences at National Institute of Radiological Science (NIRS). *Journal of Radiation Research*, 51:355–364, 2010.

[20] Maier M, Barth W, Bayer W, Dahl L, Groening L, Kleffner C, et al. Commissioning of the LINAC for the Heidelberg Heavy Ion Cancer Therapy Centre (HIT). *Proceedings of PAC07*, THPMN014:2734–2736, 2007.

[21] Sato K, Endo K, Endo M, Hattori T, Itano A, Kanai T, et al. Heavy ion medical accelerator in Chiba (HIMAC). *Particle Accelerators*, 33:147–152, 1990.

[22] `http://www.klinikum.uni-heidelberg.de/fileadmin/hit/dokumente/HIT_Broschuere.pdf`.

[23] Kamada T, Tsujii H, Blakely EA, Debus J, De Neve W, Durante M, et al. Carbon ion radiotherapy in Japan: an assessment of 20 years of clinical experience. *The Lancet Oncology*, 16(2):e93–100, 2015.

[24] Ord MJ, Danielli JF. The site of damage in amoebae exposed to X-rays. *Quarterly Journal of Microscopical Science*, pages 29–37, 1956.

[25] Munro TR. The relative radiosensitivity of the nucleus and cytoplasm of Chinese Hamster fibroblasts. *Radiation Research*, 42:451–470, 1970.

[26] Jake Cannon. Cc-by-sa 3.0 license. `http://commons.wikimedia.org/wiki/File:Cell_Structure_,_Cell_Diagram.png`.

[27] Alberts B, Johnson A, Lewis J, et al. *Molecular Biology of the Cell*. Garland Science, New York, 4th edition, 2002. (c) Reproduced by permission of Garland Science/Taylor & Francis Group LLC.

[28] Yokota H, van den Engh G, Hearst JE, Sachs RK, Trask BJ. Evidence for the organization of chromatin in megabase pair-sized loops arranged along a random walk path in the human G0/G1 interphase nucleus. *The Journal of Cell Biology*, 130:1239–1249, 1995. (c) 1995 Yokota et al. Journal of Cell Biology. 130:1239-1249. doi: 10.1083/jcb.130.6.1239.

[29] Solovjeva L, Svetlova M, Stein G, Chagin V, Rozanov Y, Zannis-Hadjopoulos M, et al. Conformation of replicated segments of chromosome fibres in human S-phase nucleus. *Chromosome Research*, 6:595–602, 1998.

[30] Ostashevsky J. A polymer model for the structural organization of chromatin loops and minibands in interphase chromosomes. *Molecular Biology of the Cell*, 9:3031–3040, 1998. CC-BY-NC-SA 3.0 license.

[31] Houtgraaf JH, Versmissen J, van der Giessen WJ. A concise review of DNA damage checkpoints and repair in mammalian cells. *Cardiovascular Revascularization Medicine*, 7:165–172, 2006.

[32] Burke DJ, Stukenberg T. Linking kinetochore-microtubule binding to the spindle checkpoint. *Developmental Cell*, 14(4):474–479, 2008.

[33] Davis PK, Ho A, Dowdy SF. Biological methods for cell-cycle synchronization of mammalian cells. *Bio Techniques*, 30:1322–1331, 2001.

[34] Ward JF. The yield of DNA double-strand breaks produced intracellularly by ionizing radiation: a review. *Internationa Journal of Radiation Biology*, 57(6):1141–1150, 1990.

[35] Kauffmann GW, Moser E, Sauer R. *Radiologie*. Urban und Fischer Verlag, Elsevier GmbH, München, Jena, 3rd edition, 2006. ISBN: 3-437-41991-9.

[36] Olive PL. The role of DNA single- and double strand breaks in cell killing by ionizing radiation. *Radiation Research*, 150:S42–S51, 1998.

[37] Iliakis G. The role of DNA double strand breaks in ionizing radiation-induced killing of eukariotic cells. *BioEssays*, 13(12):641–648, 1991.

[38] Khanna KK, Jackson SP. DNA double-strand breaks: signaling, repair and the cancer connection. *Nature Genetics*, 27:247–254, 2001. Reprinted by permission from Macmillan Publishers Ltd: Nature Genetics, (c)2001.

[39] Durante M, Bedford JS, Chen DJ, Conrad S, Cornforth MN, Natarajan AT, et al. From DNA damage to chromosome aberrations: joining the break. *Mutation Research*, 756(1–2):5–13, 2013.

[40] Obe G, Pfeiffer P, Savage JRK, Johannes C, Goedecke W, Jeppesen P, et al. Chromosomal aberrations: formation, identification and distribution. *Mutation Research*, 504:17–36, 2002.

[41] Prise K, Ahnström G, Belli M, Carlsson J, Frankenberg D, Kiefer J, et al. A review of dsb induction data for varying quality radiations. *International Journal of Radiation Biology*, 74(2):173–184, 1998.

[42] Rogakou E, Boon C, Redon C, Bonner WM. Megabase Chromatin Domains Involved in DNA double-strand breaks in vivo. *The Journal of Cell Biology*, 146(5):905–915, 1999.

[43] Kasten-Pisula U, Tastan H, Dikomey E. Huge differences in cellular radiosensitivity due to only very small variations in double-strand break repair capacity. *International Journal of Radiation Biology*, 81(6):409–419, 2005.

[44] Private communications with Thomas Friedrich.

[45] Stenerlöw B, Blomquist E, Grusell E, Hartman T, Carlsson J. Rejoining of DNA double-strand breaks induced by accelerated nitrogen ions. *International Journal of Radiation Biology*, 70(4):413–420, 1996.

[46] Löbrich M, Cooper PK, Rydberg B. Joining of correct and incorrect DNA ends at double-strand breaks produced by high-linear energy transfer radiation in human fibroblasts. *Radiation Research*, 150(6):619–626, 1998.

[47] Schmid TE, Dollinger G, Beisker W, Hable V, Greubel C, Auer S, et al. Differences in the kinetics of γ -H2AX flourescence decay after exposure to low and high LET radiation. *International Journal of Radiation Biology*, 86(8):682–691, 2010.

[48] Johnston PJ, Bryant PE. A component of DNA double-strand break repair is dependent on the spatial orientation of the lesions within the higher-order structures of chromatin. *International Journal of Radiation Biology*, 66(5):531–536, 1994.

[49] Gauter B, Zlobinskaya O, Weber KJ. Rejoining of radiation-induced DNA double-strand breaks: pulsed-field electrophoresis analysis of fragment size distributions after incubation for repair. *Radiation Research*, 157:721–7333, 2002.

[50] Tommasino F, Friedrich T, Scholz U, Taucher-Scholz G, Durante M, Scholz M. A DNA double-strand break kinetic rejoining model based on the Local Effect Model. *Radiation Research*, 180:524–538, 2013.

[51] Löbrich M, Rydberg B, Cooper PK. Repair of x-ray-induced DNA double-strand breaks in specific Not I restriction fragments in human fibroblasts: joining of correct and incorrect ends. *Proceedings of the National Academy of Sciences USA*, 92:12050–12054, 1995.

[52] Franken NAP, Rodermond HM, Stap J, Haveman J, van Bree C. Clonogenic assay of cells in vitro. *NatureProtocols*, 1(5):2315–2319, 2006.

[53] Private communications with Wilma Kraft-Weyrather.

[54] Garcia LM, Leblanc J, Wilkins D, Raaphorst GP. Fitting the linear-quadratic model to detailed data sets for different dose ranges. *Physics in Medicine and Biology*, 51:2813–2823, 2006.

[55] Sinclair WK, Morton RA. X-ray sensitivity during the cell generation cycle of cultured chinese hamster cells. *Radiation Research*, 29(3):450–474, 1966.

[56] Furusawa Y, Fukutsu K, Aoki M, Itsukaichi H, Eguchi-Kasai K, Ohara H, et al. Inactivation of aerobic and hypoxic cells from three different cell lines by accelerated ^{3}He-, ^{12}C- and ^{20}Ne-ion beams. *Radiation Research*, 154:485–496, 2000.

[57] Andisheh B, Edgren M, Belkić D, Mavroidis P, Brahme A, Lind BK. A comparative analysis of radiobiological models for cell surviving fractions at high doses. *Technology in Cancer Research and Treatment*, 12(2):183–192, 2013.

[58] Astrahan M. Some implications of linear-quadratic-linear radiation dose-response with regard to hypofractionation. *Medical Physics*, 35(9):4161–4172, 2008.

[59] Johnston PJ, Olive PL, Bryant PE. Higher-order chromatin structure-dependent repair of DNA double-strand breaks: modeling the elution of DNA from nucleoids. *Radiation Research*, 148(6):561–567, 1997.

[60] Johnston PJ, MacPhail SH, Banáth JP, Olive PL. Higher-order chromatin structure-dependent repair of DNA double-strand breaks: factors effecting elution of DNA from nucleoids . *Radiation Research*, 149(6):533–542, 1998.

[61] Hufnagl A, Herr L, Friedrich T, Durante M, Taucher-Scholz G, Scholz M. The link between cell-cycle dependent radiosensitivity and repair pathways: a model based on the local, sister-chromatid conformation dependent switch between NHEJ and HR. *DNA Repair*, 27:28–39, 2015.

[62] Friedrich T, Durante M, Scholz M. Modeling cell survival after irradiation with ultrasoft x rays using the Giant Loop Binary Lesion model. *Radiation Research*, 181:485–494, 2014.

[63] Herr L, Friedrich T, Durante M, Scholz M. A model of photon cell killing based on the spatio-temporal clustering of DNA damage in higher order chromatin structures. *PLoS ONE*, 9(1):e83923, 2014.

[64] Stephens TC, Eady JJ, Peacock JH, Steel GG. Split-dose and low dose-rate recovery in four experimental tumour systems. *International Journal of Radiation Biology*, 52(1):157–170, 1987.

[65] Stackhouse MA, Bedford JS. An ionizing radiation-sensitive mutant of CHO cells: irs-20. *Radiation Research*, 136:250–254, 1993.

[66] Wells RL, Bedford JS. Dose-rate effects in mammalian cells. *Radiation Research*, 94:105–134, 1983.

[67] Kelland LR, Steel GG. Dose-rate effects in the radiation response of four human tumour xenografts. *Radiotherapy and Oncology*, 7:259–268, 1986.

[68] Yang X, Darling JL, McMillan TJ, Peacock JH, Steel GG. Radiosensitivity, recovery and dose-rate effect in three human glioma cell lines. *Radiotherapy and Oncology*, 19:49–56, 1990.

[69] Edwards AA, Lloyd DC. Risks from ionising radiation: deterministic effects. *Journal of Radiological Protection*, 18(3):175–183, 1998.

[70] Lea DE. *Actions of Radiations on Living Cells*. Cambridge University Press, London, 1946.

[71] Catcheside DG, Lea DE, Thoday JM. The production of chromosome structural changes in tradescantia microspores in relation to dosage, intensity and temperature. *Journal of Genetics*, 47:137–149, 1946.

[72] Sachs RK, Hahnfeld P, Brenner DJ. The link between low-LET dose-response relations and the underlying kinetics of damage production/repair/misrepair. *International Journal of Radiation Biology*, 72(4):351–374, 1997.

[73] Tobias CA, Blakely EA, Ngo FQH, Yang TCH. *The Repair-Misrepair Model of cell survival, in Radiation Biology in Cancer Research (R.A. Meyn and H.R. Withers, Eds.)* . Raven Press, New York, 1980. pp. 195–230.

[74] Curtis SB. Lethal and potentially lethal lesions induced by radiation - a unified repair model. *Radiation Research*, 106:252–270, 1986.

[75] Burnham KP, Anderson DR. *Model selection and multimodel inference: a practical information-theoretic approach*. Springer Verlag, New York, Berlin, Heidelberg, 2nd edition, 2002.

[76] Andrae R, Schulze-Hertung T, Melchior P. Dos and don'ts of reduced chi-squared. arXiv:1012.3754v1.

[77] Herr L, Friedrich T, Durante M, Scholz M. Sensitivity of the Giant Loop Binary Lesion model on parameters characterising dose rate effects. *Radiation Protection Dosimetry*, 2015.

[78] GetData Graph Digitizer. `http://www.getdata-graph-digitizer.com/index.php`.

[79] Bentzen SM, Skoczylas JZ, Bernier J. Quantitative clinical radiobiology of early and late lung reactions. *International Journal of Radiation Biology*, 76(4):453–462, 2000.

[80] Van Os R, Thames HD, Konings AWT, Down JD. Radiation dose-fractionation and dose-rate relationships for long-term repopulating hemopoietic stem cells in a murine bone marrow transplant model. *Radiation Research*, 136:118–25, 1993.

[81] Núñez MI, Villalobos M, Olea N, Valenzuela MT, Pedraza V, McMillan TJ, et al. Radiation-induced DNA double-strand break rejoining in human tumour cells. *British Journal of Cancer*, 71:311–316, 1995.

[82] Carruthers SA, Wallington MM. Total body irradiation and pneumonitis risk: a review of outcomes. *British Journal of Cancer*, 90:2080–2084, 2004.

[83] Down JD, Easton DF, Steel GG. Repair in the mouse lung during low dose-rate irradiation. *Radiotherapy and Oncology*, 6:29–42, 1986.

[84] Brenner DJ, Ward JF. Constraints on energy deposition and target size of multiply damaged sited associated with DNA double-strand breaks. *International Journal of Radiation Biology*, 61(6):737–748, 1992.

[85] Ward JF. The complexity of DNA damage: relevance to biological consequences. *Internationa Journal of Radiation Biology*, 57(6):1141–1150, 1990.

[86] Ottolenghi A, Merzagora M, Tallone L, Durante M, Paretzke HG, Wilson WE. The quality of dna double-strand breaks: a monte carlo simulation of the end-structur of strand breaks produced by protons and alpha particles. *Radiation and Environmental Biophysics*, 34:239–244, 1995.

[87] Nikjoo H, O'Neill P, Wilson WE, Goodhead DT. Computational approach for determining the spectrum of DNA damage induced by ionizing radiation. *Radiation Research*, 156(5):577–583, 2001.

[88] Nikjoo H, Uehara S, Wilson WE, Hoshi M, Goodhead DT. Track structure in radiation biology: theory and applications. *International Journal of Radiation Biology*, 73(4):355–364, 1998.

[89] Goodhead DT. Initial events in the cellular effects of ionizing radiations: clustered damage in DNA. *International Journal of Radiation Biology*, 65(1):7–17, 1994.

[90] Private communications with Dudley Goodhead.

[91] Löbrich M, Shibata A, Beucher A, Fisher A, Ensminger M, Goodarzi AA, et al. γ -H2AX foci analysis for monitoring DNA double-strand break repair - strengths, limitations and optimization. *Cell Cycle*, 9(4):662–669, 2010.

[92] Neumaier T, Swenson J, Pham C, Polyzos A, Lo AT, . Evidence for formation of DNA repair centers and dose-response nonlinearity in human cells. *Proceedings of the National Academy of Sciences USA*, 109(2):443–448, 2012.

[93] Seeger A. *Modellierung des Einflusses einer Chromatin Loop Größenverteilung auf das Zellüberleben unter Verwendung des GLOBLE Photon Dose Response Modells*. Master thesis, TU Darmstadt, 2012.

[94] Foray N, Badie C, AlsbeihG, Fertil B, Malaise EP. A new model describing the curves for repair of both DNA double-strand breaks and chromosome damage. *Radiation Research*, 146(1):53–60, 1996.

[95] Fowler JF. Is repair of DNA strand break damage from ionizing radiation second-order rather than first-order? A simpler explanation of apparantly multiexponential repair. *Radiation Research*, 152(2):124–136, 1999.

[96] Herr L, Shuryak I, Friedrich T, Scholz M, Durante M, Brenner DJ. New insight into quantitative modeling of DNA double strand break rejoining. *Radiation Research*, 2015.

[97] Cucinotta FA, Nikjoo H, O'Neill P, Goodhead DT. Kinetics of DSB rejoining and formulation of simple chromosome exchange aberrations. *International Journal of Radiation Biology*, 76(11):1463–1474, 2000.

[98] Pinto M, Prise KM, Michael BD. A monte carlo model of dna double-strand break clustering and rejoining kinetics for the analysis of oulsed-field gel electrophoresis data. *Radiation Research*, 162(4):453–463, 2004.

[99] Stamato T, Guerriero S, Denko N. Two methods for assaying DNA double-strand break repair in mammalian cells by asymmetric field inversion gel electrophoresis. *Radiation Research*, 133(1):60–66, 1993.

[100] Wolfram Mathematica.
`http://www.wolfram.com/mathematica/`.

[101] Kysela BP, Michael BD, Arrand JE. Relative contributions of levels of initial DNA damage and repair of double strand breaks to the ionizing radiation-sensitive phenotype of Chinese hamster cell mutant, XR-V15B. *International Journal of Radiation Biology*, 63(5):609–616, 1993.

[102] Badie C, Iliakis G, Foray N, Alsbeih G, Cedervall B, Chavaudra N, et al. Induction and rejoining of DNA double-strand breaks and interphase chromosome breaks after exposure to X rays in one normal and two hypersensitive human fibroblast cell lines. *Radiation Research*, 144(1):26–35, 1995.

[103] Rydberg B, Löbrich M, Cooper PK. DNA double-strand breaks induced by high-energy neon and iron ions in human fibroblasts. I. Pulsed-field gel electrophoresis method. *Radiation Research*, 139(2):133–141, 1994.

[104] Radivoyevitch T, Hoel DG, Hahnfeldt PJ, Rydberg B, Sachs RK. Recent data obtained by pulsed-field gel electrophoresis suggest two types of double-strand breaks. *Radiation Research*, 149(1):52–58, 1998.

[105] Fertil B, Reydellet I, Deschavanne PJ. A benchmark of cell survival models using survival curves for human cells after completion of repair of potentially lethal damage. *Radiation Research*, 138:61–69, 1994.

[106] Herr L, Friedrich T, Durante M, Scholz M. A comparison of kinetic photon cell survival models. *Radiation Research*, 2015.

[107] Holmes A, McMillan TJ, Peacock JH, Steel GG. The radiation dose-rate effect in two human neuroblastoma cell lines. *British Journal of Cancer*, 62:791–795, 1990.

[108] Sontag W. Comparison of six different models describing survival of mammalian cells after irradiation. *Radiation and Environmental Biophysics*, 29:185–201, 1990.

[109] Brenner DJ, Hlatky LR, Hahnfeldt PJ, Huang Y, Sachs RK. The linear-quadratic model and most other common radiobiological models result in similar predictions of time-dose relationships. *Radiation Research*, 150(1):83–91, 1998.

[110] Goodhead DT. Saturable repair models of radiation action in mammalian cells. *Radiation Research Supplement*, 8:S58–S67, 1985.

[111] Stewart RD. Two-lesion kinetic model of double-strand break rejoining and cell killing. *Radiation Research*, 156(4):365–378, 2001.

[112] Wang JZ, Huang Z, Lo SS, Yuh WT, Mayr NA. A generalized linear-quadratic model for radiosurgery, stereotactic body radiation therapy, and high-dose rate brachytherapy. *Science Translational Medicine*, 2(39):39ra48, 2010.

[113] Franken NAP, Barendsen GW. In regard to Ohri N et al. *International Journal of Radiation Oncology*Biology*Physics*, 86(4):598, 2013.

[114] Hawkins RB. A microdosimetric-kinetic of cell death from exposure to ionizing radiation of any LET, with experimental and clinical applications. *International Journal of Radiation Biology*, 69(6):739–755, 1996.

[115] Inaniwa T, Suzuki M, Furukawa T, Kase Y, Kanematsu N, Shirai T, et al. Effects of dose-delivery time structure on biological effectiveness for therapeutic carbon-ion beams evaluated with Microdosimetric Kinetic Model. *Radiation Research*, 180:44–59, 2013.

[116] Minohara S, Kanai T, Endo M, Noda K, Kanazawa M. Respiratory gated irradiation system for heavy-ion radiotherapy. *International Journal of Radiation Oncology*Biology*Physics*, 47(4):1097–1103, 2000.

[117] ICRP Publication 103. The 2007 recommendations of the International Commission on Radiological Protection. *Annals of ICRP*, 37(2–4), 2007.

[118] ICRP Publication 99. Low-dose extrapolation of radiation-related cancer risk. *Annals of ICRP*, 35(4), 2005.

[119] NRC. National Research Council. *Health risks from exposure to low levels of ionizing radiation: BEIR VII - phase 2.* National Academy Press, Washington DC, 2006.

[120] Herr L, Friedrich T, Durante M, Scholz M. Investigation of time-dose relationships in the cellular response to ion irradiation with the Local Effect Model. *In preparation*, 2015.

[121] Private communications with Taku Inaniwa.

[122] Kase Y, Kanai T, Matsumoto Y, Furusawa Y, Okamoto H, Asaba T, et al. Microdosimetric measurements and estimation of human cell survival for heavy-ion beams. *Radiation Research*, 166:629–638, 2006.

[123] Matsumoto Y, Matsuura T, Wada M, Egashira Y, Nishio T, Furusawa Y. Enhanced radiobiological effects at the distal end of a clinical proton beam: in vitro study. *Journal of Radiation Research*, pages 1–7, 2014.

[124] Kase Y, Yamashita W, Matsufuji N, Takada K, Sakae T, Furusawa Y, et al. Microdosimetric calculation of relative biological effectiveness for design of therapeutic proton beams. *Jornal of Radiation Research*, pages 1–9, 2012.

[125] Wang J, Li R, Guo C, Fournier C, Kraft-Weyrather W. The influence of fractionation of cell survival and premature differentiation after carbon ion irradiation. *Journal of Radiation Research*, 49:391–398, 2008.

[126] Wada M, Suzuki M, Liu C, Kaneko Y, Fukuda S, Ando K, et al. Modeling the biological response of normal human cells, including repair processes, to fractionated carbon beam irradiation. *Journal of Radiation Research*, 54:798–807, 2013.

[127] Suzuki M, Kase Y, Kanai T, Ando K. Change in radiosensitivity with fractionated-dose irradiation of carbon-ion beams in five different human cell lines. *International Journal of Radiation Oncology*Biology*Physics*, 48(1):251–258, 2000.

[128] Ngo FQH, Blakely EA, Tobias CA. Sequential exposures of mammalian cells to low- and high-LET radiations: I. Lethal effects following x-ray and neon-ion irradiation. *Radiation Research*, 87(1):59–78, 1981.

[129] Fry RJM. A note on the dose-rate effectiveness factor and its progeny ddref. `http://three.usra.edu/articles/DDREF.pdf`.

[130] Schimmerling W, Cucinotta FA. Dose and dose rate effectiveness of space radiation. *Radiation Protection Dosimetry*, 122(1–4):349–353, 2006.

[131] Cheong N, Wang Y, Jackson M, Iliakis G. Radiation-sensitive irs mutants rejoin DNA double-strand breaks with efficiency similar to that of parental V79 cells but show altered response to radiation-induced G_2 delay. *Mutation Research, DNA Repair*, 274:111–122, 1992.

[132] Metzger L, Iliakis G. Kinetics of DNA double-strand break repair throughout the cell cycle as assayed by pulsed field gel electrophoresis in CHO cells. *International Journal of Radiation Biology*, 59(6):1325–1339, 1991.

[133] Rothkamm K, Krüger I, Thompson LH, Löbrich M. Pathways of DNA double-strand break repair during the mammalian cell cycle. *Molecular and Cellular Biology*, 23(16):5706–5715, 2003.

[134] Whitaker SJ, Ung YC, McMillan TJ. DNA double-strand break induction and rejoining as determinants of human tumour cell radiosensitivity. A pulsed-gel electrophoresis study. *International Journal of Radiation Biology*, 67(1):7–18, 1995.

[135] Stenerlöw B, Höglund E, Carlsson J, Blomquist E. Rejoining of DNA fragments produced by radiations of different linear energy transfer. *International Journal of Radiation Biology*, 76(4):549–557, 2000.

[136] Ruiz de Almodóvar JM, Bush C, Peacock JH, Steel GG, Whitaker SJ, McMillan TJ. Dose-rate effect for DNA damage induced by ionizing radiation in human tumor cells. *Radiation Research*, 138(1):S93–S96, 1994.

CV Lisa Antje Herr

Personal details	
Address	Alpenroder Straße 26 65936 Frankfurt/M.
Date of Birth	21. January 1988
Place of Birth	Frankfurt/Main-Höchst
Nationality	German

Education	
Since 2012	Research for the PhD at the department for biophysics at the GSI, Darmstadt • September 2014 - February 2015: Research at the Columbia University in New York City (USA)
2010-2012	MSc Physics with minor subjects Mathematics and Economics, Johann Wolfgang Goethe-Universität Frankfurt • Graduation: 26.04.12 • Grade: 1.0 • April 2011 - April 2012: Research for the Master thesis at the GSI Darmstadt, Topic: Modeling cell survival after photon irradiation (biophysics)
2007 - 2010	BSc Physics with minor subject Economics, Johann Wolfgang Goethe-Universität Frankfurt • 17.09.10: Graduated with distinction • Grade: 1.0 • April - July 2010: Research for the Bachelor thesis at the NRC in Ottawa (Canada), Topic: Alignment test with nitrogen molecules for a bromine dissociation experiment (atomic and laser physics)
1998 - 2007	Gymnasium (middle and high school) Albert Einstein-Gymnasium, Schwalbach • 21.06.07: Allgemeine Hochschulreife • Grade: 1.0 • Focal courses Mathematics and French
1994 - 1998	Elementary school Geschwister Scholl-Grundschule, Schwalbach

Achievements

- 2013: Philipp Siedler Preis for an excellent Master thesis
- 2013: Travel award for the MICROS International Symposium on Microdosimetry
- 2013: Participant in the NASA Space Radiation Summer School at the Brookhaven National Laboratory
- Since 2012: Member of the Helmholtz Graduate School for Hadron and Ion Research
- 2012: Awarded with a scholarship for PhD studies by the "Studienstiftung des Deutschen Volkes"
- 2010: Michael Loulakis Preis for excellent studies
- 2008-2012: Awarded with a scholarship for Bachelor- and Master studies by the "Studienstiftung des Deutschen Volkes"
- 2008-2012: Member of "YOLANTE", a support program for female students by Siemens
- 2007: Awarded for school performance in physics by the "Deutsche Physikalische Gesellschaft"
- 2007: Awarded for school performance in French by the "Robert Bosch-Stiftung"

Working experience

- Since February 2013: Employee at the GSI, Darmstadt
- June-September 2012: Internship at "Quoniam Asset Management GmbH", Frankfurt
- 2010-2011: Tutor for atomic physics, Johann Wolfgang-Goethe Universität, Frankfurt
- March-April 2009: Internship at the department of risk controlling of the "Kreditanstalt für Wiederaufbau", Frankfurt
- October-December 2008: Working experience at the "Institut für Biophysik", Johann Wolfgang Goethe-Universität, Frankfurt
- June-July 2008: Internship at the "Faculté des Sciences de Luminy" (department of biophysics of the University of Marseille)
- August-September 2007: Internship at the" Institut für Biophysik", Johann Wolfgang Goethe-Universität, Frankfurt
- January 2006: Internship at the editorial office of a regional newspaper
- October 2003: Internship at retail

Other skills

- September 2009: Englisch language course in Cambridge, graded with CEFR C2
- 1999: Student exchange with France
- Foreign languages: English, French, Spanish, Latin

Erklärung zur Dissertation

Hiermit versichere ich, die vorliegende Dissertation ohne Hilfe Dritter nur mit den angegebenen Quellen und Hilfsmitteln angefertigt zu haben. Alle Stellen, die aus Quellen entnommen wurden, sind als solche kenntlich gemacht. Diese Arbeit hat in gleicher oder ähnlicher Form noch keiner Prüfungsbehörde vorgelegen.

Darmstadt, den 26.06.15

(Lisa Herr)

Danksagung

An erster Stelle möchte ich mich gerne bei den Menschen bedanken, die meine Promotion betreut haben und mit denen ich seit meiner Masterarbeit 2012 zusammen gearbeitet habe. Vielen Dank an Marco Durante, der es mir als mein Doktorvater ermöglicht hat, in der Strahlungsgemeinschaft Fuß zu fassen. Vor allem meine Teilnahme an der NASA Summer School und mein Gastaufenthalt an der Columbia University waren sehr lehrreich und haben mich unglaublich weiter gebracht. Mein besonderer Dank gilt Michael Scholz und Thomas Friedrich, die meine Doktorarbeit betreut haben und meine Ansprechpartner waren. Außerdem gilt mein herzlicher Dank Barbara Drossel, die mir stets mit Rat und Tat zur Seite stand. So viel Engagement kann man seitens einer "externen" Betreuerin sicherlich in den seltensten Fällen erwarten.

Vielen lieben Dank auch an Gerhard Kraft für horizont-erweiternde Gespräche und gelegentliches Mut-Machen. Ein fröhliches Danke geht an Olaf Steinsträter, bei dem ich jederezeit mit Problemen im Büro auftauchen konnte und mit dem man herzlich über sich selbst lachen konnte. Danke auch an Rebecca Grün und Francesco Tommasino, die seit Beginn meiner Masterarbeit fester Bestandteil unserer Gruppe waren.

For an excellent collaboration I would also like to thank my colleagues from the Center for Radiological Research of the Columbia University. Thank you to David Brenner for giving me the opportunity to spend half a year in his group. Every single day was worth it. My sincerest thanks go to Igor Shuryak who helped me to develop an unbelievable amount of ideas about what one could investigate. It was nice to turn around and to know that my questions will be answered before I can finish them.

Des weiteren gilt mein Dank der Studienstiftung des deutschen Volkes, die mich seit Beginn meines Studiums 2007 gefördert hat. Insbesondere möchte ich meinem Vertrauensdozenten Dirk Rischke danken, der mich durchgehend begleitet und unterstützt hat. Danke auch an HGS-Hire für die Förderung meiner Promotion.

Zu guter letzt möchte ich quasi in Papierform Mama, Karen, Annika, Antje, Onkel Heinz und Vaddern umarmen. Es gibt nichts schöneres als zu wissen, dass ihr Tag und Nacht für mich da seid und dass mir nichts schlimmes passieren kann, so lange es euch gibt.